A Riemannian Geometric Mapping Technique for Identifying Incompressible Equivalents to Subsonic Potential Flows

A Thesis
Presented to
The Academic Faculty

by

Brian Joseph German

In Partial Fulfillment
of the Requirements for the Degree
Doctor of Philosophy

Daniel Guggenheim School of Aerospace Engineering
Georgia Institute of Technology
May 2007

A Riemannian Geometric Mapping Technique for Identifying Incompressible Equivalents to Subsonic Potential Flows

Approved by:

Prof. Dimitri Mavris, Committee Chair
School of Aerospace Engineering
Georgia Institute of Technology

Prof. Jechiel Jagoda
School of Aerospace Engineering
Georgia Institute of Technology

Prof. Stephen Ruffin
School of Aerospace Engineering
Georgia Institute of Technology

Prof. Lakshmi Sankar
School of Aerospace Engineering
Georgia Institute of Technology

Dr. Jim McMichael
Aerospace, Transportation, and Advanced Systems Laboratory
Georgia Tech Research Institute

Date Approved: 14 March 2007

To my parents

ACKNOWLEDGEMENTS

The dissertation process has been a long and arduous but enjoyable journey for me, and I wish to thank sincerely those who have contributed along the way.

I would first like to express profound appreciation to my thesis committee. Professors Jagoda and Ruffin were kind enough to listen to too many of my presentations over the years and to provide guidance and insights at all stages of the process. I credit Professor Ruffin's excellent teaching during my undergraduate and graduate education as inspirational for my interest in computational and theoretical fluid dynamics. I would particularly like to thank Professor Jagoda for taking an interest in meeting with me frequently over the last nine months of the effort to make sure that the end product was coalesced to an appropriate level of quality. I also appreciate his encouragement to think about this topic from the perspective of theoretical physics as much as from the standpoint of numerical methods. I asked Professor Sankar to join the committee late in the process, and I regret not having asked sooner—his insightful observations and comments, reflecting his deep experience in potential flow, helped both to improve the method and to place the work in the correct historical context. Dr. McMichael was also immensely supportive, and I appreciate our philosophical discussions on the "conservation of complexity" based on his experience in turbulence modeling as well as his willingness to offer his valuable time in the process. Thanks everyone.

Of course, I also wish to thank sincerely Professor Dimitri Mavris, my advisor, for many things including the freedom to pursue this topic. Professor Mavris has been an excellent mentor, and I will always appreciate the opportunities he has afforded me—for allowing me a year to study abroad amidst graduate school; for developing my proposal, presentation, and leadership skills; for teaching me the philosophy of research; and most importantly, for trusting me to make this thesis happen even when he should have thought otherwise. Thanks Doc.

Next, I would like to thank my friends and compatriots from the Aerospace Systems Design Laboratory of the Daniel Guggenheim School of Aerospace Engineering at Georgia Tech. Since I began graduate school, many have come and gone, but they have all contributed to creating a pleasant and rewarding intellectual environment. In particular, I wish to thank Andrew Frits, Peter Hollingsworth, Bryce Roth, Janel Nixon, Jack Zentner, Peter De Baets, Tommer Ender, Santiago Balestrini-Robinson, and Patrick Biltgen for frequently checking in to track and encourage my progress. Thanks guys.

One friend deserves more thanks than these few pages can convey. Rob McDonald has been a sounding board for almost every idea that has made its way into this dissertation. He has offered and I have called upon his unequaled engineering talent and knowledge of aerodynamics, numerical methods, and the graphical presentation of data countless times over my years in graduate school. In many ways, I consider the outcomes of this research as much a result of Rob's insights as of my own labors. Thanks Rob.

I also wish to thank Karen Feigh for tolerating the many years consumed by the production of this dissertation and for helping me to enjoy the life in between. She has been patient and supportive, in large part because she understands what this is all about. Her companionship has been instrumental in my ability to complete this work. Thanks Karen.

Finally, I wish to thank my parents, to whom this dissertation is dedicated. They have been my lifelong admirers and supporters in all things academic and all things not. My father's interest in airplanes and technology inspired my own, and my mother's dedication to my academic success has encouraged me throughout the years. From helping me with my homework when I was a youngster, to attending all academic events with me, to being interested in what I'm working on even now, they have always been there. Thanks Mom and Dad.

But enough with the sappiness.... Let's dig in.

Brian

March 2007

TABLE OF CONTENTS

LIST OF TABLES

LIST OF FIGURES

LIST OF SYMBOLS

α	Angle of attack.
γ	Ratio of specific heats.
ϕ	Velocity potential.
ψ	Stream function.
ρ_0	Stagnation density.
a	Sound speed.
c	Speed of light (Chapter 1); a constant (Chapter 4); chord (Chapter 6).
M_∞	Freestream Mach number.
p	Pressure.
u_μ	Covariant velocity vector.
V	Velocity magnitude.
ϵ	Outer loop convergence tolerance.
Ω	Undetermined conformal factor (Chapter 4); over-relaxation parameter (Chapters 5 and 6).
τ	Notation for a factor appearing in the metric tensor (Chapter 4); inner loop convergence tolerance (Chapters 5 and 6).
ζ	Off-body grid spacing parameter.
i	Index in the $\tilde{x}^1$ direction in the computational frame.
i_{max}	Number of grid points in i direction.
j	Index in the $\tilde{x}^2$ direction in the computational frame.
j_{max}	Number of grid points in j direction.
$\bar{x}^\mu$	Coordinates in the isothermal frame of the canonical flow.
$\tilde{x}^\mu$	Coordinates in the auxiliary computational frame.
x^μ	Coordinates in the frame of the original flow.
δ^α_σ	Kronecker delta tensor.
$\epsilon^{\kappa\lambda}$	Permutation pseudotensor.
σ	Arbitrary conformal factor in the metric tensor.
g	Determinant of the covariant metric tensor of the equivalent flow.

$g^{\mu\nu}$	Contravariant metric tensor of the equivalent flow.
$g_{\mu\nu}$	Covariant metric tensor of the equivalent flow.
h	Determinant of the covariant metric tensor of the original flow.
$h^{\mu\nu}$	Contravariant metric tensor of the original flow.
$h_{\mu\nu}$	Covariant metric tensor of the original flow.

SUMMARY

This research develops a technique for the solution of incompressible equivalents to planar steady subsonic potential flows. Riemannian geometric formalism is used to develop a gauge transformation of the length measure followed by a curvilinear coordinate transformation to map the given subsonic flow into a canonical Laplacian flow with the same boundary conditions. The effect of the transformation is to distort both the immersed profile shape and the domain interior nonuniformly as a function of local flow properties. The method represents the full nonlinear generalization of the classical methods of Prandtl-Glauert and Kármán-Tsien. Unlike the classical methods which are "corrections," this method gives exact results in the sense that the inverse mapping produces the subsonic full potential solution over the original airfoil, up to numerical accuracy.

The motivation for this research was provided by an observed analogy between linear potential flow and the special theory of relativity that emerges from the invariance of the d'Alembert wave equation under Lorentz transformations. This analogy is well known in an operational sense, being leveraged widely in linear unsteady aerodynamics and acoustics, stemming largely from the work of Küssner.

Whereas elements of the special theory can be invoked for compressibility effects that are *linear* and *global* in nature, the question posed in this work was whether other mathematical techniques from the realm of relativity theory could be used to similar advantage for effects that are *nonlinear* and *local*. This line of thought led to a transformation leveraging Riemannian geometric methods common to the general theory of relativity. A gauge transformation is used to geometrize compressibility through the metric tensor of the underlying space to produce an equivalent incompressible flow that lives not on a plane but on a curved surface. In this sense, forces owing to compressibility can be ascribed to the geometry of space in much the same way that general relativity ascribes gravitational forces to the curvature of space-time. Although the analogy with general relativity is fruitful, it

is important not to overstate the similarities between compressibility and the physics of gravity, as the interest for this thesis is primarily in the mathematical framework and not physical phenomenology or epistemology.

The thesis presents the philosophy and theory for the transformation method followed by a numerical method for practical solutions of equivalent incompressible flows over arbitrary closed profiles. The numerical method employs an iterative approach involving the solution of the equivalent incompressible flow with a panel method, the calculation of the metric tensor for the gauge transformation, and the solution of the curvilinear coordinate mapping to the canonical flow with a finite difference approach for the elliptic boundary value problem. This method is demonstrated for non-circulatory flow over a circular cylinder and both symmetric and lifting flows over a NACA 0012 profile. Results are validated with accepted subcritical full potential test cases available in the literature. For chord-preserving mapping boundary conditions, the results indicate that the equivalent incompressible profiles thicken with Mach number and develop a leading edge droop with increased angle of attack.

Two promising areas of potential applicability of the method have been identified. The first is in airfoil inverse design methods leveraging incompressible flow knowledge including heuristics and empirical data for the potential field effects on viscous phenomena such as boundary layer transition and separation. The second is in aerodynamic testing using distorted similarity-scaled models.

CHAPTER I

INTRODUCTION AND MOTIVATION

This dissertation presents a philosophy, theory, numerical technique, and representative results for the solution of incompressible equivalents corresponding to two-dimensional steady subsonic potential flows. The approach involves a coordinate and gauge mapping procedure leveraging Riemannian geometric techniques. At least three possible areas of applicability for the technique are anticipated:

1. Design and inverse design of airfoils and other geometries for subsonic flow applications
2. Flow similarity scaling in aerodynamic test scenarios
3. Solutions of subsonic potential flows via their incompressible equivalents.

The motivation for the particular theoretical formulation has emerged from the following observations:

- The success of the classical compressibility corrections, which function through mappings to equivalent incompressible flows
- An underlying framework for linear potential flows based on the Lorentz transformation, suggesting a special relativistic analogy
- The idea of seeking further mathematical tools and physical principles from the general theory of relativity to solve the fully nonlinear mapping problem.

In this chapter, we first discuss equivalent incompressible flow mappings within the historical context of subsonic aerodynamics and outline the promise of extensions to the classical methods. Next, we describe the underlying special relativistic framework for linear potential flows and suggest how this framework leads naturally to the idea of a fully nonlinear approach leveraging certain concepts from the general theory of relativity.

1.1 The History and Promise of Equivalent Incompressible Flow Mappings

The study of subsonic compressible aerodynamics has a history dating primarily to the fundamental inquests of Ludwig Prandtl in the 1920s–1930s in Göttingen, Germany [92, 93]. Although incompressible potential flow had been substantially understood by the time of the mid-eighteenth century and the work of d'Alembert [68], the need to address compressibility had not emerged until high subsonic flight became an aviation imperative beginning in the 1930s.

Early work in this area, epitomized by the celebrated Prandtl–Glauert rule [92, 44], achieved great success through transformation methods that linked a given subsonic flow to an equivalent incompressible flow. Another example of this type of transformation approach is provided by the Kármán–Tsien method, which achieves a similar mapping to an incompressible field through the intermediary of the hodograph plane [117, 126]. These types of transformation approaches are often collectively termed as *compressibility corrections*. In addition to mapping the flow solution itself, certain implementations of these methods also transform the coordinates of the flow, and hence, the shapes of immersed aerodynamic bodies.

The motivating factor for these transformation techniques was primarily one of practicality. Much was known from the long-studied field of incompressible flow, and there was great desire to leverage this extensive knowledge base as much as possible for the problem of compressible fluids. This knowledge included analytical techniques for solving the incompressible boundary value problem and voluminous experimental data on profiles of aerodynamic interest.

The Prandtl–Glauert and Kármán–Tsien rules saw widespread application during the early period of aerodynamics aimed at flight in the compressible regime. As more advanced techniques emerged for improved predictions of compressibility, these transformation methods remained important for providing first-order comparisons. In many instances, these early methods have been preferred for their simplicity over more advanced methods, as they generally provide good predictive capability for the flows over thin bodies that typify

common aerodynamic situations. Indeed, these methods still see ubiquitous use today as compressibility corrections to extend incompressible aerodynamic computations to reasonable approximations of subsonic flows [30].

Although these techniques saw much early success and remain relevant in certain contexts, the era of transformations was soon surpassed by the era of direct calculation. With the advent of advanced analog and rudimentary digital computers in the 1940s–1950s, the possibility of solving nonlinear compressible flows over arbitrary bodies began to emerge. Initial efforts toward these ends employed series expansion techniques such as the Rayleigh–Janzen method [55, 56, 49, 122]. This technique sought solutions at particular points in a flow field by creating a series in terms of the freestream Mach number, with each term tailored to match a particular truncated form of the original differential equation [120].

Later computational advances allowed direct solutions to subsonic flows using the relaxation technique for elliptic boundary value problems [36, 37]. This technique represents the beginning of the transition to the modern approach, in that the field is overlayed by a mesh of points and the solution to the flow is found by iteratively sweeping through this mesh to solve the discretized partial differential equation. Similar techniques existed for the solution of purely hyperbolic equations for supersonic flows, but attempts to solve mixed transonic flows with supersonic pockets surrounded by a subsonic domain proved largely unsuccessful [4]. The reason for this failure was that the numerical stencil for discretizing hyperbolic problems must be fundamentally different than that for an elliptic problem. Whereas elliptic stencils can accept information from any neighboring mesh point, hyperbolic problems involve a directional flow of information that must be respected by the discretization scheme.

This problem was later solved by the seminal work of Murman and Cole, who modified the relaxation technique to estimate the type of the flow at all points *a priori* in each sweep, such that the appropriate numerical stencil could be chosen [85]. This work led to the rapid development of computer programs for practical transonic aerodynamic analysis using the full potential equation and was successively evolved to the Euler equations. The era of computational fluid dynamics had arrived for the aerodynamic problem. The rest, as they say, is history.

Aerodynamic problems of almost any type can now be solved in reasonable time, even including three-dimensional transonic flows with complex effects such as shock/boundary layer interaction. Perhaps the only remaining fundamental challenge is to accurately model fully turbulent flows over arbitrary shapes with reasonable computational expense.

The shift in emphasis from transformation methods to direct approaches for solving subsonic flows was perhaps a natural one. Whereas transformation methods mapped to incompressible flows to make solutions tractable, the direct computational approaches obviated the need for the incompressible intermediate. The direct calculation methods also provided greatly enhanced prediction capability, and whereas most transformation techniques were valid only for subsonic flows, these direct methods could also solve flows of mixed type.

Although there was much gained in this transition to direct solution methods, there remains a great appeal to the notion of equivalent incompressible flows obtained through a transformation approach. Much of this appeal comes from the original motivation for the classical compressibility corrections—leveraging the vast knowledge base of incompressible aerodynamics. The qualitative features of incompressible flow fields are completely understood, and quantitative solutions can be calculated readily by analytical approaches or simple and efficient numerical techniques such as the boundary element method. These flows are also perhaps the best understood in terms of how the external field affects viscous phenomena such as boundary layer transition and separation.

A significant advance would be obtained if we could extend beyond the linearized approximations of the original compressibility corrections and develop truly accurate incompressible equivalents that account for the full nonlinearity of the subsonic flow. These flows would ideally represent exact solutions in the sense that the inverse mapping would produce the full potential solution over the original geometry. The idea of this capability is among the primary motivations for this thesis work.

At least three application areas for such a capability present themselves. The first is in airfoil design and inverse design. As an example of this design utility, it may be possible to geometrically tailor high lift airfoils by considering their equivalent incompressible flows

and corresponding transformed geometries. High lift flows are characterized by large suction peaks with significant localized compressibility effects even though the freestream Mach number is low. For these situations, the classical corrections fail to capture the salient compressibility effects because their action is typically a global scaling based on the freestream magnitude. Because high lift designs operate with a significant adverse pressure gradient that tends to separate the boundary layer, care must be taken to assure that the design pressure distributions provide adequate separation margin. Since separation effects are well understood in incompressible flows, equivalent flows might provide significant design insights for these situations.

A second application of incompressible equivalent flows involves similarity scaling in aerodynamic testing. In certain situations, the classical compressibility corrections are currently used to adjust results obtained in tests at lower speeds to approximately represent higher Mach subsonic flows. The advantage of this approach is that it allows facilities with lower test section velocities to be used, resulting in reduced power requirements, complexity, and cost. An example of this method is found in similarity-scaled turbomachinery rigs [132, 130]. A capability of developing accurate equivalent incompressible geometries could allow these shapes to be used for low speed tests. Results for the actual flight hardware could then be obtained through the inverse transformation of the test data.

The third application area is to use the simplicity of the equivalent incompressible flows as a means to solve the fully nonlinear subsonic flow. If an incompressible equivalent could be developed, the flow could be solved over this geometry using a simple boundary element method and then mapped to the original geometry to determine the subsonic solution. This type of capability would represent a generalization of a classical use of the Prandtl–Glauert and Kármán–Tsien type corrections. If the mapping were exact, however, the results would comprise solutions in the true full potential sense and not simply compressibility corrections.

Beyond these potential applications, a second motivation of this thesis has its roots in a scientific pursuit somewhat independent of possible practical utility. This motivation is based on observations of similarities in the classical Prandtl–Glauert type coordinate transformations and the special theory of relativity. These similarities have been noted

in the past, but their existence has served as an inspiration and guidepost for the line of thought that led to the nonlinear mapping method developed in this dissertation. This mapping method is founded on the idea of extending this special relativistic analogy, which is linear and global, to a general relativistic analogy that is nonlinear and local. In the next section, we discuss this motivating special relativistic framework, and in the following section, we describe the idea of an approach leveraging certain mathematical and physical aspects of the general theory of relativity.

1.2 A Special Relativistic Framework for Fluid Compressibility

Before describing the relationship between the theory of relativity and compressible flow, we begin with a statement regarding scope and intent. The theory of relativity is rife with deep physical meaning as well as subtle and counterintuitive implications. Einstein's great ability in formulating the theory was to trust his visionary insights and to pursue them to their logical conclusions through clear and simple thought experiments, regardless of the apparent paradoxes produced. Many observers stand at rail platforms and on trains, flashlights and clocks in hand. Others fall in elevators, and marvel that they are weightless. The insights provided by these types of mental models have been crucial, yet there is a caveat.

Popular accounts of the theory are filled with descriptions of these experiments and the unexpected and often paradoxical outcomes that can be confusing to layman and experts alike. The results are sometimes so baffling as to encourage thoughts of possible metaphysical origins of the proposed phenomena. This tendency has indeed bred an entire popular subculture of pseudoscientists with internet blogs devoted entirely to debunking, demystifying, or developing relativistic theories. At times, separating the truly scientific from the supposedly scientific is a challenging endeavor in the modern information age. In this field in particular, those who endeavor to learn should be cautioned to steer to the path of texts produced by reputable publishing houses and peer-reviewed scientific papers in respectable journals. In learning the special theory for the purposes of this research, the author found

the popular exposé by Born [19] and the introductory texts by Bergmann [11], Pauli [90], Pathria [89], French [41], and Tolman [114] especially lucid. Excellent texts covering the content of general relativity include the introductory works by Lawden [67] and Schutz [97] and the more advanced treatments of Wald [129] and Misner *et al* [80]. Perhaps the greatest insights were obtained from Einstein's original and clearly written papers, published in a compilation with the other original works by Lorentz, Weyl, and Minkowski [33].

In our description of the link between compressible potential flow and special relativity, we shall by intent avoid discussions of deep physical insights and paradoxical outcomes altogether. Our interest shall be in the aspects of the theory that are primarily *operational*, that is *mathematical*, in nature, and not *physical*. Indeed, our focus will be on the exposition of a relativistic transformation framework and not the postulates from which such a framework might physically emerge. The reason for this approach is that we are ultimately primarily interested in manifesting a mapping *method* to produce incompressible equivalent flows. Although much could possibly be gained by a quest for deeper physical meaning in the analogy, there is also much danger of overplaying the hand dealt by physics and entering an uncharted and dangerous realm. We shall therefore stay to a safer course, in which all of our mathematical transformations can be verified *by inspection* from the well known equations of potential flow. With this *modus operandi*, we now begin our relativistic foray.

The author's realization of a possible relativistic analogy stemmed from an observation about a scaling factor that appears identically in both the Prandtl–Glauert rule and in the special theory of relativity. This factor takes the form,

$$\frac{1}{\sqrt{1-V^2/c^2}}$$

where V is a velocity and c is the relevant signal speed of interest. In the Prandtl–Glauert rule, V is the velocity of the undisturbed air stream and c is the sound speed. In the Lorentz transformation, this same factor appears, but with the relevant signal speed being that of light. It turns out that this factor is indeed a result of transformation behavior in the governing equations of linear potential flow that can be thought of, in some sense, as relativistic.

In order to explore this connection, we shall need to discuss the broad meaning of relativity and its role in transformations among different reference systems. The roots of a relativistic theory lie in the interrelationships among different coordinate frames that are in many instances in motion. The term *relativity* in this context is meant more precisely as the *relativity of motion* among these various frames. The crux of the matter is that motion is a phenomenon that is fundamentally relative and not absolute. We speak of motion of one frame with respect to another.

Motion can be related by mathematical transformation laws. We shall be interested in two such transformations: Galilean and Lorentzian. In both of these, the relative motion between two frames is taken to occur at a constant velocity. The Galilean transformation is based entirely upon this constant velocity and the notion that time is universal in all reference frames. For motion with relative velocity V_∞ along the x-axis in a two-dimensional plane with time also considered a coordinate, the Galilean transformation between a frame individuated by coordinates (x, y, t) to frame with coordinates (x', y', t') is given by

$$\begin{aligned} x' &= x + V_\infty\, t \\ y' &= y \\ t' &= t. \end{aligned} \tag{1}$$

The Lorentz transformation removes the constraint on the universality of time and replaces it with the stipulation that a certain signal speed takes the same value in all reference frames [41]. In the case of Einstein's theory, this signal speed is the speed of light. In the case of potential flow, the speed is that of sound, in the sense of propagation of infinitesimal disturbances. The Lorentz transformation between frames (x, y, t) and (x'', y'', t'') with relative motion at a velocity of V_∞ oriented along the x-axis is

$$\begin{aligned} x'' &= \frac{x + V_\infty\, t}{\sqrt{1 - V_\infty^2/a_\infty^2}} \\ y'' &= y \\ t'' &= \frac{t + V_\infty/a_\infty^2\, x}{\sqrt{1 - V_\infty^2/a_\infty^2}} \end{aligned} \tag{2}$$

where a_∞ is the relevant constant signal speed.

These transformations can be brought to bear for the problem of linearized potential flow by first considering the small disturbance wave equation in a reference frame at which the air is globally at rest. Considering two spatial dimensions plus time, this equation can be written in terms of the potential as,

$$\frac{\phi_{tt}}{a_\infty^2} = \phi_{xx} + \phi_{yy} \tag{3}$$

where a_∞ is now interpreted as the constant sound speed and subscripts denote partial differentiation with respect to the indicated coordinate.

We now imagine that a disturbance is present, as manifested by a body moving at a constant subsonic velocity relative to the still air. In this rest frame of the air, the effect of the body is to induce an infinitesimal motion of the fluid as the body passes by. This motion leads to a propagating acoustic wave. With respect to this reference frame, the passage of the body is therefore an unsteady flow effect.

In the context of aerodynamics, we are typically interested not in the fluid motion relative to this freestream-fixed frame, but rather, in the motion of the air relative to a frame affixed to the moving body. We can arrive at the equation of motion in this frame by transformation from the still-air acoustic equation in at least two ways—through a Galilean transformation and through a Lorentz transformation.

Applying the Galilean transformation of Equation 1 to the Equation 3 produces

$$\frac{\phi_{t't'}}{a_\infty^2} + \frac{2\,V_\infty}{a_\infty^2}\,\phi_{x't'} = \left(1 - M_\infty^2\right)\phi_{x'x'} + \phi_{y'y'} \tag{4}$$

where we have introduced the freestream Mach number M_∞ as $M_\infty = V_\infty/a_\infty$. In the common situation that the flow can be approximated as steady in the frame of the body, the time derivatives of the potential vanish, and this result simplifies to

$$\left(1 - M_\infty^2\right)\phi_{x'x'} + \phi_{y'y'} = 0 \tag{5}$$

which is the well known equation of linear steady potential plane flow, often termed the Prandtl–Glauert equation [99].

Alternately, applying the Lorentz transformation to Equation 3 results in

$$\frac{\phi_{t''t''}}{a_\infty^2} = \phi_{x''x''} + \phi_{y''y''} \tag{6}$$

as the equation of motion in the (x'', y'', t'') system. The remarkable feature of Equation 6 is that its form is exactly identical to the original wave equation 3 except that the double-primed coordinates have replaced the original unprimed coordinates. That is, the scalar wave equation is *form invariant* or *covariant* under Lorentz transformations. For steady flow in the double-primed frame attached to the body, the time derivatives of the potential again disappear, and the equation of motion reduces to

$$\phi_{x''x''} + \phi_{y''y''} = 0 \tag{7}$$

which is the well known Cartesian form of the Laplace equation in two dimensions.

There exists an interesting relationship between these two alterative descriptions of the fluid motion relative to the fixed body that is the paramount observation that we seek. The coordinates of the two body-fixed frames are related as

$$\begin{aligned} x'' &= \frac{x'}{\sqrt{1 - M_\infty^2}} \\ y'' &= y' \\ t'' &= \frac{\left(1 - M_\infty^2\right) t' + V_\infty / a_\infty^2 \, x'}{\sqrt{1 - M_\infty^2}} \end{aligned} \tag{8}$$

as can be validated by eliminating the (x, y) coordinates from Equations 1 and 2. For the steady flow case, this relationship can be recognized immediately as one of the forms of the Prandtl–Glauert transformation [92, 44]. The temporal transformation has no effect in this case because time derivatives of the potential do not appear in either frame. For the unsteady case, this relationship forms the foundation of Küssner's transformation [63, 64, 99]. Küssner's method, which was later corrected by Sears [98] and also investigated by Truitt [115], is the inspirational basis of many of the techniques of linear unsteady aerodynamics. The framework for these various transformations is illustrated in Figure 1.

A relevant question at this point is how this framework is "relativistic" in the sense of Einstein's theory. The answer for our purposes lies in the involvement of the Lorentz transformations. Although these equations and their effect on the wave equation were known slightly before the time of Einstein's work [33], they are perhaps the primary mathematical grounding of the special theory of relativity.

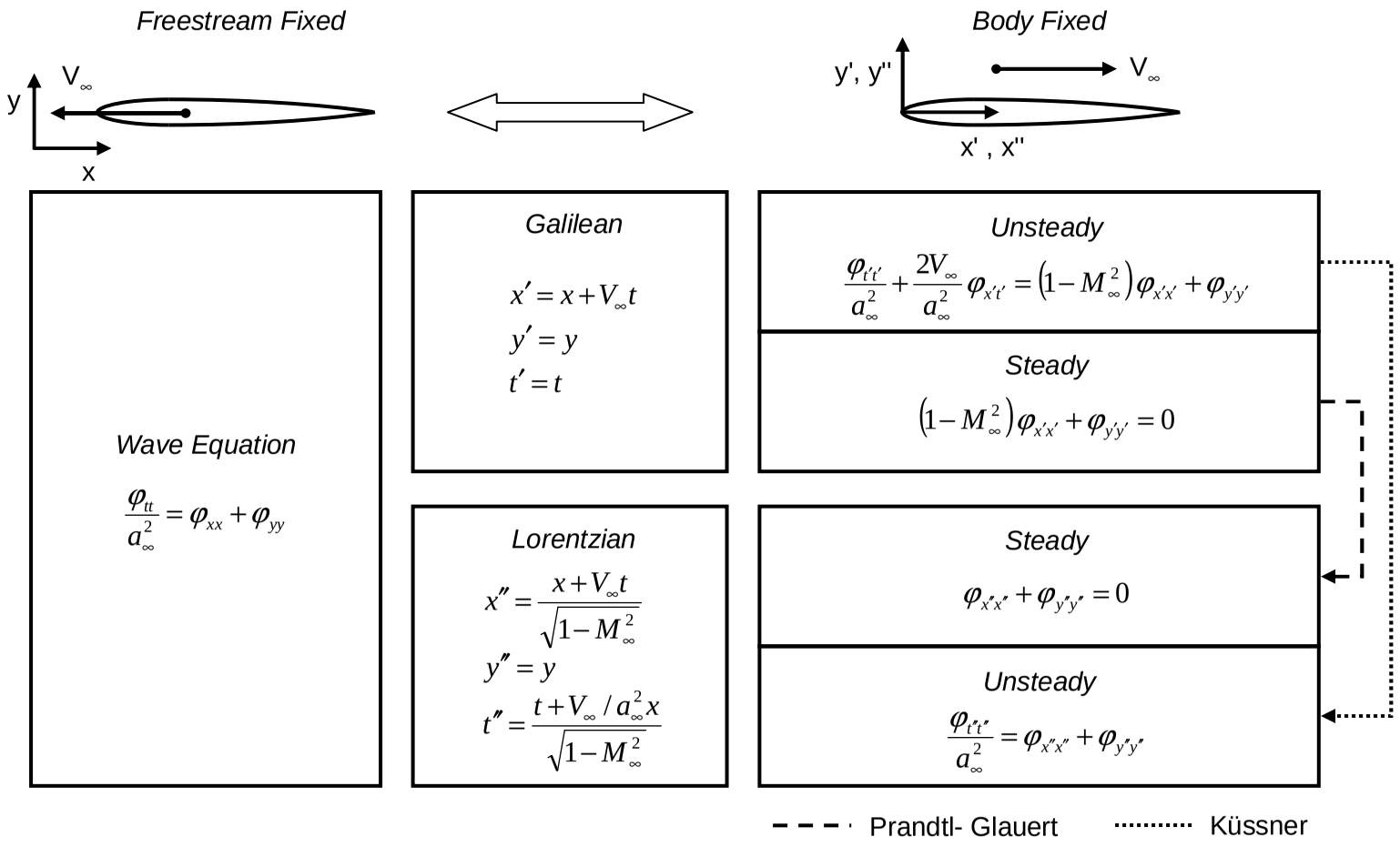

Figure 1: Relativistic Framework of Subsonic Linear Potential Flow

Regardless of the appearance of Lorentz invariance, many physicists would likely argue that this framework is not truly relativistic in the sense of Einstein's theory. The reasoning would in part have to do with the differing nature of light and sound. For many years, physicists sought to identify a medium, perhaps even a fluid, through which light propagated. This medium, termed the *luminiferous ether*, would be the physical substance whose vibrations were the mechanism of transmittal of light energy through space [41]. Even after years of searching, no such substance could be found.

Finally, in 1887, a famous experiment was conducted by Albert Michelson and Edward Morley that showed that light propagation did not behave in a way similar to sound [41]. Their apparatus measured the speed of beams of light emitted in several directions and found that the speed was direction independent. This result stands opposed to the ether hypothesis, which presumed that light passes through ether that is moving relative to the frame of the laboratory. If this ether existed, the measured speed of light would differ based on the direction of the light beam. In one orientation, the light would be carried along with the underlying ether current at a greater speed, and in the opposite orientation, it would be retarded by the ether flow. This type of behavior is precisely what we expect in the propagation of sound, where the sound velocity is directionally superimposed with the fluid velocity to find the signal speed relative to a laboratory-fixed frame. The fact that the Michelson–Morley experiment produced a null result marked the knell of the ether hypothesis.

A key feature in Einstein's formulation of relativity was that since the ether could not be found, we must search for a theory of light that does not hinge on its presence. This theory must embrace the experimental evidence of the constancy of the speed of light in all directions and in all moving frames. That is, the theory should not indicate that light propagates at different speeds in different directions based on the superposition of its signal speed with the velocity of a mean ether flow. In other words, the theory of relativity was so concocted as to obviate the need for an underlying fluid through which light propagates. Because a medium of propagation is now removed from the picture, there no longer exists the notion of an absolute frame of reference, such as the rest frame of the ether.

This concept is entirely juxtaposed with our well established conventions for the propagation of sound in a fluid. Here, we *know* that a fluid exists, and we can therefore define a definite rest frame of this fluid relative to the laboratory. Additionally, we observe that the speed of signal propagation is the superposition of the small signal sound speed with the bulk flow velocity.

In addition to the need or lack of a medium of propagation, another difference in sound and light is the nature of their waveforms and governing equations. Whereas sound waves are longitudinal, light waves are transverse. Sound is governed by a scalar potential equation, and light is governed by the vectorial Maxwell equations. Additionally, motions faster than the speed of sound are allowable; superluminal relative velocities are not. For these significant reasons, many physicists might very well question the concept of terming the framework of potential fluid motion as "relativistic," even if it involves Lorentz invariance.

Nonetheless, there is evidence of the ability to set up consistent relativistic theories in the presence of a material medium. This topic was investigated by Rosen, who showed that it is possible to establish special theories of relativity in homogenous isotropic media such as dielectric materials, and by extension, fluids [95]. Although these theories may have limited realms of applicability with respect to the broader Einsteinian theory and its implications on the world view, they can be set up to remain valid for their particular domains.

These issues, however, are largely physical and not operational. As stated earlier, our interest is in the mathematical coordinate frame relationships from relativity theory and not to dwell on the physical interpretations and caveats. The mathematical transformation structure of this relativistic analogy is solid, as is verified by the widely accepted forms of the linear potential formulation given by Equations 3–6 and the easily verified mathematical interrelationships among these forms that is indicated by the transformations of Equations 1, 2, and 8. We shall therefore sidestep these issues and simply adopt the perspective that this framework can be considered as relativistic, at least in a limited sense, because it involves the Lorentz transformation.

This transformation behavior for linear potential flow has been long recognized and

applied in aerodynamic and acoustic contexts; however, only rarely has the relativistic similarities of the framework been discussed. Acoustic examples include Morse and Ingard's solution of the pressure field of a moving acoustic point source by using the Lorentz transformation to map to a coordinate system in which the source is static and the potential equation takes on a particularly simple form [84]. Another acoustic example is provided by Chapman, who uses the Lorentz transformations to develop similarity variables for sound radiating in a mean steady flow [24].

Interestingly, much of the work in potential flow that has recognized the Lorentz transformational approach is in the area of supersonic aerodynamics. Lagerstrom appears to be the first to discuss the transformation for problems in steady supersonic flow [66]. Gardner was apparently the first to apply the transformation to unsteady supersonic flow [43]. Both of these early works examined applications to conical flow fields. In later work, Unger also applied the Lorentz transformation to flows over cones [118].

Miles extended much of the earlier work and used both the true Lorentz transformation and a modified version tailored for supersonic flow, particularly for unsteady problems [76, 77, 78]. This modified transformation approaches involves replacing the $1/\sqrt{1-M_\infty^2}$ factor, which becomes imaginary for a supersonic freestream, with the factor $1/\sqrt{M_\infty^2-1}$, which is real. In many ways, this modified form largely represents the unsteady generalization of the Ackeret rule of linear steady supersonic flow [2].

Shankara and Nandi extended the work of Miles and the general concept of Küssner's subsonic transformation by employing their own version of a modified Lorentz transformation relevant for supersonic unsteady flow [102]. Shankara and Majhi further explore this Lorentz-like transformation and present a unified description of the transformational symmetries in both the subsonic and supersonic cases [101]. This work is perhaps the first to discuss a fundamental relativistic grounding for linear potential motion, as evidenced by the statement in the paper abstract noting,"Results in the paper suggest that there is a unified relativistic foundation for the acoustics of both subsonic and supersonic sources. [101]"

In addition to the application of relativistic methods to the problem of classical potential

flow, there has been significant work in the area of truly relativistic gas dynamics, i.e. flows relativistic in the sense of the speed of light. These flows appear in astrophysical contexts in two situations: 1) Flows with relative bulk speeds appreciable to the speed of light, such as in jets from black holes and ejecta from supernovae; 2) Flows with temperatures so high that their molecules move with relativistic velocities, such as in stellar interiors.

We will not discuss the literature in this area extensively, but it is worth noting that this work is interesting in the way that the Lorentz transformations and modifications to mechanics brought about by special relativity influence the classical equations of gas dynamics and potential flow. Some of the earliest work in this area was due to Taub, who investigated the Rankine–Hugoniot shock jump conditions in relativistic flows [108] and also investigated isentropic compressible flows in relativistic conditions [109]. Frankl developed theory for the steady plane potential flow of relativistic fluids [40], and Arynov looked at the axisymmetric case [9]. Truitt, who we mentioned in the context of the relativistic analogy to classical flows, also developed theory for compressible relativistic flows in the sense of the speed of light [116]. His work indicates that it remains possible to describe subsonic, transonic, and supersonic flows consistently in a relativistic context, with all flow velocities remaining subluminal. Todeschini investigated relativistic small-perturbation potential flows in the plane [113], and he developed the relativistic generalization of the classical similarity rules including Prandt–Glauert for subsonic flow, Ackeret for supersonic, and von Kármán's transonic similarity rule. Todeschini also investigated the hodograph mapping of the relativistic equations [112]. Other work in the area of gas dynamics in the true special relativistic sense includes that of Gorskii [45] and Königl [60].

In this section, we have seen that there exists a certain limited special relativistic analogy for classical linear potential flow. The analogy is most direct for the subsonic case, where the Lorentz transformation can be used to relate flow described in a freestream-fixed frame and a body-attached frame. In this case, the conceptual framework is similar to that for the propagation of light, except that we replace light speed with sound speed. In the supersonic case, the analogy is not as direct because there exists no credible superluminal Lorentz-like transformational framework.

The interest of this relativistic analogy to the author is that it serves as a unifying transformational framework for several of the various classical compressibility corrections that map to equivalent incompressible flows. The simplifications achieved by methods such as Prandtl–Glauert can be viewed as stemming from compositions of Galilean and Lorentz transformations. The literature is also rife with similar simplifications that can be achieved in supersonic flows as a result of Lorentz-like transformations.

The success of this framework for the linear potential problem leads naturally to the question of whether similar relativistic analogies might be useful for nonlinear potential problems. Specifically, could we use mathematical or physical concepts from relativity theory to map to equivalent incompressible flows that relate to exact subsonic full potential solutions? These types of mappings would represent the full nonlinear generalization of the Prandtl–Glauert type transformations, and determining them represents the primary motivation to the approach pursued in this dissertation.

The special theory of relativity is concerned with effects that are primarily *linear* and *global* in nature. The types of mappings that are needed for the subsonic full potential problem would necessarily be *nonlinear* and *local* in character. These types of effects typify the realm of the general theory of relativity, which is concerned with the problem of fitting the concept of relativity of motion harmoniously with the effects of gravitation. In our quest to leverage relativistic techniques for the nonlinear potential problem, we are therefore motivated to search within the mathematical and physical toolkit of general relativity. This quest will lead us to draw certain loose analogies between the effects of gravitation and of fluid compressibility.

In the next section, we provide a very brief overview of the features of the general theory that have motivated its consideration for addressing the problem of fluid compressibility through equivalent flows. Our discussion will not attempt to expose the full breadth and depth of this very complicated field of physics.

1.3 Roots of a Mapping Approach Using Ideas from General Relativity

The special theory of relativity is built upon the foundation of coordinate frames that are globally *inertial*. Inertial frames form a class that is defined by the nature of motion of all of its members. Specifically, inertial frames move at constant velocities with respect to each other; they have no relative acceleration. The Lorentz transformations discussed in the previous section are relevant only amongst inertial frames.

In many cases, it is not possible to limit our purview only to inertial frames. For instance, let us consider one of the motivational problems for the development of general relativity: free-fall in a gravitational field. Imagine two frames—one an inertial frame affixed to a gravitating body and a second centered in an elevator in free-fall in the gravitational field. Owing to the presence of the field, the frame of the elevator is accelerating relative to the fixed inertial frame. In this case, the simplistic analysis of Lorentz transformations in special relativity cannot be used to directly relate events and signal propagation in these two frames because their relative velocity is not constant.

What can be done, however, is to employ the special relativistic relations between any two reference frames *infinitesimally* separated from one another in both space and time. That is, we can imagine a frame centered on the elevator floor at time t_0, moving at a velocity V_0 and a second frame centered at the same spot on the floor at time $t_0 + dt$, moving at a velocity $V_0 + dV$. These two frames *can* be related to one another using the special relativistic treatment because we do not attempt to track the relationships among their velocities for all time; rather we imagine these as infinitesimal inertial frames with a constant relative velocity dV. We can imagine an infinite number of other frames of this type existing throughout the gravitational field. The problem of gravitational acceleration is then to determine how to appropriately stitch together physical laws in these *local* frames to produce a *global* picture of relative motion that is consistent with a special relativistic treatment between all of the infinitesimally separated frames. Specifically, we wish to know how the various laws of physics change form in these different infinitesimal frames in a gravitational field.

The mechanism of performing this stitching in general relativity is the mathematics of Riemannian geometry. This field is a subset of differential geometry that is concerned with spaces that possess an entity called a *metric tensor*. The metric tensor is often denoted as $g_{\mu\nu}$, or in an alternate form, $g^{\mu\nu}$, where μ and ν are indices that can take on integer values corresponding to each dimension in the space. In relativistic theory, space is envisioned as a four-dimensional space-time. We shall discuss the metric tensor in much greater detail in Chapter 2, but for now, we note simply that knowledge of the values of the metric tensor at all points is enough to describe the curvature of space-time. Whereas certain metric tensors describe different coordinate systems in flat space, such as Cartesian and cylindrical coordinates, other metric tensors describe coordinate systems in curved spaces.

Using the language of Riemannian geometry allows us to write physical equations involving the metric tensor in an *invariant* or *covariant* form that does not single out a particular coordinate system. For instance, we can write the d'Alembert equation given in Equation 3 in the form,

$$\frac{\partial}{\partial x^\mu}\left(\sqrt{-g}g^{\mu\nu}\frac{\partial\phi}{\partial x^\nu}\right) = 0 \tag{9}$$

where $g^{\mu\nu}$ is a particular form of the metric tensor corresponding to the coordinate system x^α where the index α can take any integer value corresponding to a dimension of the space, and g is the determinant of the metric. In this notation, we interpret time normalized by the speed of sound as one of the x^α values; we will further discuss the notation used in this equation in Chapter 2. This equation is invariant in the sense that to transform it to a different set of coordinates, say $\bar{x}^\alpha$, we simply replace the coordinate labels in the partial derivatives and the metric tensor with their equivalents in the barred frame:

$$\frac{\partial}{\partial \bar{x}^\mu}\left(\sqrt{-\bar{g}}\bar{g}^{\mu\nu}\frac{\partial\phi}{\partial \bar{x}^\nu}\right) = 0. \tag{10}$$

The general theory of relativity brings Riemannian geometry to bear in the problem of gravitational physics through two physical conceptions. First, it says that space is curved by a gravitational field, as described by the prescription of a metric tensor that varies in a certain way from point to point in space-time. The metric tensor in general relativity is determined by a proposed independent physical law given by Einstein's equation [97], which

we shall encounter briefly in Chapter 3. For now, we simply note that it is a second order hyperbolic tensorial differential equation whose solution gives the metric tensor components. This process serves to *embed gravity into the geometry of space*.

The second way that Riemannian geometry is involved is through the principle of *general covariance*. This principle states that physical laws that are known to be valid in flat spaces can be carried over directly to curved spaces produced by a gravitational field simply by replacing a flat space metric tensor with a curved space metric tensor. For instance, Equation 9 could be transitioned to a curved space with metric $\tilde{g}^{\mu\nu}$ simply by supplanting the tilde on the metric label. By the application of general covariance, the effects of gravity are manifested in physical equations in the same way that the effects of different coordinate systems are manifested. For instance, the force of gravity now resembles other coordinate system induced "forces" such as the centrifugal "force."

We can therefore summarize the way that gravity affects physical laws as follows: Gravity sets the metric tensor of a Riemannian space through an independent physical law (Einstein's equation), and the metric tensor determines uniquely the form of all other physical laws in the presence of gravity. Through this conceptual framework, we no longer view gravity as an independent physical force; rather, it affects motion and mechanics by geometry.

Given this very brief depiction of general relativity, we now outline how we intend to leverage elements of this approach for the determination of equivalent incompressible flows. A much more detailed description will be provided in Chapter 3, but our intent here is simply to link the concepts of general relativity to our mapping approach.

The goal of our approach will be to *embed compressibility into the geometry of space* by setting the metric tensor in a particular way. The way we do this will be unlike the case for gravity, however. Whereas the metric tensor is set by Einstein's equation in general relativity, we shall set it by directly comparing the compressible flow continuity equation and the incompressible continuity equation. We will then absorb the effects of compressibility, including the varying density, into the metric tensor appearing in the incompressible continuity equation. In this way, we will create an equivalent incompressible flow existing in the

same coordinate system as the original compressible flow. As we will discover in Chapter 2, this approach is a type of *gauge transformation* that alters the curvature of space. With this approach, we will be able to interpret forces owing to compressibility as if they were effects of spatial curvature or a coordinate system. Once the equivalent flow is obtained, we can then perform a coordinate transformation to achieve a particularly simple form of the governing potential equation that is easy to solve—the canonical form of Laplace's equation. Through this process, we will embed all of the nonlinearities of the subsonic flow into the spatial curvature and coordinate system of a linear incompressible flow.

There is some precedent for drawing this type of connection linking general relativistic theory with acoustics and potential flow. In 1981, Unruh recognized a strong mathematical similarity between the acoustic propagation in a uniform transonic converging flow into a point sink and the gravitational effects of a black hole [119]. He identifies various features of black holes with their analogs in the acoustic situation. For instance, the sonic line corresponds to the so-called *event horizon*. This horizon represents the boundary beyond which signals cannot escape the gravitational pull of the black hole; hence, black holes are "black" because no light can propagate outward from the event horizon. This phenomenon is recognizable from an acoustic standpoint, in that signals cannot propagate upstream from the sonic line because they are convected away toward the sink at a rate faster than the sound speed. This connection represents a link between relativity theory and acoustics because the physics of black holes is entirely described by general relativity; they appear to have no Newtonian gravitational counterpart.

Visser expanded upon Unruh's analogy and described the mathematical nature in terms of Riemannian geometry [125]. The acoustical situation corresponds to linearized unsteady perturbations superimposed over a mean spherically converging flow that is allowed to accelerate slowly through sonic velocity. He showed that we can view the sound propagation as being described by a four-dimensional *acoustic Riemannian metric tensor* of the form,

$$g_{\mu\nu} = \frac{\rho}{c} \begin{bmatrix} -\left(c^2 - V^2\right) & \vdots & -V \\ \cdots & & \cdots \\ -V & \vdots & I \end{bmatrix} \tag{11}$$

where V is the mean flow velocity, c is the sound speed, ρ is the density, and I is the 3×3 identity matrix. This metric tensor is used to absorb the effects of the varying underlying mean flow into the wave equation written in tensor invariant form. In other words, Visser sets the metric tensor $g_{\mu\nu}$ through Equation 11 such that when the metric is substituted into Equation 9, the acoustic equation takes on its correct form in the presence of the mean flow. In this sense, the nonlinear mean flow effects have been embedded into the geometry of space through the metric tensor. This approach is nearly identical to our intent, except that we will not consider the four-dimensional problem with linearized acoustics, but rather, the fully nonlinear steady two-dimensional problem. Rather than embedding the mean flow effects in the metric to modify linear acoustic propagation, we will embed all compressibility effects into the metric to obtain a steady incompressible flow.

This area of work linking black holes and acoustics has been identified as a pathway toward addressing certain quantum phenomena in the problem of black holes. One of the greatest challenges with the astrophysics of black holes is that it is very difficult to test hypotheses because all observational evidence is indirect since no light is returned. The acoustic analogy has been advocated because it allows certain limited laboratory experiments to test various proposed phenomena. Other work in this area of analog models linking black holes and acoustics include Bilić's paper *Relativistic Acoustic Geometry* [17] and Fischer's *Riemannian Geometry of Irrotational Vortex Acoustics* [39].

1.4 Dissertation Overview

The general layout of the dissertation is as follows. Chapter 2 provides relevant background material in transformation methods for flow solutions and tensor analysis. This material may be regarded as optional by readers with a fresh knowledge of these areas.

The formulation of the nonlinear mapping approach inspired by Riemannian geometric and general relativistic concepts is presented in Chapter 3. This chapter outlines the hypothesis to be tested in this dissertation and presents a series of research questions that are to be answered through the theoretical development, numerical implementation, and calculation of results.

Chapter 4 derives the theory for the gauge and coordinate mappings, employing Riemannian geometric tensorial notation. Particular emphasis is placed on the primacy of the metric tensor. First, invariant forms of the governing flow equations are derived in Riemannian tensorial notation, and the mapping approach is then developed in detail.

In Chapter 5, a numerical mapping algorithm is devised to implement the transformation framework outlined in Chapter 4. The elements of the algorithm are described as well as the particular solution techniques. Much of the attention is focused on the discretized differential equations and the convergence criteria.

Chapter 6 presents a series of results obtained through the numerical method. These results correspond to various flows over a circular cylinder and a NACA 0012 profile, including solution sensitivities to solver parameters and the effects of flow parameters such as Mach number and angle of attack on the equivalent incompressible flow fields and profile shapes.

Finally, Chapter 7 concludes the thesis. In this chapter, we reconcile the hypothesis and research questions, summarize the contributions of this research, outline possible applications, and suggest continuations to this line of research.

CHAPTER II

BACKGROUND

2.1 Transformation Methods for Subsonic Potential Flow

As we discussed in Section 1.1, transformation methods formed the earliest approach for the solution of subsonic flows. These early methods typically mapped a subsonic flow to an equivalent incompressible flow. The incompressible flow could then be solved by further mappings using the complex variable techniques of conformal mapping to reduce the problem to one of several well known flows, such as the flow over a circle in a uniform stream.

In this section, we describe some of these early mapping techniques that are applicable for steady subsonic flows. We will not belabor conformal mappings of incompressible flows because they play no role in the theory and implementation pursued in this dissertation. First, we discuss the class of affine transformations of the linear potential equation that form the basis of the Prandtl–Glauert and Göthert rules. Next, we describe hodograph mapping techniques, of which the Kármán–Tsien method is the prototypical example.

2.1.1 Prandtl–Glauert and Göthert Rules

In Section 1.1, we briefly discussed the class of transformations of the linear potential equation that lead to the Prandtl–Glauert and Göthert rules. Let us now explore these methods in slightly greater depth. We follow generally the presentation and notation of Shapiro for the Göthert rule [103] and the author's own preferred approach for the Prandtl–Glauert method.

We begin with the linearized steady potential equation in the plane which can be written

$$\beta^2 \frac{\partial^2 \phi}{\partial x^2} + \frac{\partial^2 \phi}{\partial y^2} = 0 \tag{12}$$

where $\beta^2 = 1 - M_\infty^2$ and ϕ is the perturbation potential. Let us now introduce a global

affine stretching of both the coordinates and of the potential ϕ of the form

$$\begin{aligned} x' &= \lambda_x\, x \\ y' &= \lambda_y\, y \\ \phi' &= \lambda_\phi\, \phi. \end{aligned} \tag{13}$$

The interesting feature of this transformation is that the values of the scalar field ϕ are allowed to change. This allowance is uncharacteristic of a pure coordinate transformation which does not affect scalar fields. The presence of this scaling indicates that this class of similarity transformations *cannot* be categorized purely as coordinate mappings.

Applying the transformation of Equations 13 to Equation 12 results in the transformed potential equation

$$\frac{\beta^2\,\lambda_x^2}{\lambda_\phi}\,\frac{\partial^2\phi'}{\partial x'^2} + \frac{\lambda_y^2}{\lambda_\phi}\,\frac{\partial^2\phi'}{\partial y'^2} = 0. \tag{14}$$

The goal is to obtain the form corresponding to the Cartesian Laplacian:

$$\frac{\partial^2\phi'}{\partial x'^2} + \frac{\partial^2\phi'}{\partial y'^2} = 0. \tag{15}$$

It is clear from Equation 14 that this form results from the restriction on the affine mapping given by

$$\beta^2\,\lambda_x^2 = \lambda_y^2 \tag{16}$$

because this condition produces an overall nonzero multiplicative factor that can be divided through.

Having achieved the desired form of the potential equation, we next ask how the airfoil surface slopes and boundary conditions affect the transformation. These issues form the crux of the difference between the more nearly correct Göthert rule and the Prandtl–Glauert rules. We start with linearized flow tangency conditions in the $(x,\, y)$ frame given by,

$$\left.\frac{dy}{dx}\right|_{\text{surf}} = \frac{1}{V_\infty}\left.\frac{\partial\phi}{\partial y}\right|_{\text{surf}}. \tag{17}$$

In Göthert's rule, we force the body surface slopes to change in a way compatible with the transformation of the coordinates. That is, we transform the slope as

$$\left.\frac{dy}{dx}\right|_{\text{surf}} = \frac{\lambda_x}{\lambda_y}\left.\frac{dy'}{dx'}\right|_{\text{surf}}. \tag{18}$$

Substituting this relation for the slope as well as the transformation of the potential derivative into the boundary condition of Equation 17 gives

$$\left.\frac{dy'}{dx'}\right|_{\text{surf}} = \frac{\lambda_y^2}{\lambda_x\,\lambda_\phi}\frac{1}{V_\infty}\left.\frac{\partial\phi'}{\partial y'}\right|_{\text{surf}}. \tag{19}$$

The boundary conditions in the primed frame are made to look exactly like those in the original frame; that is, they are chosen to correspond to flow tangency if we think of the primed frame as forming a Cartesian pair of axes:

$$\left.\frac{dy'}{dx'}\right|_{\text{surf}} = \frac{1}{V'_\infty}\left.\frac{\partial\phi'}{\partial y'}\right|_{\text{surf}}. \tag{20}$$

This form is obtained from Equation 19 by setting $V_\infty = V'_\infty$ and imposing

$$\lambda_y^2 = \lambda_x\,\lambda_\phi \tag{21}$$

as an additional condition on the affine transformation.

In the Prandtl–Glauert rule, the airfoil slope is dissociated from the coordinate transformation and scaled independently. That is, we introduce a new scale factor λ_θ as,

$$\left.\frac{dy}{dx}\right|_{\text{surf}} = \frac{1}{\lambda_\theta}\left.\frac{dy'}{dx'}\right|_{\text{surf}}. \tag{22}$$

Substituting this relation and $V_\infty = V'_\infty$ into the boundary condition Equation 17 gives,

$$\left.\frac{dy'}{dx'}\right|_{\text{surf}} = \frac{\lambda_\theta\,\lambda_y}{\lambda_\phi}\frac{1}{V'_\infty}\left.\frac{\partial\phi'}{\partial y'}\right|_{\text{surf}}. \tag{23}$$

In order for this boundary condition to take the form of flow tangency in Cartesian axes, we require

$$\lambda_\theta\,\lambda_y = \lambda_\phi. \tag{24}$$

For the Göthert rule, we have two relations given by Equation 16 and Equation 21 for the three unknowns λ_x, λ_y, and λ_ϕ. The third condition is determined from the consideration that the solution is invariant with respect to uniform scalings in both coordinate dimensions. Because of this invariance, we can specify any positive absolute scale by setting either λ_x or λ_y for convenience. The typical approach is to set $\lambda_x = 1$ such that the mapping produces a profile in the equivalent flow that has the same chord as the original airfoil.

For the Prandtl–Glauert rule, we have two relations given by Equation 16 and Equation 24 for the *four* unknowns λ_x, λ_y, λ_ϕ, and λ_θ. As with the Göthert rule, we typically specify the absolute scale by setting $\lambda_x = 1$. The remaining condition is a free specification of the profile slope that we obtain by setting λ_θ.

Next, we investigate the transformation of the linearized surface pressure coefficient, given in the original frame by,

$$C_p|_{\text{surf}} = -\frac{2}{V_\infty} \left. \frac{\partial \phi}{\partial x} \right|_{\text{surf}}. \tag{25}$$

Introducing the transformation of Equation 13 and the condition $V_\infty = V'_\infty$ gives

$$C_p|_{\text{surf}} = \frac{\lambda_x}{\lambda_\phi} \left[-\frac{2}{V'_\infty} \left. \frac{\partial \phi'}{\partial x'} \right|_{\text{surf}} \right], \tag{26}$$

but the expression in brackets on the right hand side can be recognized simply as the surface pressure coefficient of the equivalent incompressible flow in the primed frame, so we have,

$$C_p|_{\text{surf}} = \frac{\lambda_x}{\lambda_\phi} \left. C'_p \right|_{\text{surf}}. \tag{27}$$

For the Göthert rule, the scaling factor can be determined by solving Equation 16 and Equation 21 with $\lambda_x = 1$ to give

$$\frac{C_p}{C'_p} = \frac{\lambda_x}{\lambda_\phi} = \frac{1}{\beta^2}. \tag{28}$$

For the Prandtl–Glauert rules, the factor is obtained through Equation 16 and Equation 24 with $\lambda_x = 1$ as

$$\frac{C_p}{C'_p} = \frac{\lambda_x}{\lambda_\phi} = \frac{1}{\lambda_\theta \, \beta}. \tag{29}$$

For the Prandtl–Glauert approach, it is typical to consider three different settings for λ_θ. First, we set $\lambda_\theta = 1$ such that the surface slopes are the same for both the original flow and the equivalent incompressible flow. In this case the pressure coefficients are related as $C_p = (1/\beta)\, C'_p = 1/\sqrt{1 - M_\infty}\, C'_p$. This is the common form of the Prandtl–Glauert rule for compressibility correction. The incompressible flow is solved over the original airfoil and the pressure coefficients are scaled in this way. We do not need to consider the coordinate transformation because we have allowed the slopes to change independently of the coordinate mapping, and we have then set the slopes to match those of the original profile.

In another form of the rule, we set $\lambda_\theta = 1/\beta$ such that we have $C_p = C_p'$. This produces a thicker airfoil by a factor $1/\sqrt{1 - M_\infty^2}$ in the equivalent incompressible flow. Finally, we set $\lambda_\theta = \beta$ to give $C_p = \left(1/\beta^2\right) C_p' = 1/\left(1 - M_\infty\right) C_p'$. This produces a thinner airfoil by a factor of $\sqrt{1 - M_\infty^2}$ in the equivalent incompressible flow.

Of these rules, the Göthert form is the most exact because it correctly transforms the surface streamline shape along with the coordinate mapping [46]. The fact that the Prandtl–Glauert rule distorts the surface shape incorrectly was not noticed for several years until Göthert discovered the problem when trying to apply the Prandtl–Glauert approach to axisymmetric problems. Although the Prandtl–Glauert forms are less correct because of their surface slope specification, it is widely accepted that all of the forms are accurate to within the first-order linearization of the equations of motion, boundary conditions, and pressure coefficient for planar flows. Significant errors emerge only for the axisymmetric case, for which the Göthert rule must be used.

2.1.2 Hodograph Transformations and the Kármán–Tsien Rule

Another early approach to the solution of planar subsonic potential flows was to employ the *hodograph* mapping. The hodograph is the plane coordinated by the velocity components. The mapping to this coordinate system emerges by taking the velocities as the independent variables in the flow solution and the physical coordinates as the dependent variables, inverting the dependencies in the problem. For instance, we typically think of the velocity as given at a particular location in the form $u = u\left(x, y\right)$ and $v = v\left(x, y\right)$. In the hodograph plane, however, we think of the location in physical space as being specified as a function of the velocity as $x = x\left(u, v\right)$ and $y = y\left(u, v\right)$. Alternately, the hodograph plane can be constructed with the velocity magnitude V and the stream direction θ as the independent variables.

The hodograph mapping has both a great advantage and a great disadvantage. The advantage is that, upon transformation to the hodograph plane, the nonlinear equation

governing the flow becomes a *linear* differential equation. It is typical to express the governing equation in the hodograph plane in terms of the stream function as,

$$V^2 \frac{\partial^2 \psi}{\partial V^2} + V \left(1 + \frac{V^2}{c^2}\right) \frac{\partial \psi}{\partial V} + \left(1 - \frac{V^2}{c^2}\right) \frac{\partial^2 \psi}{\partial \theta^2} = 0 \tag{30}$$

where c is the sound speed [103]. This equation is linear because the factors multiplying the partial derivatives involve only functions of V (since c is a function of V) which is an independent variable. In this plane, we *do not* think of V as being a function of ψ, although we must take this view in the physical plane.

Because the equation is linear, we can develop solutions for arbitrary flows through a summation of particular solutions. The particular solutions of the hodograph equation are not well known simple functions; rather, they are a class of so-called *hypergeometric* functions [62]. Nonetheless, these functions have been tabulated and can be used to find superposition solutions over general bodies.

The great disadvantage of the hodograph mapping is that, although the differential equation is now straightforward to solve, the boundary conditions become nonlinear and the shape of the boundary in the hodograph given by the locus of (V, θ) points cannot easily be determined *a priori* in the problem; we only know the shape of the boundary in terms of (x, y) coordinates. This boundary shape may also be especially complicated because the values of V and θ are not unique along the profile; that is the mapping $(x, y) \rightarrow (V, \theta)$ is not one-to-one. The boundary streamline may cross and/or possess several branches. These considerations make the hodograph approach approximately as difficult for flows over arbitrary bodies as the original nonlinear differential equation in the physical plane. The hodograph does allow for simple solutions in situations such as free jets, however [22, 62].

Although it can be difficult, several methods have succeeded in providing techniques for the solution of flows over arbitrary profiles using the hodograph method. The first to develop such an approach were Molenbroeck [81] and Chaplygin [22, 23]. The success of this approach was based on approximating the pressure–density relation with a relation termed the *tangent gas law*. This law can be obtained from the polytropic relation by setting the ratio of specific heats as $\gamma = -1$. Although this setting appears nonsensical, it

actually has a reasonable physical meaning: it represents the linearization of the pressure–volume relationship about a nominal point. Chaplygin took this nominal point to coincide with the stagnation condition, so the linearization was only valid for very low subsonic Mach numbers. Once the tangent gas law has been presumed, the hodograph equation is dramatically simplified such that it takes the Cartesian Laplacian form. In this form, it can be solved readily by complex variable mapping techniques.

The Kármán–Tsien approach, from which the celebrated Kármán–Tsien rule emerges, is an improvement of the Chaplygin rule that gives good approximate solutions at high subsonic Mach numbers [117, 126]. The key difference from that of Chaplygin is that the Kármán–Tsien method chooses the point of linearization for the tangent gas law to be the freestream condition as opposed to stagnation. Since most of the compressibility effects are determined by the freestream magnitude, this approach yields much improved results.

A fact about the Kármán–Tsien method that is not typically discussed in modern pedagogy is that it involves not only a pressure correction but also a transformation to the profile shape. This shape distortion is typically not applied in practical problems, however, because the transformation is complicated and the magnitude of the shape change is typically very small. It has also been found that in most cases, the error introduced by $\gamma = -1$ approximation is somewhat washed out by a counteracting error of not applying the shape transformation [103]. As is demonstrated by the large collective experience base with the Kármán–Tsien rule, this approach produces quite reasonable compressibility corrections throughout the subsonic range. Indeed, it is worth noting that the Kármán–Tsien method with the shape change represents the *exact* solution for a subsonic flow with a fluid that has a linear pressure–volume relation.

Another class of more modern methods employing the hodograph mapping include transonic numerical solution techniques such as that developed by Bauer, Garabedian, and Korn [10]. These approaches employ the hodograph as an intermediate in the solution that is carried out mainly in the physical plane.

2.2 Overview of Tensor Analysis in Riemannian Geometry

As discussed in Chapter 1, many of the techniques of general relativity that have inspired this work are based on Riemannian geometry. In this thesis, we pursue a transformation technique that leverages many of these methods. The mathematical language of Riemannian geometry is inherently intertwined with a particular form of tensor analysis in which the metric tensor plays a dominant role. In this section, we discuss tensor analysis in Riemannian geometry to the level that will be needed in the theory developed in this work. We start at a very basic level with the introduction of the tensor concept, building to tensor algebra and, finally, to tensor calculus via the metric tensor. Readers familiar with this topic area may feel free to bypass this discussion.

2.2.1 What are Tensors?

Tensors are mathematical entities that obey a particular type of transformation law under coordinate transformations. They are classified primarily by their *order* and their *type*, or *variance* [106]. In this section, we shall first investigate the concepts of order and type as well as the general notation typically used for tensors in Riemannian geometry. Next, we shall explore tensor transformation behavior and the summation convention.

2.2.1.1 Order, Type, and Notation

A tensor is denoted by a variable name that is typically a letter of the Latin alphabet, say, T. We affiliate with this letter index variables that are often selected from the Greek alphabet. For instance, we could have a tensor denoted T^{μ}. The index variable can take on any integer value from within a particular range that is determined by the dimension of the space. The range of the indices is comprised of n members, where n is an integer corresponding to the dimension of the space. Typical ranges are $0 : (n-1)$ or $1 : n$, with the particular convention depending on the application. In classical Riemannian geometry, the range is usually taken as $1 : n$, whereas in relativity theory the $0 : (n-1)$ format is typically employed.

The *order* of a tensor is indicated by the number of indices it has. For instance, T is a

zero order tensor, T^{μ} is a first order tensor, and $T^{\mu\nu}$ is a second order tensor. In certain cases, tensors with three or more indices are encountered. For instance, in describing the curvature of space, tensors with labels such as $R^{\mu\nu\omega\pi}$ occur. We shall be most interested in zero, first, and second order tensors, however, as tensors of higher order are quite rare in mathematical physics and particularly in the types of fluid flow problems addressed in this dissertation. There is some intuition that we can carry over to the world of tensors from the study of vector and matrix analysis, as zero order tensors are simply scalar values, first order tensors can be used to represent vectors, and second order tensors can represent matrices.

Although the tensors described so far have had indices only as superscripts, it is valid for any individual index to occupy either a subscript or a superscript position. It is therefore possible to have tensors denoted as $T^{\mu}{}_{\nu}$ or $T_{\mu\nu}$. The locations of these indices indicate the *type* or *variance* of the tensor. Tensors with indices located only in superscripts are termed *contravariant*, whereas tensors with indices only in subscript positions are called *covariant*. Tensors that have indices in both superscript and subscript locations are termed *mixed* tensors, or we may instead speak of them as contravariant in some indices and covariant in others. For instance, $T_{\mu\nu}$ is covariant, $T^{\mu\nu}$ is contravariant, and $T^{\mu}{}_{\nu}$ is mixed. Alternately, we can describe $T^{\mu}{}_{\nu}$ as contravariant in the index μ and covariant in the index ν. Table 2.2.1.1 summarizes the order and type of these commonly encountered tensor forms.

So far, we have described tensors as abstract symbols. A deeper meaning can be found in their role as a collection of bins in which numbers or other variables are deposited. These bins are termed the *components* or *elements* of a tensor. A component of a tensor is identified by a particular setting of each of the index values. For instance, the component of the tensor $T^{\mu\nu}$ with $\mu = 1$ and $\nu = 2$ is T^{12}. The notion of tensor components is identical to that of the elements of a vector or matrix. In many cases, a component of a tensor is taken to refer to the number or variable that occupies a particular bin. As we shall see in the next section, these numbers depend on the coordinate system in which the tensor is given; however, the concept of the bin identifier as a location within the tensor is independent of

Table 1: Examples of Tensors of Various Orders and Types

Label	Order	Type	Description in Words
T	0	Invariant	Zeroth order tensor OR Scalar
T^{μ}	1	Contravariant	First order contravariant tensor OR Contravariant vector
T_{μ}	1	Covariant	First order covariant tensor OR Covariant vector
$T^{\mu\nu}$	2	Contravariant	Second order contravariant tensor
$T_{\mu\nu}$	2	Covariant	Second order covariant tensor
$T^{\mu}{}_{\nu}$	2	Mixed	Second order mixed tensor OR Second order tensor contravariant in μ and covariant in ν

the coordinate system.

2.2.1.2 Transformation Behavior and the Summation Convention

Although we have discussed tensor notation and naming, we have not yet precisely defined the mathematical nature of tensors. One may be led to conclude at this point that any symbol with any particular combination of indices represents a tensor. This conclusion is incorrect—only certain objects possess the defining trait of tensors, or *tensorial character*. We shall describe this trait in this section.

A tensor is defined by the way its elements change under the transformation from one coordinate system to another. We shall illustrate this definition by example. For a first order contravariant tensor, the transformation law is

$$\bar{T}^{\mu} = T^{\alpha}\frac{\partial \bar{x}^{\mu}}{\partial x^{\alpha}}, \tag{31}$$

in which the tensor T^{μ} corresponds to the x^{μ} coordinate system and the tensor $\bar{T}^{\mu}$ corresponds to the $\bar{x}^{\mu}$ system [106]. The expression $\frac{\partial \bar{x}^{\mu}}{\partial x^{\alpha}}$ represents the partial derivatives of

the coordinate transformation, which are typically represented as the elements of a Jacobian matrix. This transformation behavior can be viewed as the *definition* of a first order contravariant tensor because it specifies how the tensor elements in two coordinate frames are related. If two entities T^{μ} and $\bar{T}^{\mu}$ are given in two corresponding coordinate systems x^{μ} and $\bar{x}^{\mu}$ and the elements of these entities are *not* related through Equation 31, then the entities cannot be considered to be expressions of the same tensor in two coordinate systems.

In order to fully understand Equation 31, we shall have to introduce several new concepts. The first of these is the so–called *Einstein summation convention*. This convention represents a notational convenience for indicating sums within tensorial expressions. It can be summarized as follows:

> Any index name that is written in both a subscript and a superscript location indicates a summation of the respective tensor elements indicated by the index. The index is incremented to successively take on all allowable values from within its range, and the resulting term from each setting is added to the summation. This convention holds for indices within a single tensor, across products involving several tensors, and within expressions involving differentiation.

An example of the summation convention appears in Equation 31 through the index α. The index is repeated in the superscript of T^{α} and in the superscript of the denominator of $\frac{\partial \bar{x}^{\mu}}{\partial x^{\alpha}}$. In order to apply the summation convention to this situation, we shall need to add the following qualification:

> A superscript in the denominator occurring within a partial derivative is to be interpreted as a subscript.

The reason for this distinction is that we could equivalently denote the partial derivative $\frac{\partial \bar{x}^{\mu}}{\partial x^{\alpha}}$ as ${x^{\mu}}_{,\alpha}$ where the comma denotes partial differentiation with respect to the subsequent index. In this notation, it is clear that α is meant as a subscripted index.

The summation convention tells us that Equation 31 can be expanded by requiring α to successively take on all values from within its range and summing each of the resulting

terms. Presuming that we are in dimension $n = 3$ with the range on the indices being $1 : n$, this expansion gives,

$$\bar{T}^{\mu} = T^1 \frac{\partial \bar{x}^{\mu}}{\partial x^1} + T^2 \frac{\partial \bar{x}^{\mu}}{\partial x^2} + T^3 \frac{\partial \bar{x}^{\mu}}{\partial x^3}.$$

We can therefore see that the summation convention is actually shorthand for the expression,

$$\bar{T}^{\mu} = \sum_{\alpha=1}^{n} T^{\alpha} \frac{\partial \bar{x}^{\mu}}{\partial x^{\alpha}}.$$

The implications of the summation convention lead us to distinguish two particular types of indices. Indices that do not occur within summations are called *free*, whereas repeated indices that imply summation are termed *dummy*. A free index is allowed to take on any particular value from within its range, and any tensor expression that includes a free index is implied to be valid for *all* possible values of the index from within the range. Indeed, we can write an individual component expression for each setting of the free index. For example, the tensorial Equation 31 can be expanded into three separate equations by allowing its free index μ to take on all values in the range $1 : n$ for $n = 3$:

$$\begin{aligned} \bar{T}^1 &= T^{\alpha} \frac{\partial \bar{x}^1}{\partial x^{\alpha}} \\ \bar{T}^2 &= T^{\alpha} \frac{\partial \bar{x}^2}{\partial x^{\alpha}} \\ \bar{T}^3 &= T^{\alpha} \frac{\partial \bar{x}^3}{\partial x^{\alpha}}. \end{aligned}$$

A free index therefore has the effect of indicating all of the particular components of a tensorial expression that have independent significance in the expression.

Within these classifications, there is wide latitude in the particular symbol used to denote an index. For instance, in Equation 31, we could just as well have written ν in place of μ or β in place of α. The only requirement is that we always repeat a dummy index intended to imply summation and never repeat a free index. In certain situations in tensor analysis, it will be necessary to *relabel* an index that appears in a tensor equation. This relabeling is often applied to dummy indices, for instance by relabeling all occurrences of the symbol α with the symbol β. The primary use of relabeling is to recognize when it is allowable to combine groups of tensorial terms.

Now that we have described the summation convention, we can return to our discussion of tensorial character and the definition of a tensor. Although our example of the transformation law was based on a first order contravariant tensor, similar relations hold for tensors of all orders and types. Let us next consider the transformation of a first order covariant tensor. Its transformation behavior is given by,

$$\bar{T}_\mu = T_\alpha \frac{\partial x^\alpha}{\partial \bar{x}^\mu} \tag{32}$$

where summation is again on the α indices and μ is a free index. This transformation behavior can be viewed as the *definition* of a first order covariant tensor. Note that the covariant tensor transformation involves the forward derivatives of the coordinate mapping $\bar{x}^\mu \rightarrow x^\mu$ given by $\frac{\partial x^\alpha}{\partial \bar{x}^\mu}$ whereas the contravariant transformation given in Equation 31 involves the inverse derivatives of this transformation given by $\frac{\partial \bar{x}^\mu}{\partial x^\alpha}$.

This mechanism of defining tensors by their transformation laws can be extended to second order tensors in a straightforward way. For a second order contravariant tensor, we have,

$$\bar{T}^{\mu\nu} = T^{\alpha\beta} \frac{\partial \bar{x}^\mu}{\partial x^\alpha} \frac{\partial \bar{x}^\nu}{\partial x^\beta}. \tag{33}$$

That is, we have simply appended an additional factor of $\frac{\partial \bar{x}^\nu}{\partial x^\beta}$ in the transformation expression to correspond to the additional free index ν included in the notation for the tensor $T^{\mu\nu}$. This factor contains a subscript index β which is dummy because it also appears in $T^{\alpha\beta}$ in the product. A similar approach of appending the appropriate forward or inverse coordinate derivatives can be applied to arrive at the transformation laws for other types of second and higher order tensors. Table 2 summarizes the transformation laws for first and second order tensors.

It will be instructive to consider two special cases of first order tensors that we can recognize by their transformation laws. Consider a coordinate transformation in dimension $n = 2$ from the coordinates (x^1, x^2) to the coordinates $(\bar{x}^1, \bar{x}^2)$. Under the transformation, the coordinate differentials dx^1 and dx^2 become $d\bar{x}^1$ and $d\bar{x}^2$. A familiar result from

Table 2: Transformation Laws for Zeroth, First, and Second Order Tensors

Order	Type	Transformation Law
0	Invariant	$\bar{T} = T$
1	Contravariant	$\bar{T}^{\mu} = T^{\alpha} \frac{\partial \bar{x}^{\mu}}{\partial x^{\alpha}}$
1	Covariant	$\bar{T}_{\mu} = T_{\alpha} \frac{\partial x^{\alpha}}{\partial \bar{x}^{\mu}}$
2	Contravariant	$\bar{T}^{\mu\nu} = T^{\alpha\beta} \frac{\partial \bar{x}^{\mu}}{\partial x^{\alpha}} \frac{\partial \bar{x}^{\nu}}{\partial x^{\beta}}$
2	Mixed	$\bar{T}^{\mu}{}_{\nu} = T^{\alpha}{}_{\beta} \frac{\partial \bar{x}^{\mu}}{\partial x^{\alpha}} \frac{\partial x^{\beta}}{\partial \bar{x}^{\nu}}$
2	Covariant	$\bar{T}_{\mu\nu} = T_{\alpha\beta} \frac{\partial x^{\alpha}}{\partial \bar{x}^{\mu}} \frac{\partial x^{\beta}}{\partial \bar{x}^{\nu}}$

elementary calculus is the transformation behavior of these differentials:

$$\begin{aligned} d\bar{x}^1 &= \frac{\partial \bar{x}^1}{\partial x^1} dx^1 + \frac{\partial \bar{x}^1}{\partial x^2} dx^2 \\ d\bar{x}^2 &= \frac{\partial \bar{x}^2}{\partial x^1} dx^1 + \frac{\partial \bar{x}^2}{\partial x^2} dx^2. \end{aligned}$$

If we now interpret the superscript denoting the name of the coordinate as a free index and consider the summation convention, we can recognize a shorthand for these equations immediately as,

$$d\bar{x}^{\mu} = dx^{\alpha} \frac{\partial \bar{x}^{\mu}}{\partial x^{\alpha}}.$$

This form of the equations is precisely the form used to define a first order contravariant tensor. Therefore, we can conclude that the vector comprising the coordinate differentials is a tensor of this type and order. This first order tensor is considered to be the prototypical contravariant form.

Now let us examine the behavior of the gradient of a scalar value under a coordinate transformation. The gradient is a vector whose elements are the partial derivatives of the scalar with respect to each individual coordinate. Considering a scalar field ω and again taking the example of a coordinate transformation in $n = 2$ from (x^1, x^2) to $(\bar{x}^1, \bar{x}^2)$, the transformation behavior of the gradient of ω is given by the chain rule of partial derivatives

as,

$$\begin{aligned} \frac{\partial \omega}{\partial \bar{x}^1} &= \frac{\partial \omega}{\partial x^1}\frac{\partial x^1}{\partial \bar{x}^1} + \frac{\partial \omega}{\partial x^2}\frac{\partial x^2}{\partial \bar{x}^1} \\ \frac{\partial \omega}{\partial \bar{x}^2} &= \frac{\partial \omega}{\partial x^1}\frac{\partial x^1}{\partial \bar{x}^2} + \frac{\partial \omega}{\partial x^2}\frac{\partial x^2}{\partial \bar{x}^2} \end{aligned} .$$

If we now interpret the superscript in the denominator of the partial derivative as a subscripted free index and consider the summation convention, we can recognize a shorthand for these equations as,

$$\bar{\omega}_\mu = \omega_\alpha \frac{\partial x^\alpha}{\partial \bar{x}^\mu}$$

where we have defined $\bar{\omega}_\mu = \frac{\partial \omega}{\partial \bar{x}^\mu}$ and $\omega_\alpha = \frac{\partial \omega}{\partial x^\alpha}$. This form of the equations is precisely the form used to define a first order covariant tensor. Therefore, we can conclude that the vector comprising the gradient of a scalar is a tensor of this type and order. This first order tensor is considered as the prototypical covariant form.

Before we leave this section, it is worth pointing out an example of a mathematical object that is *not* a tensor. Consider an entity that we denote by the symbol $\Gamma^\mu_{\alpha\beta}$. This symbol has three indices located in both superscript and subscript locations, so we might be inclined to think that it is a third order mixed tensor. This suspicion need not be correct, however, as we cannot make any conclusion until we know the transformation law for the symbol under coordinate mappings.

Let us say that this transformation law is given by,

$$\bar{\Gamma}^\nu_{\sigma\tau} = \Gamma^\mu_{\alpha\beta}\frac{\partial \bar{x}^\nu}{\partial x^\mu}\frac{\partial x^\alpha}{\partial x^\sigma}\frac{\partial x^\beta}{\partial x^\tau} + \frac{\partial \bar{x}^\nu}{\partial x^\mu}\frac{\partial^2 x^\mu}{\partial \bar{x}^\sigma \partial \bar{x}^\tau}. \tag{34}$$

The first set of terms displays the correct behavior for a tensorial transformation, with one coordinate partial derivative factor of the contravariant type and two partial derivative factors of the covariant type. The problem with characterizing the symbol as a tensor lies in the second set of terms. They involve second derivatives of the coordinate transformation and do not multiply the symbol itself. This set of terms implies that the symbol $\Gamma^\mu_{\alpha\beta}$ does not have tensorial character and cannot be classified as a tensor. Although it is not a tensor, this symbol is of critical importantance in Riemannian geometry. It is termed the *Christoffel symbol of the second kind*, and it is the key to the concept of differentiation in curvilinear

coordinate systems and curved spaces. We shall revisit it shortly in our discussion of tensor calculus.

2.2.2 Tensor Algebra

In the previous section, we examined the transformation behavior of tensors. The tensor transformation laws that we discussed involved the addition of products of tensor components and coordinate transformation derivatives. The implication of this behavior is that both addition and multiplication of tensors have meaning. This is indeed the case, and in this section, we shall investigate the addition and multiplication of tensors of arbitrary type and order.

Addition is allowed for tensors of the same type and order. For instance, we can add the tensors $D_{\mu\nu}$ and $E_{\mu\nu}$ to obtain $F_{\mu\nu}$:

$$D_{\mu\nu} + E_{\mu\nu} = F_{\mu\nu}.$$

Similarly, we could add tensors of other types and orders, so long as the type and order of all of the tensors in the summation match.

Note that we described all of the tensors in this expression with the same indices μ and ν. Because neither μ nor ν appear in both subscript and superscript locations within the same tensor or in a tensor product, they are free indices. We could have chosen to name the free indices in each of the tensors within the sum differently; however, because we are always allowed to relabel indices so long as dummy indices remain dummy and free indices remain free, we can therefore always choose to make the names in the corresponding locations match.

Tensor subtraction is defined analogously in the expected way. For instance, we can rewrite the above expression as

$$D_{\mu\nu} = F_{\mu\nu} - E_{\mu\nu}.$$

Because addition is defined as a valid operation only among tensors of the same type and order, summation expressions in which the types and orders do not match such as

$$A^{\mu}_{\nu} + B^{\kappa\mu\nu}$$

have no meaning. This behavior is as we should expect from experience with vector and matrix analysis, because, for instance, we can add a vector to another vector and a matrix to another matrix but not a matrix to a vector.

We will now examine tensor multiplication. Whereas tensor addition is quite straightforward, tensor multiplication is more subtle. For instance, there are two types of tensor products, namely the *inner product* and the *outer product*.

Let us first discuss the outer product. The outer product of two tensors is a third tensor with the tensor character of the concatenation of the set of indices of its factors. For instance, let us multiply the second order contravariant tensor $H^{\mu\nu}$ by the second order covariant tensor $K_{\alpha\beta}$. The outer product of these two tensors can be called $M^{\mu\nu}{}_{\alpha\beta}$, which is a fourth order mixed tensor with two contravariant indices and two covariant indices. We can write this product as the expression

$$H^{\mu\nu}\, K_{\alpha\beta} = M^{\mu\nu}{}_{\alpha\beta}. \tag{35}$$

From this example, it is clear that the operation of multiplication to obtain an outer product *expands* the tensor character of the factors to produce a higher order tensor. Specifically, if we outer multiply a tensor of order m by a tensor of order n, the outer product is a tensor of order $m + n$.

It is important to note that all of the indices in the expression above for the outer product are unique and are hence free indices. If we had repeated any of the indices within the outer product, the Einstein convention would imply that the product involves a summation. For instance, let us consider the product

$$N^{\mu\nu}\, P_{\mu\beta} = Q^{\mu\nu}{}_{\mu\beta}. \tag{36}$$

In this product, the index μ is repeated in a superscript and a subscript, so summation is implied.

This summation leads to the question of the tensorial character of the product $Q^{\mu\nu}{}_{\mu\beta}$. Because tensors are fundamentally defined by their transformation laws, we must investigate the tensor character of the product by its transformation law. To do this, we follow a similar approach to that given by Synge and Schild [106].

Considering the tensor $Q^{\mu\nu}{}_{\alpha\beta}$ given in coordinate system x^χ, the transformation law indicates that it should be given by

$$\bar{Q}^{\mu\nu}{}_{\alpha\beta} = Q^{\sigma\tau}{}_{\kappa\lambda} \frac{\partial \bar{x}^\mu}{\partial x^\sigma} \frac{\partial \bar{x}^\nu}{\partial x^\tau} \frac{\partial x^\kappa}{\partial \bar{x}^\alpha} \frac{\partial x^\lambda}{\partial \bar{x}^\beta}$$

in the frame $\bar{x}^\chi$. Next, we set $\alpha = \mu$ to imply summation and obtain the desired form $\bar{Q}^{\mu\nu}{}_{\mu\beta}$. This gives

$$\bar{Q}^{\mu\nu}{}_{\mu\beta} = Q^{\sigma\tau}{}_{\kappa\lambda} \frac{\partial \bar{x}^\mu}{\partial x^\sigma} \frac{\partial \bar{x}^\nu}{\partial x^\tau} \frac{\partial x^\kappa}{\partial \bar{x}^\mu} \frac{\partial x^\lambda}{\partial \bar{x}^\beta}.$$

Tensor multiplication is commutative, so we can rearrange the order of the coordinate derivatives (which are first order covariant tensors) to obtain

$$\bar{Q}^{\mu\nu}{}_{\mu\beta} = Q^{\sigma\tau}{}_{\kappa\lambda} \left(\frac{\partial \bar{x}^\mu}{\partial x^\sigma} \frac{\partial x^\kappa}{\partial \bar{x}^\mu} \right) \frac{\partial \bar{x}^\nu}{\partial x^\tau} \frac{\partial x^\lambda}{\partial \bar{x}^\beta}.$$

The factors in parentheses have a particular behavior that defines the mixed second order tensor called the *Kronecker delta tensor*,

$$\delta^\kappa_\sigma = \frac{\partial \bar{x}^\mu}{\partial x^\sigma} \frac{\partial x^\kappa}{\partial \bar{x}^\mu}$$

where

$$\begin{aligned} \delta^\kappa_\sigma &= 1 \quad \text{for } \kappa = \sigma \\ \delta^\kappa_\sigma &= 0 \quad \text{for } \kappa \neq \sigma. \end{aligned} \tag{37}$$

Substituting this expression into the transformation law gives

$$\bar{Q}^{\mu\nu}{}_{\mu\beta} = Q^{\sigma\tau}{}_{\kappa\lambda} \delta^\kappa_\sigma \frac{\partial \bar{x}^\nu}{\partial x^\tau} \frac{\partial x^\lambda}{\partial \bar{x}^\beta}.$$

In this expression, summation is implied on the indices κ and σ. Because of the definition of the Kronecker delta tensor, the terms in this summation will be nonzero only when $\kappa = \sigma$. We can therefore, rewrite the expression in terms of a single summation over σ as

$$\bar{Q}^{\mu\nu}{}_{\mu\beta} = Q^{\sigma\tau}{}_{\sigma\lambda} \frac{\partial \bar{x}^\nu}{\partial x^\tau} \frac{\partial x^\lambda}{\partial \bar{x}^\beta}$$

in which the Kronecker delta tensor δ^κ_σ does not explicitly appear. This expression can be recognized as the definition of a transformation law for a second order mixed tensor

covariant in β and contravariant in ν; therefore, we can identify the entity $\bar{Q}^{\mu\nu}{}_{\mu\beta}$ as a tensor of this type and order.

From this exercise, we can see that the type of tensor multiplication exemplified by Equation 36 in which a dummy index appears in the product is different from the type indicated in Equation 35 in which there is no implied summation. Whereas the outer product of Equation 35 *expands* the tensor order of the product relative to its factors, the multiplication in Equation 36 *contracts* the tensor order of the corresponding outer product that would have been obtained had we not repeated an index. This latter type of multiplication that involves a dummy index is termed the *inner product*. This process of replacing a free index within an outer product with a dummy index to obtain an inner product contracts the tensor order of the outer product, and is appropriately termed *contraction*.

Now that we have investigated tensor addition and multiplication, we are ready to discuss a very important second order tensor that is crucial to Riemannian geometry—the metric tensor.

2.2.3 The Metric Tensor

2.2.3.1 Definition through the Line Element

We shall introduce the metric tensor by consideration of the *line element*. The line element is the square of the measure of an infinitesimal distance between points in space. We denote it by the symbol ds^2 in which the d indicates that we are concerned with a differential or infinitesimal element and s is the typical symbol used as the measure of the distance along a path.

In the Cartesian coordinate system (x^1, x^2) in two–dimensional space (which we may also denote by the shorthand x^α), the line element is given by the familiar geometric relation

$$ds^2 = \left(dx^1\right)^2 + \left(dx^2\right)^2 \tag{38}$$

where we imply ds^2 as the squared length element and not a tensorial notation. This expression can be recognized immediately as an application of the Pythagorean theorem to infinitesimal coordinate increments. That is, the elements dx^1 and dx^2 form the legs of an

infinitesimal right triangle with hypotenuse ds. The fact that the infinitesimal triangle is a right triangle stems from the orthogonality of the Cartesian coordinates (x^1, x^2).

Cartesian coordinates are a very special and simple case, so let us now consider the line element expressed in polar coordinates (r^1, r^2) where r^1 is the radius (typically denoted simply as r) and r^2 is the polar angle (often termed θ). We adopt this naming convention for consistency with the tensorial index approach.

The mathematical mechanism for determining infinitesimal lengths is well known for polar coordinates. We could obtain the relation directly from the geometric construction of the polar coordinate system or by transformation from a Cartesian frame through the commonly known relations

$$\begin{aligned} x^1 &= r^1 \sin r^2 \\ x^2 &= r^1 \cos r^2. \end{aligned} \tag{39}$$

To determine the line element from this transformation, we first take differentials of Equation 39 to give

$$\begin{aligned} dx^1 &= dr^1 \sin r^2 + r^1 \cos r^2 dr^2 \\ dx^2 &= dr^1 \cos r^2 - r^1 \sin r^2 dr^2 \end{aligned} \tag{40}$$

then square them

$$\begin{aligned} \left(dx^1\right)^2 &= \left(dr^1\right)^2 \sin^2 r^2 + 2r^1 \sin r^2 \cos r^2 dr^1 dr^2 + \left(r^1\right)^2 \cos^2 r^2 \left(dr^2\right)^2 \\ \left(dx^2\right)^2 &= \left(dr^1\right)^2 \cos^2 r^2 - 2r^1 \sin r^2 \cos r^2 dr^1 dr^2 + \left(r^1\right)^2 \sin^2 r^2 \left(dr^2\right)^2 \end{aligned} \tag{41}$$

and add the squares to obtain

$$ds^2 = \left(dx^1\right)^2 + \left(dx^2\right)^2 = \left[\sin^2 r^2 + \cos^2 r^2\right] \left[\left(dr^1\right)^2 + \left(r^1\right)^2 \left(dr^2\right)^2\right] \tag{42}$$

which can be recognized through the trigonometric identity $\cos^2 r^2 + \sin^2 r^2 = 1$ to be

$$ds^2 = \left(dr^1\right)^2 + \left(r^1\right)^2 \left(dr^2\right)^2. \tag{43}$$

As is clear from this exposition, the infinitesimal length ds that we derive for Cartesian coordinates is the same as that found from polar coordinates. That is, ds is *invariant* with

respect to the transformation between Cartesian and polar coordinates. This invariance is in fact a general result true for all coordinate transformations. It is also a result that is intuitive and physical: no matter how we choose to label points by laying out a coordinate grid, we always measure the *length* of the line between specific points to be the same if we use the same "ruler."

The main difference in the expression for the line element in polar coordinates given by Equation 43 and that given by Equation 38 for Cartesian coordinates is the coefficient $\left(r^1\right)^2$ that multiplies the second term. This coefficient is necessary because the second coordinate r^2 is fundamentally an *angular* measurement, whereas the line element is fundamentally a measurement of *length*. This coefficient is effectively the transfer function that determines the magnitude of length change associated with an infinitesimal unit of angular change. The coefficient multiplying the $\left(dr^1\right)^2$ term is unity, indicating that the radial coordinate is expressed directly in the same length units as the line element itself. It is clear that these coefficients are fundamental to the concept of length. Indeed, they represent the way coordinates relate to our "ruler" that we use in measurements, and we can expect the coefficients to be different in different coordinate systems.

These coefficients form the elements of a second order covariant tensor called the *metric tensor*. The adjective *metric* evokes the fundamental importance of this tensor in the measurement of length. To understand the tensorial character of these coefficients, let us extend our purview from Cartesian and polar coordinates to consider the general case. We can write a quite general expression for the line element in two dimensions in the form

$$ds^2 = g_{11}\left(dx^1\right)^2 + g_{12}\,dx^1\,dx^2 + g_{21}\,dx^2\,dx^1 + g_{22}\left(dx^2\right)^2. \tag{44}$$

Using the Einstein summation convention, we can abbreviate this expression as

$$ds^2 = g_{\mu\nu}\,dx^\mu\,dx^\nu. \tag{45}$$

For a space of arbitrary dimension n, we take both μ and ν to range $1:n$.

As we illustrated in Section 2.2.1.2, the coordinate differentials dx^μ are contravariant vectors. Although we shall not derive the result here, it can be shown that a second order

covariant entity must have tensorial character if its inner product with two contravariant vectors produces an invariant [106]. In our case ds^2 is an invariant, so we conclude that $g_{\mu\nu}$ is a tensor.

We can make one additional statement about this tensor: it is *symmetric*. That is, it satisfies the condition $g_{\mu\nu} = g_{\nu\mu}$. This condition is largely a choice that we make for convenience based on the nature of the metric tensor's appearance within the line element. We can see this for the two–dimensional case from Equation 44. Because both g_{12} and g_{21} multiply the same differential expression $dx^1\,dx^2$, we can write

$$ds^2 = g_{11}\left(dx^1\right)^2 + \left[g_{12} + g_{21}\right]\,dx^1\,dx^2 + g_{22}\left(dx^2\right)^2 .$$

There is therefore no independent significance to either g_{12} or g_{21}, so we can always choose to set $g_{21} = g_{12}$ and write the line element as

$$ds^2 = g_{11}\left(dx^1\right)^2 + 2\,g_{12}\,dx^1\,dx^2 + g_{22}\left(dx^2\right)^2 . \tag{46}$$

We can now make some observations about the metric tensor for the Cartesian and polar coordinate systems examined earlier. In both cases, the elements of the metric tensors can be determined by simply reading off the values of the coefficients in the line element and matching them to the general expression given by Equation 46. For the Cartesian system, we can see from Equation 38 that the metric tensor elements are

$$\begin{aligned} g_{11} &= 1 \\ g_{12} &= 0 \\ g_{22} &= 1 \end{aligned} \tag{47}$$

and for the polar system, Equation 43 shows that the metric is given by

$$\begin{aligned} g_{11} &= 1 \\ g_{12} &= 0 \\ g_{22} &= \left(r^1\right)^2 . \end{aligned} \tag{48}$$

In both of these systems, the off–diagonal element $g_{12} = g_{21}$ is zero. Coordinate systems such as these in which the terms $g_{\mu\nu} = 0$ for $\mu \neq \nu$ are *orthogonal* systems. As implied

by this description, the coordinate curves of orthogonal coordinate systems meet at right angles. Most commonly encountered curvilinear coordinate systems are orthogonal. If one has the option of choosing a coordinate frame for analysis, it is often preferred to consider an orthogonal system because many of the equations of Riemannian geometry become substantially simpler in such systems.

We shall frequently have need of an alternate manifestation of the metric tensor. Whereas the metric tensor $g_{\mu\nu}$ is a second order covariant tensor, a second order contravariant tensor $g^{\mu\nu}$ can also be defined. This tensor is often termed the *conjugate metric tensor* [106] or *contravariant metric tensor*. It can be obtained from the covariant metric tensor through an analogy with matrices. We can treat the covariant metric tensor $g_{\mu\nu}$ as a matrix with n^2 components, of which $n(n+1)/2$ are unique because of the symmetry requirement. The elements of the inverse of this matrix are the components of the contravariant metric tensor $g^{\mu\nu}$, which is also symmetric. Therefore, the relation

$$g_{\alpha\nu}\, g^{\mu\alpha} = \delta^{\mu}_{\nu} \tag{49}$$

holds where δ^{μ}_{ν} is the Kronecker delta tensor. In this context, the Kronecker delta is the analog to the identity matrix.

2.2.3.2 Raising and Lowering Indices

Having defined the metric tensor and its conjugate through the line element, we shall begin to explore how it is used for analysis in Riemannian geometry. The first application we consider is in relating the covariant and contravariant components of tensors.

In Section 2.2.1, tensors were described as being either covariant, contravariant, or mixed based on their transformation behavior and the location of their indices. Based on this discussion, one may have been led to believe that this variance behavior is somehow fundamental and intrinsic to the definition of the tensor itself, perhaps stemming from the physical phenomenon that the tensor describes. In this section, we shall see that although the *order* of a tensor is fundamental and perhaps physical, its *variance* is related to how we choose to express the tensor components. The metric tensor allows us to choose whether we express the same *physical components* as either a covariant, contravariant, or mixed tensor.

Let us suppose that a first order contravariant tensor T^μ is given. We can take the inner product of this tensor with the metric tensor $g_{\mu\nu}$. From the discussion of inner products in Section 2.2.2, we know that the resulting entity will be a first order covariant tensor with the free index ν, say, L_ν. That is,

$$L_\nu = g_{\mu\nu} T^\mu.$$

In this special type of an inner product involving the metric tensor, we make the notational identification $L_\nu = T_\nu$ so that

$$T_\nu = g_{\mu\nu} T^\mu. \tag{50}$$

The operation of obtaining the tensor T_ν from the tensor T^μ through an inner product involving the metric tensor is called *lowering the index*.

The inverse operation of obtaining T^μ from T_ν involves the conjugate metric tensor. This operation is given by

$$T^\mu = g^{\mu\nu} T_\nu \tag{51}$$

and is called *raising the index*.

Raising and lowering of indices can be performed on tensors of any type or order. For instance, we can lower indices of the tensors $F^{\mu\alpha}$ and $H^\alpha{}_\mu$ to obtain

$$\begin{aligned} F^\mu{}_\nu &= g_{\alpha\nu}\, F^{\mu\alpha} \\ H_{\mu\nu} &= g_{\alpha\nu}\, H^\alpha{}_\mu, \end{aligned} \tag{52}$$

and we can raise the indices of the tensors $Q_{\mu\alpha}$ and $P^\mu{}_\alpha$ as

$$\begin{aligned} Q^\nu{}_\mu &= g^{\alpha\nu}\, Q_{\mu\alpha} \\ P^{\mu\nu} &= g^{\alpha\nu}\, P^\mu{}_\alpha. \end{aligned} \tag{53}$$

We can think of a new tensor obtained from raising or lowering an index as having the same *physical* meaning as the original tensor. The differences in the numerical values of the elements of the original and altered tensors is a result of the *geometric* implications of the metric.

2.2.3.3 Length of a Vector

In Section 2.2.3.1, we discussed the invariance of the length of an infinitesimal line segment under coordinate transformations. Length was interpreted as a concept that transcends the parametrization of any particular coordinate grid, depending instead on the "ruler" we use for measurement. Whereas our interest in Section 2.2.3.1 was on the infinitesimal length associated with the contravariant vector of coordinate differentials dx^α separating two nearby points in physical space, we shall see in this section that the concept of length invariance extends to all vectors.

The length T of a contravariant vector T^μ is defined through

$$T^2 = g_{\mu\nu}\, T^\mu\, T^\nu. \tag{54}$$

Inspecting the right hand side, we see that the multiplication is a type of inner product involving a double summation. Both index μ and index ν are dummy and summed over. The result of this operation is to contract the outer product $T^\mu\, T^\nu$ to a scalar, which is coordinate system invariant. Invariance is a characteristic of any scalar value; however, only in the particular case that this contraction is accomplished with the metric tensor $g_{\mu\nu}$ do we call the associated scalar the *length* or *magnitude* of the vector T^μ.

We can now rewrite the contravariant vectors on the right hand side of Equation 54 by raising the index of the associated covariant vectors. This operation gives,

$$T^2 = g_{\mu\nu}\, \left(g^{\mu\sigma}\, T_\sigma\right)\, \left(g^{\nu\tau}\, T_\tau\right).$$

Since tensor multiplication is commutative, we can rearrange this expression as

$$T^2 = g_{\mu\nu}\, g^{\mu\sigma}\, g^{\nu\tau}\, T_\sigma\, T_\tau.$$

Noting that $g_{\mu\nu}\, g^{\mu\sigma} = \delta^\sigma_\nu$, this expression becomes

$$T^2 = \delta^\sigma_\nu\, g^{\nu\tau}\, T_\sigma\, T_\tau.$$

The Kronecker delta tensor implies that the only contribution to the summation occurs when $\nu = \sigma$, so we can omit the delta tensor, relabel ν as σ, and write

$$T^2 = g^{\sigma\tau}\, T_\sigma\, T_\tau. \tag{55}$$

This expression is directly analogous to Equation 54 that defines the length of a contravariant vector, except that we have replaced the contravariant vector T^ν with the covariant vector T_ν and the metric tensor $g_{\mu\nu}$ with the conjugate metric tensor $g^{\mu\nu}$. We therefore describe Equation 55 as the recipe for determining the length of a covariant vector T_ν. As is clear from the way in which Equation 55 was derived, the length T of the covariant vector T_ν is the same as the length of the contravariant vector T^ν. The concept of length is therefore independent of the variance of a vector.

To summarize our exposition of tensor analysis thus far, we have explained the notation and nature of tensors, discussed their addition and multiplication, and described the role of the metric tensor in the algebraic operations of index raising and lowering and determining lengths. We are now ready to examine how the metric tensor affects tensor calculus.

2.2.4 Tensor Differentiation

A common approach to introducing the differentiation of tensors in Riemannian geometry is through the concept of *parallel transport* of a vector along a path. Closely associated with this concept are *geodesics*, which are curves whose lengths are stationary with respect to small but arbitrary perturbations [106]. A detailed exposition of these concepts is unnecessary for the work presented in this dissertation, so in this section, we shall instead present only the key results necessary for carrying out the process of tensorial differentiation. We shall have need of tensor differentiation in developing the fluid dynamic theory presented in Chapter 4. If the reader is interested in studying the concepts of parallel transport and geodesics, the classical reference is Eisenhart's 1926 text on Riemannian geometry [34]. Excellent presentations are also given by Kreyszig [61] as well as Synge and Schild [106].

The first concept that we will need for tensor differentiation is that of the *Christoffel symbols*. These symbols are tensor–like entities that are functions of the metric tensor and its partial derivatives. There are two types of Christoffel symbols, termed simply the *Christoffel symbols of the first kind* and the *Christoffel symbols of the second kind*. In Section 2.2.1.2, we showed that the Christoffel symbols of the second kind are not tensors because their transformation law contains an additional set of terms involving the second

derivatives of the coordinate transformation. Nonetheless, these symbols take indices in a way similar to a third order mixed tensor.

The Christoffel symbols of the first kind are represented by three indices enclosed in brackets in the form $[\mu\nu,\ \sigma]$. The symbols are defined as a combination of the partial derivatives of the metric tensor with respect to the coordinates x^α as,

$$[\mu\nu,\ \sigma] = \frac{1}{2}\left(\frac{\partial g_{\sigma\mu}}{\partial x^\nu} + \frac{\partial g_{\sigma\nu}}{\partial x^\mu} - \frac{\partial g_{\mu\nu}}{\partial x^\sigma}\right). \tag{56}$$

As described previously, the Christoffel symbols of the second kind are represented by three indices, two subscripted and one superscripted. Common notations are $\Gamma^\alpha_{\mu\nu}$ and $\left\{ {\alpha \atop \mu\nu} \right\}$. They are defined with respect to the symbols of the first kind as

$$\Gamma^\alpha_{\mu\nu} = g^{\alpha\beta}\,[\mu\nu,\ \beta]. \tag{57}$$

Considering Equation 56, the symbols can also be expressed directly in terms of the metric tensor as

$$\Gamma^\alpha_{\mu\nu} = \frac{1}{2}\,g^{\alpha\beta}\,\left(\frac{\partial g_{\beta\mu}}{\partial x^\nu} + \frac{\partial g_{\beta\nu}}{\partial x^\mu} - \frac{\partial g_{\mu\nu}}{\partial x^\beta}\right). \tag{58}$$

The Christoffel symbols make their appearance in tensor calculus through the *covariant derivative* of a tensor. The covariant derivative of a first order contravariant tensor T^ν with respect to the coordinate x^α is given by the expression

$$T^\nu{}_{;\,\alpha} = \frac{\partial T^\nu}{\partial x^\alpha} + \Gamma^\nu_{\beta\alpha}\,T^\beta \tag{59}$$

where we denote the operation of covariant differentiation with a semicolon followed by an index. The first term in the derivative is simply the partial derivative of the tensor component T^ν with respect to the coordinate x^α and the second term represents the contribution of the metric tensor embodied through the Christoffel symbol of the second kind. We will frequently abbreviate the operation of partial differentiation with a comma followed by an index, so Equation 59 can also be expressed as

$$T^\nu{}_{;\,\alpha} = T^\nu{}_{,\,\alpha} + \Gamma^\nu_{\beta\alpha}\,T^\beta \tag{60}$$

In Equation 60, the index of differentiation, α, is free. Therefore, the equation defines a separate covariant derivative of T^ν for all allowable values of the index in the range $1 : n$.

It is also possible to take the index of differentiation as a dummy index. As we discussed in the description of the Einstein convention, an index repeated in both a superscript or subscript position, even in tensor products and derivatives, indicates summation. We can therefore write the expression

$$T^{\nu}_{\ ;\,\nu} = T^{\nu}_{\ ,\,\nu} + \Gamma^{\nu}_{\beta\nu}\, T^{\beta} \tag{61}$$

with summation implied on the index ν. The Christoffel symbol $\Gamma^{\nu}_{\beta\nu}$ also contains an implied summation. It can be shown that this expression for the contracted Christoffel symbol is equivalent to

$$\Gamma^{\nu}_{\beta\nu} = \frac{1}{\sqrt{g}}\,(\sqrt{g})_{,\,\beta} \tag{62}$$

where g is the determinant of the metric tensor $g_{\mu\nu}$ obtained by treating the tensor as a matrix [106]. Equation 61 can therefore be written

$$\begin{aligned} T^{\nu}_{\ ;\,\nu} &= T^{\nu}_{\ ,\,\nu} + \frac{1}{\sqrt{g}}\,(\sqrt{g})_{,\,\beta}\, T^{\beta} \\ &= \frac{1}{\sqrt{g}}\left[\sqrt{g}\; T^{\nu}_{\ ,\,\nu} + (\sqrt{g})_{,\,\beta}\, T^{\beta}\right] \\ &= \frac{1}{\sqrt{g}}\,(\sqrt{g}\, T^{\nu})_{,\,\nu}\,. \end{aligned} \tag{63}$$

Equation 63 is the tensorial expression of the *divergence* of a vector and is equivalent to $\nabla \cdot \vec{T}$ in ∇ operator notation.

We can arrive at another useful form of Equation 63 by relating the contravariant vector T^{ν} to its covariant form as $T^{\nu} = g^{\nu\alpha}T_{\alpha}$. This gives

$$(g^{\nu\alpha}T_{\alpha})_{\ ;\,\nu} = \frac{1}{\sqrt{g}}\,(\sqrt{g}\, g^{\nu\alpha}T_{\alpha})_{,\,\nu}\,. \tag{64}$$

The *curl*, which is defined with respect to a covariant vector, is given by

$$\omega_{\alpha\beta} = T_{\alpha,\,\beta} - T_{\beta,\,\alpha}. \tag{65}$$

In the special case that the covariant vector T_{α} satisfies $\omega_{\alpha\beta} = 0$, it can be represented as the gradient of a scalar, say ϕ, as $T_{\alpha} = \phi_{,\,\alpha}$. Substituting this representation into Equation 64 results in

$$(g^{\nu\alpha}\phi_{,\,\alpha})_{\ ;\,\nu} = \frac{1}{\sqrt{g}}\,(\sqrt{g}\, g^{\nu\alpha}\phi_{,\,\alpha})_{,\,\nu}\,. \tag{66}$$

Equation 66 is the *Laplacian* of the scalar ϕ and is the equivalent to the $\nabla^2\phi$ in ∇ operator notation.

It is also possible to define the covariant derivatives of tensors of other orders and types. For a covariant vector, the result is

$$T_{\nu;\,\alpha} = T_{\nu,\,\alpha} - \Gamma^{\beta}_{\nu\alpha}\, T_{\beta}.$$

The covariant derivatives of second order tensors contain a second set of terms involving the Christoffel symbols. For a contravariant tensor of second order, we have

$$T^{\mu\nu}{}_{;\,\alpha} = T^{\mu\nu}{}_{,\,\alpha} + \Gamma^{\mu}_{\beta\alpha}\, T^{\beta\nu} + \Gamma^{\nu}_{\beta\alpha}\, T^{\mu\beta}.$$

A covariant second order tensor has the covariant derivative

$$T_{\mu\nu;\,\alpha} = T_{\mu\nu,\,\alpha} - \Gamma^{\beta}_{\mu\alpha}\, T_{\beta\nu} - \Gamma^{\beta}_{\nu\alpha}\, T_{\mu\beta}$$

and for a mixed second order tensor, we obtain

$$T^{\mu}{}_{\nu;\,\alpha} = T^{\mu}{}_{\nu,\,\alpha} - \Gamma^{\mu}_{\beta\alpha}\, T^{\beta}{}_{\nu} - \Gamma^{\beta}_{\nu\alpha}\, T^{\mu}{}_{\beta}.$$

Before we leave this discussion of covariant differentiation, we need to establish one additional result—the covariant derivative of the metric tensor. For the metric tensor and its conjugate, the following special results hold:

$$\begin{aligned} g_{\mu\nu;\,\alpha} &= 0 \\ g^{\mu\nu}{}_{;\,\alpha} &= 0 \end{aligned}$$

This fact that all covariant derivatives of the metric tensor vanish is called *Ricci's lemma* or the *metricity condition* [34]. These results can be validated by direct substitution of the metric tensor into the expression for the covariant derivative and by employing the definition of the Christoffel symbols.

CHAPTER III

RESEARCH FORMULATION

In Chapter 1, we examined several known analogies relating compressible potential flow to elements of relativity theory. A key facet of these analogies that is of interest to this work is that they indicate the possibilities of *transformations* among *equivalent flows*. The special relativistic framework of potential fluid motion provides a mathematical mechanism for linking a given linear compressible flow to an equivalent incompressible flow based on the invariance of the wave equation under Lorentz transformations. This mechanism has been successfully exploited to produce the classical compressibility corrections of Prandtl, Glauert, Göthert, and Küssner.

Most of the literature in this area has focused on transformation techniques devised for *linearized* compressible fluid motion in a context relevant to the special theory of relativity. In many ways, however, the success of these transformation methods and the very interesting recent work linking black holes and acoustics suggests the possibility to pursue transformation techniques based on a *nonlinear* analogy with aspects more akin to the general theory of relativity. While the general theory was devised as a geometric manifestation of gravity, such an analogy might ultimately put forward a geometric theory of fluid compressibility with similar phenomenological features.

In this chapter, we will pose a research problem for a nonlinear transformation technique inspired by a general relativistic viewpoint. The intent of this transformation is to produce an equivalent incompressible flow corresponding to a given planar steady subsonic potential flow. Based on the general relativistic inspiration, the proposed method leverages many mathematical procedures from this field including Riemannian geometric techniques. Although the method is inspired by a general relativistic viewpoint, it is important to emphasize that the approach taken in this thesis is *not* intended to produce a true general

relativistic theory of classical fluid motion with deep philosophical and physical implications. Rather, our primary intent is to develop a transformation technique of practical value in solving and understand flow problems.

The problem statement for the research is intended to reflect the scientific method in the following paradigm: *Observations* based on the existing analogies suggest a *primary research question* whose answer is provided by a *hypothesis* that is to be investigated and tested as the main focus of the dissertation.

The hypothesis proposes a mathematical transformation technique that links a subsonic potential flow to an equivalent incompressible flow. The hypothesis is to be tested by developing the necessary transformation theory based on the governing flow equations and then performing analytical and numerical calculations to solve known subsonic flow test cases with the mathematical theory.

In the first section, the observations, primary research question, and hypothesis statement are presented. The second section details the research tasks that must be accomplished to test the hypothesis and poses specific scientific or mathematical questions to be answered in accomplishing each task. As it is inappropriate to press the analogy with general relativity too far, the chapter concludes with a final section that describes the limitations of the analogy and summarizes the similarities and differences between the proposed compressibility theory and the relativistic description of gravitation.

3.1 A Transformation Technique Inspired by General Relativity

3.1.1 Observations and Primary Question

Based on the discussion in Chapter 1, we make several observations regarding the status of relativistic analogies for compressible flow. These observations are presented below.

Observations:

- A *special relativistic analogy* for transformations involving *linearized* compressible potential flows and moving acoustic sources based on the invariance of the wave equation under Lorentz transformations is well known.
- This invariance has been leveraged for a variety of subsonic compressibility corrections including the Prandtl–Glauert, Göthert, and Küssner rules that enable or simplify flow solutions by transformation to a canonical Laplacian or d'Alembertian form.
- An analogy noting similarities between acoustic point sinks and black holes has been discovered. The approach embeds certain elements of the acoustic wave equation into the metric tensor to define an underlying manifold or coordinate system. The work also points to the notion of varying this metric tensor throughout space and time as a function of flow properties.
- This analogy with black holes coupled with the notion of a metric tensor that varies from point to point as a function of the flow suggests that we are on the verge of a *general relativistic analogy* for describing transformations involving *nonlinear* compressible potential flow.

These observations lead us to the following question that is the primary source of scientific motivation for the approach taken in this research.

Primary Question: Inspired by the success of the special relativistic viewpoint and the potential for a general relativistic analogy, can we *geometrize nonlinear compressibility through the metric tensor* and create a mapping to an equivalent incompressible flow in canonical Laplacian form?

In forming this question, primary importance has been given to the metric tensor. This emphasis stems from observations about the importance of the metric in the general theory

of relativity and in Riemannian geometry. We shall review some of these observations now as we begin to establish a mechanism for answering the primary research question through a hypothesis.

3.1.2 Hypothesis

The metric tensor is the geometric entity that embodies the forces ascribed to gravitation in the general theory of relativity. The connection of this geometric object to the physics of gravity is provided by Einstein's equation,

$$G_{\mu\nu} = 8\pi T_{\mu\nu} \tag{67}$$

where $G_{\mu\nu}$ is the Einstein tensor, a function of the second derivatives of the metric tensor components $g_{\mu\nu}$, and $T_{\mu\nu}$ is the stress–energy tensor of a matter distribution [80]. The distribution of matter is typically taken to be a fluid, such as the fluid comprising a star or the cosmological fluid made up of stars, galaxies, and interstellar dust that comprise the universe. The Einstein equation is a second order hyperbolic differential equation whose solution gives the metric tensor as a function of location in space–time. It is the relativistic equivalent of Newton's law of universal gravitation [129].

The results and predictions of the general theory hinge entirely upon the metric tensor. In the presence of distributed matter, the metric tensor is nontrivial and varies from point to point. This variation gives rise to the curvature of space–time, and the forces of gravity are ascribed to this curvature as effects of geometry, much in the same way that so-called "centrifugal force" is an artifact of the geometry of circular motion. The notion of space–time curvature, as manifested by the variation of the metric tensor, was perhaps the primary innovation of the general theory.

This perspective of curvature was enabled by Einstein's use of Riemannian geometry. As we saw in Chapter 2, the metric tensor plays a key role in Riemannian geometric theory. A very important contribution of the theory is to describe the conditions on the metric tensor that dictate when a space is flat and when it is intrinsically curved. This distinction is important, as metric tensors that vary from point to point can describe either certain coordinate systems in flat space or coordinate systems in a curved space. For instance, even

simple systems such as cylindrical and spherical coordinates have metric tensors that vary as a function of the radius from a fixed origin.

The first issue that we must address in answering the research question is to understand the mechanism by which the metric tensor affects the governing equations for the fluid flow. A very important result from the general theory of relativity is the *strong equivalence principle*. This principle asserts (among other things) that any physical equation that can be written in covariant form involving the metric tensor can be transitioned from a flat–space equation to a curved–space equation simply by replacing a flat–space metric tensor with a curved–space metric tensor [67]. As equations written in covariant form are also invariant with respect to all allowable coordinate transformations, the strong equivalence principle can be viewed as putting all metrics on equal footing with respect to their impact on the covariant form of physical equations. That is, any metric, produced either through gravity or through a coordinate transformation affects the physical equations through the same mathematical transformation law.

The notion of the strong equivalence principle has a great appeal for our problem of the geometrization of fluid compressibility. Namely, it suggests a way to determine the metric tensor: write the incompressible flow equations in covariant form and select the metric such that it produces the varying density of a subsonic flow. That is, we start with the covariant form of the incompressible flow equations, and we try to choose the metric such that the equations look like the compressible equations corresponding to a particular coordinate system of interest. We therefore hope to find an equivalent incompressible flow to a compressible flow that is given in a particular coordinate system.

The metric determined by this recipe would then be a function of the flow properties that differs from the originally given metric only by terms involving the density and other varying flow properties. In the limit of $M_\infty \to 0$, the influence of compressibility vanishes and the metric should ideally attain the same form for both the compressible and equivalent incompressible flows. In this way, the change we induce to the given metric is precisely the amount needed to absorb the effects of compressibility. As in the case of gravity, we can now ascribe all forces owing to compressibility to the geometry induced by the change in

metric tensor from the compressible flow to the equivalent incompressible flow.

One might question whether it is valid to extend the strong equivalence principle in this way from gravity to our problem of fluid motion. There are many interpretations of the equivalence principle in relativity theory, and some debate surrounds its physical, mathematical, and philosophical status [87]. Much of this debate involves the question of whether extending the form invariance (covariance) of physical equations from coordinate invariance in flat spaces to curved spaces represents the correct generalization for all of the equations of mathematical physics. In particular, one might ask whether curvature should introduce new terms or factors in certain equations. This concept is termed *curvature coupling*, and no conclusive evidence supporting the concept has been found [97]. For this reason, the physics community seems content at present to extend covariance through the simple mechanism of the strong equivalence principle without resorting to curvature coupling on the basis of Occam's Razor. Indeed, it seems that there is broad consensus that this approach is *mathematically* correct, and most of the debate centers around the physical interpretation of the resulting equations in the presence of gravity.

In our case for potential flow, we shall adopt an equivalence principle linking compressible and incompressible flows that is substantially similar to the equivalence principle of general relativity; however, we shall substantiate our use of the principle on purely mathematical grounds. In the case of gravity, the situation is somewhat uncertain, as most physical laws have been confirmed by experimental means only for the case of weak gravitational fields in our terrestrial neighborhood. In our case, however, we have the great advantage of knowing both the incompressible form of the equations of motion *and* the compressible form. For this reason, we have the ability to match the compressible and the equivalent incompressible forms through our choice of a metric tensor and validate as a *matter of inspection* that the equations we produce are correct.

We have now found an overall approach to geometrizing compressibility by embedding it into the metric tensor of an equivalent incompressible flow that exists in the same coordinate system. It is important to note, however, that at this point we have not actually changed the fundamental governing equations describing the flow. Indeed, the equations for both

the compressible flow and its incompressible equivalent are completely identical at this point when they are written out in terms of partial derivatives with respect to the given coordinate system. The fact that equations are the same is precisely what we mean by the notion of an *equivalent* incompressible flow. We have simply chosen to associate the concept of compressibility with a *geometric* effect in a flow that has the same invariant kinematic equation as an incompressible flow instead of with the *physical* effect to which it is ascribed in the invariant kinematic equation for a compressible flow. It is therefore important to note that the term "equivalent incompressible flow" is not intended to mean that the density does not vary but rather that the invariant forms of the governing equations are those corresponding to the incompressible form.

One may ask about the nature of the transformation that has just been achieved. In producing the equivalent incompressible flow, we have generated a new metric tensor that is very similar to the metric corresponding to the coordinate system in which the compressible flow is given. However, we have not transformed the coordinates because the governing equations for both flows are taken to correspond. The correspondence cannot be maintained unless the coordinate system is the same. If the coordinate system has not changed, the implication is that the new metric tensor has instead altered the measure of length between nearby points. This trait is the defining characteristic of a *gauge transformation* of the length measure [83].

A gauge transformation has the effect of changing the curvature of space. If we envision the compressible flow boundary value problem to be specified on a plane, a gauge transformation may then define a new nonplanar two-dimensional surface that would appear curved to an observer living in a three-dimensional world. A question that is of interest here is whether the curvature that is produced by the gauge transformation has physical significance with respect to the problem of fluid motion. We shall ultimately see that our interest in two dimensional spaces will have bearing on this question.

Although we have altered the curvature of space through a gauge transformation, we have not changed the nature of the boundary value problem for the flow. Because the compressible and equivalent incompressible flows have the same forms in the originally

given coordinate system, we cannot solve the incompressible equations any more easily than the compressible versions. One of the guiding goals of this dissertation, however, is to simplify flow solutions by achieving a form of the incompressible flow equations that can easily be solved. Incompressible potential flow obeys Laplace's equation, and a wide variety of simple numerical and analytical methods are available to solve this equation in its Cartesian coordinate form. In particular, boundary element methods that are implemented in so-called panel codes are particularly useful and computationally efficient for solving this form of Laplace's equation over arbitrary body shapes. As their name implies, boundary element methods require that a flow geometry be discretized only on its boundaries; a mesh of the interior area/volume is not required.

In order to leverage these boundary element techniques, we shall attempt to achieve this canonical Cartesian form of the Laplace equation through a *curvilinear coordinate transformation* of the equivalent incompressible flow. This transformation must relate all aspects of the flow in the originally given reference frame to the flow in the new coordinate system in which the canonical Laplace equation holds. For instance, we shall eventually need to know how the boundary conditions for the flow problem transform and how the flow properties such as the thermodynamic variables and velocity vector differ in the two coordinate systems. Definite mathematical transformation rules are provided by Riemann geometric theory that can be used to link coordinates and their transformation derivatives as well as vector and tensor components in both flows. Therefore, we can expect to leverage these transformation rules to establish the required interrelationships.

Based on these considerations, we are ready to propose an answer to the primary research question in the form of an overall theoretical approach. We state this approach as a hypothesis which we shall investigate and test in the remainder of this dissertation.

Hypothesis: The nonlinear effects of compressibility in a planar subsonic potential flow can be geometrized by writing the governing equations of an incompressible flow in covariant form and choosing the corresponding metric tensor such that the governing equation becomes equivalent to that of the given subsonic flow. This association creates an *equivalent incompressible flow* corresponding to the given subsonic compressible flow. The transformation from the given metric tensor in which the subsonic flow boundary value problem is posed to the calculated metric tensor for the equivalent incompressible flow comprises a *gauge transformation*. The governing equation for this equivalent incompressible flow can be transformed to a canonical form of the Laplace equation through a *curvilinear coordinate transformation*. In this canonical frame, the flow can be solved by a boundary element method. The mathematical transformation rules for the gauge and coordinate transformations provide a framework in which the coordinates, boundary conditions, and flow properties in the subsonic and canonical Laplacian fields can be meaningfully related.

This hypothesis may appear abstract at this point, but its specific formulation is intended to serve as a guidepost for the theoretical development pursued in this dissertation. The specificity of its formulation is intended to facilitate its testing through the theoretical development and subsequent numerical validation.

3.2 Specific Research Tasks and Questions

Having posed the research problem, we are now ready to outline the specific research tasks and questions that are to be addressed in the remainder of this dissertation. These tasks and questions can be organized into two general focus areas: the theory development for the geometrization of compressibility and the implementation of the theory for flow solutions. The first area comprises the analytical derivations that will produce the transformation linking a subsonic plane potential flow to its incompressible equivalent. The second area focuses on the application of the transformation technique for flow solutions. The implementation tasks are intended to fulfill three purposes: 1) produce a numerical method to

develop equivalent flows for arbitrary bodies of engineering interest, 2) provide evidence for the validation of the theory by comparison to known flow solutions, and 3) provide data from which further conclusions about the ramifications of the theory can be drawn. The collective intent of these tasks is primarily to test the hypothesis posed in Section 3.1.1. The following sections describe the specific tasks and questions to be addressed in each of these focus areas.

3.2.1 Theory for the Geometrization of Compressibility

The first task in developing the theory is to write the governing fluid flow equations in a covariant form in which the metric tensor appears explicitly. Equations for both compressible potential flow and incompressible flow will be required. Although practitioners of potential flow are typically familiar with the governing equations written in vector form, a presentation in terms of Riemannian geometric terminology, and in particular, the metric tensor, is less well known. For example, the author is not aware of an example in the literature of the full nonlinear potential equation cast in this form. The derivation of these Riemannian forms in this task therefore represents a contribution of this research independent of the broader objectives. In the opinion of the author, the Riemannian tensor form can be useful for understanding geometric features and may facilitate certain types of analytical approaches to flow problems.

The second task is to develop the approach to ascribe compressibility to the metric tensor of the equivalent incompressible flow. The general approach will be to select the metric such that the governing *kinematic* equation of the incompressible flow takes on the form of the given subsonic flow. The metric we generate will embody the *dynamic* aspects of the subsonic flow including the density variation from point to point. An important question that we will encounter in this task is whether the metric can be determined algebraically based on the flow quantities or whether it must be found by the solution to an additional partial differential equation in the domain. The choice of metric tensor may prove to be non-unique, and we may be faced with the selection of a particular metric from among a class of allowable choices. In this case, our intent shall be to select the simplest possible

metric, and if possible, one that can be determined algebraically from the flow properties rather than through a separate differential equation. The metric tensor derived in this task is the manifestation of the gauge transformation defining the equivalent incompressible flow.

The third task in the theory development is to derive the curvilinear coordinate transformation that will produce the canonical Laplacian form of the potential equation for the equivalent flow. The primary focus in this task will be to determine the partial derivatives of one set of coordinates with respect to the other. These derivatives, which are of the form, $\frac{\partial \bar{x}^\nu}{\partial x^\mu}$, can be assembled into a matrix whose determinant is the Jacobian of the coordinate mapping. The mapping is allowable as long as the Jacobian is nonzero. These transformation derivatives govern the relationship between the scalar, vector, and tensor components of the various flow properties in the originally given coordinate system and the canonical Laplacian frame.

The primary challenge of a curvilinear coordinate transformation is to ensure *integrability* of the mapping. That is, the transformation must satisfy the requirement that the mixed second partial derivatives of the transformation commute, i.e.,

$$\frac{\partial^2 \bar{x}^\nu}{\partial x^\mu x^\sigma} = \frac{\partial^2 \bar{x}^\nu}{\partial x^\sigma x^\mu}$$

for all values ν, μ, and σ. For an arbitrary curvilinear coordinate transformation, ensuring integrability involves the solution of a partial differential equation with specified boundary conditions. This solution is typically very difficult and will pose the main challenge of this task.

As we shall see in the next chapter, the equations governing the coordinate transformation are substantially similar to the governing equations for the flow itself. Indeed, the solution of a two dimensional potential flow produces the potential ϕ and the stream function ψ which can be viewed as two new coordinates determined by the flow solution. In this case, the integrability conditions for the transformation are precisely the kinematic governing equations of irrotationality and continuity. Ideally, we might be able to use this similarity to construct the transformation in such a way as to obtain integrability *automatically*, that is, *as a consequence of the governing equations of the flow.* This approach would

substantially reduce the difficulty of carrying out a coordinate transformation; therefore, the question of whether this formulation is possible will be a crucial focus of this research task.

The fourth task in the theory development is to determine the boundary conditions on the curvilinear coordinate transformation. As discussed previously, it is possible that the transformation will require the solution to a separate differential equation. If such a solution is pursued, the differential equation will require boundary conditions in order to be appropriately posed. The primary research question in this task is to determine whether such a boundary condition must be prescribed in a certain way on physical or mathematical grounds or whether it is free to be selected for convenience. In the case that a separate differential equation is not required to determine the metric, no separate boundary conditions will be required. This eventuality may occur, for instance, if we are able to obtain coordinate integrability automatically as a function of the flow solution. In this case, the boundary values for the coordinate transformation would follow as a consequence of the boundary conditions for the flow.

Up to this point, we have considered how to select a metric tensor and how to establish a transformation that produces the desired form of the governing equations of an equivalent incompressible flow. The resulting transformation procedure will establish linkages between flow properties in the corresponding coordinate systems. In this dissertation, the focus is on steady subsonic potential flow. The governing equations for this type of flow are *elliptic* in character, and therefore, they require that boundary conditions be given at all boundaries of the domain, both interior to the flow field, i.e. along the surface of an immersed body, and exterior to the flow, i.e. at a finite or even infinite distance from the body. For a body in free flow, the boundary conditions are typically taken as flow tangency to the surface at the inner boundary and vanishing of the perturbation potential at infinite distance from the body. Unlike the case for Euler and Navier–Stokes flows, only a single condition is needed at each boundary for a potential flow problem because the flow is governed by a single partial differential equation.

The final task is therefore to determine how the flow boundary conditions transform

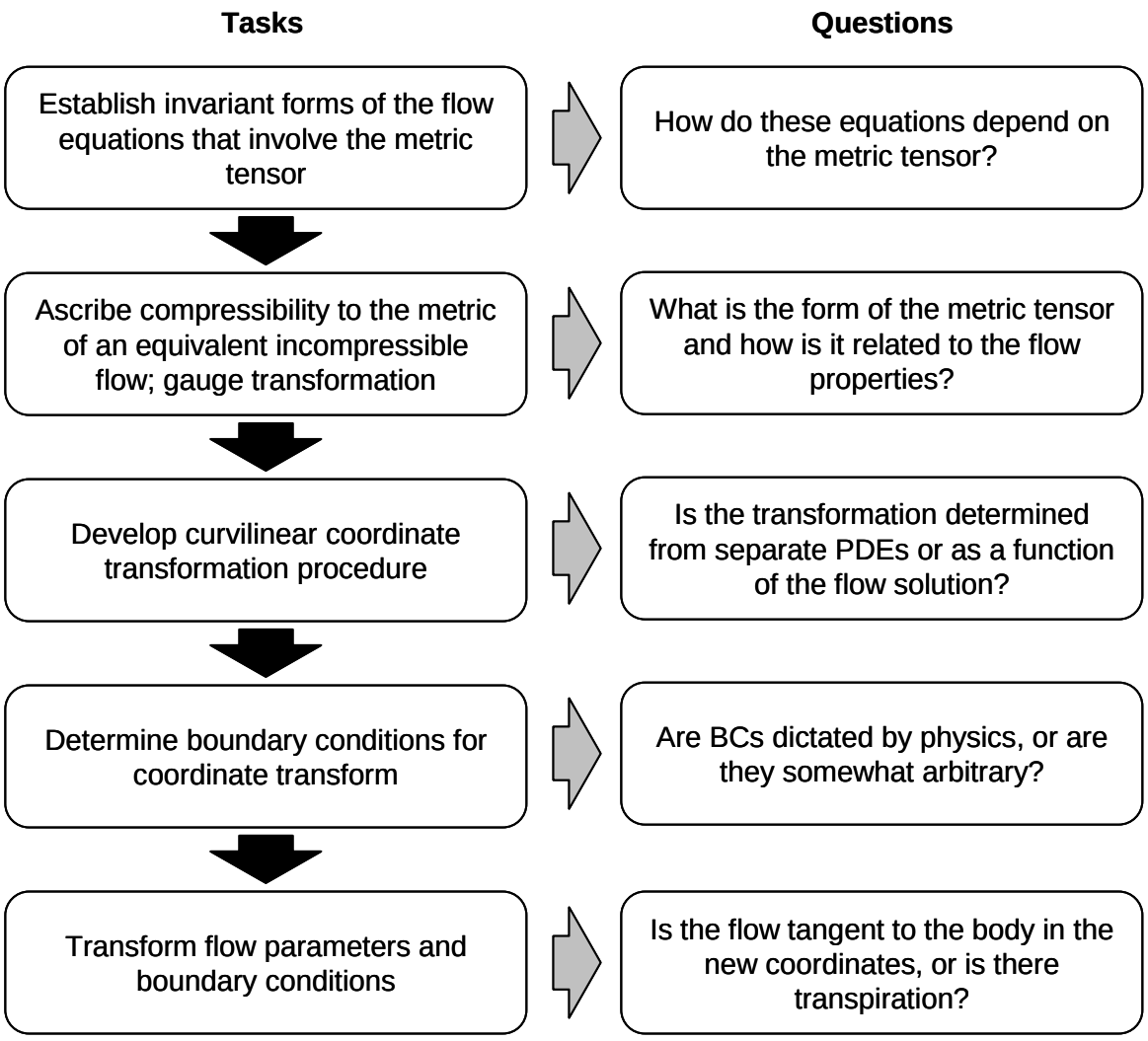

Figure 2: Research Tasks and Questions for Theory Development

between the originally given domain and the transformed domain. A key question in this task is whether the boundary conditions for the equivalent flow correspond to flow tangency at the body surface or whether transpiration of flow across the boundary is present.

A summary of these specific research tasks and questions for the theory development is presented as Figure 2.

3.2.2 Implementation for Flow Solutions

After establishing the overall theoretical framework for matching compressible flows to their incompressible equivalents, the next research focus is to explore flow solutions using

the method. This effort has the following three primary objectives:

- Produce numerical solutions for comparison to known flow test cases to provide evidence supporting or refuting the transformation theory and approach
- Develop a method to implement the theory for obtaining flow solutions over arbitrary two-dimensional bodies
- Examine the characteristics of the equivalent flow solutions to gain physical insight into the effects of the transformation and to suggest further refinements or extensions to the theory

In order to achieve these goals, we shall pursue the implementation plan outlined in Figure 3. The plan consists of four main tasks. The first task is to establish and implement an algorithm for the numerical solution of the mapping problem. A numerical method will be necessary for developing solutions for validation purposes, and it will also fulfill the goal of obtaining solutions for flows over arbitrarily shaped bodies. Important questions associated with this task regard the nature of the algorithm that is necessary for the numerical solution. In particular, will it be iterative and what steps will be involved? As the metric tensor will depend on flow quantities, it is likely that the numerical method will be iterative, with successive iterations refining the metric tensor and the mapping problem while simultaneously converging the flow solution. It is also apparent that some method for solving the equivalent incompressible flow will be required, as will a numerical approach for determining the curvilinear coordinate transformation.

The second task is to investigate the sensitivity of the algorithm to numerical solution parameters. These types of parameters, which include factors such as convergence tolerances and grid point density, typically have significant bearing on the quality of numerical solutions to partial differential equations. The primary focus of this task is therefore to establish an understanding of the effects of these parameters on the solution quality such that subsequent results will be credible. This task also has the intrinsic value of revealing the behavior of the method and implying possible improvements..

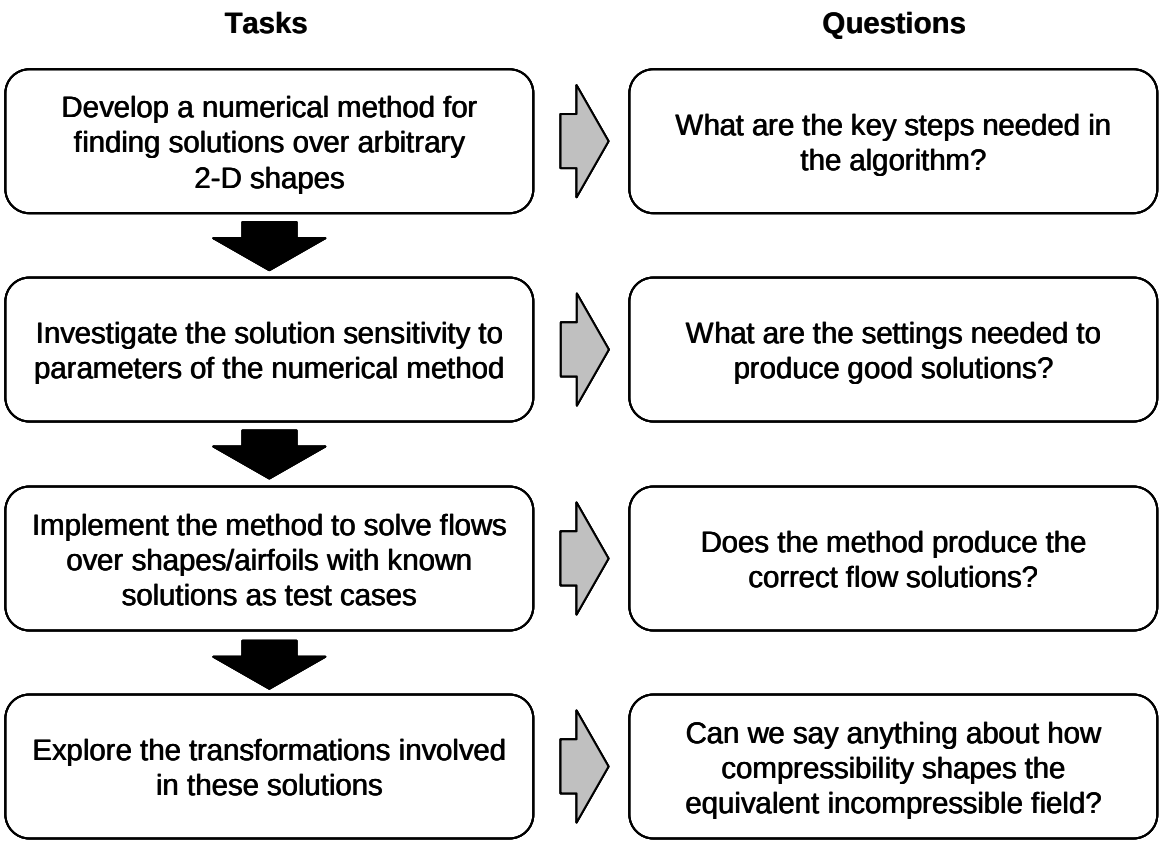

Figure 3: Research Tasks and Questions for Solution Implementation

The third task in the implementation effort is to employ the numerical method to solve flows over profile shapes for which good solutions are known. The purpose of this task is to provide evidence for validating or refuting the theory and numerical method. In order to serve in the role of validation, the chosen test cases will ideally comprise well–trusted numerical solutions to the full potential equation. The full potential equation involves the same physical and mathematical assumptions as the solution technique developed in this research and is therefore the "gold standard" of comparison, surpassing even experimental results which contain the compounding of the unmodeled effects of viscosity, experimental error, etc. If correspondence with one or several full potential solutions can be obtained, the evidence will strongly support the validity of the theoretical and numerical approach.

The final task is to glean understanding of the nature of equivalent incompressible flows from the solutions we obtain through the numerical procedure. For example, we shall seek to understand the relationships among flow properties at corresponding points in the compressible and equivalent incompressible domains. We shall also investigate how the transformation distorts the shape of the airfoil in the equivalent flow. Additionally, we shall explore how these effects vary as a function of Mach number and angle of attack. These numerical experiments are expected to yield insights into how the technique developed in this work differs from the classical compressibility correction methods.

3.3 Limits of the Analogy

This chapter has proposed a transformation method that maps a compressible flow to an equivalent incompressible flow with the intent of simplifying or clarifying subsonic flow solutions. The motivation for the approach has been the success of the various transformation techniques in linearized aerodynamic theory that leverage the Lorentz transformations of the special theory of relativity. These successes formed the inspiration for an extended analogy linking nonlinear potential fluid flows with elements from general theory of relativity. This analogy is based primarily on the concept of extending the notion of the strong principle of equivalence from gravity to the problem of compressible flow. In this paradigm, the effects of compressibility will be embedded into the metric tensor of an underlying shaped

manifold or curvilinear coordinate system, much in the same way that the effects of gravity are introduced into the metric tensor in general relativity through Einstein's equation.

This analogy is philosophically compelling, and we may be inclined to seek broader similarities between our flow problem and the relativistic problem of gravity. Indeed, a significant amount of effort during this dissertation work was devoted to attempting to further the analogy and form it on more fundamental considerations. This effort was largely unsuccessful. Perhaps this lack of success should have been expected. If a nearly exact analogy could be obtained based on fundamental equivalencies between gravity and compressible fluid flow, one would be inclined to suggest a fluid dynamic basis for the force of gravity. The pursuit of this type of theory of an *ether* permeating space was a major focus of 19th century physics [79]. Such a fluid was never discovered experimentally, and most hypotheses supposing it proved cumbersome in the way they produced observed physical phenomena based on fluid motion. The basis of much of Einstein's success was predicated on his insistence that, since the fluid cannot be observed, we should not base physical theories upon its hypothesized existence.

Based on the insights gained by the author during this quest for a deeper connection, it is the purpose of this section to caution against pushing the analogy suggested in this thesis too far. In support of this caution, we shall discuss several distinct differences in the theory developed here and that of gravity.

One significant difference is the manner in which the equivalence principle is applied in this approach compared to that of general relativity. The general theory of relativity is based on an equivalence principle that has a readily identifiable physical interpretation, specifically that particles travel along geodesics of the space–time manifold defined by the matter distribution forming the source of the gravitational field. This principle of equivalence also leads to predictions of how all physical laws change in the presence of gravitation through the general covariance of equations. In the formulation of the compressible flow problem examined here, however, our application of an equivalence principle is more *operational* as opposed to *physical*. That is, we use the notion of general covariance as a mathematical edifice. We write the flow equations in covariant form and choose the metric

tensor for the incompressible flow in such a way as to make the incompressible equations take on the same form as the compressible equations corresponding to a particular coordinate system. This method of geometrizing compressibility follows immediately because we know *a priori* both the compressible and incompressible forms of the equations we wish to relate. In the problem of gravity, however, the forms of physical equations in a gravitational field are not known in advance, and the source of the gravitational field is determined from an independent physical law given by Einstein's equation.

A third difference concerns dimensionality. We are considering a problem consisting of two spatial dimensions with time taken as universal. Relativity theory describes a fully four-dimensional problem, comprised of the three spatial dimensions and the temporal dimension. The mathematics of the Riemannian geometries of dimension $n = 2$ and $n = 4$ is dramatically different in terms of the types of allowable transformations, the number of integrability conditions for coordinate transformations (2 for $n = 2$ and 24 for $n = 4$), and the dramatically different number of independent components of the curvature tensor (1 for $n = 2$ versus 20 for $n = 4$). Because of these substantial differences, it is unlikely that pairwise comparisons can be made of the transformations of the general theory to those developed in this thesis.

Another related difference is in the way that compressibility affects space in this theory compared to the way that gravity affects space–time in general relativity. In both theories, the structure of space (or space–time) is taken to be adequately described by Riemannian geometry. This difference boils down to the way in which the metric tensor influences the shape of the space. In producing an equivalent incompressible flow, we shall embed compressibility into the spatial curvature of the domain. This embedding may be somewhat similar to the way that the effects of gravity are embedded into curvature through Einstein's equations; however, significant differences will be present owing to the dissimilar dimensionality and incongruities between the mathematical and physical structures that set the values of the metric tensor components in the two situations.

These differences should not be underestimated, and it would therefore be inappropriate to draw too many conclusions that would strongly link this theory of compressibility

with the theory of gravity. Nonetheless, there does remain a possibility for future extensions of the theory that may enhance the parallelism and remove some of these differences. Dimensionality is perhaps the most straightforward example. One could extend the two-dimensional theory to a full four-dimensional theory quite readily by introducing the third spatial dimension and time. This approach would require the introduction of a characteristic signal speed, such as the speed of sound to fill the analogous role of the light speed in relativity theory. In this transition to a 4–D world, however, the coordinate transformation to produce the canonical Laplacian form (or in this case, d'Alembertian form) will likely become substantially more complicated. More progress might also be made in refining the method of embedding compressibility into the metric tensor. The success of Einstein's equation in relativity theory suggests that an approach of directly setting the metric based on the 4–D stress-energy tensor of the fluid might be successful. In initial explorations, this approach has not yielded fruit, but it nonetheless remains an attractive possibility.

Although the limitations of the proposed analogy are substantial, let us forge onward to see what we can discover.

CHAPTER IV

THEORY

In this chapter, we shall follow the general plan of research tasks and questions outlined in Figure 2 of Chapter 3. In the first section, we establish invariant forms of the governing equations of potential flow in both vector operator and Riemannian tensor notation. This approach is taken in order to acclimatize the reader slowly to the Riemannian formalism by pairwise comparison to the more familiar vector invariant forms. The Riemannian forms indicate the explicit dependence of the equations on the metric tensor that we shall require in later steps.

The second section outlines the method of geometrizing compressibility through the metric tensor of an equivalent incompressible flow. The governing equations from the first section are employed, and the metric tensor is chosen such that the invariant form of the incompressible flow equations become identical to the compressible form in a particular coordinate system of choice. Several interesting results and implications concerning the resulting metric tensor are also explored.

The third section provides the detailed mathematical formulation necessary to manifest the curvilinear coordinate transformation to arrive at the canonical Laplacian form of the incompressible potential equation. The primary challenge that must be addressed in this process is to ensure integrability of the coordinate system corresponding to the newly found metric. As described in Chapter 2, integrability is a requirement of the holonomic coordinate systems described by the standard form of Riemannian geometry. Two methods of achieving integrability are investigated. The first attains it through the solution of a separate partial differential equation in the domain of the flow, and the second suggests an approximative method for obtaining integrability as a consequence of the flow solution itself. Each of these methods will play a significant role in the implementation approaches presented subsequently.

The fourth section documents certain key relationships among the originally given compressible flow and the canonical Laplacian form of the incompressible flow. First, the transformation of the flow boundary conditions is explored. Next, we examine the transformation of the velocity vector and the scalar flow parameters. Finally, the transformation properties of the angle of attack and the Kutta condition are explored to allow the mapping to be completed for flows with circulation.

The final section describes how the approach developed in this chapter interfaces with the theory of quasiconformal mappings and how it compares and contrasts with a similar technique developed by Bers in the 1940s and 1950s.

4.1 Governing Equations in Invariant Form

The equations of motion for potential fluid flow are well known to most engineers and scientists who work in the areas of hydro- or aerodynamics. The common pedagogical practice in engineering is to derive these equations from the fundamental conservation laws of mass, momentum, and energy and to present them in both differential and volume integral form. Although the conservation equations are often first presented in Cartesian coordinates, it is typical for the differential form then to be presented in a coordinate independent manner using vector identities such as the gradient, divergence, and curl. These vector operators are usually described in terms of notation based on the nabla operator, ∇.

With the coordinate invariant form known, the solution of flow problems is usually approached by selecting appropriate coordinates from among several standard systems such as Cartesian, cylindrical, or spherical. To determine the equations of motion in the selected coordinate system, one then typically looks up the representation of the gradient, divergence, and curl operators in terms of partial derivatives with respect to the chosen coordinates or derives the operators through a laborious coordinate transformation from the well-known Cartesian form. In this way, the coordinate independent expressions of the equations can be cast in a specific form from which analytical and numerical solutions of the flow can be pursued.

An alternative but equivalent approach to posing the coordinate invariant equations is

to employ a tensorial representation using the notation of Riemannian geometry. These tensor equations, like those written in terms of the ∇ operator, are form invariant, or *covariant* with respect to arbitrary curvilinear coordinate transformations. As in the case with the ∇ form, operations such as gradient, divergence, and curl are well defined, but their representation is in terms of the mechanism of Riemannian tensor calculus.

If the approaches are equivalent, one might ask, why should we spend the time to learn and use the Riemannian tensor formalism if we are already familiar with the ∇ approach? The answer is that the tensor form provides a tractable, compact, and natural method for dealing with transformations among arbitrary coordinate systems and is widely used in the formulations of differential geometry and general relativity which inspired this work. In the opinion of the author, the Riemannian tensor approach elucidates the relationship with geometry and coordinate systems in a way that is more transparent than the ∇ operator approach. The Riemannian formalism has been a key enabler for simplifying many of the transformation procedures developed in this dissertation.

As an example of the utility of the Riemannian approach, the tensor equations can be cast in terms of a particular set of coordinates through the specification of the so-called *metric tensor* corresponding to the coordinate system. All of the operators appearing in the governing equations depend exclusively on this entity and combinations of its partial derivatives known as *Christoffel symbols*. Although determining the metric tensor and Christoffel symbols for an arbitrary coordinate system is by no means a simple task, it is often appreciably less challenging and tedious than determining the gradient, divergence, and curl operators by direct transformation of the partial derivatives. This is especially true for cases when these operators are not tabulated for the desired coordinate system. Whereas the tensor components and Christoffel symbols may also not be tabulated, a very definite and straightforward recipe is available through which they can be calculated with tensor analysis.

In the following sections, the tensor forms of the equations of steady incompressible and compressible potential flow are presented following their equivalents posed in the ∇ operator notation. Choosing the appropriate place to begin the presentation of the equations is a

difficult decision. As most practitioners are familiar with many of the various forms in ∇ notation, we will begin with the conservative differential forms as a reasonable starting point that is well known and derive from these the key forms used in this dissertation. This choice was made to allow reasonable brevity by avoiding a lengthy first principles derivation while also facilitating some degree of vector and tensor manipulations to illustrate the differences between the ∇ and Riemannian tensor approaches.

The presentation will feature classical elements of Riemannian tensor algebra and calculus including the Einstein summation convention, covariant and contravariant vector and tensor forms, index raising and lowering with the metric tensor, Christoffel symbols, and covariant differentiation. If these concepts are unfamiliar or unfresh, the reader is encouraged to examine the brief overview of Riemannian tensor analysis presented in Section 2.2.

4.1.1 Vector Operator Form

4.1.1.1 Incompressible Flow

The differential equations for steady flow of an incompressible inviscid fluid with no externally applied forces can be written in conservative form in terms of the ∇ vector operator as,

$$\begin{aligned} \nabla \cdot \vec{u} &= 0 \qquad \text{Continuity} \\ \rho_0 \nabla \cdot (u_i \, \vec{u}) + \nabla p &= 0 \qquad \text{Momentum} \end{aligned} \tag{68}$$

where $\vec{u}$ is the velocity vector, u_i is component i of the vector $\vec{u}$, p is the pressure, and ρ_0 is the constant density [8, 18]. The vector momentum equation is comprised of n scalar equations where n is the dimension of the space. In this work, our primary interest is plane flow with $n = 2$.

If we take the flow also to be irrotational, the curl of the velocity or *vorticity* vanishes,

$$\nabla \times \vec{u} = 0$$

and a scalar velocity potential ϕ can be introduced as,

$$\nabla \phi = \vec{u}.$$

This representation satisfies irrotationality automatically because of the vector identity

$$\nabla \times (\nabla \phi) = 0.$$

Alternatively, one may reason in the converse, i.e. if we choose to represent the velocity as the gradient of a scalar potential, the velocity field *cannot* support a nonzero curl. Regardless of the reasoning, the irrotationality statement represents a physical approximation that is well founded and widely used for inviscid incompressible flows, and insomuch as incompressible flows represent the $M \rightarrow 0$ limit of a compressible flow, Crocco's theorem indicates that a steady isentropic flow is irrotational [5].

Introducing the irrotationality requirement dramatically simplifies the vector momentum equations to a single algebraic scalar equation. This simplification is achieved as follows. First, we rewrite the momentum equation using the chain rule of differentiation for the first term to obtain

$$\rho_0 \, u_i \, (\nabla \cdot \vec{u}) + \rho_0 \, \vec{u} \, \nabla u_i + \nabla p = 0.$$

From the continuity equation, the first term in brackets vanishes, and we have,

$$\rho_0 \, \vec{u} \, \nabla u_i + \nabla p = 0$$

which is typically written as,

$$\rho_0 \, (\vec{u} \cdot \nabla) \, \vec{u} + \nabla p = 0.$$

Next we apply the vector identity

$$(\vec{u} \cdot \nabla) \, \vec{u} = \frac{1}{2} \nabla \|\vec{u}\|^2 + (\nabla \times \vec{u}) \times \vec{u}$$

to give

$$\rho_0 \left[\frac{1}{2} \nabla \|\vec{u}\|^2 + (\nabla \times \vec{u}) \times \vec{u} \right] + \nabla p = 0$$

where $\|\vec{u}\|$ is the magnitude of the velocity vector. Substituting the irrotationality condition causes the second term in brackets to vanish, leaving,

$$\nabla p = -\frac{\rho_0}{2} \nabla \|\vec{u}\|^2.$$

Because this expression relates only terms involving gradients of scalar quantities, it is possible to multiply each of the vector components by its corresponding coordinate differential and sum to give an expression on total differentials,

$$dp = -\frac{\rho_0}{2}\, d\left(\|\vec{u}\|^2\right). \tag{69}$$

Finally, this expression can be integrated immediately to give Bernoulli's equation,

$$p + \frac{1}{2}\rho_0 \|\vec{u}\|^2 = p_0 \tag{70}$$

where p_0 is a constant of motion for the flow termed the *stagnation pressure*.

Summarizing the situation now, we have the following governing equations for an incompressible, inviscid, and irrotational flow with no external forces:

$$\begin{aligned} \nabla \cdot \vec{u} &= 0 && \text{Continuity} \\ \nabla \times \vec{u} &= 0 && \text{Irrotationality} \\ p + \tfrac{1}{2}\rho_0 \|\vec{u}\|^2 &= p_0 && \text{Momentum/Bernoulli} \end{aligned} \tag{71}$$

In this form, the kinematics of the fluid flow are completely dissociated from the dynamics. That is, one can solve for the flowfield by consideration of the *linear* partial differential equations for continuity and irrotationality with specified boundary conditions and then determine the pressures *a posteriori* through the algebraic Bernoulli equation.

We can now write these equations in the form of the velocity potential as,

$$\begin{aligned} \nabla^2 \phi &= 0 && \text{Continuity/Potential} \\ p + \tfrac{1}{2}\rho_0 \|\nabla\phi\|^2 &= p_0. && \text{Momentum/Bernoulli} \end{aligned} \tag{72}$$

The irrotationality condition is unnecessary here because it is automatically satisfied by the introduction of a potential as previously described.

4.1.1.2 Compressible Flow

The continuity and momentum equations for steady flow of a compressible inviscid fluid without externally applied forces can be written in conservative form in terms of the ∇

vector operator as,

$$\begin{aligned} \nabla \cdot (\rho\, \vec{u}) &= 0 \qquad \text{Continuity} \\ \nabla \cdot (\rho\, u_i\, \vec{u}) + \nabla p &= 0 \qquad \text{Momentum} \end{aligned} \tag{73}$$

where $\vec{u}$ remains the velocity vector, u_i is component i of the vector $\vec{u}$, p is the pressure, and ρ is the density which is now taken to vary as a function of the flow.

For compressible flow, additional relations linking the thermodynamic variables are needed to close the system. These relations are generically termed *specifying equations* by von Mises [128]. For the case of an arbitrary compressible inviscid flow, the specifying equations are typically an energy conservation equation coupled with the state equation for thermally perfect gases; however, for irrotational flow with

$$\nabla \times \vec{u} = 0$$

the flow is also isentropic as shown by Crocco's theorem [5]. With the entropy fixed throughout the field, only one additional relation among the thermodynamic variables p and ρ is needed to close the system. This relation can be expressed in a variety of ways through the use of the isentropic relations, but we shall initially state it as,

$$\frac{p}{p_0} = \left(\frac{\rho}{\rho_0}\right)^{\gamma} \tag{74}$$

where p_0 and ρ_0 are stagnation values and γ is the ratio of specific heats.

To obtain a relation similar to the Bernoulli equation for incompressible flow, we first rewrite the momentum equation using the chain rule of differentiation for the first term to obtain

$$u_i\, [\nabla \cdot (\rho\, \vec{u})] + \rho\, \vec{u}\, \nabla u_i + \nabla p = 0.$$

The first term in brackets vanishes from the continuity equation, and we have,

$$\rho\, \vec{u}\, \nabla u_i + \nabla p = 0$$

which is typically written as,

$$\rho\, (\vec{u} \cdot \nabla)\, \vec{u} + \nabla p = 0. \tag{75}$$

Next we apply the vector identity

$$(\vec{u} \cdot \nabla)\, \vec{u} = \frac{1}{2}\, \nabla \|\vec{u}\|^2 + (\nabla \times \vec{u}) \times \vec{u}$$

to give

$$\rho \left[\frac{1}{2}\, \nabla \|\vec{u}\|^2 + (\nabla \times \vec{u}) \times \vec{u} \right] + \nabla p = 0.$$

Substituting the irrotationality condition causes the second term in brackets to vanish, leaving,

$$\nabla p = -\frac{\rho}{2}\, \nabla \|\vec{u}\|^2.$$

This expression relates only terms involving gradients of scalar quantities; therefore, it is possible to multiply each of the vector components by its corresponding coordinate differential and sum to give an expression on total differentials,

$$dp = -\frac{\rho}{2}\, d\left(\|\vec{u}\|^2\right). \tag{76}$$

Unlike the situation in the incompressible case, this expression cannot be integrated immediately because the density varies as a function of the flow. However, we can obtain an integrable equation by differentiating the isentropic relation given by Equation 74 to obtain,

$$\frac{dp}{p_0} = \gamma \rho^{\gamma - 1} \frac{d\rho}{{\rho_0}^{\gamma}}.$$

Substituting this expression into Equation 76 for dp and dividing by ρ gives,

$$\left(\frac{p_0}{{\rho_0}^{\gamma}} \right) \gamma \rho^{\gamma - 2} d\rho = -\frac{1}{2}\, d\left(\|\vec{u}\|^2\right)$$

which can be integrated at once to,

$$\left(\frac{p_0}{{\rho_0}^{\gamma}} \right) \frac{\gamma\, \rho^{\gamma - 1}}{\gamma - 1} = -\frac{1}{2}\, \|\vec{u}\|^2 + \text{const.}$$

The constant can be set by requiring that the relation gives the stagnation density when $\|\vec{u}\| = 0$. This requirement results in,

$$\left(\frac{p_0}{{\rho_0}^{\gamma}} \right) \frac{\gamma\, \rho^{\gamma - 1}}{\gamma - 1} = -\frac{1}{2}\, \|\vec{u}\|^2 + \left(\frac{p_0}{\rho_0} \right) \frac{\gamma}{\gamma - 1}$$

or,

$$\left(\frac{\gamma\, p_0}{\rho_0}\right)\left(\frac{\rho}{\rho_0}\right)^{\gamma-1}\frac{1}{\gamma-1} = -\frac{1}{2}\,\|\vec{u}\|^2 + \left(\frac{\gamma\, p_0}{\rho_0}\right)\frac{1}{\gamma-1}.$$

Using the well known isentropic relation that defines the sound speed a as

$$a^2 = \frac{\gamma p}{\rho} \tag{77}$$

the expression can finally be solved for ρ/ρ_0 to give,

$$\frac{\rho}{\rho_0} = \left(1 - \frac{\gamma-1}{2\,{a_0}^2}\,\|\vec{u}\|^2\right)^{1/(\gamma-1)} \tag{78}$$

where a_0 is the stagnation sound speed.

Summarizing the situation as it stands now, the governing equations for steady compressible isentropic flow can be written as follows:

$$\begin{aligned}
\nabla\cdot(\rho\,\vec{u}) &= 0 && \text{Continuity}\\
\nabla\times\vec{u} &= 0 && \text{Irrotationality}\\
\frac{\rho}{\rho_0} &= \left(1-\frac{\gamma-1}{2\,{a_0}^2}\,\|\vec{u}\|^2\right)^{1/(\gamma-1)} && \text{Density–Velocity Relation}\\
\frac{p}{p_0} &= \left(\frac{\rho}{\rho_0}\right)^{\gamma} && \text{Specifying/State Equation}
\end{aligned} \tag{79}$$

This statement of the governing equations is rather unconventional, but it will nonetheless serve a important role in this work. In this form, it is apparent that the dynamics and thermodynamics of the flow, as embodied by the density–velocity relation, are inextricably linked to the flow solution through the density's appearance in the continuity equation. The boundary value problem formed by the partial differential continuity and irrotationality equations are therefore *nonlinear* functions of the velocity, with the nonlinearity arising from the nontrivial nature of the density–velocity relation. Once the boundary value problem has been solved, the pressures can be determined *a posteriori* by the density–velocity and isentropic state relations.

To arrive at the more conventional statement of the fluid motion given by the full potential equation, we note that the density and pressure can also be related directly through

the sound speed. Differentiating (74) gives,

$$\frac{dp}{p_0} = \gamma \left(\frac{\rho}{\rho_0}\right)^{\gamma} \frac{d\rho}{\rho}.$$

Substituting Equation 74 for $\left(\frac{\rho}{\rho_0}\right)^{\gamma}$ and multiplying by p_0 gives,

$$dp = \frac{\gamma p}{\rho}\, d\rho.$$

Now using the well known isentropic relation that defines the sound speed a as

$$a^2 = \frac{\gamma p}{\rho}$$

gives,

$$dp = a^2\, d\rho. \tag{80}$$

Introducing (80) into (76) and dividing by $a^2\,\rho$ results in,

$$\frac{1}{\rho}\, d\rho = -\frac{1}{2\,a^2}\, d\left(\|\vec{u}\|^2\right)$$

This expression holds also for individual component directions, so we can write it in terms of the gradient as,

$$\frac{1}{\rho}\, \nabla\rho = -\frac{1}{2\,a^2}\, \nabla\left(\|\vec{u}\|^2\right).$$

The squared magnitude of the velocity is given by the scalar product of the velocity vector with itself,

$$\|\vec{u}\|^2 = \vec{u}\cdot\vec{u}$$

so,

$$\frac{1}{\rho}\, \nabla\rho = -\frac{1}{2\,a^2}\, \nabla\left(\vec{u}\cdot\vec{u}\right) \tag{81}$$

Next, expanding the continuity equation from (73) with the chain rule gives,

$$\nabla\rho\cdot\vec{u} + \rho\,\nabla\cdot\vec{u} = 0.$$

Dividing this equation by ρ and substituting (81) results in,

$$-\frac{1}{2\,a^2}\, \nabla\left(\vec{u}\cdot\vec{u}\right)\cdot\vec{u} + \nabla\cdot\vec{u} = 0.$$

Substituting $\vec{u} = \nabla\phi$ into this relation and rearranging yields

$$\nabla^2\phi - \frac{1}{2\,a^2}\,\nabla\left(\nabla\phi\cdot\nabla\phi\right)\cdot\nabla\phi = 0. \tag{82}$$

This relation can be rewritten by expanding the gradient of the scalar product in the second term as,

$$\nabla\left(\nabla\phi\cdot\nabla\phi\right) = 2\,\left(\nabla\phi\cdot\nabla\right)\nabla\phi$$

which can be introduced in (82) to result in,

$$\nabla^2\phi - \frac{1}{a^2}\left[\left(\nabla\phi\cdot\nabla\right)\nabla\phi\right]\cdot\nabla\phi = 0. \tag{83}$$

Equations (82) and (83) are equivalent invariant forms of the full potential equation in ∇ operator notation.

4.1.2 Riemannian Covariant Form

We shall now proceed to develop the Riemannian covariant tensor forms of the governing equations. To do this, we could simply replace the ∇ operators by their equivalents in the tensor formalism and arrive at the answer nearly immediately. Instead, however, we shall start at the same point as with the ∇ derivation to illustrate some of the salient features of tensor analysis and to show the parallels of the technique with the previous presentation.

4.1.2.1 Incompressible Flow

The differential conservation equations for steady flow of an incompressible inviscid fluid with no externally applied forces can be written in tensor covariant form in terms of the *contravariant* velocity vector u^ν as,

$$\begin{aligned} u^{\nu}{}_{;\,\nu} &= 0 \quad \text{Continuity} \\ T^{\mu\nu}{}_{;\,\nu} &= 0 \quad \text{Momentum} \end{aligned} \tag{84}$$

where

$$T^{\mu\,\nu} = \rho_0\,u^\mu u^\nu + g^{\mu\nu}\,p \tag{85}$$

is the momentum tensor. Here, Einstein summation applies, i.e. an index appearing in the same tensor expression in both the superscript and subscript is summed over, and semicolons denote covariant differentiation. The combination of a summation within a covariant differentiation as ${}^{\nu}{}_{;\,\nu}$ appearing in the first equation is the tensorial expression for the divergence and is equivalent to the operator $\nabla \cdot (\ \ )$.

The condition of irrotationality can be expressed in the language of Riemannian tensor formalism as,

$$u_{\mu;\,\nu} - u_{\nu;\,\mu} = 0. \tag{86}$$

Expanding the covariant derivatives in terms of partial derivatives and the Christoffel symbols as shown in Section 2.2 gives,

$$\left[u_{\mu,\,\nu} - \Gamma^{\alpha}_{\mu\,\nu}\, u_{\alpha}\right] - \left[u_{\nu,\,\mu} - \Gamma^{\alpha}_{\nu\,\mu}\, u_{\alpha}\right] = 0.$$

Because the Christoffel symbols are symmetric in their lower indices, i.e.,

$$\Gamma^{\alpha}_{\mu\,\nu} = \Gamma^{\alpha}_{\nu\,\mu},$$

equation (86) can be written entirely in terms of partial derivatives of the covariant velocity vector as,

$$u_{\mu,\,\nu} - u_{\nu,\,\mu} = 0 \tag{87}$$

This statement specifies that the curl of the *covariant* velocity vector is zero.

At this point, we have expressions for the continuity and momentum equations in terms of the *contravariant* velocity components and the irrotationality condition in terms of the *covariant* velocity components. The theory developed in this dissertation will leverage primarily the equations written in terms of the covariant components; therefore, we shall proceed to write equations (84) in this form.

We begin with the continuity equation. As shown in Section 2.2, the divergence of the velocity vector can be expanded in terms of partial derivatives and the determinant of the metric tensor $g = \det g_{\mu\,\nu}$ as,

$$u^{\nu}{}_{;\,\nu} = \frac{1}{\sqrt{g}}\left(\sqrt{g}\, u^{\nu}\right)_{,\,\nu}.$$

The contravariant velocity vector u^ν can be obtained from its covariant counterpart by *raising the index* with the inverse metric tensor $g^{\nu\alpha}$:

$$u^\nu = g^{\nu\alpha}\, u_\alpha. \tag{88}$$

Introducing this relation into the expression for the divergence gives,

$$u^\nu{}_{;\,\nu} = \frac{1}{\sqrt{g}} \left(\sqrt{g}\, g^{\nu\alpha}\, u_\alpha\right)_{,\,\nu}.$$

Finally, substituting this expression into the first of equations (84) results in a new statement of the continuity equation in terms of the metric tensor and partial derivatives of the covariant velocity vector:

$$\frac{1}{\sqrt{g}} \left(\sqrt{g}\, g^{\nu\alpha}\, u_\alpha\right)_{,\,\nu} = 0 \tag{89}$$

To proceed with the momentum equations, we first rewrite the form in (84) by substituting the expression for the momentum tensor $T^{\mu\nu}$ given by (85) to give

$$\left(\rho_0\, u^\mu u^\nu\right)_{;\,\nu} + \left(g^{\mu\nu}\, p\right)_{;\,\nu} = 0.$$

Expanding the first and second terms with the chain rule of differentiation gives,

$$\rho_0 \left[u^\mu{}_{;\,\nu}\, u^\nu + u^\mu\, u^\nu{}_{;\,\nu}\right] + \left[g^{\mu\nu}{}_{;\,\nu}\, p + g^{\mu\nu}\, p_{,\,\nu}\right] = 0.$$

The second term in the first set of brackets vanishes from the continuity equation (84), and the first term in the second set of brackets vanishes from the *metricity condition*,

$$g^{\mu\nu}{}_{;\,\alpha} = 0,$$

where α is a free index that can take any value. The metricity condition requires that all covariant derivatives of the metric tensor are zero. It is a fundamental result of Riemannian geometry that holds for any valid metric tensor [34]. Setting these terms to zero gives,

$$\rho_0\, u^\mu{}_{;\,\nu}\, u^\nu + g^{\mu\nu} p_{,\,\nu} = 0. \tag{90}$$

Next, we apply equation (88) to the velocity within the covariant derivative,

$$\rho_0\, \left(g^{\mu\alpha} u_\alpha\right)_{;\,\nu}\, u^\nu + g^{\mu\nu} p_{,\,\nu} = 0.$$

Expanding the covariant derivative with the chain rule gives,

$$\rho_0 \left(g^{\mu\alpha}{}_{;\,\nu} u_\alpha + g^{\mu\alpha}\, u_{\alpha;\,\nu} \right) u^\nu + g^{\mu\nu} p_{,\,\nu} = 0.$$

The first term is zero from the metricity condition, so the expression simplifies to,

$$\rho_0\, g^{\mu\alpha}\, u_{\alpha;\,\nu}\, u^\nu + g^{\mu\nu} p_{,\,\nu} = 0.$$

To further simplify the first term, we first apply the irrotationality condition (86) to rewrite the covariant derivative as,

$$u_{\alpha;\,\nu} = u_{\nu;\,\alpha}.$$

Substituting this expression gives,

$$\rho_0\, g^{\mu\alpha}\, u_{\nu;\,\alpha}\, u^\nu + g^{\mu\nu} p_{,\,\nu} = 0. \tag{91}$$

Now we note from the chain rule that the terms involving the covariant derivatives can be rewritten as,

$$u_{\nu;\,\alpha}\, u^\nu = \left(u_\nu\, u^\nu \right)_{;\,\alpha} - u^\nu{}_{;\,\alpha}\, u_\nu.$$

The second covariant derivative can be rewritten in terms of the covariant velocity components to give,

$$u_{\nu;\,\alpha}\, u^\nu = \left(u_\nu\, u^\nu \right)_{;\,\alpha} - \left(g^{\nu\beta} u_\beta \right)_{;\,\alpha} u_\nu$$

which from the metricity condition becomes,

$$u_{\nu;\,\alpha}\, u^\nu = \left(u_\nu\, u^\nu \right)_{;\,\alpha} - g^{\nu\beta} u_{\beta;\,\alpha}\, u_\nu.$$

This expression is equivalent to,

$$u_{\nu;\,\alpha}\, u^\nu = \left(u_\nu\, u^\nu \right)_{;\,\alpha} - u_{\beta;\,\alpha}\, u^\beta$$

as seen by applying (88) to the second term.

Indices β and ν are summed over, and are hence dummy indices. Because they occur in the same summation positions for the same vectors, we can relabel β as ν and rearrange the equation to give,

$$2\, u_{\nu;\,\alpha}\, u^\nu = \left(u_\nu\, u^\nu \right)_{;\,\alpha}.$$

We now note that $u_\nu\, u^\nu$ is the squared magnitude of the velocity vector as shown in Section 2.2. The magnitude of a vector is a scalar quantity and is therefore invariant with respect to coordinate transformations. The covariant derivative of an invariant is simply its partial derivative, so we can replace the semicolon with a comma to give,

$$u_{\nu;\,\alpha}\, u^\nu = \frac{1}{2}\left(V^2\right)_{,\,\alpha} \tag{92}$$

where V defined as $V^2 = u_\nu\, u^\nu$ is introduced as shorthand for the velocity magnitude.

Now we substitute expression (92) into the momentum equations (91) to give,

$$\rho_0\, g^{\mu\alpha}\, \frac{1}{2}\left(V^2\right)_{,\,\alpha} + g^{\mu\nu} p_{,\,\nu} = 0. \tag{93}$$

Contracting these equations by multiplying by $g_{\mu\sigma}$ sums over the index μ, and we obtain

$$\rho_0\, \delta^\alpha_\sigma\, \frac{1}{2}\left(V^2\right)_{,\,\alpha} + \delta^\nu_\sigma\, p_{,\,\nu} = 0.$$

To recognize this form, we have applied the identity,

$$g_{\mu\sigma}\, g^{\mu\alpha} = g^\alpha_\sigma = \delta^\alpha_\sigma$$

where δ^α_σ is the Kronecker delta symbol which takes the value 1 for $\alpha = \sigma$ and 0 for $\alpha \neq \sigma$.

Finally, we multiply this equation by dx^σ,

$$\rho_0\, \delta^\alpha_\sigma\, \frac{1}{2}\left(V^2\right)_{,\,\alpha}\, dx^\sigma + \delta^\nu_\sigma\, p_{,\,\nu}\, dx^\sigma = 0$$

which can be recognized as a fully contracted expression equivalent to an statement on perfect differentials,

$$dp = -\frac{\rho_0}{2}\, d\left(V^2\right). \tag{94}$$

This equation is identical with (69) derived with ∇ notation if we recognize $V = \|\vec{u}\|$. As in the case with the ∇ approach, this equation can be integrated immediately to give Bernoulli's equation.

To summarize, we can write the tensor invariant forms of the governing equations of

incompressible, inviscid, irrotational flow as,

$$\begin{aligned} \frac{1}{\sqrt{g}}\left(\sqrt{g}\, g^{\nu\mu}\, u_\mu\right)_{,\,\nu} &= 0 \qquad \text{Continuity} \\ u_{\mu,\,\nu} - u_{\nu,\,\mu} &= 0 \qquad \text{Irrotationality} \\ p + \tfrac{1}{2}\rho_0 V^2 &= p_0 \qquad \text{Momentum/Bernoulli} \end{aligned} \tag{95}$$

where $V^2 = u_\nu\, u^\nu = g^{\mu\nu} u_\mu u_\nu$ is the squared magnitude of the velocity. These equations are a Riemannian tensorial form of equations (71) derived in ∇ notation.

Introducing the velocity potential by equating its gradient to the covariant velocity vector as,

$$\phi_{,\,\mu} = u_\mu$$

equations (95) can be restated as,

$$\begin{aligned} \frac{1}{\sqrt{g}}\left(\sqrt{g}\, g^{\nu\mu}\, \phi_{,\,\mu}\right)_{,\,\nu} &= 0 \qquad \text{Continuity} \\ p + \tfrac{1}{2}\rho_0 \left(g^{\mu\nu}\phi_{,\,\mu}\phi_{,\,\nu}\right) &= p_0 \qquad \text{Momentum/Bernoulli} \end{aligned} \tag{96}$$

which are the equivalent to (72). As in the ∇ formulation, the irrotationality condition is omitted here because it is automatically satisfied through the introduction of a scalar potential.

4.1.2.2 Compressible Case

The differential conservation equations for steady flow of an compressible inviscid fluid without externally applied forces can be written in tensor covariant form in terms of the *contravariant* velocity vector u^ν as,

$$\begin{aligned} \left(\rho\, u^\nu\right)_{;\,\nu} &= 0 \quad \text{Continuity} \\ T^{\mu\nu}{}_{;\,\nu} &= 0 \quad \text{Momentum} \end{aligned} \tag{97}$$

where

$$T^{\mu\,\nu} = \rho\, u^\mu u^\nu + g^{\mu\nu}\, p \tag{98}$$

As for the incompressible case, the condition of irrotationality is a condition on the *covariant* velocity vector given by equation (86),

$$u_{\mu;\,\nu} - u_{\nu;\,\mu} = 0,$$

which is equivalent to,

$$u_{\mu,\,\nu} - u_{\nu,\,\mu} = 0$$

through the symmetry of the Christoffel symbols in their lower indices, as discussed in the previous section.

We will now proceed write the momentum and continuity equations in terms of the covariant velocity components. For the continuity equation, we can expand the divergence as in the last section and substitute $u^\nu = g^{\nu\alpha}u_\alpha$ to give,

$$\frac{1}{\sqrt{g}}\left(\sqrt{g}\, g^{\nu\alpha}\rho\, u_\alpha\right)_{,\,\nu} = 0 \tag{99}$$

The momentum equation can be rewritten by substituting the momentum tensor from (98) into (97), resulting in,

$$\left(\rho\, u^\mu u^\nu\right)_{;\,\nu} + \left(g^{\mu\nu}\, p\right)_{;\,\nu} = 0.$$

Expanding this expression with the chain rule and applying the metricity condition gives,

$$\left(\rho\, u^\nu\right)_{;\,\nu}\, u^\mu + \rho\, u^\mu{}_{;\,\nu}\, u^\nu + g^{\mu\nu}\, p_{,\,\nu} = 0.$$

The first term vanishes from the continuity equation leaving,

$$\rho\, u^\mu{}_{;\,\nu}\, u^\nu + g^{\mu\nu}\, p_{,\,\nu} = 0. \tag{100}$$

Equation (100) is the compressible flow equivalent to equation (90) derived in the previous section. These equations are identical except that ρ replaces ρ_0 in the compressible case. Because ρ does not appear in any derivatives in this equation, the manipulations leading to the form of the momentum equation involving only perfect differentials of scalar quantities proceeds in an identical fashion to that shown in the previous section. The equation therefore takes the same form as equation (94) except that that ρ replaces ρ_0:

$$dp = -\frac{\rho}{2}\, d\left(V^2\right). \tag{101}$$

As before, $V^2 = u_\nu\, u^\nu = g^{\mu\nu} u_\mu u_\nu$ is the squared magnitude of the velocity. This equation is identical to form (76) derived in ∇ notation if we recognize that $V = \|\vec{u}\|$.

The next task is to apply the specifying relation linking the thermodynamic variables to close the system. This relation is identical to that presented as (74) in the ∇ approach:

$$\frac{p}{p_0} = \left(\frac{\rho}{\rho_0}\right)^\gamma. \tag{102}$$

As this relation involves only the scalar quantities p and ρ and no vector or tensor entities, we need not repeat the same manipulations to transition from equation (101) to the density velocity relation. Instead, we can simply write down the relation obtained in the ∇ approach, replacing $\|\vec{u}\|$ with V to give

$$\frac{\rho}{\rho_0} = \left(1 - \frac{\gamma - 1}{2\, {a_0}^2}\, V^2\right)^{1/(\gamma-1)} \tag{103}$$

where a_0 remains the stagnation sound speed. This equation is the equivalent to (78) derived in the ∇ approach.

Summarizing the situation as it stands now, the governing equations for steady compressible isentropic flow can be written in Riemannian tensorial form as,

$$\begin{aligned}
\frac{1}{\sqrt{g}} \left(\sqrt{g}\, g^{\nu\mu}\, \rho\, u_\mu\right)_{,\,\nu} &= 0 && \text{Continuity} \\
u_{\mu,\,\nu} - u_{\nu,\,\mu} &= 0 && \text{Irrotationality} \\
\frac{\rho}{\rho_0} &= \left(1 - \frac{\gamma - 1}{2\, {a_0}^2}\, V^2\right)^{1/(\gamma-1)} && \text{Density–Velocity Relation} \\
\frac{p}{p_0} &= \left(\frac{\rho}{\rho_0}\right)^\gamma && \text{Specifying/State Equation}
\end{aligned} \tag{104}$$

where again, $V^2 = u_\nu\, u^\nu = g^{\mu\nu} u_\mu u_\nu = \|\vec{u}\|^2$ is the squared magnitude of the velocity vector. These equations are the Riemannian tensorial equivalent of the ∇ form (79).

We can also obtain the full potential equation in this Riemannian notation. Repeating equation (80) which relates density and pressure differentials to the sound speed

$$dp = a^2\, d\rho,$$

and introducing the relation into (101) and dividing by $a^2\, \rho$ results in,

$$\frac{1}{\rho}\, d\rho = -\frac{1}{2\, a^2}\, d\left(V^2\right).$$

This expression holds also for individual component directions, so we can write it in terms of the gradient as,

$$\frac{1}{\rho}\,\rho_{,\,\nu} = -\frac{1}{2\,a^2}\,\left(V^2\right)_{,\,\nu}.$$

We can now use equation (92) with the dummy indices relabeled to replace $\left(V^2\right)_{,\,\alpha}$ as,

$$\left(V^2\right)_{,\,\nu} = 2\,u_{\alpha;\,\nu}\,u^{\alpha}$$

to give,

$$\frac{1}{\rho}\,\rho_{,\,\nu} = -\frac{1}{a^2}\,u_{\alpha;\,\nu}\,u^{\alpha}. \tag{105}$$

Next, expanding the continuity equation from (97) with the chain rule gives,

$$\rho_{,\,\nu}\,u^{\nu} + \rho\,u^{\nu}{}_{;\,\nu} = 0.$$

Dividing this equation by ρ and substituting (105) results in,

$$-\frac{1}{a^2}\,u_{\alpha;\,\nu}\,u^{\alpha}\,u^{\nu} + u^{\nu}{}_{;\,\nu} = 0.$$

Noting that the contravariant velocity in the second term can be replaced by the covariant velocity with a raised index gives,

$$-\frac{1}{a^2}\,u_{\alpha;\,\nu}\,u^{\alpha}\,u^{\nu} + \left(g^{\nu\alpha}u_{\alpha}\right)_{;\,\nu} = 0,$$

which is equivalent to

$$-\frac{1}{a^2}\,u_{\alpha;\,\nu}\,u^{\alpha}\,u^{\nu} + g^{\nu\alpha}u_{\alpha;\,\nu} = 0$$

by the metricity condition. Grouping terms and noting the symmetry of the inverse metric tensor, i.e. $g^{\nu\alpha} = g^{\alpha\nu}$, shows,

$$\left(g^{\alpha\nu} - \frac{1}{a^2}\,u^{\alpha}\,u^{\nu}\right)u_{\alpha;\,\nu} = 0. \tag{106}$$

By expanding the the covariant derivative in terms of the partial derivatives and the Christoffel symbols as shown in Section 2.2, equation (106) becomes

$$\left(g^{\alpha\nu} - \frac{1}{a^2}\,u^{\alpha}\,u^{\nu}\right)\left(u_{\alpha,\,\nu} - \Gamma^{\beta}_{\alpha\nu}u_{\beta}\right) = 0. \tag{107}$$

Replacing the remaining contravariant vectors by raising the indices of covariant vectors gives,

$$\left(g^{\alpha\nu} - \frac{1}{a^2}\, g^{\alpha\sigma} u_\sigma\, g^{\nu\tau} u_\tau\right)\left(u_{\alpha,\,\nu} - \Gamma^{\beta}_{\alpha\nu} u_\beta\right) = 0. \tag{108}$$

Finally, introducing the potential by substituting $\phi_\mu = \phi_{,\,\mu} = u_\mu$ where the subscript on ϕ denotes partial differentiation with respect to the index gives,

$$\left(g^{\alpha\nu} - \frac{1}{a^2}\, g^{\alpha\sigma} \phi_\sigma\, g^{\nu\tau} \phi_\tau\right)\left(\phi_{\alpha,\,\nu} - \Gamma^{\beta}_{\alpha\nu} \phi_\beta\right) = 0 \tag{109}$$

which is the full potential equation in Riemannian tensor form.

As a check of this derivation, we can use (109) to arrive immediately at the Cartesian form. For Cartesian coordinates, all of the Christoffel symbols $\Gamma^{\beta}_{\alpha\nu}$ vanish and the inverse metric takes the form of the Kronecker delta $\delta^{\alpha\nu}$, so we have,

$$\left(\delta^{\alpha\nu} - \frac{1}{a^2}\, \delta^{\alpha\sigma} \phi_\sigma\, \delta^{\nu\tau} \phi_\tau\right)\phi_{\alpha,\,\nu} = 0 \tag{110}$$

which can be recognized as the well known Cartesian form of the full potential equation.

4.2 Geometrization of Compressibility through the Metric Tensor

Having developed the invariant forms of the governing equations, we will now proceed to establish a linkage between a compressible flow and an incompressible equivalent through the selection of a metric tensor. We shall base this connection on the invariant forms of the continuity equations presented in the preceding section. In particular, we are interested in Equation 95 for incompressible flow and Equation 104 for compressible flow. We rewrite these here as,

$$\begin{aligned} \frac{1}{\sqrt{g}}\left(\sqrt{g}\, g^{\nu\mu}\, u_\mu\right)_{,\,\nu} &= 0 \qquad \text{Incompressible Continuity} \\ \frac{1}{\sqrt{h}}\left(\sqrt{h}\, h^{\nu\mu}\, \rho\, u_\mu\right)_{,\,\nu} &= 0 \qquad \text{Compressible Continuity} \end{aligned} \tag{111}$$

where we distinguish the metric tensors as $g^{\mu\nu}$ (or alternately $g_{\mu\nu}$) corresponding to the incompressible flow and $h^{\mu\nu}$ (or alternately $h_{\mu\nu}$) for the compressible flow, and we consider the equations to describe the same covariant velocity vector u_μ.

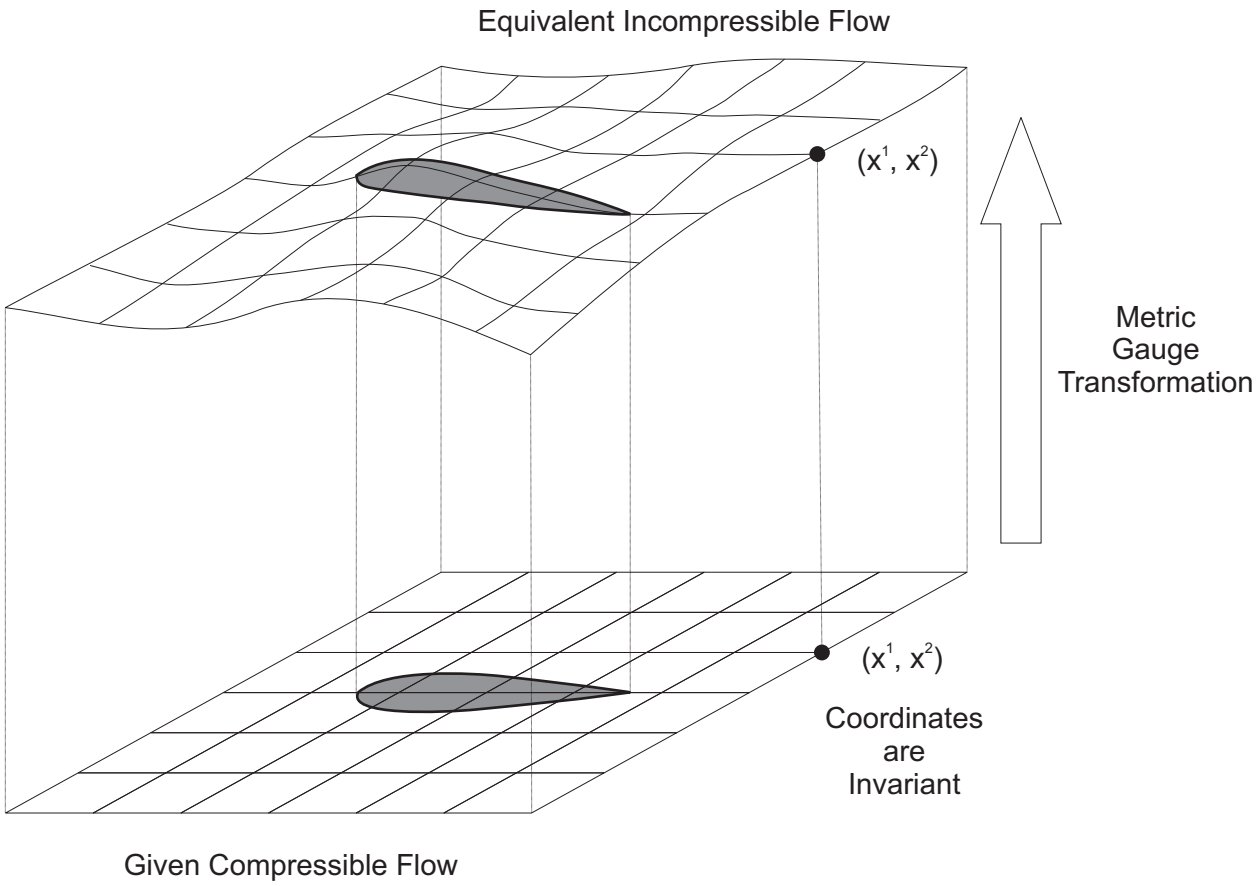

Figure 4: Transformation of the Domain Under a Gauge Transformation to Produce an Equivalent Incompressible Flow

Our goal now is as follows. Given a metric $h_{\mu\nu}$ describing the coordinate system in which the compressible flow boundary value problem is posed, determine a metric $g_{\mu\nu}$ describing an equivalent incompressible flow in the same coordinate system such that both flows have the same covariant velocity vector throughout the field. That is, we are asking for the metric that produces a *kinematically equivalent* incompressible flow that exists in the same coordinate system as the compressible flow. The selection of this metric comprises a *gauge transformation* that produces an incompressible flow living in a curved space defined by the same coordinates but having different lengths between adjacent points than the original space. This gauge transformation is illustrated in Figure 4.

The notion of differing lengths between points can best be viewed from the standpoint of an observer living in three–dimensional space. This observer can use a straight ruler

to connect points on the curved surface and measure distances. Measurements between adjacent points in the curved space will differ from those between corresponding points in a flat plane because the ruler measurement includes a contribution from the out-of-plane dimension.

A procedure to determine the metric tensor $g_{\mu\nu}$ can be discovered by examining Equations 111. Because both equations equal zero we can set them equal to each other, up to some nonzero real scalar factor σ to give,

$$\frac{1}{\sqrt{g}}\left(\sqrt{g}\, g^{\nu\mu}\, u_\mu\right)_{,\,\nu} = \frac{\sigma}{\sqrt{h}}\left(\sqrt{h}\, h^{\nu\mu}\, \rho\, u_\mu\right)_{,\,\nu}. \tag{112}$$

We make the distinction that σ be nonzero because we intend to require that the disappearance of the left hand side of the equation be a consequence of the compressible continuity equation and not of σ. That is, we wish to ensure that if we enforce the continuity condition for the compressible flow, continuity for the equivalent incompressible flow will follow automatically. If σ were zero, this consequence is not assured, as one of the continuity equations could then be equal to a nonzero value and the vanishing of σ would still allow Equation 112 to hold.

The continuity equations are scalar equations, so Equation 112 gives only one differential relation for the components of the metric. The metric tensor for a space with dimension $n = 2$ has $n(n+1)/2 = 3$ independent components because it is symmetric [34]; therefore, it appears upon first inspection that we need to determine two additional relations.

It seems that no additional physical conditions need to be placed on the metric at this point, so we shall attempt to set the remaining conditions for convenience. The main difficulty with the condition provided by Equation 112 is that it is a nonlinear partial differential equation. Therefore, if we set the other conditions on the metric arbitrarily, we shall be required to solve a nonlinear boundary value problem to determine the remaining condition. This problem would be substantially similar in difficulty to the boundary value problem for the flow itself. Because we have the freedom to set additional conditions, however, we can choose these conditions to avoid having to solve this differential equation.

To do this, let us first rearrange Equation 112 by multiplying by $\sqrt{g}$ to give,

$$\left(\sqrt{g}\, g^{\nu\mu}\, u_\mu\right)_{,\,\nu} = \frac{\sigma\sqrt{g}}{\sqrt{h}} \left(\sqrt{h}\, h^{\nu\mu}\, \rho\, u_\mu\right)_{,\,\nu}.$$

We now absorb the factor $\frac{\sigma\sqrt{g}}{\sqrt{h}}$ into the derivative and subtract the term produced by consideration of the chain rule, resulting in

$$\left(\sqrt{g}\, g^{\nu\mu}\, u_\mu\right)_{,\,\nu} = \left(\sigma\sqrt{g}\, h^{\nu\mu}\, \rho\, u_\mu\right)_{,\,\nu} - \sqrt{h}\, h^{\nu\mu}\, \rho\, u_\mu \left(\frac{\sigma\sqrt{g}}{\sqrt{h}}\right)_{,\,\nu}.$$

We can now rearrange this expression to obtain,

$$\left(\sqrt{g}\, g^{\nu\mu}\, u_\mu - \sigma\sqrt{g}\, h^{\nu\mu}\, \rho\, u_\mu\right)_{,\,\nu} + \sqrt{h}\, h^{\nu\mu}\, \rho\, u_\mu \left(\frac{\sigma\sqrt{g}}{\sqrt{h}}\right)_{,\,\nu} = 0. \tag{113}$$

The simplification that we are seeking is to satisfy the differential Equation 113 *identically*, that is by requiring that it holds throughout the flow automatically and not as the result of solving a boundary value problem. We can satisfy Equation 113 identically by requiring that the separate expressions within each set of parentheses take on particular forms such that the derivatives are automatically zero for all values of ν in the summation. The forms we desire can be written as,

$$\sqrt{g}\left(g^{\nu\mu}\, u_\mu - \sigma\, h^{\nu\mu}\, \rho\, u_\mu\right) = f^\nu \tag{114}$$

$$\frac{\sigma\sqrt{g}}{\sqrt{h}} = c \tag{115}$$

in which c is a constant, and f^ν satisfies $f^1 = f^1(x^2)$ and $f^2 = f^2(x^1)$ where x^1 and x^2 are the coordinates in the frame in which both flows are described. Since the index ν is now free and not dummy as it was in Equation 113, Equation 114 represents two algebraic equations for the components $g^{\mu\nu}$ of the inverse metric tensor corresponding to the incompressible flow, and Equation 115 provides a third condition expressed in terms of the metric determinant $\sqrt{g}$. These requirements therefore collectively form three algebraic conditions for the three components of the metric tensor that satisfy Equation 112 identically.

We can determine the functions f^ν by requiring that the metric components remain finite in the limit as the velocity components u_μ go to zero at stagnation points in the flow. The left hand side of the Equation 114 vanishes at $u_\mu = 0$, so we must require that

$f^\nu = 0$ at these points also. There are precisely two stagnation points in plane subsonic potential motion for the typical external flow problem over a single airfoil; however, more points may be present in the case of multiple bodies such as high lift configurations. The locations of the stagnation points depend on the boundary value problem for the flow and must be considered as arbitrary. We must therefore apparently set $f^\nu = 0$ throughout the field, as the conditions $f^1 = f^1(x^2)$ and $f^2 = f^2(x^1)$ would otherwise place restrictions on the behavior of the flow solution. These restrictions cannot be maintained because the flow must be obtained uniquely from the specified body shape, boundary conditions, and freestream parameters. Specifying $f^\nu = 0$ in Equation 114 and dividing by $\sqrt{g}$ gives,

$$g^{\nu\mu}\, u_\mu - \sigma\, h^{\nu\mu}\, \rho\, u_\mu = 0. \tag{116}$$

We can now solve for the components of the inverse metric tensor. To do this, let us first determine the metric tensor determinant g in terms of the individual components of the contravariant metric tensor $g^{\mu\nu}$ for our case of dimension $n = 2$. Because the contravariant metric is a second order tensor, we can represent it as a symmetric matrix with components

$$g^{\nu\mu} = \begin{bmatrix} g^{11} & g^{12} \\ g^{12} & g^{22} \end{bmatrix}. \tag{117}$$

The contravariant and covariant metric tensors are inverses of each other, so their matrices are also inverses of each other. We can therefore determine the covariant metric tensor by taking the matrix inverse of the contravariant form, resulting in,

$$g_{\nu\mu} = \frac{1}{g^{11}\, g^{22} - \left(g^{12}\right)^2} \begin{bmatrix} g^{22} & -g^{12} \\ -g^{12} & g^{11} \end{bmatrix}.$$

The determinant of this matrix is what we mean by the determinant of the metric tensor, g, which is given by

$$g = \frac{1}{g^{11}\, g^{22} - \left(g^{12}\right)^2} \tag{118}$$

in terms of the components of the inverse metric tensor.

Now, expanding the summation in Equation 116 in terms of the components of the inverse metric tensor given in Equation 117 and noting the symmetry condition $g^{21} = g^{12}$, we have the two equations

$$\begin{aligned} \left(g^{11}\,u_1 + g^{12}\,u_2\right) - \sigma\,\rho\left(h^{11}\,u_1 + h^{12}\,u_2\right) &= 0 \\ \left(g^{12}\,u_1 + g^{22}\,u_2\right) - \sigma\,\rho\left(h^{12}\,u_1 + h^{22}\,u_2\right) &= 0. \end{aligned} \tag{119}$$

Squaring and rearranging Equation 115 and substituting Equation 118 and its equivalent for h gives

$$g^{11}\,g^{22} - \left(g^{12}\right)^2 = \frac{\sigma^2}{c^2}\,\left(h^{11}\,h^{22} - \left(h^{12}\right)^2\right). \tag{120}$$

Equations 119 and 120 provide three equations that can now be solved for the contravariant metric components g^{11}, g^{12}, and g^{22}. Solving and simplifying gives,

$$\begin{aligned} g^{11} &= \tau\frac{\sigma}{c}\left[\frac{1}{h}\,(u_2)^2 + (c\rho)^2\left(h^{11}u_1 + h^{12}u_2\right)^2\right] \\ g^{12} &= \tau\frac{\sigma}{c}\left[-\frac{1}{h}\,(u_1)(u_2) + (c\rho)^2\left(h^{11}u_1 + h^{12}u_2\right)\left(h^{12}u_1 + h^{22}u_2\right)\right] \\ g^{22} &= \tau\frac{\sigma}{c}\left[\frac{1}{h}\,(u_1)^2 + (c\rho)^2\left(h^{12}u_1 + h^{22}u_2\right)^2\right] \end{aligned} \tag{121}$$

where

$$\tau = 1/\left\{(c\rho)\left[h^{11}(u_1)^2 + 2h^{12}u_1u_2 + h^{22}(u_2)^2\right]\right\}.$$

Considering Equation 115, we can also write down the expressions $\sqrt{g}g^{\nu\mu}$ which appear in the governing flow equations as,

$$\begin{aligned} \sqrt{g}g^{11} &= \tau\sqrt{h}\left[\frac{1}{h}\,(u_2)^2 + (c\rho)^2\left(h^{11}u_1 + h^{12}u_2\right)^2\right] \\ \sqrt{g}g^{12} &= \tau\sqrt{h}\left[-\frac{1}{h}\,(u_1)(u_2) + (c\rho)^2\left(h^{11}u_1 + h^{12}u_2\right)\left(h^{12}u_1 + h^{22}u_2\right)\right] \\ \sqrt{g}g^{22} &= \tau\sqrt{h}\left[\frac{1}{h}\,(u_1)^2 + (c\rho)^2\left(h^{12}u_1 + h^{22}u_2\right)^2\right] \end{aligned} \tag{122}$$

In Equations 121, σ appears as a scalar multiplier on each component of the metric tensor. Our only requirements on σ were that it be nonzero and real. That is, any nonzero real value of σ will produce a viable metric in terms of the transformation of the governing equations for the flow. Equations 121 therefore represent an *equivalence class* of metrics. Any two metrics in this class, say $\bar{g}^{\nu\mu}$ and $\tilde{g}^{\nu\mu}$ are related to one another as,

$$\bar{g}^{\nu\mu} = \frac{\bar{\sigma}}{\tilde{\sigma}}\tilde{g}^{\nu\mu}$$

where $\bar{\sigma}$ is a particular value of σ that corresponds to $\bar{g}^{\nu\mu}$ and $\tilde{\sigma}$ is the value corresponding to $\tilde{g}^{\nu\mu}$. Metrics related to one another in this way by a scalar multiplication are said to be *conformal* [34, 42]. This terminology has a deep connection to conformal coordinate transformations on two–dimensional surfaces, as the metrics corresponding to two coordinate systems related through a such a transformation are scalar multiples of one another.

As seen in (111), the governing kinematic equation for the equivalent incompressible flow does not depend on $g^{\nu\mu}$ directly. It depends only on the product $\sqrt{g}g^{\nu\mu}$. This expression does not depend on σ, as shown by Equations 122. Therefore, the governing equations do not change for any metric in the conformal equivalence class defined by Equations 121. This result stems from the conformal invariance of the continuity equation itself. This behavior has been used to great effect in incompressible aerodynamics. Because the potential equation is invariant with respect to conformal transformations, we can solve flows over simple two–dimensional shapes such as circles and map the solution through a conformal coordinate transformation to the solution over an airfoil of a prescribed shape. This conformal invariance of the continuity equation holds for both incompressible and compressible flows.

For the flow problems in which we are usually interested we can make additional simplifications to Equations 121. In typical situations, the coordinate system in which the compressible flow boundary value problem is described is an *orthogonal* system. As implied by their name, orthogonal systems have coordinate curves that intersect at right angles. These systems have metric tensors whose matrices are diagonal. That is, all components of the metric $h_{\mu\nu}$ and the inverse metric $h^{\mu\nu}$ with $\mu \neq \nu$ are zero [106]. Most standard coordinate systems including Cartesian, polar/cylindrical, and spherical coordinates are orthogonal. Presuming that the compressible flow is given in an orthogonal system, the component h^{12} vanishes and Equations 121 simplify to,

$$\begin{aligned} g^{11} &= \frac{\sigma\, h^{11}\left[h^{11}(u_1)^2(c\rho)^2 + h^{22}\,(u_2)^2\right]}{c\,(c\rho)\left[h^{11}(u_1)^2 + h^{22}(u_2)^2\right]} \\ g^{12} &= \frac{\sigma\, h^{11}\, h^{22}\,(u_1)(u_2)\left[(c\rho)^2 - 1\right]}{c\,(c\rho)\left[h^{11}(u_1)^2 + h^{22}(u_2)^2\right]} \\ g^{22} &= \frac{\sigma\, h^{22}\left[h^{22}(u_2)^2(c\rho)^2 + h^{11}\,(u_1)^2\right]}{c\,(c\rho)\left[h^{11}(u_1)^2 + h^{22}(u_2)^2\right]} \end{aligned} \tag{123}$$

where we have substituted $h^{11}\,h^{22} = 1/h$ as indicated by Equation 118 for $h^{12} = 0$. Considering Equation 115, we can also write down the expressions $\sqrt{g}g^{\nu\mu}$ which appear in the governing flow equations as,

$$\begin{aligned}
\sqrt{g}g^{11} &= \frac{h^{11}\left[h^{11}(u_1)^2(c\rho)^2 + h^{22}\,(u_2)^2\right]}{(c\rho)\left[h^{11}(u_1)^2 + h^{22}(u_2)^2\right]} \\
\sqrt{g}g^{12} &= \frac{h^{11}\,h^{22}\,u_1u_2\left[(c\rho)^2 - 1\right]}{(c\rho)\left[h^{11}(u_1)^2 + h^{22}(u_2)^2\right]} \\
\sqrt{g}g^{22} &= \frac{h^{22}\left[h^{22}(u_2)^2(c\rho)^2 + h^{11}\,(u_1)^2\right]}{(c\rho)\left[h^{11}(u_1)^2 + h^{22}(u_2)^2\right]}.
\end{aligned} \tag{124}$$

Let us now further simplify Equations 124 for the case of a Cartesian coordinate system. We will do this for two reasons. First, we shall have occasion to employ this form in the flow solution algorithm presented subsequently in Chapter 5, and second, the Cartesian form has an interesting mathematical interpretation. To arrive at this form, we recognize that the contravariant metric tensor for Cartesian coordinates is simply the contravariant Kronecker delta tensor $\delta^{\nu\mu}$. Substituting $h^{11} = \delta^{11} = 1$ and $h^{22} = \delta^{22} = 1$, Equations 123 become

$$\begin{aligned}
g^{11} &= \frac{\sigma\left[(u_1)^2(c\rho)^2 + (u_2)^2\right]}{c\,(c\rho)\left[(u_1)^2 + (u_2)^2\right]} \\
g^{12} &= \frac{\sigma\left[(c\rho)^2 - 1\right]u_1u_2}{c\,(c\rho)\left[(u_1)^2 + (u_2)^2\right]} \\
g^{22} &= \frac{\sigma\left[(u_2)^2(c\rho)^2 + (u_1)^2\right]}{c\,(c\rho)\left[(u_1)^2 + (u_2)^2\right]}
\end{aligned} \tag{125}$$

and Equations 124 become

$$\begin{aligned}
\sqrt{g}g^{11} &= \frac{(u_1)^2(c\rho)^2 + (u_2)^2}{(c\rho)\left[(u_1)^2 + (u_2)^2\right]} \\
\sqrt{g}g^{12} &= \frac{\left[(c\rho)^2 - 1\right]u_1u_2}{(c\rho)\left[(u_1)^2 + (u_2)^2\right]} \\
\sqrt{g}g^{22} &= \frac{(u_2)^2(c\rho)^2 + (u_1)^2}{(c\rho)\left[(u_1)^2 + (u_2)^2\right]}.
\end{aligned} \tag{126}$$

We can note an interesting mathematical significance to Equations 126 by multiplying Equation 116 by $\sqrt{g}$ and applying Equation 115 to the second term to give,

$$\sqrt{g}g^{\nu\mu}\,u_\mu - \sqrt{h}\,h^{\nu\mu}\,(c\rho)\,u_\mu = 0. \tag{127}$$

For Cartesian coordinates, we have $\sqrt{h}h^{\nu\mu} = \delta^{\nu\mu}$. Substituting this relation and rearranging gives,

$$\sqrt{g}g^{\nu\mu}\, u_\mu = \delta^{\nu\mu}\,(c\rho)\, u_\mu \tag{128}$$

which can be written in terms of matrix components as,

$$\begin{bmatrix} \sqrt{g}g^{11} & \sqrt{g}g^{12} \\ \sqrt{g}g^{12} & \sqrt{g}g^{22} \end{bmatrix} \begin{bmatrix} u_1 \\ u_2 \end{bmatrix} = (c\rho) \begin{bmatrix} u_1 \\ u_2 \end{bmatrix}.$$

This matrix equation has the form

$$A\vec{u} = \lambda\vec{u}$$

which can be recognized as the eigenanalysis problem with $\vec{u}$ as the eigenvector and λ as the eigenvalue. Therefore, for Cartesian coordinates, the problem of determining the metric expression $\sqrt{g}g^{\nu\mu}$ is equivalent to asking for a 2×2 symmetric matrix with eigenvalue $(c\rho)$ and eigenvector u_μ.

Our definition of the metric corresponding to the equivalent incompressible flow is now nearly complete. One unknown remains—the constant c. We can set c by considering the situation in which the given compressible flow is locally incompressible. This situation manifests itself at neighborhoods in the flow where the velocities are so small that the density does not vary much from point to point even in the presence of finite velocity gradients. We can determine these locations by combining Equations 101 and 77 to give,

$$d\rho = -\frac{\rho}{2a^2} d\left(V^2\right) = -\frac{\rho}{a^2} V\, dV.$$

In the case where $V = 0$, we have $d\rho = 0$ indicating that the density does not vary, presuming that dV is finite in this region. Points in the flow at which the velocity vanishes and its derivatives are finite are the stagnation points. In the local neighborhoods surrounding stagnation points, the flow is therefore effectively incompressible.

We can now set c by requiring that the metrics for the given compressible flow and the equivalent incompressible flow are the same at these points, at least up to some conformal factor. That is, we can require, $\sqrt{g}g^{\nu\mu} = \sqrt{h}h^{\nu\mu}$ at the stagnation conditions. Our reason for applying this condition stems from the requirement that the compressible continuity

equation relaxes to the incompressible continuity equation in stagnation regions. At stagnation, $d\rho = 0$, so the density is locally constant and can be divided through the compressible continuity equation, so Equations 111 show that we must then have $\sqrt{g}g^{\nu\mu} = \sqrt{h}h^{\nu\mu}$ in order that the two equations be identical. Applying this condition to Equation 127 gives

$$\sqrt{h}h^{\nu\mu}\, u_\mu \left[1 - (c\rho)\right] = 0$$

which is satisfied by $c = 1/\rho$. This condition holds only at stagnation points at which ρ takes on its stagnation value ρ_0 which is a constant of motion; therefore, we finally arrive at $c = 1/\rho_0$. Substituting this value for c into Equations 126 for a compressible flow given in Cartesian coordinates results in

$$\begin{aligned}
\sqrt{g}g^{11} &= \frac{(u_1)^2 \left(\frac{\rho}{\rho_0}\right)^2 + (u_2)^2}{\left(\frac{\rho}{\rho_0}\right)\left[(u_1)^2 + (u_2)^2\right]} \\
\sqrt{g}g^{12} &= \frac{\left[\left(\frac{\rho}{\rho_0}\right)^2 - 1\right] u_1 u_2}{\left(\frac{\rho}{\rho_0}\right)\left[(u_1)^2 + (u_2)^2\right]} \\
\sqrt{g}g^{22} &= \frac{(u_2)^2 \left(\frac{\rho}{\rho_0}\right)^2 + (u_1)^2}{\left(\frac{\rho}{\rho_0}\right)\left[(u_1)^2 + (u_2)^2\right]}
\end{aligned} \tag{129}$$

which is the form of the metric that we shall study further and apply in Chapter 5. Note that in the limit of $\rho \to \rho_0$, which is the case both at stagnation points and as $M_\infty \to 0$ for the given compressible flow, we have

$$\begin{aligned}
\sqrt{g}g^{11} &= 1 \\
\sqrt{g}g^{12} &= 0 \\
\sqrt{g}g^{22} &= 1
\end{aligned}$$

which corresponds to a metric conformally equivalent to the Cartesian metric specified for compressible flow, as we had desired.

Before moving on, it is important to review the key results obtained in this section. The goal was to establish an equivalent incompressible flow that resides in the same coordinate

system as a given compressible flow. This equivalence was obtained by deriving a metric tensor $g^{\mu\nu}$ (or equivalently $g_{\mu\nu}$) for an incompressible flow whose velocity vector matches that of the compressible flow. The metric tensor was determined by setting the continuity equations for the both flows equal, up to some nonzero scalar factor σ, and requiring that the resulting partial differential equation be satisfied identically throughout the field. This process determined the metric tensor up to a scalar conformal factor that multiplies each of the tensor components. This conformal factor turns out to equal σ, and can be taken to remain arbitrary as a result of the conformal invariance of the governing equations.

The resulting metric for the equivalent incompressible flow looks very similar to the given metric for the compressible flow, except that it is perturbed by factors that are a function of the varying density ρ and the velocity vector u_μ. That is, the effects of compressibility, as given by variations in ρ, have been introduced into the geometry of the space in which the equivalent incompressible flow resides, as embodied by its metric tensor. In this way, we have *geometrized* the effects of compressibility. In the region of stagnation points or in the limit of vanishing freestream Mach number for the compressible flow, the metric for the equivalent incompressible flow becomes equal to the given metric for the compressible flow. This occurs because the compressible flow is effectively incompressible in these limits and therefore becomes its own incompressible equivalent. We have termed the equivalent flow "incompressible," but that is not to say that the density does not actually vary from point to point. Rather, we now interpret the density field not as something resulting from the flow but as some independent field that affects the space in which an incompressible flow is defined.

Although we have now embedded the effects of compressibility into the space through the introduction of a metric tensor defining an equivalent incompressible flow, this flow is not easier to solve than the compressible flow in the coordinate system in which it is described. The reason is that we have simply placed the difficulty of compressibility into another entity; the governing equation for the equivalent flow looks exactly the same as that for the original compressible flow when the new metric is written explicitly in terms of flow parameters. To be more concrete, let us consider a compressible flow given in Cartesian

coordinates, which has the continuity equation

$$\left(\sqrt{h}\, h^{\nu\mu}\, \rho\, u_\mu\right)_{,\,\nu} = 0 \tag{130}$$

and its equivalent incompressible flow, which has

$$\left(\sqrt{g}\, g^{\nu\mu}\, u_\mu\right)_{,\,\nu} = 0 \tag{131}$$

as the continuity equation. For Cartesian coordinates, we have

$$\sqrt{h} h^{\nu\mu} = \delta^{\nu\mu} \tag{132}$$

for the compressible metric and, from Equation 128, the incompressible metric satisfies,

$$\sqrt{g} g^{\nu\mu}\, u_\mu = \delta^{\nu\mu}\, (c\rho)\, u_\mu. \tag{133}$$

Substituting (132) into (130) for the compressible flow, and substituting (133) into (131) and dividing by c gives the same equation:

$$\left(\delta^{\nu\mu}\, \rho\, u_\mu\right)_{,\,\nu} = 0. \tag{134}$$

The difference between the two flows is therefore determined not by differences in the governing equations but by differences in the metric tensors describing the spaces in which each flow resides. The fundamental nonlinearity of the compressible flow remains present in the governing equations.

A primary goal of this dissertation is to use the concept of the equivalent incompressible flow in an attempt to simplify practical flow solutions. In order to attain these simplified solutions, we must therefore transform the coordinate system in which this equivalent incompressible flow is given to one in which the governing equation takes on a particularly simple form that is easily solved. The form that we desire is the so–called canonical form of Laplace's equation. We shall attempt to determine the type and nature of the transformation required to obtain this equation in the following section.

4.3 Coordinate Transformation to Produce the Canonical Laplace Equation

In the last section, we determined an incompressible flow that is kinematically equivalent to a given compressible flow in the same coordinate system. Establishing this equivalence

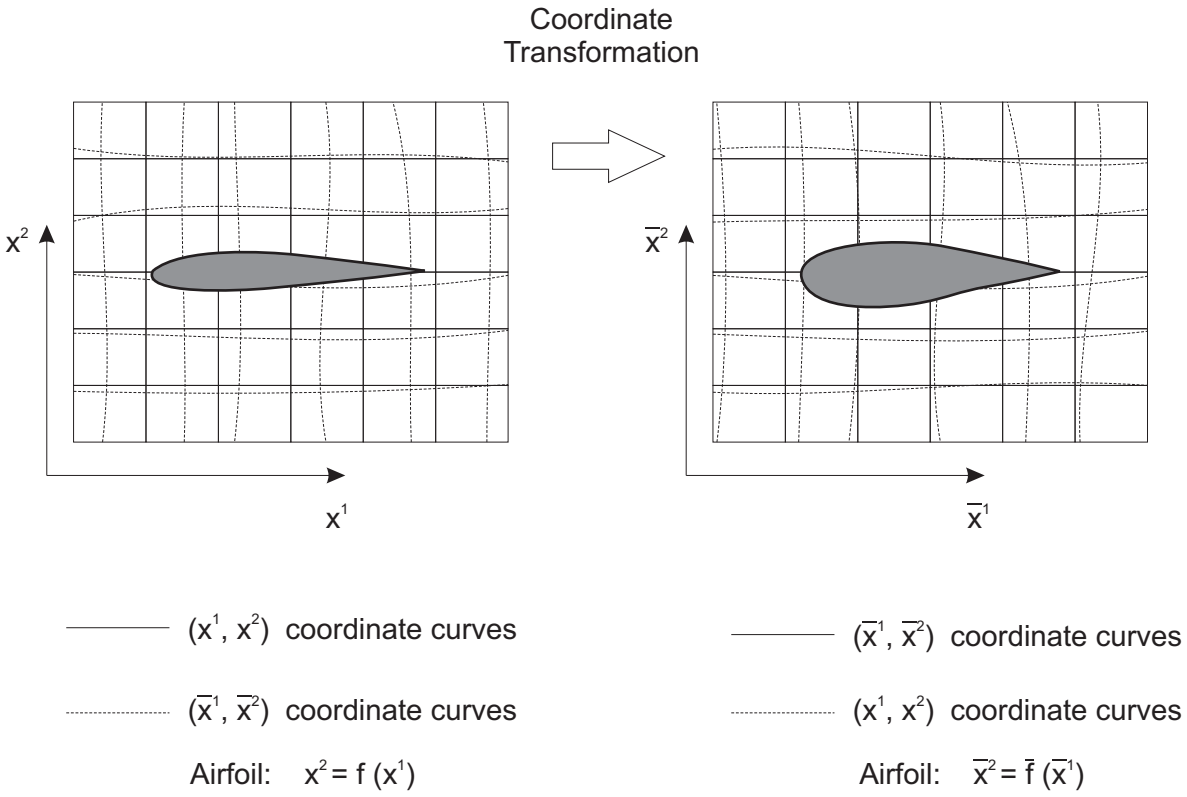

Figure 5: Transformation of the Domain of the Equivalent Incompressible Flow Under a Coordinate Mapping

did not result in a fundamental simplification of the boundary value problem for the flow, however, as we simply shuffled the nonlinearity of the compressibility effects to another mathematical entity without altering the governing equations.

In this section, we shall attempt to simplify the boundary value problem for the flow solution by developing a transformation that maps the equivalent incompressible flow to a coordinate system in which the potential equation takes on the canonical Cartesian form of the Laplace equation. Unlike the gauge transformation that we achieved in the previous section, this transformation is a mapping of coordinate curves and not a transformation of the underlying space. Indeed, we can envision the transformation as creating new coordinate lines on the shaped surface shown in Figure 4. If we project the coordinate lines from this surface onto a plane for visualization purposes, this transformation has the effect indicated in Figure 5.

The mapping that we desire will turn out to be equivalent to a well known problem in

the differential geometry of two-dimensional surfaces, namely the introduction of so-called *isothermal coordinates*. This nomenclature does not appear to have any connection to the concept of thermodynamic temperature, insofar as documented in exposés of the classical literature. The transformation to isothermal coordinates in two dimensions is a special case of a *quasiconformal mapping* [3]. These types of mappings have a rich history in the study of subsonic potential flow, stemming from the work of Lipman Bers in the 1940s and 1950s [12, 13, 14, 15, 16]. Isothermal coordinate mappings have also been used in the field of elliptic grid generation [74, 7]. We shall examine quasiconformal mappings and the approach taken by Bers in Section 4.5.

In this section, we shall initially describe the motivation for our introduction of isothermal coordinates and outline the differential equations necessary for their generation. Next, we shall investigate two general approaches for solving these differential equations. The first approach is to introduce them through the solution of a separate boundary value problem, and the second is to obtain them as a consequence of the flow solution itself.

4.3.1 Description of the Isothermal Coordinate Mapping

Our goal is to transform the coordinate system such that the equivalent incompressible flow is governed by the Cartesian coordinate form of the Laplace equation. In Section 4.2, we determined the metric tensor expression $\sqrt{g}g^{\nu\mu}$ that defines an equivalent incompressible flow in the same coordinate system in which the original compressible flow boundary value problem was posed. Let us call this original coordinate system x^α. The continuity equation for this incompressible flow took on the form,

$$\left(\sqrt{g}\, g^{\nu\mu}\, u_\mu\right)_{,\,\nu} = 0. \tag{135}$$

Although we have written this equation in terms of our particular metric tensor $g^{\nu\mu}$ corresponding to coordinates x^α, it is invariant with respect to coordinate transformations because it has been written in a tensorial form. We can therefore say that in a coordinate system $\bar{x}^\alpha$, the invariant equation takes on the form

$$\left(\sqrt{\bar{g}}\, \bar{g}^{\nu\mu}\, \bar{u}_\mu\right)_{,\,\nu} = 0. \tag{136}$$

where the coordinates with respect to which we differentiate with the comma are now taken to be those of the barred frame. This new frame is completely arbitrary, so long as it can be obtained from the original frame through an allowable coordinate transformation.

Because of this form invariance, we can ask that the $\bar{x}^\alpha$ frame take on a particular form such that its metric tensor satisfies

$$\sqrt{\bar{g}}\,\bar{g}^{\nu\mu} = \delta^{\nu\mu}. \tag{137}$$

With this metric tensor, Equation 136 becomes

$$\left(\delta^{\nu\mu}\,\bar{u}_\mu\right)_{,\,\nu} = 0. \tag{138}$$

Through the irrotationality condition given by

$$\bar{u}_{\mu,\,\nu} = \bar{u}_{\nu,\,\mu}$$

we can introduce a potential for the velocity as $\phi_{,\,\mu} = \bar{u}_\mu$. Note that, as we saw in Section 4.1, the irrotationality condition does not involve the metric and takes the same form in all coordinate systems. Introducing the potential into Equation 138 gives,

$$\left(\delta^{\nu\mu}\,\phi_{,\,\mu}\right)_{,\,\nu} = 0 \tag{139}$$

which is the Cartesian form of Laplace's equation that we desired to achieve.

The challenge now is to determine the metric $\bar{g}^{\nu\mu}$ and the coordinate system $\bar{x}^\alpha$ in which this equation holds. To do this, let us first examine the implications of Equation 137 more carefully. Because $\sqrt{\bar{g}}$ multiplies all elements of the tensor $\bar{g}^{\nu\mu}$, this tensor must have the same overall form as the Kronecker delta tensor to which we wish to equate it. That is, it must be orthogonal ($g^{\bar{1}2} = g^{\bar{2}1} = 0$) and have equal diagonal elements. Setting $\bar{g}^{22} = \bar{g}^{11} = 1/\Omega$ and writing the tensor as a matrix gives

$$\bar{g}^{\nu\mu} = \begin{bmatrix} 1/\Omega & 0 \\ 0 & 1/\Omega \end{bmatrix}. \tag{140}$$

The covariant metric tensor is obtained as the inverse of this matrix, which is given by taking the reciprocal of the diagonal elements:

$$\bar{g}_{\nu\mu} = \begin{bmatrix} \Omega & 0 \\ 0 & \Omega \end{bmatrix}. \tag{141}$$

The determinant of this matrix is $\bar{g} = \Omega^2$, so we can write,

$$\sqrt{\bar{g}}\bar{g}^{\nu\mu} = \begin{bmatrix} 1 & 0 \\ 0 & 1 \end{bmatrix} = \delta^{\nu\mu} \tag{142}$$

which satisfies Equation 137. From this exercise, we see that any metric of the form given by Equation 140 (or equivalently by Equation 141) will produce the desired Cartesian form of the Laplace equation regardless of the particular nonzero value of Ω. As with our determination of the metric $g^{\nu\mu}$ in the original reference frame, the allowable metrics in the $\bar{x}^\alpha$ frame therefore comprise a class in which all members are *conformal* to one another. This result is again indicative of the conformal structure of two-dimensional spaces.

Metrics of the form given by Equation 141 produce the line element

$$ds^2 = \Omega\left(\bar{x}^1, \bar{x}^2\right)\left[\left(d\bar{x}^1\right)^2 + \left(d\bar{x}^2\right)^2\right]. \tag{143}$$

Coordinates $(\bar{x}^1, \bar{x}^2)$ in which the line elements take this form are termed *isothermal* or *isothermic* coordinates [131]. The frame in which the equivalent incompressible flow is described by the Cartesian form the Laplace equation is therefore an isothermal coordinate system. These types of coordinates are well known in the classical study of the differential geometry of surfaces, as they arise from a conformal mapping from an arbitrary surface to a plane. A general result from the theory of surfaces is that any of the wide classification of simply-connected surfaces can be mapped conformally into a plane [61].

We will now investigate the requirements on the transformation from our original reference frame x^α to the isothermal frame $\bar{x}^\alpha$, which can be expressed as,

$$\bar{x}^\alpha = \bar{x}^\alpha\left(x^1, x^2\right). \tag{144}$$

In this investigation, we will generally follow the procedure outlined by Kreyszig [61]. Considering the transformation law for second order contravariant tensors, we can relate the inverse metric in frame x^α to the inverse metric in the isothermal system $\bar{x}^\alpha$ as,

$$\bar{g}^{\nu\mu} = g^{\alpha\beta}\frac{\partial\bar{x}^\nu}{\partial x^\alpha}\frac{\partial\bar{x}^\mu}{\partial x^\beta}. \tag{145}$$

Substituting Equation 140 for $\bar{g}^{\nu\mu}$ gives

$$\delta^{\nu\mu}/\Omega = g^{\alpha\beta}\frac{\partial\bar{x}^\nu}{\partial x^\alpha}\frac{\partial\bar{x}^\mu}{\partial x^\beta}. \tag{146}$$

For the case $\nu = 1$ and $\mu = 2$, this relation becomes,

$$g^{\alpha\beta}\frac{\partial\bar{x}^1}{\partial x^\alpha}\frac{\partial\bar{x}^2}{\partial x^\beta} = 0 \tag{147}$$

which has the identical form as the case $\mu = 1, \nu = 2$. For $\nu = \mu = 1$ we have,

$$g^{\alpha\beta}\frac{\partial\bar{x}^1}{\partial x^\alpha}\frac{\partial\bar{x}^1}{\partial x^\beta} = 1/\Omega$$

and for $\nu = \mu = 2$ the transformation is,

$$g^{\alpha\beta}\frac{\partial\bar{x}^2}{\partial x^\alpha}\frac{\partial\bar{x}^2}{\partial x^\beta} = 1/\Omega.$$

Since these latter two relations each equal $1/\Omega$ we can set them equal to each other and eliminate the $1/\Omega$ term to arrive at,

$$g^{\alpha\beta}\frac{\partial\bar{x}^1}{\partial x^\alpha}\frac{\partial\bar{x}^1}{\partial x^\beta} = g^{\tau\omega}\frac{\partial\bar{x}^2}{\partial x^\tau}\frac{\partial\bar{x}^2}{\partial x^\omega}. \tag{148}$$

It can be verified by direct substitution that if the transformation derivatives satisfy the relations

$$\frac{\partial\bar{x}^1}{\partial x^\alpha} = g_{\alpha\kappa}\epsilon^{\kappa\lambda}\frac{\partial\bar{x}^2}{\partial x^\lambda} \tag{149}$$

then they also satisfy Equations 147 and 148. The symbol $\epsilon^{\kappa\lambda}$ is a second order contravariant *tensor density* defined as $\epsilon^{11} = 0$, $\epsilon^{12} = 1/\sqrt{g}$, $\epsilon^{21} = -1/\sqrt{g}$, and $\epsilon^{22} = 0$. Tensor densities have similar transformation laws as tensors, except that the form of a tensor law is multiplied by powers of g [106].

Equation 149 has one free index, α; therefore, it represents two independent conditions on the coordinate derivatives in our two-dimensional space. These two coordinate equations are often termed the *generalized Cauchy–Riemann equations* or the *Beltrami equations* [16]. The reason for this terminology can be seen by considering the case in which $g_{\alpha\kappa}/\sqrt{g} = \delta_{\alpha\kappa}$ corresponding to coordinates conformal to Cartesian. In this case, the equations can be expanded in terms of the coordinates to give,

$$\begin{aligned}\frac{\partial\bar{x}^1}{\partial x^1} &= \frac{\partial\bar{x}^2}{\partial x^2}\\ \frac{\partial\bar{x}^1}{\partial x^2} &= -\frac{\partial\bar{x}^2}{\partial x^1}\end{aligned}$$

which can be recognized immediately as the classical form of the Cauchy–Riemann equations in complex analysis.

Since the generalized Cauchy–Riemann equations provide adequate restrictions to completely satisfy the tensor transformation law given by Equation 145, it may appear that we can *arbitrarily* specify an additional two conditions on the four coordinate derivatives $\frac{\partial \bar{x}^\mu}{\partial x^\nu}$. Unfortunately, this is not the case. We must ensure that the coordinate system that we produce forms a *coordinate basis* in order that our form of tensorial equations is consistent. As we saw in Chapter 2, the conditions required to produce a coordinate basis are the so-called *integrability conditions* which demand that the mixed partial derivatives of the coordinate mapping commute. In our two-dimensional case, there are two such conditions, one corresponding to each isothermal coordinate:

$$\begin{aligned} \frac{\partial^2 \bar{x}^1}{\partial x^1 \partial x^2} &= \frac{\partial^2 \bar{x}^1}{\partial x^1 \partial x^2} \\ \frac{\partial^2 \bar{x}^2}{\partial x^1 \partial x^2} &= \frac{\partial^2 \bar{x}^2}{\partial x^2 \partial x^1}. \end{aligned} \tag{150}$$

If these integrability conditions were not required to hold, the problem of obtaining the coordinate mapping would be dramatically simplified, since we could then specify the two additional conditions on the coordinate derivatives *algebraically*. Because of the integrability requirement, however, we shall see that the mapping must be determined by the solution of a set of two partial differential equations. Although we shall examine ways to simplify the solution of these equations, the fact that we must solve them represents the most fundamental impediment to the application of the theory outlined in this dissertation to practical flow solutions.

There are at least two possible approaches to obtaining integrability in the coordinate mapping. The first is to solve a separate boundary value problem that describes the coordinate mapping independently of the fluid flow. In this case, boundary conditions on the isothermal coordinates can be specified independently of the flow boundary conditions, and there is significant freedom in the specific nature of the mapping. The second approach is to attempt to satisfy the partial differential equations *identically* as a consequence of the flow. This approach is similar to the method used in Section 4.2 to solve for the metric

tensor algebraically. In this case, the boundary value problem for the isothermal coordinate mapping will follow directly from the boundary value problem for the flow itself, and there will be little or no freedom for specifying boundary conditions on the mapping independently. In Sections 4.3.2 and 4.3.3, we shall explore these two approaches to producing the isothermal coordinate mapping.

4.3.2 Integrability through a Separate Boundary Value Problem

In order to introduce isothermal coordinates through a separate boundary value problem, we shall first need to write the partial differential equations dictated by the integrability conditions in terms of the metric tensor in the original x^α frame. To begin, we rewrite the first of Equations 150 as

$$\sqrt{g}\epsilon^{\alpha\beta}\frac{\partial^2 \bar{x}^1}{\partial x^\alpha \partial x^\beta} = 0.$$

From the definition of $\epsilon^{\alpha\beta}$, the product $\sqrt{g}\epsilon^{\alpha\beta}$ consists entirely of constant elements, i.e. $\sqrt{g}\epsilon^{11} = 0$, $\sqrt{g}\epsilon^{12} = 1$, $\sqrt{g}\epsilon^{21} = -1$, and $\sqrt{g}\epsilon^{22} = 0$, so we can absorb this factor into the partial derivatives and write,

$$\frac{\partial}{\partial x^\beta}\left(\sqrt{g}\epsilon^{\alpha\beta}\frac{\partial \bar{x}^1}{\partial x^\alpha}\right) = 0.$$

Substituting Equation 149 for $\frac{\partial \bar{x}^1}{\partial x^\alpha}$ gives,

$$\frac{\partial}{\partial x^\beta}\left(\sqrt{g}\epsilon^{\alpha\beta}g_{\alpha\kappa}\epsilon^{\kappa\lambda}\frac{\partial \bar{x}^2}{\partial x^\lambda}\right) = 0.$$

We can now eliminate the tensor densities from this equation. First, we relate the contravariant tensor density $\epsilon^{\alpha\beta}$ to covariant tensor densities of the form $\epsilon_{\tau\omega}$ by index raising with the metric tensor in the x^α frame as,

$$\epsilon^{\alpha\beta} = \epsilon_{\tau\omega}g^{\alpha\tau}g^{\beta\omega}.$$

Substituting this relation results in,

$$\frac{\partial}{\partial x^\beta}\left(\sqrt{g}\epsilon_{\tau\omega}g^{\alpha\tau}g^{\beta\omega}g_{\alpha\kappa}\epsilon^{\kappa\lambda}\frac{\partial \bar{x}^2}{\partial x^\lambda}\right) = 0.$$

Grouping the product of the contravariant metric tensor $g^{\alpha\tau}$ and the covariant metric $g_{\alpha\kappa}$ and noting

$$g^{\alpha\tau} g_{\alpha\kappa} = \delta^{\tau}_{\kappa},$$

gives,

$$\frac{\partial}{\partial x^{\beta}} \left(\sqrt{g} \epsilon_{\tau\omega} \, \delta^{\tau}_{\kappa} \, g^{\beta\omega} \epsilon^{\kappa\lambda} \, \frac{\partial \bar{x}^2}{\partial x^{\lambda}} \right) = 0.$$

The Kronecker delta tensor implies that the only contribution to the summation occurs when $\tau = \kappa$, so we have,

$$\epsilon_{\tau\omega} \, \delta^{\tau}_{\kappa} = \epsilon_{\kappa\omega}$$

which simplifies our coordinate derivative expression to

$$\frac{\partial}{\partial x^{\beta}} \left(\sqrt{g} \epsilon_{\kappa\omega} \, g^{\beta\omega} \epsilon^{\kappa\lambda} \, \frac{\partial \bar{x}^2}{\partial x^{\lambda}} \right) = 0.$$

Substituting the additional relation

$$\epsilon_{\kappa\omega} \epsilon^{\kappa\lambda} = \delta^{\lambda}_{\omega},$$

which can be verified by direct calculation, we have,

$$\frac{\partial}{\partial x^{\beta}} \left(\sqrt{g} \, \delta^{\lambda}_{\omega} \, g^{\beta\omega} \, \frac{\partial \bar{x}^2}{\partial x^{\lambda}} \right) = 0.$$

Finally, we again note that the Kronecker delta tensor implies that the only contribution to the sum occurs when $\omega = \lambda$, so we can write,

$$\delta^{\lambda}_{\omega} \, g^{\beta\omega} = g^{\beta\lambda}$$

and the coordinate derivative condition becomes

$$\frac{\partial}{\partial x^{\beta}} \left(\sqrt{g} \, g^{\beta\lambda} \, \frac{\partial \bar{x}^2}{\partial x^{\lambda}} \right) = 0. \tag{151}$$

We can arrive at a similar equation for $\bar{x}^1$. If we solve Equation 149 for $\frac{\partial \bar{x}^2}{\partial x^{\alpha}}$ to give

$$\frac{\partial \bar{x}^2}{\partial x^{\alpha}} = -g_{\alpha\kappa} \epsilon^{\kappa\lambda} \, \frac{\partial \bar{x}^1}{\partial x^{\lambda}}, \tag{152}$$

substitute these relations into the second of Equations 150, and follow an analogous process to eliminate the tensor densities, we arrive at the relation,

$$\frac{\partial}{\partial x^\beta}\left(\sqrt{g}\, g^{\beta\lambda}\, \frac{\partial \bar{x}^1}{\partial x^\lambda}\right) = 0. \tag{153}$$

If we apply the convention of using commas to denote partial differentiation, Equations 151 and 153 can be written more compactly as

$$\begin{aligned} \left(\sqrt{g}\, g^{\beta\lambda}\, \bar{x}^1{}_{,\lambda}\right)_{,\beta} &= 0 \\ \left(\sqrt{g}\, g^{\beta\lambda}\, \bar{x}^2{}_{,\lambda}\right)_{,\beta} &= 0 \end{aligned} \tag{154}$$

These expressions can be recognized immediately as Laplace equations for the scalar values $\bar{x}^1$ and $\bar{x}^2$ that represent the coordinates of the isothermal reference frame.

In our derivation, we imply that these Laplace equations are expressed in terms of the metric tensor and the coordinates of the originally given x^α frame in which the compressible flow boundary value problem is given; however, the resulting equations are valid tensor equations and are therefore coordinate system independent. We can therefore generalize the problem and recognize that isothermal coordinates can be obtained by starting from *any arbitrary coordinate system*, say $\tilde{x}^\alpha$, by solving the Laplace equations,

$$\begin{aligned} \frac{\partial}{\partial \tilde{x}^\beta}\left(\sqrt{\tilde{g}}\, \tilde{g}^{\beta\lambda}\, \frac{\partial \bar{x}^1}{\partial \tilde{x}^\lambda}\right) &= 0 \\ \frac{\partial}{\partial \tilde{x}^\beta}\left(\sqrt{\tilde{g}}\, \tilde{g}^{\beta\lambda}\, \frac{\partial \bar{x}^2}{\partial \tilde{x}^\lambda}\right) &= 0 \end{aligned} \tag{155}$$

or equivalently, with commas representing partial differentiation with respect to the $\tilde{x}^\alpha$ system,

$$\begin{aligned} \left(\sqrt{\tilde{g}}\, \tilde{g}^{\beta\lambda}\, \bar{x}^1{}_{,\lambda}\right)_{,\beta} &= 0 \\ \left(\sqrt{\tilde{g}}\, \tilde{g}^{\beta\lambda}\, \bar{x}^2{}_{,\lambda}\right)_{,\beta} &= 0. \end{aligned} \tag{156}$$

This invariance will prove to be especially important in the numerical implementation of this isothermal coordinate mapping procedure, as we shall choose the system $\tilde{x}^\alpha$ as an auxiliary computational frame.

So far, we have established a series of partial differential equations that link any given set of coordinates to the desired isothermal coordinate system. In the isothermal system, the

equivalent incompressible flow is governed by the Cartesian form of the Laplace equation which is especially simple to solve numerically. The next task is to determine how to solve these partial differential equations to actually produce the isothermal system. Once we have the solutions, we will be able to relate coordinates in the x^α frame where the compressible flow is given to the $\bar{x}^\alpha$ isothermal frame where the incompressible flow is easy to solve. Additionally, the solutions for the coordinate mapping will provide the information necessary to relate all flow properties between the two frames.

In order to solve the partial differential equations, we must specify boundary conditions on the coordinate mapping. To do this, we must first determine the edges of the domain along which we must provide boundary conditions. This question is largely a function of the *classification* or *type* of the partial differential equations for the coordinate transformation. Hyperbolic and parabolic equations require conditions only along certain particular boundaries or portions of boundaries, whereas elliptic equations require conditions on all surfaces or edges defining the border of the domain.

Evidence points toward the conclusion that our mapping equations are elliptic in character. We have noted that Equations 154 are identical in form to the coordinate independent form of the Laplace equation, and the Laplace equation is the prototypical elliptic equation. Also, we have restricted our interest to subsonic flows. The potential equation for purely subsonic flows is uniformly elliptic. The metric expression $\sqrt{g}g^{\nu\mu}$ which defines the nature of our mapping equation is a function of these subsonic velocities and flow properties, so we may expect that these "forcing functions" on the mapping will cause it also to be elliptic. Before we make this conclusion, however, it will be reassuring to mathematically verify the type of the mapping equations.

A partial differential equation of the form

$$A\frac{\partial^2 w}{\partial x^1 \partial x^1} + B\frac{\partial^2 w}{\partial x^1 \partial x^2} + C\frac{\partial^2 w}{\partial x^2 \partial x^2} + D\frac{\partial w}{\partial x^1} + E\frac{\partial w}{\partial x^2} + Fw = G \tag{157}$$

is classified based on the value of the quantity $B^2 - 4AC$ which is known as the *discriminant*. The equation is hyperbolic if the discriminant is positive, parabolic if the discriminant equals zero, and elliptic if the discriminant is negative [38]. Expanding Equation 153, grouping

terms, and noting the symmetry $g^{21} = g^{12}$ gives,

$$\begin{aligned}
&\sqrt{g}\, g^{11} \frac{\partial^2 \bar{x}^1}{\partial x^1 \partial x^1} + 2\sqrt{g}\, g^{12} \frac{\partial^2 \bar{x}^1}{\partial x^1 \partial x^2} + \sqrt{g}\, g^{22} \frac{\partial^2 \bar{x}^1}{\partial x^2 \partial x^2} \\
&+ \left[\frac{\partial \left(\sqrt{g}\, g^{11} \right)}{\partial x^1} + \frac{\partial \left(\sqrt{g}\, g^{12} \right)}{\partial x^2} \right] \frac{\partial \bar{x}^1}{\partial x^1} + \left[\frac{\partial \left(\sqrt{g}\, g^{12} \right)}{\partial x^1} + \frac{\partial \left(\sqrt{g}\, g^{22} \right)}{\partial x^2} \right] \frac{\partial \bar{x}^1}{\partial x^2} = 0
\end{aligned} \tag{158}$$

which can be related to the form of Equation 157 by identifying

$$\begin{aligned}
w &= \bar{x}^1 \\
A &= \sqrt{g}\, g^{11} \\
B &= 2\sqrt{g}\, g^{12} \\
C &= \sqrt{g}\, g^{22} \\
D &= \left[\frac{\partial \left(\sqrt{g}\, g^{11} \right)}{\partial x^1} + \frac{\partial \left(\sqrt{g}\, g^{12} \right)}{\partial x^2} \right] \\
E &= \left[\frac{\partial \left(\sqrt{g}\, g^{12} \right)}{\partial x^1} + \frac{\partial \left(\sqrt{g}\, g^{22} \right)}{\partial x^2} \right] \\
F &= 0 \\
G &= 0.
\end{aligned}$$

Based on this identification, the discriminant is given by,

$$\begin{aligned}
B^2 - 4AC &= \left(2\sqrt{g}\, g^{12} \right)^2 - 4 \left(\sqrt{g}\, g^{11} \right) \left(\sqrt{g}\, g^{22} \right) \\
&= 4g \left[\left(g^{12} \right)^2 - \left(g^{11} \right) \left(g^{22} \right) \right] \\
&= 4g \left[-\frac{1}{g} \right] \\
&= -4.
\end{aligned} \tag{159}$$

Since the discriminant is a negative constant, this result confirms the expectation that the mapping equation for $\bar{x}^1$ is always elliptic. Following an exactly analogous process for the equation for $\bar{x}^2$ gives the same result, indicating that it too is elliptic.

Because the discriminant does not depend on the flow properties, the mapping equations will remain elliptic even when the flow equations change type at sonic and supersonic Mach numbers. Although the mapping equations do not change type with the change in type of the flow, it is important to recognize that the mapping solution cannot be expected to be valid when the freestream Mach number of the flow is supercritical. This expectation emerges from the well–known result from the theory of partial differential equations that the

type of an equation cannot be changed by an allowable coordinate transformation [38]. We have obtained Laplace's equation, which is always elliptic, by a coordinate transformation to an isothermal frame, so we cannot expect to obtain a correct mapping when the flow equations for the compressible flow become locally or globally parabolic or hyperbolic above the critical Mach number.

Since the mapping equations are elliptic, the problem requires that conditions be prescribed on all boundaries surrounding the domain of the flow. The next task is to determine the spatial locations of these boundaries enclosing the domain.

In the typical external aerodynamic problem in two dimensions, the internal boundary coincides with the surface of one or several airfoils or other bodies, and the true physical external boundary is prescribed at an infinite distance from the immersed bodies. Since the coordinate mapping is to be a function of the flow, we can require that the domain of the mapping correspond to the domain of the flow solution, at least in an approximative sense. This consideration implies that the inner boundary for the coordinate mapping should be taken as the boundary including the immersed bodies. The external boundary, however, deserves additional attention.

Some clarity regarding the exterior boundary can be obtained by considering how it is typically handled in flow solutions. In the case of boundary element methods for incompressible flows, a typical solution method is to choose singularity elements along the airfoil surface that each satisfy the governing equations and then to create a weighted sum of these elemental solutions that satisfies the boundary conditions. It is often possible to choose singularity elements such that the solution satisfies the infinity condition automatically; therefore, only the inner boundary conditions need to be prescribed in these cases.

For compressible flows, however, a typical approach is to consider a discretized domain of finite extent. This need arises from the fact that compressible flows are fundamentally nonlinear. Singularity solutions to compressible flows oriented along an airfoil surface cannot, in general, be superimposed such that their sum still satisfies the field equations for the fluid motion. Excepting some techniques such as the field panel method, the difficultly of nonlinearity is often addressed by solving the field equations for compressible flow through

finite difference or finite volume approaches. These approaches require that the domain be discretized into a grid of small volume elements and that the field equations be solved at all nodes or cell centers of this grid. Because this entire grid must be solved, it is clearly impossible to locate the outer boundary at a truly infinite distance from the body or bodies comprising the inner boundary.

The approach taken is therefore to locate the outer boundary at a distance far enough removed from the inner airfoil boundary such that the strengths of the disturbances in its vicinity are very small. For flows over single airfoils, this distance from the inner boundary is measured as several, say three to ten, airfoil chord lengths. It is likely that larger distances must be chosen for flows with higher Mach numbers because disturbances persist at greater distances from the airfoil as Mach number increases [54].

In the case of the coordinate mapping problem we are now examining, the field equations depend nonlinearly on the flow solution, and we shall choose to implement their solution through a finite difference approach. Therefore, we shall locate an outer boundary at a finite distance from the airfoil and enforce the appropriate boundary conditions there.

A relevant question is whether this outer boundary for the coordinate mapping must coincide with our outer boundary for the flow solution, that is, whether it must approximate an "infinity" boundary condition. If it were not necessary for this boundary to form an infinity condition, it may be possible to set its location arbitrarily close to the immersed body or bodies and perhaps even infinitesimally close. If the boundary could be set in this way, the the solution of the boundary value problem could potentially be dramatically simplified.

There appears to be no physical reason for the outer boundary to enforce an infinity condition insofar as the field equations for the flow are concerned, as their effects are completely encapsulated within the metric tensor driving the coordinate mapping. However, we will see that locating the outer boundary far enough away such that it can be considered an infinity condition will have several advantages. In particular, it will allow us to consider the coordinate mapping derivatives far from the airfoil as constants whose value we can easily determine. The knowledge of these constants will be particularly useful in determining the

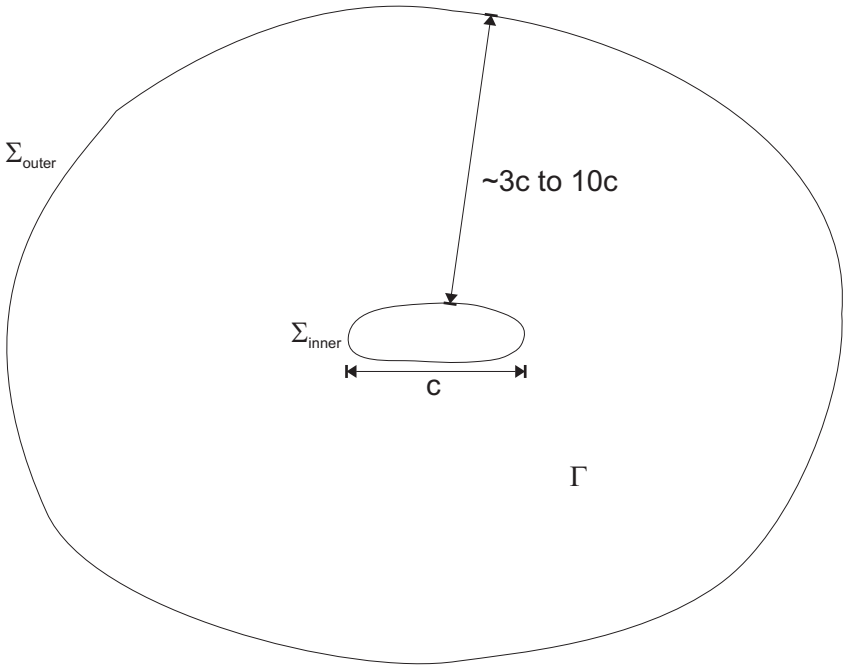

Figure 6: Boundaries (Σ) and Domain (Γ) for the Coordinate Mapping and Flow Solution

manner in which parameters of the freestream flow such as the angle of attack transform under the coordinate mapping. For this reason, we shall locate the outer boundary such that it approximates a boundary at infinity, and we can view this boundary to correspond approximately to the location at which the infinity conditions on the flow boundary value problem are given. That is, the boundary location will be chosen such that it is far enough away from the body that the local perturbations of the flow from freestream conditions are vanishingly weak. As discussed above, a typical approach in finite difference flow solutions is to locate the far field boundary from three to ten body chord lengths from an immersed airfoil. We shall therefore adopt this general range for the coordinate boundary. A depiction of the domain and boundaries that we shall model is provided by Figure 6. As indicated in the figure, we shall refer to the domain as Γ and the boundary as Σ.

At this point, we have determined the need for an inner boundary corresponding to a curve containing the immersed airfoil(s) and a finite outer boundary that approximates a boundary at infinity. We are now at the point of determining the actual conditions on the coordinate transformation that must be prescribed on both of these boundaries.

For the case of the flow boundary value problem, the boundary conditions are dictated by physics. At the surface of a closed airfoil, the flow must be tangent to the surface (except in the rare case that the design incorporates orifices for the injection of a secondary flow or bleed of the primary flow). The tangency condition simply states that flow is not allowed to pass through the airfoil surface. At the far field boundary at infinity, the flow perturbations must vanish such that the freestream flow is obtained. These conditions are therefore precisely the ones needed to describe how the airfoil and far field will physically influence the field equations to produce the flow solution.

For the coordinate transformation, however, there appears to be no particular physical requirements on the specific nature of the boundary conditions. Indeed, there appears to be wide freedom available in selecting these conditions, with restrictions stemming perhaps only from certain mathematical considerations such as continuity and smoothness. In general, we could require either *Dirichlet* conditions of the type

$$\bar{x}^1 \big|_\Sigma = l^1 \left[\left(x^1, x^2\right) \big|_\Sigma \right], \quad \bar{x}^2 \big|_\Sigma = l^2 \left[\left(x^1, x^2\right) \big|_\Sigma \right]$$

or *Neumann* conditions of the type

$$\left(A^\alpha \frac{\partial \bar{x}^1}{\partial x^\alpha} \right) \Big|_\Sigma = m^1 \left[\left(x^1, x^2\right) \big|_\Sigma \right], \quad \left(A^\alpha \frac{\partial \bar{x}^2}{\partial x^\alpha} \right) \Big|_\Sigma = m^2 \left[\left(x^1, x^2\right) \big|_\Sigma \right]$$

where l^1, l^2, m^1, and m^2 are functions given along the boundary curves and A^α is the vector whose inner product with the coordinate derivatives produces the derivative in the normal direction from the boundary. In addition to these typical forms, other *mixed* boundary conditions such as *Cauchy* and *Robin* conditions which represent weighted averages of Dirichlet and Neumann conditions could be chosen.

Although we have substantial freedom in specifying the boundary conditions, what is clear, however, is that we are allowed to choose the boundary condition on precisely *one* of the coordinates in the barred frame. That is, we can specify Dirichlet, Neumann, or mixed conditions on *either* $\bar{x}^1$ *or* $\bar{x}^2$ but *not both* coordinates. Once we specify boundary conditions for one of the isothermal coordinates, we can solve the boundary value problem to obtain the coordinate and its derivatives at all points on the boundary and within the domain. This information can then be used to uniquely determine the other coordinate

throughout the field. If we were to try to specify boundary conditions on both isothermal coordinates *arbitrarily*, we would overspecify the problem.

The reason for this interrelationship stems from the generalized Cauchy–Riemann conditions given by Equations 149. To illustrate the situation, let us imagine that we specify boundary conditions on $\bar{x}^1$. With these conditions known, we now have all of the information needed to solve for $\bar{x}^1$ as well as $\frac{\partial \bar{x}^1}{\partial x^\alpha}$ on both the interior of the domain Γ and the boundary Σ. Once the derivatives $\frac{\partial \bar{x}^1}{\partial x^\alpha}$ are known, we must require that they relate to the derivatives $\frac{\partial \bar{x}^2}{\partial x^\beta}$ as required by Equations 149. This restriction will yield unique values for all of the derivatives $\frac{\partial \bar{x}^2}{\partial x^\beta}$ in Γ and on Σ. With these derivatives, the entire coordinate field $\bar{x}^2$ could be obtained by simple integration once a single point such as an origin to the coordinates is given. The values for $\bar{x}^2$ are therefore uniquely determined from the boundary value problem for $\bar{x}^1$. For this reason, it is clear that we could not also specify arbitrary boundary conditions on $\bar{x}^2$, as *arbitrary* conditions would conflict with the values obtained through solving the boundary value problem for $\bar{x}^1$, and the problem would be overdetermined.

Although we cannot specify *arbitrary* conditions on the second coordinate, we could specify *compatible* boundary conditions that respect the generalized Cauchy–Riemann equations along the boundaries. As we shall discuss in Chapter 5, this complementary boundary condition is taken in the numerical implementation developed in this research. This approach is chosen compared to the direct integration from known partial derivatives because it provides for smoother coordinate curves for a given grid resolution.

As a means of illustrating the coordinate interdependence implied by the generalized Cauchy–Riemann equations, we can look to the more familiar situation of the boundary value problem for a two dimensional incompressible potential flow. We can choose to solve the flow either by solving a boundary value problem for the potential function, ϕ, or the stream function, ψ. If we pose the problem in terms of the potential function, the airfoil tangency condition requires that we impose the Neumann condition $\frac{\partial \phi}{\partial n} = 0$ where n corresponds to the direction normal to the airfoil surface. Solving the flow gives values for ϕ and its first derivatives. Alternately, we could pose the problem in terms of the stream

function ψ and impose the condition that the airfoil surface is a streamline of the flow. Values of ψ along streamlines are constant, so we could take $\psi = c$ with c a constant as the airfoil boundary condition. The key point is that once we solve for either ϕ or ψ through one of these formulations, we will also obtain the value for the other at all points on the boundary and within the domain. As for the coordinate mapping, this result stems from the Cauchy–Riemann conditions that connect the derivatives of ϕ and ψ:

$$\begin{aligned} \frac{\partial \phi}{\partial x} &= \frac{\partial \psi}{\partial y} \\ \frac{\partial \phi}{\partial y} &= -\frac{\partial \psi}{\partial x}. \end{aligned}$$

The similarity between a flow solution determined by ϕ and ψ and our coordinate transformation is even deeper still, as it is possible to think of ψ as a set of coordinates aligned in the streamline direction of a flow and ϕ as a set of orthogonal trajectories to these streamlines. The orthogonal net formed by ϕ and ψ is enough to uniquely determine points in the flowfield, at least for flows without circulation. This perspective puts the solution of two-dimensional potential flows on the same mathematical footing as the boundary value problem for coordinate mappings.

Having found that we can specify boundary conditions on one of the isothermal coordinates arbitrarily, we can now choose the conditions. The most appropriate candidates seem to be Dirichlet conditions requiring equivalence of one of the isothermal coordinates to its counterpart in the originally given frame. For instance, we could require either,

$$\bar{x}^1 \big|_\Sigma = x^1 \big|_\Sigma \tag{160}$$

or

$$\bar{x}^2 \big|_\Sigma = x^2 \big|_\Sigma . \tag{161}$$

The advantage of these types of formulations is that they allow simple comparisons of the airfoil and outer boundary shapes between the original compressible frame and the equivalent canonical Laplacian frame. For instance, if we align an immersed airfoil such that its chord is oriented along the x^1 direction, the condition $\bar{x}^1 \big|_\Sigma = x^1 \big|_\Sigma$ will cause the chords

of the originally given airfoil and the transformed airfoil to coincide. The transformation will therefore affect primarily the thickness and camber of the airfoil.

These Dirichlet conditions also have particularly nice equivalents in the case of linearized transformations. In the linearized case, the boundary value problem reduces to a simple uniform affine stretching in one coordinate direction. That is, conditions such as $\bar{x}^1 = x^1$ hold not only along the boundary, but also within the domain. The various forms of the Prandtl–Glauert and Göthert rules prescribe different variants of affine stretching to produce the same effect, up to the precision available in the linear approximation. For instance, one form employs $\bar{x}^1 = x^1$, whereas another form specifies $\bar{x}^2 = x^2$ [103, 70].

In the cases examined in the results chapter of this dissertation, we shall employ the boundary condition provided by Equation 160 exclusively.

In this section, we have determined the precise nature of a separate boundary value problem that we can solve in order to obtain the isothermal coordinate system $\bar{x}^\alpha$ in which the canonical form of the Laplace equation governs the fluid flow. In this coordinate system, the flow can be solved as if it were incompressible. We first found two partial differential equations that simultaneously satisfy the integrability conditions and also obey the generalized Cauchy–Riemann equations. Next, we determined that these equations are of the elliptic type, and therefore, that they require boundary conditions to be specified along curves both interior and exterior to the solution domain. The interior boundary was identified to coincide with a curve containing the airfoil(s) or other immersed bodies, and the exterior boundary was identified with a curve in the far field intended to approximate a boundary condition at infinity. We next found that we must specify boundary conditions on precisely *one* of the isothermal coordinates, with the other boundary condition found through the generalized Cauchy–Riemann relations. Finally, we identified Dirichlet conditions equating one of the isothermal coordinates to its corresponding coordinate in the compressible flow frame along the boundary as particularly attractive for enabling comparisons between shapes in the original and transformed frames. In the subsequent implementation, the condition $\bar{x}^1 \big|_\Sigma = x^1 \big|_\Sigma$ will be used exclusively. With the partial

differential equations, boundary locations, and boundary conditions determined in this section, the coordinate transformation can be determined by a numerical method capable of solving elliptic boundary value problems. Such a method will be developed in Chapter 5 of this dissertation.

The boundary value problem that has been outlined in this section is of similar difficulty as the original boundary value problem for the compressible flow itself. This difficulty stems from the nonlinear nature of the forcing functions $\sqrt{g}g^{\nu\mu}$ that depend on the flow solution and appear in the partial differential equations governing the mapping. The primary difficulty that introduces the complexity of the problem is the enforcement of the integrability conditions for the mapping. A dramatic simplification of the coordinate transformation could be obtained if the integrability condition could somehow be satisfied *as a consequence of the flow solution*. We investigate the possibility of this approach in the next section.

4.3.3 Integrability as a Consequence of the Flow Solution

In order to obtain integrability of the coordinate transformation as a consequence of the flow solution, the transformation derivatives must be functions of the flow that satisfy the coordinate integrability conditions of Equations 151 and 153 automatically. In other words, we seek a situation in which substitution of the derivatives $\frac{\partial \bar{x}^\mu}{\partial x^\nu}$ into these integrability conditions solves them trivially, and we are no longer required to solve them through the specification of boundary conditions and integration.

One possible approach towards this end is revealed if we set the transformation derivatives to the values

$$\begin{aligned}
\frac{\partial \bar{x}^1}{\partial x^1} &= u_1 \\
\frac{\partial \bar{x}^1}{\partial x^2} &= u_2 \\
\frac{\partial \bar{x}^2}{\partial x^1} &= -\left(\frac{\rho}{\rho_0}\right) u_2 \\
\frac{\partial \bar{x}^2}{\partial x^2} &= \left(\frac{\rho}{\rho_0}\right) u_1
\end{aligned} \tag{162}$$

and introduce the metric tensor components given in Equation 129. With these substitutions, the integrability condition of Equation 153 takes on the simplified form,

$$\frac{\partial}{\partial x^1}\left[\left(\frac{\rho}{\rho_0}\right)u_1\right]+\frac{\partial}{\partial x^2}\left[\left(\frac{\rho}{\rho_0}\right)u_2\right]=0 \tag{163}$$

and the condition of Equation 151 becomes

$$\frac{\partial u_2}{\partial x^1}-\frac{\partial u_1}{\partial x^2}=0. \tag{164}$$

These equations are simply the continuity and irrotationality conditions, respectively, for the originally given subsonic compressible flow. Because these equations have emerged from a choice of the mapping, and we wish to enforce them to solve the compressible flow, we can think of this particular isothermal mapping as achieving integrability of the coordinate system as a consequence of the flow solution.

Through careful inspection of Equations 162, we recognize that these can be rewritten in terms of the potential, ϕ, and the stream function, ψ, as,

$$\begin{aligned}
\frac{\partial \bar{x}^1}{\partial x^1} &= \frac{\partial \phi}{\partial x^1}\\
\frac{\partial \bar{x}^1}{\partial x^2} &= \frac{\partial \phi}{\partial x^2}\\
\frac{\partial \bar{x}^2}{\partial x^1} &= \frac{\partial \psi}{\partial x^1}\\
\frac{\partial \bar{x}^2}{\partial x^2} &= \frac{\partial \psi}{\partial x^2}
\end{aligned} \tag{165}$$

from which it is clear that the isothermal coordinates are identical to potential/stream function coordinates with

$$\begin{aligned}
\bar{x}^1 &= \phi\\
\bar{x}^2 &= \psi.
\end{aligned} \tag{166}$$

This result indicates that one particular isothermal coordinate system that can be developed from the mapping corresponds to the mapping into stream function and potential coordinates. This mapping is precisely that which is solved by the flow solution itself.

The next task is to determine where this result takes us in terms of simplifying the flow or mapping solutions. To discover the answer, we consider that the purpose of our

application of an isothermal coordinate transformation is that it guarantees that the flow in the isothermal frame is governed by the canonical Laplace equation,

$$\frac{\partial}{\partial \bar{x}^1}\left(\frac{\partial \phi}{\partial \bar{x}^1}\right) + \frac{\partial}{\partial \bar{x}^2}\left(\frac{\partial \phi}{\partial \bar{x}^2}\right) = 0. \tag{167}$$

If we substitute the isothermal coordinates with their ϕ and ψ values, this equation becomes,

$$\frac{\partial}{\partial \phi}\left(\frac{\partial \phi}{\partial \phi}\right) + \frac{\partial}{\partial \psi}\left(\frac{\partial \phi}{\partial \psi}\right) = 0, \tag{168}$$

but the coordinate derivatives have the trivial values

$$\begin{aligned} \frac{\partial \phi}{\partial \phi} &= 1 \\ \frac{\partial \phi}{\partial \psi} &= 0 \end{aligned} \tag{169}$$

throughout the flow field. This result shows that the canonical Laplace equation for the equivalent incompressible flow is trivially and automatically satisfied, *as a consequence of the isothermal mapping*. Because it is trivially satisfied, we cannot specify boundary conditions and use the equation to solve the flow.

To recapitulate what has happened here, we chose a particular set of coordinate derivatives based on flow properties and noted that the integrability conditions for the mapping then became identical to the equations for the original compressible flow. Because we wish to solve the flow such that these equations are obeyed, we conclude that the coordinate derivatives that we chose do indeed represent an allowable integrable isothermal coordinate system. This system turned out to be a mapping into stream function and potential coordinates. We had originally hoped to solve an equivalent incompressible flow in its canonical Laplacian form in this coordinate system; however, we found that this equivalent flow was trivially satisfied as a consequence of the mapping. What has happened is that we have simply recast the flow problem as a mapping problem without obtaining any simplification—the governing continuity and irrotationality conditions for the original compressible flow given by Equations 163 and 164 must still be solved, but their interpretation is not as flow equations, but as mapping equations.

This result suggests that the particular choice of isothermal mapping indicated by Equations 162 does not help in solving our problem, even though we have attained the intended integrability for the coordinate system as a consequence of the flow solution. A relevant question is whether there exists other possible isothermal mappings that attain integrability from the flow solution and that do not produce the trivial result we have just discovered.

One possibility that appears promising but that has not been substantiated is to attempt to obtain a series solution by specifying the inverse coordinate mapping derivatives in the form,

$$\frac{\partial x^\mu}{\partial \bar{x}^\nu} = A^\mu_\nu + B^{\mu\alpha}_\nu \, \bar{u}_\alpha + C^{\mu\alpha\beta}_\nu \, \bar{u}_\alpha \, \bar{u}_\beta + \ldots \tag{170}$$

in which the tensors A^μ_ν, $B^{\mu\alpha}_\nu$, and $C^{\mu\alpha\beta}_\nu$ have constant elements. This form can be thought of as a Taylor series for the inverse coordinate derivatives in terms of the velocity components in the isothermal reference frame.

The coordinate integrability condition can be expressed in terms of these inverse derivatives in tensor form as,

$$\epsilon^{\tau\nu} \frac{\partial}{\partial \bar{x}^\tau} \left(\frac{\partial x^\mu}{\partial \bar{x}^\nu} \right) = 0 \tag{171}$$

where $\epsilon^{\tau\nu}$ is again the permutation pseudotensor with elements $\epsilon^{11} = 0$, $\epsilon^{12} = 1/\sqrt{\overline{g}}$, $\epsilon^{21} = -1/\sqrt{\overline{g}}$, and $\epsilon^{22} = 0$. Truncating the series in Equation 170 to terms only up to first order in the velocities, this integrability condition requires,

$$\epsilon^{\tau\nu} \, B^{\mu\alpha}_\nu \, \bar{u}_{\alpha,\,\tau} = 0. \tag{172}$$

We now make the decisive step of identifying this integrability condition with conditions on the flow. In the isothermal coordinate system, the Laplace equation holds in its Cartesian form. Therefore, we can write the flow equations in tensor form as,

$$\begin{aligned} \delta^{\alpha\tau} \, \bar{u}_{\alpha,\,\tau} &= 0 \\ \epsilon^{\alpha\tau} \, \bar{u}_{\alpha,\,\tau} &= 0 \end{aligned} \tag{173}$$

where the first equation is continuity and the second is irrotationality. Comparing Equations 173 with Equation 172 shows that we can satisfy the coordinate integrability condition

from the flow equations if we set

$$\sqrt{\bar{g}}\epsilon^{\tau\nu}B^{\mu\alpha}_{\nu} = K^{\mu}\delta^{\alpha\tau} + L^{\mu}\sqrt{\bar{g}}\epsilon^{\alpha\tau} \tag{174}$$

where K^{μ} and L^{μ} are contravariant vectors of constants and we have included the $\sqrt{\bar{g}}$ to make the expressions involving the permutation pseudotensor become constants. A similar process for achieving integrability automatically in this way can be carried out for higher order terms in the series expansion by employing the chain rule to recognize the implications of the continuity and irrotationality conditions on derivatives such as $(\bar{u}_{\alpha}\bar{u}_{\beta})_{,\tau}$ that appear in taking the integrability derivatives.

If the values of the tensor $B^{\mu\alpha}_{\nu}$ can be chosen to satisfy the form of Equation 174, then the transformation will satisfy coordinate integrability up to first order in the velocity components. With integrability achieved, the only remaining requirement is to satisfy the generalized Cauchy–Riemann equations given by Equation 149. The components of $B^{\mu\alpha}_{\nu}$ must now be set to satisfy approximately these equations based on the metric tensor components given by Equations 129, with the restriction that the resulting form of $B^{\mu\alpha}_{\nu}$ satisfies Equation 174. Satisfying the generalized Cauchy–Riemann equations in this way requires the expansion of the metric tensor components in similar series expansions of the velocity components. If $B^{\mu\alpha}_{\nu}$ can be chosen to consistently satisfy these requirements, then the isothermal coordinate mapping will be specified up to first order in these components.

This process has been attempted, but the intricacies and tedium of the method have heretofore precluded a complete analysis from being achieved. The method appears promising, but it must be noted that even if successful, it could attain only an approximative mapping solution. However, the great advantage of the method, if successful, is that it would obviate the need for solving a separate boundary value problem for the coordinate mapping. This would allow the flow to be solved iteratively as an incompressible flow in the isothermal frame. Although promising, we will not further investigate this method in the present work. We will instead pursue a mapping approach that achieves integrability through a separate boundary value problem as described in the previous section.

4.4 Relating the Compressible and Canonical Laplacian Flows

Summarizing the results obtained so far in this chapter, we have derived the tensorial covariant forms of the governing equations of fluid motion, embedded the phenomenon of compressibility into the metric tensor of an equivalent incompressible flow, and established the boundary value problem for a mapping to coordinates in which the flow problem takes on the canonical form of the Laplace equation. The flow solution that is obtained in this special coordinate system is kinematically equivalent to an incompressible flow described in Cartesian coordinates; that is, the velocities match those obtained in the solution of a Cartesian incompressible flow. This kinematical equivalence does not imply that the flow described in the isothermal frame is actually incompressible. Rather, we term it an "equivalent incompressible flow" only because it possesses the same governing equations for the flow kinematics. The point properties including the thermodynamic variables such as density and pressure do not necessarily match those of an incompressible flow.

In order that we can determine these point properties and other parameters correctly, the next question is how this equivalent incompressible flow relates to the originally given subsonic compressible flow. In particular, we need to know how the boundary conditions of flow tangency in the originally given frame transform to the new isothermal system, how flow scalars transform, how the velocities are related, and how the angle of attack of the airfoil is changed. Determining these relationships is the focus of this section.

4.4.1 Boundary Conditions

In the development of the theory presented in this chapter, the focus has been on determining a canonical Laplacian flow corresponding to a given compressible flow. This compressible flow lives in coordinate frame x^α. In this frame, the compressible continuity, momentum, and state equations hold, and we presume that the location and shape of one or several airfoils or other bodies are given. In order to completely specify the flow in frame x^α, we must also impose boundary conditions.

Boundary conditions are critically important. They are the only mechanism through which the governing equations sense the presence of tangible objects such as airfoils as

well as transfers of mass, momentum, or energy across the perimeter of the flow domain. In particular, they provide the mathematical linkage of the specific geometric shaping of the boundaries to the flow solution. For instance, it is boundary conditions that demark the difference between exterior flow problems with airfoils immersed in a free stream and internal flows within walled channels. In other words, it is largely the boundary conditions that distinguish one flow from another.

As a general rule, boundary conditions are required on each partial differential equation for the flow that must be solved within the domain. In the case of the Euler or Navier–Stokes equations, there are one continuity equation, k momentum equations, and one energy equation, where k is the dimension of the space. For two dimensional flows, there are therefore four partial differential equations that must hold throughout the domain, and we must correspondingly supply four boundary conditions. These boundary conditions are often posed in terms of specifications on the behavior of the density, the momentum components in each coordinate direction, and the energy along the boundary curves or surfaces.

For the case of potential flows, however, the boundary conditions are dramatically simplified. This simplification occurs because these flows require the solution of only a single partial differential equation for the potential, ϕ. We must therefore prescribe only one condition along the appropriate domain boundaries. Because the focus of this work is on subsonic flows, the potential equation in the originally given x^α reference frame is always elliptic. As in the case with the coordinate mapping, we must therefore apply boundary conditions on an interior boundary comprised of the airfoil(s) and an exterior boundary completely surrounding the domain.

The typical condition at the interior boundary prescribes flow tangency to the body surface. We may state this alternately as a condition that there is no velocity component in the direction normal to the surface. This requirement is a manifestation of the physical reality that flow does not penetrate a solid closed body. In terms of the potential, this condition takes the form,

$$\frac{\partial \phi}{\partial n} = 0$$

where n describes the direction normal to the body surface. This statement is therefore a Neumann boundary condition on the potential.

The tangency condition is usually framed mathematically by requiring the inner product of the velocity vector with a normal vector drawn from the surface to be zero, i.e.,

$$\vec{u} \cdot \vec{n} = 0$$

where $\vec{u}$ is the velocity vector and $\vec{n}$ is a normal vector. As we saw in Chapter 2, we can express this inner product in classical Riemannian tensor notation as

$$h^{\alpha\beta} u_\alpha n_\beta = 0 \tag{175}$$

where $h^{\alpha\beta}$ is the metric tensor corresponding to coordinate system x^α in which the compressible flow is given, u_α is the covariant velocity vector in this frame, and n_β is a covariant vector oriented normal to the airfoil surface.

This equation is written in tensor covariant form, so it is valid in all gauges and coordinate systems if we simply replace the metric tensor and covariant vectors with their equivalents in the new gauge or coordinate frame. We can therefore examine how the boundary condition transforms under the gauge transformation and the isothermal coordinate mapping simply by describing how the metric and covariant vectors are altered. In the gauge transformation, we geometrized the effects of compressibility by embedding the varying density into a new metric tensor while keeping the coordinates fixed. We also required that the covariant velocity be invariant in defining the transformation. As a result of this requirement, all other covariant vectors will also be invariant in the transformation [42]. For instance, vectors u_α and n_β are the same as in the original gauge in which the compressible flow boundary value problem is given. Considering this transformation behavior, the tangency boundary condition expressed by Equation 175 becomes in the new gauge,

$$g^{\alpha\beta} u_\alpha n_\beta = 0 \tag{176}$$

where $g^{\alpha\beta}$ is the metric tensor that we derived in Section 4.2.

Following the gauge transformation, we described a curvilinear coordinate transformation that produced a mapping to the isothermal coordinate system $\bar{x}^\alpha$. In this transformation, both the metric tensor and the covariant vectors transform nontrivially. Denoting the new metric tensor and covariant vectors with overbars, Equation 176 becomes,

$$\bar{g}^{\alpha\beta}\bar{u}_\alpha\bar{n}_\beta = 0. \tag{177}$$

The isothermal coordinate frame is special because its metric tensor is conformal to the Cartesian metric. As we saw in Section 4.2, we can write the covariant metric tensor in the isothermal frame as,

$$\bar{g}_{\alpha\beta} = \Omega\,\delta_{\alpha\beta} \tag{178}$$

and the corresponding contravariant metric tensor as

$$\bar{g}^{\alpha\beta} = 1/\Omega\,\delta^{\alpha\beta}. \tag{179}$$

Substituting Equation 179 into the boundary condition given by Equation 177 and multiplying through by Ω therefore gives,

$$\delta^{\alpha\beta}\bar{u}_\alpha\bar{n}_\beta = 0 \tag{180}$$

which is the desired tangency boundary condition expressed in the isothermal coordinate frame in which the flow obeys the Cartesian Laplace equation.

The result expressed by Equation 180 is significant. It indicates that the flow in the isothermal frame acts identically to an incompressible flow with tangency boundary conditions over a solid body in a Cartesian coordinate system. We chose to map to an isothermal frame precisely because the mapping causes the potential equation for the flow to take on the Cartesian form of the Laplace equation (the descriptor of incompressible potential flows), and Equation 180 indicates that the boundary conditions also look exactly as they would for flow tangency in a Cartesian system. This result has an immediate practical implication: because the boundary value problem for the equivalent incompressible flow looks exactly the same as the typical flow tangency case, we can use any available incompressible flow solver without modification to determine the flow in this reference frame. We shall

take precisely this approach in developing a numerical technique to implement this theory in Chapter 5.

Although the boundary conditions in the isothermal system look very similar to those prescribed in the original compressible flow frame, it is important to note that the *shape of the boundary* comprising the airfoil described by the coordinates $\bar{x}^\alpha$ of this Cartesian-like system differs from the shape of the originally given airfoil in terms of the coordinates x^α of the compressible flow. The shape itself is dictated by the coordinate transformation, which is a function of the varying density throughout the flowfield.

The transformation behavior of this boundary condition stems from the fact that the metric in the isothermal frame is conformal to the Cartesian metric. Because the right hand side of Equation 180 is zero, any nonzero conformal factor defined by Ω divides through the equation and hence has no impact on the boundary condition. Interestingly, however, this transformation behavior may change in the presence of a boundary condition that allows transpiration of flow across the airfoil surface. In such a situation, the right hand side of Equation 180 would be nonzero such that the factor involving Ω would not divide out. Its presence would apparently indicate an effect on the scaling of the mass flux across the surface. Although this represents an interesting phenomenon, we shall not investigate these types of boundary conditions in this dissertation.

Now that we have addressed the transformation of the boundary conditions at the interior of the domain, we can proceed to examine the situation at the outer boundary. In this work, we shall limit our interest to the external aerodynamic problem for flows with an outer boundary at infinity (or a finite approximation thereof). The boundary condition in terms of the potential for subsonic full potential flow is typically taken to be a function of the circulation around the airfoil of the form

$$\hat{\phi} = \frac{\Gamma}{2\pi} \arctan\left(\sqrt{1 - M_\infty^2}\, \frac{y}{x}\right) \tag{181}$$

where $\hat{\phi}$ is the perturbation potential and $x = x^1$ and $y = x^2$ are the signed coordinate distances in the x^α frame from any particular boundary point to a discrete vortex with strength Γ located along the airfoil chord line [96]. In the case of nonlifting flows without

circulation, Γ vanishes and the condition reduces to $\hat{\phi} = 0$ along the far-field boundary. Equation 181 can be shown to satisfy

$$\left(1 - M_\infty^2\right) \frac{\partial^2 \hat{\phi}}{\partial x^2} + \frac{\partial^2 \hat{\phi}}{\partial y^2} = 0 \tag{182}$$

which is the linearized small perturbation potential equation of steady plane flow with the freestream oriented along the x-axis. The implication of this result is that Equation 182 is the correct limiting form of the full potential equation at an infinite distance from the body.

In the implementation pursued in this thesis, we shall solve the flow with a panel method employed in the isothermal reference frame in which the flow looks to be incompressible. Because of the logarithmic decay behavior of singularity solutions to the Laplace equation for plane flows, the typical far-field boundary conditions for the equivalent incompressible flow will automatically be satisfied, as long as the appropriate singularity elements are included in the panel method formulation. In particular, a doublet or vortex formulation is required to capture the circulation of a lifting flow. In the isothermal coordinates that describe this Laplacian flow, these far-field conditions take the form

$$\hat{\phi} = \frac{\Gamma}{2\pi} \arctan \frac{\bar{y}}{\bar{x}} \tag{183}$$

where $\bar{x} = \bar{x}^1$ and $\bar{y} = \bar{x}^2$. This equation can be shown to satisfy the Laplace equation in the form

$$\frac{\partial^2 \hat{\phi}}{\partial \bar{x}^2} + \frac{\partial^2 \hat{\phi}}{\partial \bar{y}^2} = 0 \tag{184}$$

as expected.

The only question is therefore whether the boundary condition for the equivalent incompressible flow given by Equation 183 maps to the correct boundary condition for the subsonic flow given by Equation 181 under the coordinate transformation. Because Equation 181 satisfies the linear potential Equation 182 and Equation 183 satisfies the Laplace Equation 184, the boundary conditions are consistent as long as the mapping in the far field transforms Equation 182 into Equation 184. The transformation to achieve this result

is a form of the Prandtl–Glauert transformation. As we will see in Section 4.4.3, our coordinate mapping will indeed reduce to this linearized transformation in the far field, except that we will not restrict the freestream to lie along the x-axis as described here. With this appropriate far-field transformation, the boundary conditions for the subsonic flow will follow directly from the standard external flow boundary conditions that are satisfied automatically by the singularity solutions forming the panel method implementation.

4.4.2 Scalar Flow Parameters and the Velocity Vector

In order to relate the originally given subsonic flow to the canonical Laplacian flow, we will also need to understand how the flow parameters transform. By flow parameters, we mean the scalar thermodynamic point properties such as pressure and density as well as vectorial entities such as the velocity.

In Section 4.2, we indicated that the effect of the gauge transformation in developing an equivalent incompressible flow is to transfer the meaning of the fluid density from an independent physical entity of the flow to a property of the space in which the flow resides. This transfer of meaning was accomplished by absorbing the varying density into the metric tensor of the space. This perspective implies that the meaning of the density in the transformed space is intrinsically geometric and not physical.

For this reason, we shall adopt the policy of defining the density in the space and coordinate frame corresponding to the originally given compressible flow. Because density, pressure, and other thermodynamic parameters are scalar values, they are invariant under coordinate transformations, and we can carry over the values obtained in the compressible frame to the canonical Laplacian frame directly. This process indicates that even in the "equivalent incompressible flow," the true thermodynamic density varies from point to point, and it is for this reason that we must interpret our terminology to mean simply that the flow in the canonical Laplacian frame is only *kinematically* equivalent, i.e. its continuity equation matches that of an incompressible flow.

An alternative perspective from that taken here may be to treat the thermodynamic density as a *scalar density*. A scalar density is equivalent to a zeroth-order tensor density

in the parlance of tensor analysis. As we discussed in Section 4.3.1 in defining $\epsilon^{\mu\nu}$, tensor densities transform like tensors, except that they are multiplied by powers of the metric determinant g in the transformation. A scalar density is an entity that behaves like a scalar under coordinate transformations, except for multiplication by g raised to a nonzero power. Treating the thermodynamic density as a scalar density may yield a slightly enhanced picture of the physical–geometric connection, but based on the author's observations from the literature, it is unlikely to provide a more compelling description relative to the additional complexity it introduces. For this reason, we shall not pursue the scalar density approach in this work. A good resource illustrating the application of scalar and tensor densities to conformal gauge transformations of physical differential equations is described by Fulton [42].

We now return to the perspective of treating the density as being physically defined in the original compressible frame. As we saw in Section 4.1, the density in this frame is related to the velocity magnitude of the compressible flow through the density–velocity relation given in Equations 104. Therefore, we can determine the density from the flow solution obtained in the canonical Laplacian frame by simply transforming the velocity components to those in the compressible frame. Other thermodynamic variables such as pressure and temperature can then be determined using the isentropic relations provided in Equations 104.

The velocity components and the coordinates in the original compressible frame are the same as those obtained after the gauge transformation. Therefore, we need only to write down the transformation induced by the coordinate mapping from the isothermal coordinates $\bar{x}^\alpha$ to the original compressible flow coordinates x^α. If we know the velocity in the Laplacian frame and wish to determine it in the compressible frame, the transformation for the covariant velocity components is given by,

$$u_\mu = \bar{u}_\nu \frac{\partial \bar{x}^\nu}{\partial x^\mu}, \tag{185}$$

or, expanding the sums for our two–dimensional space, we obtain

$$\begin{aligned} u_1 &= \bar{u}_1 \frac{\partial \bar{x}^1}{\partial x^1} + \bar{u}_2 \frac{\partial \bar{x}^2}{\partial x^1} \\ u_2 &= \bar{u}_1 \frac{\partial \bar{x}^1}{\partial x^2} + \bar{u}_2 \frac{\partial \bar{x}^2}{\partial x^2}. \end{aligned} \tag{186}$$

Alternately, if we know the velocity in the compressible frame and wish to find it in the Laplacian frame, we can use the inverse transformation given by,

$$\bar{u}_\mu = u_\nu \frac{\partial x^\nu}{\partial \bar{x}^\mu}, \tag{187}$$

or, in terms of coordinates,

$$\begin{aligned} \bar{u}_1 &= u_1 \frac{\partial x^1}{\partial \bar{x}^1} + u_2 \frac{\partial x^2}{\partial \bar{x}^1} \\ \bar{u}_2 &= u_1 \frac{\partial x^1}{\partial \bar{x}^2} + u_2 \frac{\partial x^2}{\partial \bar{x}^2}. \end{aligned} \tag{188}$$

To determine the density, ρ, we employ the density–velocity relation of Equation 104, which we repeat here as,

$$\frac{\rho}{\rho_0} = \left(1 - \frac{\gamma - 1}{2\, {a_0}^2} V^2\right)^{1/(\gamma-1)} \tag{189}$$

where a_0 is the stagnation sound speed, ρ_0 is the stagnation density, γ is the ratio of specific heats, and V is the velocity magnitude in the originally given coordinate system of the compressible flow. We can obtain V from the velocity components as,

$$V^2 = h^{\mu\nu} u_\mu u_\nu \tag{190}$$

where $h^{\mu\nu}$ is the contravariant metric tensor in the original coordinate system. Once ρ is known, we can determine the pressure as,

$$\frac{p}{p_0} = \left(\frac{\rho}{\rho_0}\right)^\gamma \tag{191}$$

and the temperature as,

$$\frac{T}{T_0} = \left(\frac{\rho}{\rho_0}\right)^{(\gamma-1)}. \tag{192}$$

4.4.3 Angle of Attack and the Kutta Condition

Now that we have determined the transformation of the flow boundary conditions, velocity, and point properties, the last task is to determine how parameters affecting the solution of lifting flows transform. These parameters include the angle of attack and the trailing edge Kutta condition.

The angle of attack is defined as a measure of the arc subtended by the freestream velocity vector and the fixed chord line of a particular airfoil in the flow. The freestream itself is defined as the uniform flow that exists in the limit of infinite distance from the immersed bodies. In order to determine the transformation behavior of this angle, we shall therefore need to carefully consider the limiting behavior of our coordinate transformation at distances very far removed from the airfoil boundary. To do this, we will work with the potential equations in their expanded non-tensorial form. In this section, we will denote the $\bar{x}^\mu$ coordinates as $\bar{x} = \bar{x}^1$ and $\bar{y} = \bar{x}^2$ with similar notation for the x^μ frame.

To determine the angle of attack transformation, we must first consider the appropriate limiting form of the compressible continuity equation at a distance far removed from the profile at which the freestream condition is attained. In the limit of an infinite distance from an airfoil, the induced disturbances must be vanishingly weak because of the die–off behavior of the flow solution with distance from the source. The continuity equation in this limit should take on its appropriate linearized form. The correct linearized form that is valid over the range of subsonic Mach numbers is well known from the small–perturbation theory of subsonic flows [99]. It is frequently called the *Prandtl–Glauert equation* and can be written in terms of the velocity components as,

$$\left(1 - \frac{u_\infty^2}{a_\infty^2}\right)\frac{\partial^2\phi}{\partial x^2} - \frac{2u_\infty v_\infty}{a_\infty^2}\frac{\partial^2\phi}{\partial x \partial y} + \left(1 - \frac{v_\infty^2}{a_\infty^2}\right)\frac{\partial^2\phi}{\partial y^2} = 0 \tag{193}$$

where u_∞ and v_∞ are the x and y components of the freestream velocity respectively and a_∞ is the freestream sound speed.

In the isothermal frame, the potential equation takes on our desired form of the canonical Laplace equation:

$$\frac{\partial^2\phi}{\partial \bar{x}^2} + \frac{\partial^2\phi}{\partial \bar{y}^2} = 0. \tag{194}$$

Our goal is to determine the coordinate mapping in the freestream limit that transforms Equation 193 in the originally given coordinates of the subsonic flow into Equation 194 in the isothermal coordinate system. To determine the mapping, we first begin by relating derivatives of the potential in the two frames. The partial derivative operators transform as,

$$\begin{aligned}
\frac{\partial}{\partial \bar{x}} &= \frac{\partial}{\partial x}\frac{\partial x}{\partial \bar{x}} + \frac{\partial}{\partial y}\frac{\partial y}{\partial \bar{x}} \\
\frac{\partial}{\partial \bar{y}} &= \frac{\partial}{\partial x}\frac{\partial x}{\partial \bar{y}} + \frac{\partial}{\partial y}\frac{\partial y}{\partial \bar{y}}
\end{aligned} \tag{195}$$

so the first derivatives of the potential are

$$\begin{aligned}
\frac{\partial \phi}{\partial \bar{x}} &= \frac{\partial \phi}{\partial x}\frac{\partial x}{\partial \bar{x}} + \frac{\partial \phi}{\partial y}\frac{\partial y}{\partial \bar{x}} \\
\frac{\partial \phi}{\partial \bar{y}} &= \frac{\partial \phi}{\partial x}\frac{\partial x}{\partial \bar{y}} + \frac{\partial \phi}{\partial y}\frac{\partial y}{\partial \bar{y}}.
\end{aligned} \tag{196}$$

The second derivatives appearing in the Laplace equation transform as

$$\begin{aligned}
\frac{\partial^2 \phi}{\partial \bar{x}^2} &= \frac{\partial}{\partial \bar{x}}\left(\frac{\partial \phi}{\partial \bar{x}}\right) = \frac{\partial}{\partial \bar{x}}\left(\frac{\partial \phi}{\partial x}\frac{\partial x}{\partial \bar{x}} + \frac{\partial \phi}{\partial y}\frac{\partial y}{\partial \bar{x}}\right) \\
\frac{\partial^2 \phi}{\partial \bar{y}^2} &= \frac{\partial}{\partial \bar{y}}\left(\frac{\partial \phi}{\partial \bar{y}}\right) = \frac{\partial}{\partial \bar{y}}\left(\frac{\partial \phi}{\partial x}\frac{\partial x}{\partial \bar{y}} + \frac{\partial \phi}{\partial y}\frac{\partial y}{\partial \bar{y}}\right).
\end{aligned} \tag{197}$$

Applying the first derivative operators of Equations 195 to the expressions in the rightmost parentheses in Equations 197, expanding the resulting derivatives with the chain rule, and grouping terms gives,

$$\begin{aligned}
\frac{\partial^2 \phi}{\partial \bar{x}^2} &= \left(\frac{\partial x}{\partial \bar{x}}\right)^2 \frac{\partial^2 \phi}{\partial x^2} + 2\left(\frac{\partial x}{\partial \bar{x}}\frac{\partial y}{\partial \bar{x}}\right)\frac{\partial^2 \phi}{\partial x \partial y} + \left(\frac{\partial y}{\partial \bar{x}}\right)^2 \frac{\partial^2 \phi}{\partial y^2} \\
&\quad + \frac{\partial \phi}{\partial x}\frac{\partial^2 x}{\partial \bar{x}^2} + \frac{\partial \phi}{\partial y}\frac{\partial^2 y}{\partial \bar{x}^2} \\
\frac{\partial^2 \phi}{\partial \bar{y}^2} &= \left(\frac{\partial x}{\partial \bar{y}}\right)^2 \frac{\partial^2 \phi}{\partial x^2} + 2\left(\frac{\partial x}{\partial \bar{y}}\frac{\partial y}{\partial \bar{y}}\right)\frac{\partial^2 \phi}{\partial x \partial y} + \left(\frac{\partial y}{\partial \bar{y}}\right)^2 \frac{\partial^2 \phi}{\partial y^2} \\
&\quad + \frac{\partial \phi}{\partial x}\frac{\partial^2 x}{\partial \bar{y}^2} + \frac{\partial \phi}{\partial y}\frac{\partial^2 y}{\partial \bar{y}^2}
\end{aligned} \tag{198}$$

Because we expect the linearized Prandtl–Glauert equation to hold as the governing equation of the subsonic flow at infinite distance from the airfoil, we also expect that

the coordinate transformation in this neighborhood looks in many ways like the Prandtl–Glauert coordinate transformation. In particular, we expect the coordinate transformation derivatives to be constants. That is, at distances far from the airfoil, the coordinate transformation appears to be a uniform stretching or shrinking. The second derivatives of the coordinate transformation therefore vanish in this region, and Equations 198 simplify to

$$\begin{aligned}
\frac{\partial^2\phi}{\partial\bar{x}^2} &= \left(\frac{\partial x}{\partial\bar{x}}\right)^2 \frac{\partial^2\phi}{\partial x^2} + 2\left(\frac{\partial x}{\partial\bar{x}}\frac{\partial y}{\partial\bar{x}}\right)\frac{\partial^2\phi}{\partial x\partial y} + \left(\frac{\partial y}{\partial\bar{x}}\right)^2 \frac{\partial^2\phi}{\partial y^2} \\
\frac{\partial^2\phi}{\partial\bar{y}^2} &= \left(\frac{\partial x}{\partial\bar{y}}\right)^2 \frac{\partial^2\phi}{\partial x^2} + 2\left(\frac{\partial x}{\partial\bar{y}}\frac{\partial y}{\partial\bar{y}}\right)\frac{\partial^2\phi}{\partial x\partial y} + \left(\frac{\partial y}{\partial\bar{y}}\right)^2 \frac{\partial^2\phi}{\partial y^2}.
\end{aligned} \tag{199}$$

Substituting Equations 199 into Equation 194 and grouping terms gives

$$\begin{aligned}
\frac{\partial^2\phi}{\partial\bar{x}^2} + \frac{\partial^2\phi}{\partial\bar{y}^2} &= \left[\left(\frac{\partial x}{\partial\bar{x}}\right)^2 + \left(\frac{\partial x}{\partial\bar{y}}\right)^2\right]\frac{\partial^2\phi}{\partial x^2} \\
&\quad + 2\left[\left(\frac{\partial x}{\partial\bar{x}}\right)\left(\frac{\partial y}{\partial\bar{x}}\right) + \left(\frac{\partial x}{\partial\bar{y}}\right)\left(\frac{\partial y}{\partial\bar{y}}\right)\right]\frac{\partial^2\phi}{\partial x\partial y} \\
&\quad + \left[\left(\frac{\partial y}{\partial\bar{x}}\right)^2 + \left(\frac{\partial y}{\partial\bar{y}}\right)^2\right]\frac{\partial^2\phi}{\partial y^2} \\
&= 0.
\end{aligned} \tag{200}$$

We now require Equation 200 to match Equation 193. To obtain this matching, we must require that each of the coefficients multiplying the second derivatives of the potential equate up to some overall multiplicative factor in both expressions. This multiplicative factor, which we will denote λ, is allowed because the equations equal zero and any factor multiplying all of the terms can be divided through. The matching therefore requires

$$\begin{aligned}
\left(\frac{\partial x}{\partial\bar{x}}\right)^2 + \left(\frac{\partial x}{\partial\bar{y}}\right)^2 &= \lambda\left(1 - \frac{u_\infty^2}{a_\infty^2}\right) \\
\left(\frac{\partial x}{\partial\bar{x}}\right)\left(\frac{\partial y}{\partial\bar{x}}\right) + \left(\frac{\partial x}{\partial\bar{y}}\right)\left(\frac{\partial y}{\partial\bar{y}}\right) &= -\lambda\left(\frac{u_\infty\, v_\infty}{a_\infty^2}\right) \\
\left(\frac{\partial y}{\partial\bar{x}}\right)^2 + \left(\frac{\partial y}{\partial\bar{y}}\right)^2 &= \lambda\left(1 - \frac{v_\infty^2}{a_\infty^2}\right).
\end{aligned} \tag{201}$$

Equations 201 provide three relations in five unknowns (the four coordinate derivatives plus λ). Two additional conditions are therefore required. These are given by the far-field

boundary condition on the coordinate mapping that we determined previously as

$$x = \bar{x}. \tag{202}$$

Since the coordinate derivatives are presumed to be constant in the far-field region, this condition implies that the relations

$$\begin{aligned} \frac{\partial x}{\partial \bar{x}} &= 1 \\ \frac{\partial x}{\partial \bar{y}} &= 0 \end{aligned} \tag{203}$$

also hold in this neighborhood. These relations are the two equations needed to close the system and completely determine the coordinate mapping. Solving Equations 201 and 203 for λ and the coordinate derivatives gives,

$$\lambda = 1/\left(1 - \frac{u_\infty^2}{a_\infty^2}\right) \tag{204}$$

and

$$\begin{aligned} \frac{\partial x}{\partial \bar{x}} &= 1 \\ \frac{\partial x}{\partial \bar{y}} &= 0 \\ \frac{\partial y}{\partial \bar{x}} &= -\lambda \frac{u_\infty v_\infty}{a_\infty^2} \\ \frac{\partial y}{\partial \bar{y}} &= \lambda \sqrt{1 - M_\infty^2} \end{aligned} \tag{205}$$

where $M_\infty^2 = \left(u_\infty^2 + v_\infty^2\right)/a_\infty^2$.

We are now poised to determine the transformation of the angle of attack, α. In the original frame of the subsonic flow, it is defined as

$$\tan\alpha = \frac{v_\infty}{u_\infty}. \tag{206}$$

We can relate the freestream velocity components in the original frame to those in the isothermal frame using the transformation law for covariant vectors as

$$\begin{aligned} \bar{u}_\infty &= u_\infty \frac{\partial x}{\partial \bar{x}} + v_\infty \frac{\partial y}{\partial \bar{x}} \\ \bar{v}_\infty &= u_\infty \frac{\partial x}{\partial \bar{y}} + v_\infty \frac{\partial y}{\partial \bar{y}}. \end{aligned} \tag{207}$$

Substituting Equations 205 and simplifying gives

$$\begin{aligned} \bar{u}_\infty &= \lambda \left(1 - M_\infty^2\right) u_\infty \\ \bar{v}_\infty &= \lambda \sqrt{1 - M_\infty^2}\, v_\infty. \end{aligned} \tag{208}$$

Employing Equations 208 in Equation 206 gives,

$$\tan\alpha = \frac{\left(1 - M_\infty^2\right)}{\sqrt{1 - M_\infty^2}} \frac{\bar{v}_\infty}{\bar{u}_\infty} = \sqrt{1 - M_\infty^2}\, \frac{\bar{v}_\infty}{\bar{u}_\infty}, \tag{209}$$

but the definition of the angle of attack in the isothermal frame is simply

$$\tan\bar{\alpha} = \frac{\bar{v}_\infty}{\bar{u}_\infty} \tag{210}$$

so Equation 209 becomes

$$\tan\alpha = \sqrt{1 - M_\infty^2}\, \tan\bar{\alpha} \tag{211}$$

or

$$\tan\bar{\alpha} = \frac{1}{\sqrt{1 - M_\infty^2}}\, \tan\alpha. \tag{212}$$

Equation 212 is the transformation of the angle of attack that we seek. It indicates that the tangent of the angle of attack in the canonical Laplacian flow is larger than that of the subsonic flow by a factor identical to that obtained in certain forms of the Prandtl–Glauert rule. This result is reassuring because we have predicated this transformation on the fact that the subsonic flow can be treated as a linear compressible flow in the far-field region.

The last goal in this section is to establish the transformation behavior of the Kutta condition for lifting flows. The Kutta condition prescribes that the flow should leave the airfoil trailing edge smoothly, and for airfoils with a finite trailing edge angle, the trailing edge must be a stagnation point [82]. The Kutta condition must be enforced in order to prescribe the circulation for lifting flows around airfoils in both incompressible flows and subsonic flows. Without the Kutta condition, the elliptic boundary value problem is not completely determined [58].

One interpretation of the Kutta condition is that the tangential velocities on both the upper and lower surfaces of an airfoil at infinitesimal distance from the trailing edge are equal

[82]. In the isothermal coordinate transformation defined in this research, the tangency boundary condition of the original flow is preserved during the transformation. That is, the flow is tangent both to the original airfoil surface and to the airfoil surface in the transformed frame. Because the Kutta condition can be described in terms of tangency, we can therefore expect that it too remains invariant in the coordinate transformation. That is, we can prescribe the Kutta condition in the same way for both the original compressible flow and the transformed canonical Laplacian flow.

4.5 Connection to Quasiconformal Mappings and the Method of Bers

As described in the introduction to this chapter, the type of coordinate transformation that we have examined in this research is similar to a class of mappings for subsonic flow problems examined primarily by the mathematician Lipman Bers in a series of works in the 1940s and 1950s [12, 13, 14, 16]. In particular, both types of transformations are termed *quasiconformal mappings*. Bers' work is among the first to describe potential flows and their transformations through the use of a Riemannian metric tensor, and this perspective has been central to the research outlined in this dissertation. He was also perhaps the first to study the related problem of quasiconformal mappings in potential flow. In this section, we shall therefore examine quasiconformal mappings and elements of the mapping approach devised by Bers and compare his approach to that developed in this research.

A quasiconformal mapping can be viewed as a transformation that maps infinitesimal circles into infinitesimal ellipses of bounded eccentricity [3]. We can see this in the following way. Let us consider an infinitesimal circle described in a Cartesian coordinate system $\bar{x}^\alpha$. The equation of this circle is given by the relation,

$$\left(d\bar{x}^1\right)^2 + \left(d\bar{x}^2\right)^2 = (ds)^2 \tag{213}$$

where we describe the coordinates in terms of differentials and ds is an infinitesimal distance that describes the radius the circle. This relation can be recognized immediately as the definition of the line element in Cartesian coordinates because we could have just as well

written

$$\bar{g}_{11}\,\left(d\bar{x}^1\right)^2 + 2\,\bar{g}_{12}\,\left(d\bar{x}^1\right)\,\left(d\bar{x}^2\right) + \bar{g}_{22}\,\left(d\bar{x}^2\right)^2 = (ds)^2 \tag{214}$$

with $\bar{g}_{11} = 1$, $\bar{g}_{12} = 0$, and $\bar{g}_{22} = 1$.

We now perform a coordinate transformation to a system x^α. In this transformation, the scalar distance ds is invariant, but the metric tensor changes as dictated by the tensor transformation law. We can therefore write the transformed version of Equation 213 in the new coordinates as

$$g_{11}\,\left(dx^1\right)^2 + 2\,g_{12}\,\left(dx^1\right)\,\left(dx^2\right) + g_{22}\,\left(dx^2\right)^2 = (ds)^2\,. \tag{215}$$

If we place no restrictions on the metric tensor coefficients $g_{\mu\nu}$ obtained through this transformation, then Equation 215 is the general form of the equation for an arbitrary conic section. The type of conic section is determined by the discriminant of the equation, given by $D = (2\,g_{12})^2 - 4\,g_{11}\,g_{22} = -4\,g$. If $D < 0$, the equation is that of an ellipse, if $D = 0$ the equation describes a parabola and if $D > 0$ the conic is a hyperbola [48]. In all allowable coordinate transformations in Riemannain geometry, we must require that the determinant of the metric tensor, g, is strictly positive [34]. For this reason, $D = -4\,g$ is always negative, and hence, the conic is always an ellipse, or in the special case of $g_{11} = g_{22}$ and $g_{12} = 0$, a circle.

Quasiconformal mappings therefore comprise a very general class of allowable coordinate transformations in two dimensions that map infinitesimal circles into ellipses. The primary restriction compared to any arbitrary coordinate transformation is the concept of bounded eccentricity, which implies that the characteristic dimensions of the infinitesimal ellipses have a finite and real ratio. This restriction can be stated in terms of the mathematical concept of the degree of quasiconformality, but we shall not have need of this concept in our discussion.

Conformal mappings can be thought of as a special case of quasiconformal mappings that map infinitesimal circles into other infinitesimal circles of different radii. This can be seen by considering a conformal transformation from a coordinate system $\bar{x}^\alpha$ with $\bar{g}_{11} = \bar{g}_{22} = \sigma$

and $\bar{g}_{12} = 0$. This system has the line element,

$$\sigma \left(d\bar{x}^1\right)^2 + \sigma \left(d\bar{x}^2\right)^2 = (ds)^2 . \tag{216}$$

A conformal transformation alters the metric tensor only by an overall multiplicative factor, so we can write the metric in the frame x^α obtained through the transformation as $g_{11} = g_{22} = \tau$, $g_{12} = 0$. The line element in this system is therefore,

$$\tau \left(dx^1\right)^2 + \tau \left(dx^2\right)^2 = (ds)^2 . \tag{217}$$

Equation 216 can be thought of as the equation for a circle in coordinates $\bar{x}^\alpha$ of radius $ds/\sqrt{\sigma}$, and Equation 217 is the equation for a circle in coordinates x^α of the radius $ds/\sqrt{\tau}$. Therefore, the effect of the transformation from $\bar{x}^\alpha$ to x^α is to stretch or shrink the radii of infinitesimal circles drawn in the planes of their respective coordinates by the ratio $\sqrt{\sigma/\tau}$. The values of σ and τ can vary from point to point within the domain.

Quasiconformal mappings arise through a coordinate transformation dictated by the *Beltrami equations* [12, 16]. These equations, expressed for the transformation from $\bar{x}^\alpha$ where the line element is the equation for infinitesimal circle to x^α where the line element produces infinitesimal ellipses, are given by,

$$\frac{\partial \bar{x}^1}{\partial x^\alpha} = g_{\alpha\kappa}\epsilon^{\kappa\lambda}\,\frac{\partial \bar{x}^2}{\partial x^\lambda}. \tag{218}$$

These equations are identical in form to the generalized Cauchy–Riemann equations that we employed in the isothermal coordinate transformation developed in this chapter. Indeed, the terminologies are apparently completely synonymous.

Having established a basic definition of quasiconformal mappings, we can now proceed to examine how they describe coordinate transformations common in the study of subsonic flows, including the transformation derived in this research as well as that of Bers. These types of transformations can describe almost all of the relevant mappings for problems in subsonic potential flow. This is perhaps best said by Bers [16]:

> ... In every flow of variable density the mapping of the physical plane into the potential plane (ϕ, ψ) is quasiconformal provided that the density is bounded and bounded away from zero.

> The mapping from the physical plane into the hodograph plane ... is also quasiconformal if the flow is uniformly subsonic, i.e., if the Mach number is bounded away from one .... For a uniformly subsonic flow, the mapping of the hodograph plane into the potential plane, as well as the mapping of the hodograph plane into the physical plane, is also quasiconformal ....

Bers describes a very general set of conditions on the metric tensor produced in a quasiconformal mapping involving potential flows [12]. In terms of our notation, he considers a system x^α with a metric given by

$$\begin{aligned} g_{11} &= \cos^2\theta + \frac{B^2}{A^2}\sin^2\theta \\ g_{12} &= \left(1 - \frac{B^2}{A^2}\right)\sin\theta\cos\theta \\ g_{22} &= \sin^2\theta + \frac{B^2}{A^2}\cos^2\theta \end{aligned} \tag{219}$$

where he defines $\theta = \tan^{-1}(u_2/u_1)$. In terms of the velocity components u_1 and u_2, the metric can therefore be recast as

$$\begin{aligned} g_{11} &= \frac{(u_1)^2 + \left(B^2/A^2\right)(u_2)^2}{(u_1)^2 + (u_2)^2} \\ g_{12} &= \frac{\left[1 - \left(B^2/A^2\right)\right] u_1\, u_2}{(u_1)^2 + (u_2)^2} \\ g_{22} &= \frac{(u_2)^2 + \left(B^2/A^2\right)(u_1)^2}{(u_1)^2 + (u_2)^2}. \end{aligned} \tag{220}$$

In this system, the flow equations can be written

$$\begin{aligned} \frac{\partial\phi}{\partial x^1} &= A\,\frac{\partial\psi}{\partial x^2} \\ \frac{\partial\phi}{\partial x^2} &= -A\,\frac{\partial\psi}{\partial x^1}. \end{aligned} \tag{221}$$

Through a quasiconformal mapping, this system is transformed to frame $\bar{x}^\alpha$ with metric $\bar{g}_{11} = \bar{g}_{22}$, $\bar{g}_{12} = 0$ conformal to the Cartesian metric. In this system, the flow equations

take the form

$$\begin{aligned} \frac{\partial \phi}{\partial \bar{x}^1} &= B \frac{\partial \psi}{\partial \bar{x}^2} \\ \frac{\partial \phi}{\partial \bar{x}^2} &= -B \frac{\partial \psi}{\partial \bar{x}^1}. \end{aligned} \tag{222}$$

Using this general transformation behavior, Bers considers a mapping from the physical plane to the hodograph plane using this Riemannian metric form, where he takes $A = 1/\rho$ and $B = \sqrt{1 - M^2}/\rho$. Bers terms this transformation as "conformal with respect to the flow" [12]. This terminology apparently stems from the observation that the angle measurement defined by the metric $g_{\mu\nu}$ given by Equation 219 is equivalent to the angle defined by the Cartesian metric in the original system, and transformations that preserve angles are said to be conformal. It is important to note, however, that this transformation is perhaps more appropriately described as quasiconformal based on the terminology we consider in this section [12].

The mapping method Bers develops is similar to that in this research because it allows one to determine a subsonic flow corresponding to a given incompressible flow. The method is quite complicated and involves the aforementioned quasiconformal mapping from the physical plane of an incompressible flow to the hodograph plane followed by conformal mappings in the hodograph plane to solve the flow. The method finally culminates in a transformation back to the physical plane of a subsonic flow. He terms the incompressible and associated subsonic flows as "conjugate flows", which is an analogous term to "equivalent flow" used in this work.

For an arbitrary equation of state, Bers' method requires the solution of a separate boundary value problem for the coordinate mapping, similar to the isothermal coordinate mapping problem established in this research. For the case of the linearized equation of state with $\gamma = -1$, Bers finds a closed form solution for the mapping very similar to that of the method of Kármán and Tsien. Indeed, the method appears to be identical to the Kármán–Tsien approach (for the complete mapping problem, not just the pressure correction) except that it also works for flows with circulation. Bers demonstrated the method for symmetric flows around closed profiles without circulation for both the linearized equation of state [13]

and with the correct isentropic state relation for air [14].

This mapping developed by Bers distorts the profile of the incompressible flow only slightly in producing the conjugate compressible flow, except that for lifting flows, it introduces a cusp singularity at the leading edge stagnation point which makes the solution somewhat challenging. This singularity as well as the complexity of the Riemannian perspective led Lin to devise an alternative method for the mapping solution of $\gamma = -1$ flows with circulation that involves an arbitrary complex analytic function [71]. Lin's method seems to have gained greater acceptance, and the connection Bers drew to Riemannian geometry seems to have been lost in most of the subsequent literature on potential flows.

Although the transformation developed in this research has significant differences from that of Bers, it does have many similarities. These similarities include the following:

- Generation of a conjugate/equivalent incompressible flow corresponding to a subsonic flow or vice versa
- Use of Riemannian geometric terminology and notation
- Application of quasiconformal mappings

In particular, we can show that the type of quasiconformal mapping we consider in this work can be described in Bers' general framework provided in Equations 219-222. To do this, we shall first need to convert our metric expressions $\sqrt{g}g^{\nu\mu}$ into the form $g_{\nu\mu}$ for comparison with the form of Equation 220. In Section 4.2, we determined that the inverse metric tensor can be written in the form of Equation 125, which we repeat here (identifying $c = 1/\rho_0$) as,

$$\begin{aligned} g^{11} &= (\sigma\rho_0)\,\frac{\left[(u_1)^2(\rho/\rho_0)^2 + (u_2)^2\right]}{(\rho/\rho_0)\left[(u_1)^2 + (u_2)^2\right]} \\ g^{12} &= (\sigma\rho_0)\,\frac{\left[(\rho/\rho_0)^2 - 1\right]u_1u_2}{(\rho/\rho_0)\left[(u_1)^2 + (u_2)^2\right]} \\ g^{22} &= (\sigma\rho_0)\,\frac{\left[(u_2)^2(\rho/\rho_0)^2 + (u_1)^2\right]}{(\rho/\rho_0)\left[(u_1)^2 + (u_2)^2\right]}. \end{aligned} \tag{223}$$

The corresponding covariant metric tensor obtained by taking the matrix inverse is

$$\begin{aligned} g_{11} &= \frac{1}{(\sigma\rho_0)} \frac{\left[(u_1)^2 + (u_2)^2(\rho/\rho_0)^2\right]}{(\rho/\rho_0)\left[(u_1)^2 + (u_2)^2\right]} \\ g_{12} &= \frac{1}{(\sigma\rho_0)} \frac{\left[1 - (\rho/\rho_0)^2\right] u_1 u_2}{(\rho/\rho_0)\left[(u_1)^2 + (u_2)^2\right]} \\ g_{22} &= \frac{1}{(\sigma\rho_0)} \frac{\left[(u_2)^2 + (u_1)^2(\rho/\rho_0)^2\right]}{(\rho/\rho_0)\left[(u_1)^2 + (u_2)^2\right]}. \end{aligned} \tag{224}$$

In developing the theory, we have heretofore left σ completely arbitrary, excepting our requirements that it be nonzero and real. We can therefore set $\sigma = 1/\rho$ such that Equation 224 becomes,

$$\begin{aligned} g_{11} &= \frac{(u_1)^2 + (u_2)^2(\rho/\rho_0)^2}{(u_1)^2 + (u_2)^2} \\ g_{12} &= \frac{\left[1 - (\rho/\rho_0)^2\right] u_1 u_2}{(u_1)^2 + (u_2)^2} \\ g_{22} &= \frac{(u_2)^2 + (u_1)^2(\rho/\rho_0)^2}{(u_1)^2 + (u_2)^2}. \end{aligned} \tag{225}$$

With this definition of σ, we can recognize immediately that this metric tensor is consistent with Bers' general form given by Equation 220 if we identify $B^2/A^2 = (\rho/\rho_0)^2$. Because our intent is to map a subsonic flow to an incompressible flow, we can go one step further and require $A = 1/\rho$, $B = 1/\rho_0$ in order that Equations 221 and 222 become,

$$\begin{aligned} \frac{\partial\phi}{\partial x^1} &= \frac{1}{\rho}\frac{\partial\psi}{\partial x^2} \\ \frac{\partial\phi}{\partial x^2} &= -\frac{1}{\rho}\frac{\partial\psi}{\partial x^1}. \end{aligned} \tag{226}$$

and

$$\begin{aligned} \frac{\partial\phi}{\partial \bar{x}^1} &= \frac{1}{\rho_0}\frac{\partial\psi}{\partial \bar{x}^2} \\ \frac{\partial\phi}{\partial \bar{x}^2} &= -\frac{1}{\rho_0}\frac{\partial\psi}{\partial \bar{x}^1}. \end{aligned} \tag{227}$$

These equations express the appropriate relations between the stream and potential functions in our original frame x^α corresponding to a compressible flow and in the transformed isothermal frame $\bar{x}^\alpha$ corresponding to a flow that appears to be incompressible because of the constant ρ_0.

Our usage of the quasiconformal transformation can be thought of as a direct transformation from the "physical plane" of a compressible flow, to the "physical plane" of an equivalent incompressible flow. Although Bers employs a transformation to the hodograph as an intermediate step, he too arrives at a transformation linking a subsonic and an incompressible flow. In his mapping, the airfoil profiles of the two flows are only slightly different, whereas in our method, we shall see that the shapes may be altered significantly.

It appears that there are therefore many possible routes to obtain a valid linkage between incompressible and subsonic flows, depending on one's particular choice of the factors A and B in Bers formulation for the quasiconformal mapping. It is conjectured by the author that these different types of allowable mappings are the nonlinear generalization of the alternative forms of the Prandtl–Glauert and Göthert rules. The differences in these rules stem from how the airfoil shape and/or boundary conditions are allowed to vary. Even in the linear case, these differences can be subtle and challenging to understand. The complications introduced in the fully nonlinear mapping problem further add to this difficulty. Although interesting, this question shall be left as a topic for later research.

The theoretical development is now complete. Although we have achieved a mapping linking a subsonic flow to an equivalent incompressible flow, it does not appear possible to solve the transformation in closed form using common mathematical techniques. The next task is therefore to devise a numerical method to allow us to accomplish the transformation and solve flows using the theory.

CHAPTER V

IMPLEMENTATION

The theory developed in the previous chapter described a mapping of a subsonic compressible flow to an equivalent incompressible field. The mapping is closely coupled with the flow, as it depends on parameters such as the fluid velocity and density.

This coupling as well as the nonlinear nature of compressibility impose significant difficulty on the development of equivalent incompressible flows and their application for subsonic solutions. These difficulties have precluded the development of exact analytical solutions for the coordinate mapping in this dissertation research, even for simple prototypical flows. Approximate solutions could perhaps be found analytically, for instance using the tangent gas law approximation in a similar way to the Kármán–Tsien method; however, approximations would not provide significant additional value for practical use. Additionally, it is highly unlikely that analytical solutions could be found for the flows over arbitrary bodies and airfoils that are of most interest for engineering analysis and design.

In this chapter, we will therefore develop a numerical method that will facilitate the solution of flows over arbitrary two–dimensional bodies using the theory developed in the previous chapter. This numerical method will serve two roles. First, it will provide a means by which the mapping theory can be validated by comparison of the flow solution results with known and trusted test cases. Second, it will allow for the development of equivalent incompressible flows and corresponding subsonic solutions for profile shapes of typical engineering interest.

An approach based on the solution of a separate boundary value problem for the coordinate mapping is implemented, leveraging the theory developed in Section 4.3.2. The selected numerical method requires that equations be solved at a grid of points within the interior of the solution domain. This method can be thought of as nearly exact, up to numerical errors stemming from issues such as discretization of the grid and truncation of

higher order terms in numerical derivatives. The use of a domain grid makes the method somewhat computationally expensive; however, its high accuracy will allow for validation of the underlying theory. The results of applying this method comprise the solution of the given compressible flow, the solution of the equivalent incompressible flow, and the distorted geometry and grid corresponding to the equivalent incompressible flow.

5.1 Solution Algorithm

As we saw in Chapter 4, the metric tensor plays a fundamental role in the mapping problem. The components of the metric tensor appear within the partial differential equations for the isothermal coordinate transformation, serving as forcing functions influencing the behavior of the mapping. The metric tensor, in turn, is a function of the varying properties of the compressible flow throughout the solution domain.

One approach would therefore be first to solve the compressible potential flow directly and then to solve the boundary value problem for the coordinate mapping. The solution to the equivalent incompressible flow could then be found based on the geometry obtained through the transformation. Because the compressible flow is nonlinear, the solution of *both* the flow *and* the coordinate mapping in this approach would require the use of a reasonably expensive technique involving a domain grid or at least field points, depending on the method chosen. Although this method involves two expensive domain solutions, it has the advantage of being a direct and non-iterative method of solving both the compressible flow and the equivalent incompressible flow and geometry.

A second approach would be to solve the mapping through a domain grid but to solve the equivalent incompressible flow with a boundary element method. As their name implies, boundary element methods, also known in aerodynamic contexts as panel methods, can be used to solve incompressible flows at points along portions of the domain boundary without discretizing the domain interior [58]. Computationally efficient domain solutions can be obtained using the surface solutions obtained through these methods in a process often called a field survey.

The challenge with this solution method is that the metric tensor depends on the solution

to the *compressible* flow in the frame x^α, whereas the panel method produces the solution to the equivalent *incompressible* flow in the frame $\bar{x}^\alpha$. This method must therefore be fundamentally iterative, with each iteration involving the solution of an estimate for the incompressible flow, the mapping of the flow parameters to the compressible flow such that the metric can be determined, and then the domain solution to the coordinate mapping. Convergence is obtained when either the equivalent incompressible geometry or the flow does not change much from one iteration to the next. This necessity of iteration will likely make this method substantially more expensive than the direct approach.

Although it is likely more computationally expensive, we will pursue the iterative approach involving a panel method in this dissertation. There are two reasons for this choice. The first stems from the original engineering motivation for this research—to solve compressible subsonic flows by mapping to an incompressible equivalent and then solving this simple flow. This motivation was formulated under the presumption that the resulting solution method would not require a domain grid and would therefore be less expensive than the direct solution of the subsonic flow itself. Although we have seen that a domain solution is indeed required, this iterative method is nonetheless more aligned to the the inspiration by which this research was conceived.

A second reason for pursuing this approach is that it provides crisp evidence that the equivalent flow can truly be viewed as if it were incompressible. As we saw in Chapter 4, the equivalent flow is described by the Cartesian form of the Laplace equation, and the boundary conditions for the flow correspond to flow tangency in the isothermal reference frame. Therefore, in terms of the solution method, the equivalent flow is in all appearances an incompressible flow. For this reason, any of the myriad of standard panel codes devised for the typical external aerodynamic problem can be used to solve the equivalent flow without modification. In the iterative approach using a panel code, we implicitly presume that the equivalent flow is incompressible by our use of an incompressible solver, and we can validate that the resulting compressible flow solutions match known test cases. On the other hand, if we had chosen the non-iterative approach of first solving the subsonic flow directly and then solving the mapping, we would need somehow to validate that the resulting

equivalent flow is indeed incompressible, perhaps by re-solving it using an incompressible solver and comparing the results to those obtained through the direct approach.

The solution algorithm for the iterative approach that we will develop is shown in Figure 7. The major steps in this approach include generation of an initial grid, solution of the equivalent incompressible flow, calculation of the metric tensor, and solution of the coordinate mapping.

The first step in the solution is to develop a domain grid corresponding to the geometry of the given subsonic compressible flow. For this research, a structured O-grid topology is used. A structured grid is necessary for compatibility with the finite difference approach that is used for the coordinate mapping method. A detailed description of the initial grid generation step is provided in Section 5.2.

Next, the iterative loop is begun. In this loop, the equivalent incompressible flow is first solved using a standard panel code implementation. For the first iteration, the airfoil shape and domain of the incompressible flow is taken to be the same as that provided by the initial grid for the subsonic flow. Alternately, one could first distort the subsonic domain through a uniform stretching corresponding to an approximate Prandtl–Glauert type correction. This approach was investigated, but no substantial reduction in the number of iterations required for convergence was noted. This lack of improvement may be due to the incorrect tangency boundary conditions corresponding to the form of the Prandtl–Glauert rule that maps to an airfoil of the same chord that we discussed in Chapter 2. This error in the boundary conditions may tend to wash out improvements that would otherwise result from the shape and pressure corrections. Because the Prandtl–Glauert initial guess was not found to produce noticeable improvements, it was not implemented in the algorithm.

The choice of panel code used in this step is largely arbitrary; however, most pedagogical implementations provide solutions only of the surface velocity distribution and pressure integrals and do not provide the field solution. This situation is not difficult to resolve, however, as the field solution is quite easily determined from the surface singularity strengths provided by typical panel codes. The process of determining domain point solutions is often termed a field survey, and we integrate this capability as a postprocessing operation to the

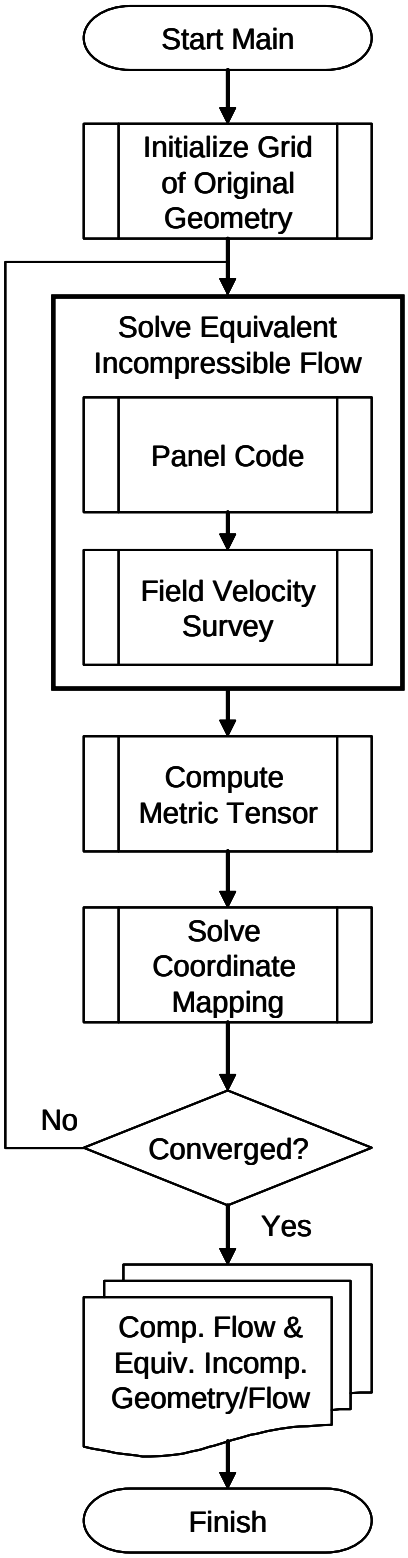

Figure 7: Solution Algorithm

panel code in this implementation. The panel code and field survey implementation are described in more detail in Section 5.3.

After an estimate of the equivalent incompressible flow is obtained, the next step is to develop an estimate of the metric tensor that drives the coordinate transformation. Because the metric is posed as a function of the compressible flow, this process involves several intermediate steps including first transforming the velocities obtained in the incompressible solution to the compressible frame and also transforming the resulting metric to a computational frame for use by the coordinate mapping algorithm.

Next, the coordinate mapping is solved. As inputs, the solver takes the estimates of the metric tensor components provided by the previous step as well as the boundary conditions for the mapping. Although several types of solution methods could be used for this step, an iterative finite difference technique known as Successive Over-Relaxation by Lines (SLOR) is adopted for this work. This method requires a structured grid of the solution domain and sweeps along lines in the grid until a converged mapping is obtained. The method employs an auxiliary computational coordinate system such that finite difference approximations to derivatives can easily be developed. The coordinate mapping step is described in detail in Section 5.5.

After the coordinate mapping is complete, the solution must be checked for convergence. As pointed out previously, the iterative nature of the solution is necessary because of the interdependence of the metric tensor and flow solution. A variety of convergence tests could be devised, based either on flow parameters, the metric tensor, or the coordinate mapping. In this implementation, we base convergence on the coordinate mapping. There is no particular reason for this particular choice, but it has proven effective in tests of the method.

To denote the convergence criterion mathematically, we first adopt a new notation that breaks from the tensorial approach employed earlier. First, we replace the tensorial superscript indices corresponding to the isothermal coordinates by the notation $\bar{x} = \bar{x}^1$ and $\bar{y} = \bar{x}^2$. Similarly, we denote points in the original coordinate grid as $x = x^1$ and $y = x^2$. Specific grid points are indicated with two comma–delimited subscripts that correspond

to respective coordinate directions in the computational plane of the structured grid. We typically take these subscripts to be in the ranges $1 : i_{max}$ and $1 : j_{max}$ where i_{max} and j_{max} specify the number of grid points in each direction. Relative indices such as $i-1$ and $j+1$ are allowed, presuming that the index values remain in the valid range. Superscripts such as m denote the particular iteration in the convergence loop. This nomenclature, typical of the type used in computational fluid dynamics, is adopted consistently for the remainder of this dissertation.

The chosen convergence criterion is a specified change in the sum-squared difference of the grid points in the isothermal coordinates relative to the difference at the second iteration in the loop. Using the new notation, the grid residual is given by

$$R^m = \sum_{i=1}^{i_{max}} \sum_{j=1}^{j_{max}} \left[\left(\bar{x}_{i,\,j}^{\,m} - \bar{x}_{i,\,j}^{\,m-1} \right)^2 + \left(\bar{y}_{i,\,j}^{\,m} - \bar{y}_{i,\,j}^{\,m-1} \right)^2 \right]. \tag{228}$$

Convergence is obtained when the residual R^m satisfies

$$R^m < \epsilon \, R^2 \tag{229}$$

where ϵ is a specified tolerance, and iteration zero corresponds to the initial grid. Typically, the tolerance is taken within the range $10^{-10} \leq \epsilon \leq 10^{-4}$. Once convergence is achieved, the grid and flow solutions are complete and results for both the subsonic compressible flow and the equivalent incompressible flow can be examined. We choose to base convergence on comparison to the second iteration because of the rapid step change in the residual between the first and second iterations that typically occurs because of the quality of the initial guess. We will explore this convergence phenomenon in greater detail in Chapter 6.

Having outlined the overall solution algorithm and its convergence criterion, we will now examine each of the primary subtasks of the algorithm in more detail. First, the initial grid generation procedure is described, and next the panel method flow solution approach is presented. The final two subsections then outline the procedure for calculating the metric tensor and developing the isothermal coordinate mapping.

5.2 Initial Grid Generation

The initial grid comprises a representation of the domain of the originally given subsonic compressible flow. This grid must therefore include the inner airfoil boundary over which we wish to develop the subsonic solution as well as the outer far-field boundary that is intended to approximate the location of the infinity conditions.

Based on the intent to solve the coordinate transformation with a finite difference method, a structured grid is required. This requirement stems from the need to develop numerical derivatives along lines of constant grid direction.

A variety of structured grid topologies could be used. Our interest in this research is focused only on domains with single-element airfoils. For these types of domains, topologies including O–grid, C–grid, and H–grid layouts are possible. In conducting this research, both O–grid and C–grid topologies were examined in detail. Typical layouts of these topologies are shown in Figures 8 and 9.

In these structured grids, the coordinate direction oriented generally in the direction parallel to the inner and outer boundaries is indexed as i whereas the direction oriented generally normal to the boundaries is indexed as j. The values of i and j can be interpreted as forming a net of auxiliary computational coordinates describing a rectangular domain. We shall refer to this coordinate frame as $\tilde{x}^{\mu}$, or alternately $(\tilde{x}, \tilde{y})$. This computational coordinate system is useful because finite difference derivative approximations can be developed easily within this frame for use in the metric computation and the coordinate mapping algorithm.

At times, we will have need to determine the mappings between this computational domain and both the original subsonic flow frame and the isothermal coordinate frame. These mappings are especially simple, as the mapping of the original frame is accomplished by the generation of the initial grid itself through the association of physical points x and y with i and j indexes.

An important finding that influences our choice of the type of structured grid is that the solution method is very sensitive to the smoothness of the interior and exterior boundary

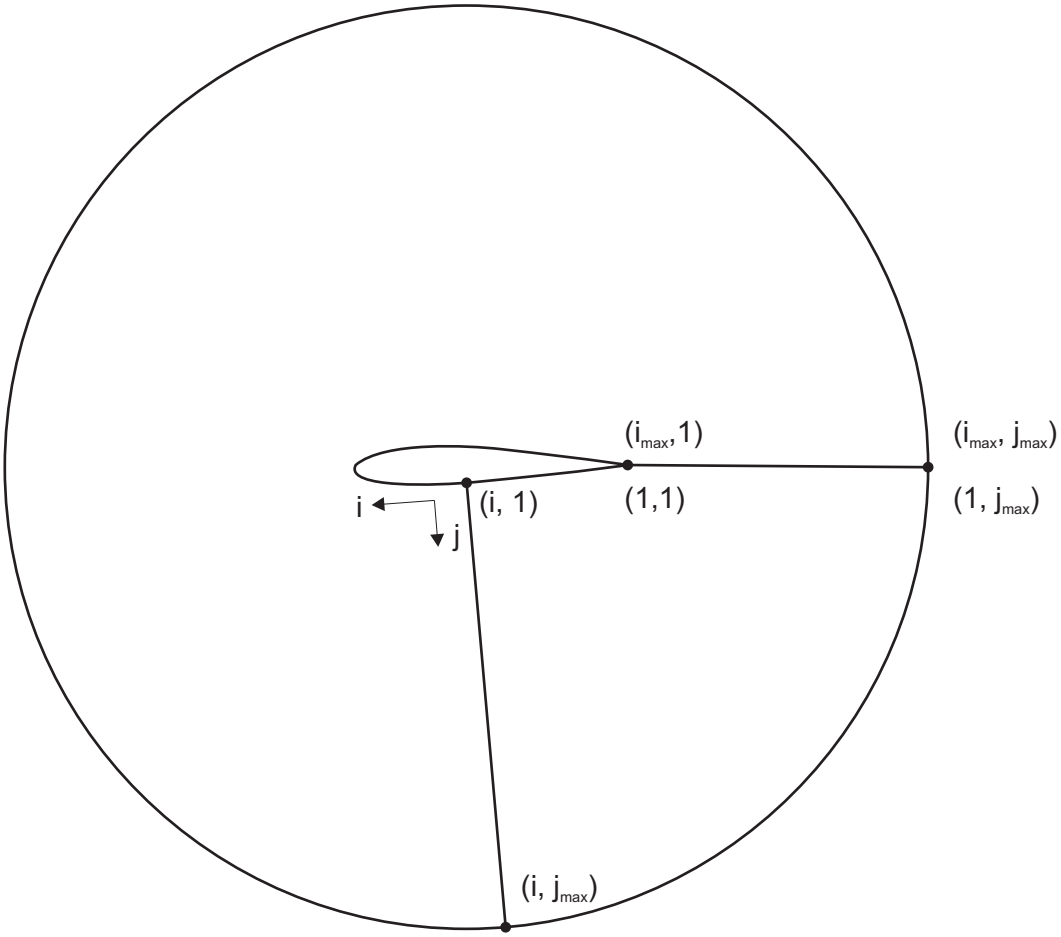

Figure 8: Typical O–Grid Layout

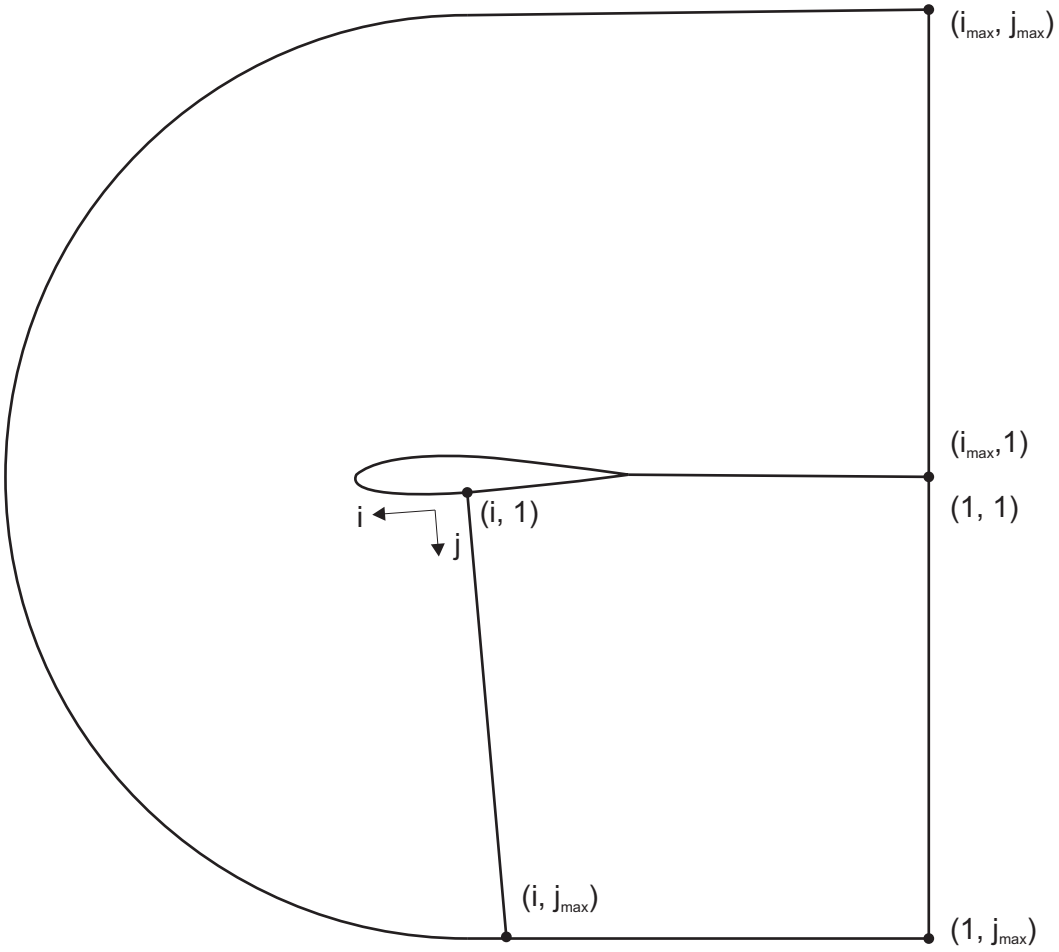

Figure 9: Typical C–Grid Layout

shape and parametrization. The solution method was found to perform poorly if discontinuities in either first or second derivatives of the boundary curves were present. This type of discontinuity is typical in many C–grid topologies because the outer boundary is often composed of a semicircle stitched to a rectangular section. In this case, a discontinuity in the second derivatives at the intersection of the semicircular and rectangular regions is present. Similarly, C–grids typically have an inner boundary comprised of the airfoil connected to line segments that extend downstream from the trailing edge. The intersections of these segments with the trailing edge also represent first derivative discontinuities along a particular grid direction that cause numerical difficulties in the solution.

In addition to smoothness of the grid in the physical plane, the method is also sensitive to smoothness of the grid point spacing along the boundaries. In a C–grid, it is difficult to obtain good control of this smoothness. For instance, it is often desirable to choose a smoothly varying function such as a sinusoid or polynomial to distribute points along the airfoil surface. The usual goal is to refine the grid locally around both the leading and trailing edges. In the region downstream of the airfoil, however, the point spacing should ideally expand from a fine spacing at the trailing edge to a coarse spacing in the region of the outer boundary. These traits are typically obtained by using different spacing functions along the airfoil portion of the inner boundary and along the downstream line segments. If these spacing functions are arbitrarily chosen, a discontinuity in the first derivatives is typically present. This discontinuity has been found to produce numerical difficulties in the solution.

It is possible to employ a completely smooth spacing function along the inner boundary for the C–grid topology; however, the development of an adequate function is somewhat challenging. The challenge stems from the many requirements on the function including local refinements at both the leading and trailing edges, specification of the desired number of points along both the airfoil and along the aft line segments, and coarsening of the point distribution in the vicinity of the outer boundary. Several polynomial spacing functions were investigated in this research to meet these goals. The polynomial coefficients were set based on conditions on the point spacing or its derivatives. To meet the many requirements,

the polynomials were typically required to be of tenth or twelfth order, and even these high order functions did not provide a particularly pleasant point distribution.

Because of these difficulties with C–grids, an O–grid was chosen for final implementation in this research. The overall layout for the grid indices was taken to be the same as shown in Figure 8. The primary advantage of the O–topology is that it is straightforward to obtain smoothness along the entirety of both the interior and exterior boundaries. The exterior boundary can be selected as a circle and parameterized by specifying a constant angular increment. This method ensures smoothness of the boundary in both physical space as well as in the point spacing. Along the inner boundary, the problem of stitching aft–extending line segments is obviated, as the coordinate direction containing the inner boundary consists only of the airfoil itself.

In CFD applications, O–grids present difficulties, owing largely to the highly skewed and nonorthogonal cells that are formed at the trailing edge. Results indicate that this difficulty does not appear using the solution method presented in this dissertation. This occurrence is likely driven by the fact that the solution for the flow itself is found from a panel method and not from a finite difference or finite volume method. Panel methods require a smooth point distribution along the airfoil boundary, but there is no difficulty that stems from particular point distributions in the domain. In finite difference and finite volume methods, however, the nature of this domain distribution is critical.

The procedure for generating the initial grid is shown in Figure 10. We use a so–called "algebraic" grid generation method that develops the structured O–grid topology using simple functions. In generating this grid, we will treat the coordinate frame x^α as a Cartesian system.

The first step in this procedure is to set the outer boundary points. The primary requirements of the parametrization are to maintain adequate offset distance from the airfoil such that local flow disturbances in the neighborhood of the boundary are vanishingly weak and to ensure smoothness of the boundary shape and point distribution. In this research, we employ a circular outer boundary. The advantages of this shape are its smoothness in the physical plane and the simplicity of obtaining a smooth point distribution. The points

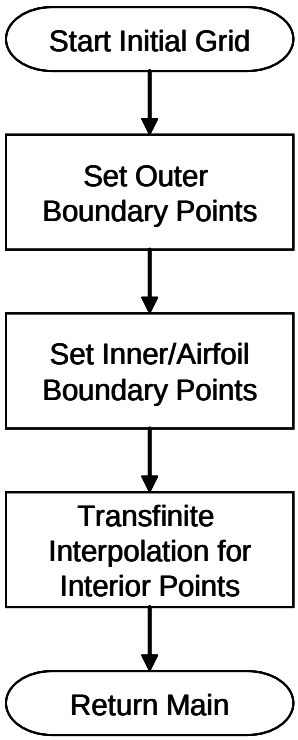

Figure 10: Procedure for Generation of the Initial Grid

comprising grid nodes of the circular outer boundary are specified according to the relation

$$\begin{aligned} x_{i,\,j_{max}} &= R\cos\chi_i + b \\ y_{i,\,j_{max}} &= R\sin\chi_i + c \end{aligned} \tag{230}$$

where χ_i is a central angle, R is a specified radius, and b and c are offsets to the origin of the circle. Typically, we set R in the range of $3 \leq R \leq 10$, $b = 1/2$, and $c = 0$. These values of b and c are selected to center the circle along the chord line and at the mid-chord location of the inner airfoil. Substantiation of the particular choice of R is provided in Chapter 6. The central angle χ_i is set as,

$$\chi_i = \frac{-2\pi\,(i-1)}{(i_{max}-1)}. \tag{231}$$

The next step in generating the grid is to specify the inner boundary grid nodes. These points are set to coincide with a particular airfoil or other body of interest. In this research, two example bodies are investigated for validation of the method: a circular body and a

NACA 0012 airfoil. The circular body is set using Equation 230 and Equation 231, by replacing $j = j_{max}$ with $j = 1$ and indicating the inner circle radius as r instead of R. Typical parameter settings are $r = 1/2$, $b = 1/2$, and $c = 0$. These settings prescribe a body with unit chord centered as $0 \leq x_{i,\,1} \leq 1$.

The NACA 0012 body is generated by the defining relations for NACA 4-series airfoils. A standard reference for these generating functions is Abbott and von Doenhoff's classical text [1]. We use these generating functions to produce the airfoil ordinate values $y_{i,\,1}$ comprising the inner domain boundary as a function of specified abscissa values $x_{i,\,1}$.

As described previously, the numerical method was found to be particularly sensitive to the type and smoothness of the point distributions along the boundary curves. This sensitivity has significant bearing on the choice of the distribution of the airfoil abscissa points $x_{i,\,1}$. In general, it is desirable to position points more densely around both the leading and trailing edges and to place points more coarsely around the remaining portions of the airfoil. However, investigations using the numerical method have shown that better results can be obtained by distributing the points more finely only at the leading edge. Locally refining the grid density at both the fore and aft ends of the airfoil was found to produce divergent behavior of the solution near the trailing edge.

An adequate point distribution was found to be obtained by using a sinusoidal function of the form

$$x_{i,\,1} = d\,(\cos\theta_i + 1) \tag{232}$$

with angles θ_i determined by a constant angular spacing as

$$\theta_i = \frac{\pi}{2} + \frac{\pi\,(i-1)}{(i_{max}-1)}. \tag{233}$$

This specification biases points toward the leading edge because the minimum of the half–period cosine function occurs at π which corresponds to the leading edge index. Results indicate that global refinements of point density can be achieved without trailing edge numerical difficulties by increasing i_{max}.

To produce an airfoil of unit chord, we take $d = 1$. In Chapter 6, we set $d = 1.0089$ to compare the results with those of Lock [73]. Whereas the NACA 4-series airfoils have a

finite trailing edge thickness, this alternate specification of d extends the airfoil such that the trailing edge approximately closes.

After the outer and inner boundary points have been set, the next step is to determine the interior grid points by interpolation. A variety of interpolation functions could be used, the simplest of which is linear interpolation in each of the coordinate directions. A more sophisticated approach is to choose interpolating functions that cluster points toward the interior boundary of the domain. This approach is useful because the steepest gradients in the flowfield occur near the body due to the maximum principle of subsonic flows [16], and it is typically advantageous to cluster points in the vicinities of the steepest gradients. Anticipating this behavior, we select interpolating functions containing exponential factors that clusters points near the body:

$$x_{i,\,j} = x_{i,\,1} + \frac{(x_{i,\,j_{max}} - x_{i,\,1})}{(\exp\zeta - 1)} \left(\exp\left[\frac{\zeta\,(j-1)}{(j_{max}-1)} \right] - 1 \right) \tag{234}$$

$$y_{i,\,j} = y_{i,\,1} + \frac{(y_{i,\,j_{max}} - y_{i,\,1})}{(\exp\zeta - 1)} \left(\exp\left[\frac{\zeta\,(j-1)}{(j_{max}-1)} \right] - 1 \right). \tag{235}$$

Here, ζ is a spacing parameter that is to be selected subject to $\zeta > 0$. In the limit of $\zeta \to 0$, linear interpolation is recovered.

An elliptic differential equation approach could be used for smoothing the interior points of the algebraic grid found in this process. As described previously, however, the solution appears to be very insensitive to skewing and non-orthogonality of points in the domain interior, as long as the boundary point distributions are smooth. An elliptic smoother was implemented and tested, but improvement in the quality of the results was found to be negligible, and the additional complexity was not needed. For this reason, elliptic smoothing is not used for the results obtained in this dissertation.

Once the interior points have been determined, the solution loop can be entered in order to converge the flow and geometry solutions. The first step in this loop is to calculate an estimate for the solution of the equivalent incompressible flow using a panel method. This topic is addressed in the next section.

5.3 Equivalent Incompressible Flow Solution

As described in Section 5.1, a panel method was chosen to solve the equivalent incompressible flow. The term "panel method" is used by practitioners in hydrodynamics and aerodynamics to refer to a particular class of boundary element methods that were developed chiefly by J. L. Hess and A. M. O. Smith at Douglas Aircraft during the 1960s [52].

Panel methods operate by using a Green's function approach to transform a domain integral for a partial differential equation into a boundary integral [58]. The boundary is then discretized into elements. Panel methods are given their name because the boundary elements can be thought of as small panels that are stitched together.

After discretizing the boundary, fundamental solutions to the field equation are then distributed along the panels. These distributed fundamental solutions, also known as particular solutions, are initially taken to have unknown *strengths*, which are simply multiplicative constants. For a linear partial differential equation, the fundamental solutions can be additively superimposed to produce new solutions that automatically satisfy the differential equation. For the case of incompressible aerodynamics and the equivalent incompressible flows of interest in this work, the relevant partial differential equation is the linear Laplace equation.

The solution of the boundary integral is achieved by determining the strengths of the distributed fundamental solutions in such a way that the boundary conditions are satisfied. The strengths are typically determined by posing and solving a linear system of equations that accounts for the influence of each fundamental solution on all of the boundary elements. Once the strengths are found, the potential and the fluid velocities can be determined both on the boundaries and throughout the interior of the domain.

Panel methods have attained a high level of development, and a wide variety of panel codes have been described in the literature. An excellent source outlining a variety of alternative implementations is the text by Katz and Plotkin [58]. Some of the primary alternatives may be categorized as follows:

- Order of panel strength distribution: point singularities, constant strength elements, linearly varying strength elements, higher order varying strength elements
- Types of fundamental solutions: sources, doublets, vortices
- Panel shape (for three–dimensional methods): triangular, quadrilateral

Even amongst this wide variety of possible implementations, however, most panel methods share a common overall algorithm. This procedure is outlined in Figure 11. The first step in the method is to discretize the panels and to determine their relevant geometric features including their orientation relative to a global reference system. Next, a matrix of *influence coefficients* is determined. The influence coefficients represent the normalized components of the perturbation velocities induced by any one panel on any other. In the next step, the influences of the freestream velocity components on all of the panels is computed and assembled into a vector. To impose the correct circulation on the flow, the Kutta condition is next applied by modifying the influence coefficients and freestream contributions such that the flow leaves the trailing edge smoothly. The linear system composed of the influence coefficient matrix and the freestream contribution vector is then solved to produce the strengths of the distributed fundamental solutions. Finally, surface velocities and integral measures such as the lift and moment coefficients are computed.

For this work, a particular choice of panel code implementation is not critical to the solution method. The objective is simply to develop a good solution for the equivalent incompressible flow. As we found in Section 4.4.1, the boundary conditions for the equivalent incompressible flow correspond to flow tangency. For this reason, any panel method that solves external incompressible flows with flow tangency boundary conditions is applicable for the overall solution approach developed in this research. This type of flow is the standard application for panel codes, and a vast number of possible implementations have been described in the literature. We may therefore think of the panel code as an off-the-shelf "drop in" component that can be selected and implemented without change for our solution method.

Although the choice is largely arbitrary, there are several desirable features that guide

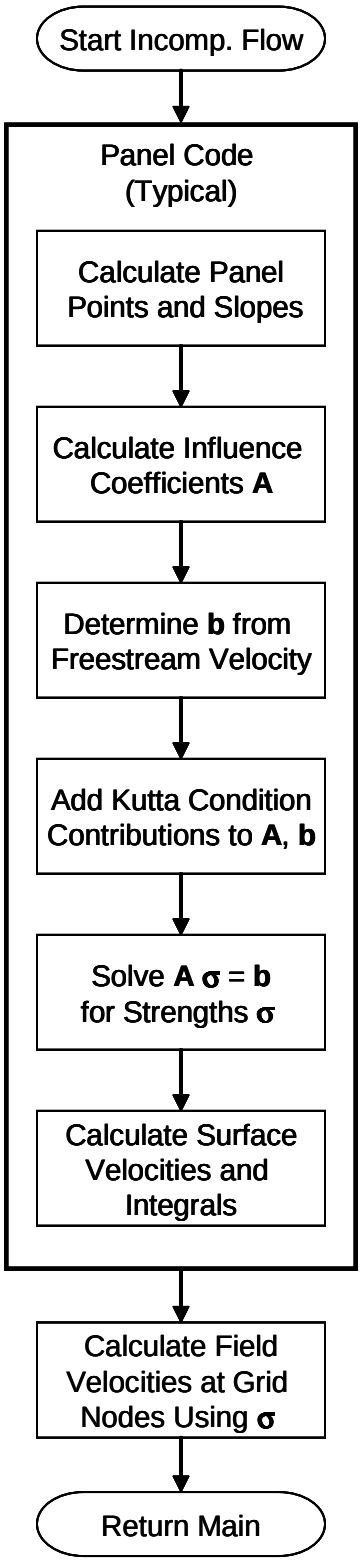

Figure 11: Panel Code Flow Solution

the selection of the method for this research. First, we need only a two–dimensional implementation. Second, we need a method that can be used to solve flows with circulation in anticipation of demonstrating the method for lifting airfoils. Typically, doublet or vortex singularity elements must be incorporated in the method for lifting flows, as sources can be used only to determine thickness effects. Third, the method should ideally allow for solutions to flows over airfoils with a finite trailing edge thickness. This capability is extremely useful because many tabulated airfoil shapes have trailing edges that do not close. Finally, the method must incorporate the ability to determine fluid velocities within the domain and not only at the body surface. The process of calculating velocities throughout the field is sometimes referred to as a *field survey*. Field surveys are necessary for our method because we must determine the metric tensor at all of the grid points within the solution domain, and the metric tensor is a function of the velocities at these points.

The only minor challenges among these requirements are the ability to deal with finite thickness trailing edges and the necessity for conducting field surveys. Many pedagogical panel method implementations such as those described by Katz and Plotkin lack these capabilities [58]. The approach taken in this work is to select an available panel code that has the capability for solving thick trailing edges and then to add an additional post-processing routine to conduct field surveys based on the determined solution strengths.

The panel code we select for this research is a formulation described by Moran and based on some of the earliest implementations developed by Hess and Smith [82]. The formulation consists of a constant–strength source panel method that incorporates a single discrete vortex located at the quarter–chord location. The source distribution accounts for the airfoil thickness effects and provides excellent ability for dealing with thick trailing edges. The discrete vortex is used to satisfy the Kutta condition and enforce the proper circulation for lifting cases. We will not discuss the details of the method here, as the formulation is typical and described in the literature. The reader is referred to the reference above for detailed descriptions and code implementation.

Although we will not describe the details of the panel solution method itself, we will

briefly outline the additional post-processing capability implemented to perform field surveys. This capability was not originally included in the code developed by Moran, but it represents only a minor extension. To determine the velocity at an arbitrary field point, an identical algorithm to that used for the calculation of the influence coefficients is employed. Only two changes to this algorithm are introduced. First, the coordinates of the field point replace the coordinates of the panel on which the influence is to be calculated. That is, we evaluate the influence of the fundamental solutions at all of the panels on the field point. Second, because the source strengths are already known from the solution of the linear system of the panel influences, we multiply the normalized influences of each panel by their respective strengths. With these two changes, the influences of each of the panels are summed to determine the total perturbation velocities at any field point. This overall approach is applicable for implementing field survey capability in panel codes of all types. For use in this research, the field survey technique is used to determine the velocities at the grid nodes throughout the domain.

There remains one additional caveat with the field survey that is related to the grid node points located on the surface of the immersed body. To describe the airfoil shape to the panel code, we provide the geometry along the innermost j grid line. The velocities at these grid nodes will be needed to develop the metric tensor values that define the curvilinear coordinate transformation along the body surface. The problem is that these surface grid nodes correspond to endpoints of the panels discretized by the panel code. Based on the formulation of the singularity solutions, the velocities induced at these endpoints by the adjacent panels are infinite. In reality, these contributions have effects that balance each other to produce a finite velocity at these surface nodes; however, we must do something special at these points for the numerical implementation. The choice we make in this work is instead to determine the velocities at the panel centers and then to interpolate to the panel endpoints. This interpolation process is found to be effective for generating the required data at the surface nodes.

After an estimate for the equivalent incompressible flow has been developed using the panel method procedure, the next step in the algorithm is to determine the metric tensor

throughout the domain. In addition to calculating the metric tensor in the original compressible flow reference frame, we will also need to transform the tensor to a computational coordinate system to facilitate the coordinate mapping solution. These steps are the focus of the next section.

5.4 Metric Tensor Calculation

The procedure for calculating the metric tensor is shown in Figure 12. The process consists of four primary steps. First, we calculate a series of coordinate transformation derivatives linking the original compressible flow reference frame both to the frame of the equivalent incompressible flow and to the auxiliary computational reference frame. Second, we transform the velocities for the equivalent incompressible flow obtained through the panel code solution to the compressible flow frame. Third, the metric tensor in the original compressible flow frame is computed. Finally, the resulting metric tensor is transformed to the auxiliary computational frame for use in the subsequent coordinate mapping.

We first describe the generation of the transformation derivatives to the auxiliary computational frame $\tilde{x}^\alpha$. We will need derivatives relative both to the original frame x^α and to the isothermal frame $\bar{x}^\alpha$. The derivatives linking the original frame x^α to the computational frame need to be computed only once based on the initial structured grid, whereas the derivatives involving the isothermal frame $\bar{x}^\alpha$ must be computed at each iteration of the solution loop because the coordinate values $\bar{x}^\alpha$ change as the solution converges.

The relevant derivatives can be expressed in tensorial form as $\frac{\partial x^\mu}{\partial \tilde{x}^\nu}$, $\frac{\partial \bar{x}^\mu}{\partial \tilde{x}^\nu}$, $\frac{\partial \tilde{x}^\mu}{\partial x^\nu}$, and $\frac{\partial \tilde{x}^\mu}{\partial \bar{x}^\nu}$. For notational convenience, we will continue the practice adopted in prior sections of this chapter of identifying $x = x^1$, $y = x^2$, $\bar{x} = \bar{x}^1$, $\bar{y} = \bar{x}^2$, $\tilde{x} = \tilde{x}^1$, and $\tilde{y} = \tilde{x}^2$. The coordinate $\tilde{x}$ is identical to the i index in the structured grid, and $\tilde{y}$ is identical to the j index.

To calculate the x^α and $\bar{x}^\alpha$ derivatives with respect to $\tilde{x}^\alpha$, we use finite difference approximations. For derivatives at interior points, we use second order accurate central differences such as

$$\left.\frac{\partial x}{\partial \tilde{x}}\right|_{i,\,j} = \frac{x_{i+1,\,j} - x_{i-1,\,j}}{(i+1) - (i-1)} = \frac{x_{i+1,\,j} - x_{i-1,\,j}}{2} \tag{236}$$

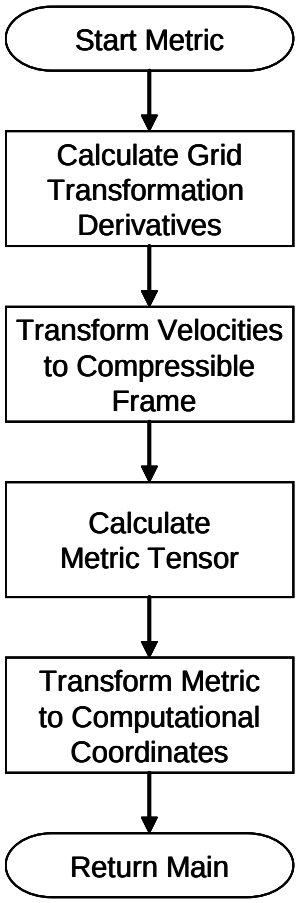

Figure 12: Metric Computation

and

$$\left.\frac{\partial x}{\partial \tilde{y}}\right|_{i,\,j} = \frac{x_{i,\,j+1} - x_{i,\,j-1}}{(j+1)-(j-1)} = \frac{x_{i,\,j+1} - x_{i,\,j-1}}{2}. \tag{237}$$

At the $i = 1$ and $j = 1$ boundaries, we use first order one sided differences such as

$$\left.\frac{\partial x}{\partial \tilde{x}}\right|_{1,\,j} = \frac{x_{2,\,j} - x_{1,\,j}}{2-1} = x_{2,\,j} - x_{1,\,j} \tag{238}$$

and

$$\left.\frac{\partial x}{\partial \tilde{y}}\right|_{i,\,1} = \frac{x_{i,\,2} - x_{i,\,1}}{2-1} = x_{i,\,2} - x_{i,\,1}, \tag{239}$$

whereas along $i = i_{max}$ and $j = j_{max}$ boundaries, we employ differences such as,

$$\left.\frac{\partial x}{\partial \tilde{x}}\right|_{i_{max},\,j} = \frac{x_{i_{max},\,j} - x_{i_{max}-1,\,j}}{i_{max} - (i_{max}-1)} = x_{i_{max},\,j} - x_{i_{max}-1,\,j} \tag{240}$$

and

$$\left.\frac{\partial x}{\partial \tilde{y}}\right|_{i,\,j_{max}} = \frac{x_{i,\,j_{max}} - x_{i,\,j_{max}-1}}{j_{max} - (j_{max}-1)} = x_{i,\,j_{max}} - x_{i,\,j_{max}-1}. \tag{241}$$

Similar relations hold for the other coordinate derivatives with respect to $\tilde{x}^\alpha$. In all of the finite differences presented above, subscripts refer to relative locations in the structured grid and not to covariant tensor indices.

Once these derivatives have been computed, we can calculate the corresponding inverse derivatives as

$$\begin{aligned}
\frac{\partial \tilde{x}}{\partial x} &= \frac{1}{J}\frac{\partial y}{\partial \tilde{y}} \\
\frac{\partial \tilde{x}}{\partial y} &= -\frac{1}{J}\frac{\partial x}{\partial \tilde{y}} \\
\frac{\partial \tilde{y}}{\partial x} &= -\frac{1}{J}\frac{\partial y}{\partial \tilde{x}} \\
\frac{\partial \tilde{y}}{\partial y} &= \frac{1}{J}\frac{\partial x}{\partial \tilde{x}}
\end{aligned} \tag{242}$$

where

$$J = \frac{\partial x}{\partial \tilde{x}}\frac{\partial y}{\partial \tilde{y}} - \frac{\partial x}{\partial \tilde{y}}\frac{\partial y}{\partial \tilde{x}} \tag{243}$$

is the Jacobian of the transformation. These relations are obtained by taking the inverse of the matrix whose elements are the derivatives $\frac{\partial x^\mu}{\partial \tilde{x}^\nu}$. Similar relations hold for the inverse derivatives of $\bar{x}^\alpha$ with respect to $\tilde{x}^\alpha$.

After calculating all of the derivatives linking the frames x^α and $\bar{x}^\alpha$ to the computational frame $\tilde{x}^\alpha$, we can compute the derivatives directly linking x^α to $\bar{x}^\alpha$. These can be computed by the transformation law for covariant vectors. For example, we can write

$$\begin{aligned} \frac{\partial \bar{x}}{\partial x} &= \frac{\partial \bar{x}}{\partial \tilde{x}} \frac{\partial \tilde{x}}{\partial x} + \frac{\partial \bar{x}}{\partial \tilde{y}} \frac{\partial \tilde{y}}{\partial x} \\ \frac{\partial \bar{x}}{\partial y} &= \frac{\partial \bar{x}}{\partial \tilde{x}} \frac{\partial \tilde{x}}{\partial y} + \frac{\partial \bar{x}}{\partial \tilde{y}} \frac{\partial \tilde{y}}{\partial y} \end{aligned} \tag{244}$$

and similar relations for the $\bar{y}$ derivatives. Once these derivatives have been computed, we can proceed to the next step in computing the metric tensor—transforming the velocities.

The metric tensor derived in Chapter 4 was found to be a function of the covariant velocity components in the coordinate system x^α of the originally given subsonic flow. In the previous section, we discussed how the velocities of the equivalent incompressible flow are determined in the isothermal coordinate system $\bar{x}^\alpha$ by a panel method. To calculate the metric, we need to transform these velocities to the original frame x^α using the coordinate derivatives determined by Equation 244. As we saw in Section 4.4.2, the covariant velocities transform as

$$u_\mu = \bar{u}_\nu \frac{\partial \bar{x}^\nu}{\partial x^\mu}. \tag{245}$$

Expanding this tensor expression and making the notational identifications $x^1 = x$, $x^2 = y$, etc., we obtain

$$\begin{aligned} u_1 &= \bar{u}_1 \frac{\partial \bar{x}}{\partial x} + \bar{u}_2 \frac{\partial \bar{y}}{\partial x} \\ u_2 &= \bar{u}_1 \frac{\partial \bar{x}}{\partial y} + \bar{u}_2 \frac{\partial \bar{y}}{\partial y}. \end{aligned} \tag{246}$$

After the velocities in the frame of the given subsonic flow have been computed through Equation 246, we can now proceed to calculate the metric in this frame. We will actually have need only of the metric tensor expression $\sqrt{g}g^{\mu\nu}$ and not of the metric tensor itself; however, as we saw in Section 4.2, this expression is simply the representation of all metrics

in the same conformal equivalence class. Since all metrics in this class are equivalent in terms of the approach in this thesis, we can abuse the terminology slightly and identify $\sqrt{g}g^{\mu\nu}$ simply as the metric tensor.

In Section 5.2, we defined the frame x^α as a Cartesian coordinate system. We can therefore use the metric tensor that we developed for Cartesian systems in Section 4.2. We repeat this expression, which was given as Equation 129 as

$$\begin{aligned}
\sqrt{g}g^{11} &= \frac{(u_1)^2\left(\frac{\rho}{\rho_0}\right)^2 + (u_2)^2}{\left(\frac{\rho}{\rho_0}\right)\left[(u_1)^2 + (u_2)^2\right]} \\
\sqrt{g}g^{12} &= \frac{\left[\left(\frac{\rho}{\rho_0}\right)^2 - 1\right] u_1 u_2}{\left(\frac{\rho}{\rho_0}\right)\left[(u_1)^2 + (u_2)^2\right]} \\
\sqrt{g}g^{22} &= \frac{(u_2)^2\left(\frac{\rho}{\rho_0}\right)^2 + (u_1)^2}{\left(\frac{\rho}{\rho_0}\right)\left[(u_1)^2 + (u_2)^2\right]}.
\end{aligned} \tag{247}$$

The density can be calculated from Equation 103 which we repeat here as

$$\frac{\rho}{\rho_0} = \left(1 - \frac{\gamma - 1}{2\,{a_0}^2}\,V^2\right)^{1/(\gamma-1)} \tag{248}$$

where $V^2 = (u_1)^2 + (u_2)^2$.

The last step in the computation procedure is to transform this metric tensor to the computational coordinate system. This form is necessary for the coordinate mapping solution that is described in the next section. We can determine this transformation by considering the transformation law for the contravariant metric tensor:

$$\tilde{g}^{\mu\nu} = g^{\alpha\beta}\,\frac{\partial \tilde{x}^\mu}{\partial x^\alpha}\,\frac{\partial \tilde{x}^\nu}{\partial x^\beta}. \tag{249}$$

Multiplying this expression by $\sqrt{\tilde{g}}$ gives,

$$\sqrt{\tilde{g}}\tilde{g}^{\mu\nu} = \sqrt{\tilde{g}}g^{\alpha\beta}\,\frac{\partial \tilde{x}^\mu}{\partial x^\alpha}\,\frac{\partial \tilde{x}^\nu}{\partial x^\beta}. \tag{250}$$

As shown in Synge and Schild [106], $\sqrt{\tilde{g}}$ and $\sqrt{g}$ can be related as

$$\sqrt{\tilde{g}} = J\sqrt{g} \tag{251}$$

where J is the Jacobian given by Equation 243. Substituting Equation 251 into Equation 250 results in

$$\sqrt{\tilde{g}}\tilde{g}^{\mu\nu} = J\sqrt{g}g^{\alpha\beta}\frac{\partial\tilde{x}^{\mu}}{\partial x^{\alpha}}\frac{\partial\tilde{x}^{\nu}}{\partial x^{\beta}}. \tag{252}$$

Expanding this tensorial relation and using the notational convention of this chapter gives

$$\begin{aligned}
\sqrt{\tilde{g}}\tilde{g}^{11} &= J\left\{\left(\frac{\partial\tilde{x}}{\partial x}\right)^2\sqrt{g}g^{11} + 2\left(\frac{\partial\tilde{x}}{\partial x}\right)\left(\frac{\partial\tilde{x}}{\partial y}\right)\sqrt{g}g^{12} + \left(\frac{\partial\tilde{x}}{\partial y}\right)^2\sqrt{g}g^{22}\right\} \\
\sqrt{\tilde{g}}\tilde{g}^{12} &= J\left\{\left(\frac{\partial\tilde{x}}{\partial x}\right)\left(\frac{\partial\tilde{y}}{\partial x}\right)\sqrt{g}g^{11} + \left[\left(\frac{\partial\tilde{x}}{\partial x}\right)\left(\frac{\partial\tilde{y}}{\partial y}\right) + \left(\frac{\partial\tilde{x}}{\partial y}\right)\left(\frac{\partial\tilde{y}}{\partial x}\right)\right]\sqrt{g}g^{12}\right. \\
&\quad \left. + \left(\frac{\partial\tilde{x}}{\partial y}\right)\left(\frac{\partial\tilde{y}}{\partial y}\right)\sqrt{g}g^{22}\right\} \\
\sqrt{\tilde{g}}\tilde{g}^{22} &= J\left\{\left(\frac{\partial\tilde{y}}{\partial x}\right)^2\sqrt{g}g^{11} + 2\left(\frac{\partial\tilde{y}}{\partial x}\right)\left(\frac{\partial\tilde{y}}{\partial y}\right)\sqrt{g}g^{12} + \left(\frac{\partial\tilde{y}}{\partial y}\right)^2\sqrt{g}g^{22}\right\}.
\end{aligned} \tag{253}$$

These relations are the desired form of the metric tensor in the computational coordinate system that are necessary for the coordinate mapping algorithm presented in the next section.

5.5 Coordinate Mapping Solution

As we saw in Section 4.3.2, the partial differential equations governing the coordinate mapping are elliptic. A variety of numerical techniques are available for the solution of elliptic partial differential equations. Several categories of methods such as finite difference, finite volume, finite element, and spectral element techniques involve the discretization of the solution domain [107]. The governing equations are then solved at points, volumes, or elements within this domain. This series of techniques have formed the basis for modern computational fluid dynamics.

Another class of methods involves the conversion of arbitrary elliptic equations into a canonical form of the Poisson equation [65]. Once a Poisson form is obtained, Green's functions are used to develop and superimpose fundamental solutions at points distributed on the boundary and within the domain. For nonlinear problems, the particular solutions at these field points must typically be iteratively updated and converged.

The focus of this research is not to investigate subtleties associated with particular elliptic boundary value problem methods; rather, we desire a method that is well established and understood in the computational fluid dynamics community. As with the case of the panel code implementation, we ideally prefer a solution method that has been validated and documented in the literature. For this reason, we pursue a finite difference solution technique in this research. Finite difference techniques comprise the most widely investigated class of methods for the solution of elliptic boundary value problems, and a variety of specific finite difference approaches for are available in standard texts [28, 107].

One requirement of finite difference approaches is that the domain be discretized in a structured manner such that finite difference approximations to derivatives can easily be computed. This requirement has motivated the use of the types of structured grids discussed in this chapter.

Within the category of finite difference methods for elliptic boundary value problems, a variety of specific techniques are available. Among these are the point iterative techniques including the Jacobi method, the Gauss–Seidel method, and the Successive Over-Relaxation (SOR) refinement to Gauss–Seidel. More advanced line and block iterative methods include Successive Over-Relaxation by Lines (SLOR) and Alternating Direction Implicit (ADI) methods [28]. These finite difference methods have been used extensively for the problem of coordinate mappings, especially in the context of elliptic smoothing of structured grids. In the line iterative methods, the approach consists of the following overall steps.

- Discretize the partial differential equation for the coordinate mapping by developing finite difference approximations to the derivatives.
- Arrange the terms in these discretized equations to form a linear system that allows the coordinates to be determined along a particular grid line as a function of points on adjacent grid lines.
- Sweep through the grid, solving the linear system at each line.
- Iterate through the grid sweep until the coordinate mapping converges.

Aside from these general steps, each of the methods has particular subtleties to its implementation. These subtleties lead to differences in the rate of convergence and stability of each method. For instance, the point Jacobi approach uses coordinate values only from the prior iteration in solving the linear system, whereas the Gauss–Seidel method uses coordinate values as soon as they become available in the grid sweep [107]. For this reason, the Gauss–Seidel method generally converges in many fewer iterations than point Jacobi. The SLOR method improves over the line Gauss–Seidel method by over-relaxing the values of the coordinates obtained in each iteration to further speed convergence. Over-relaxation is a process of creating a linear combination of the prior iteration value and the current iteration value that is substantially biased toward the current value. In general, the tradeoff with higher converge rate is typically reduced stability for certain types of boundary value problems.

In this work, both line Gauss–Seidel and SLOR methods were investigated. No stability problems were encountered in the transition from Gauss–Seidel to SLOR, and the latter method proved to converge in fewer iterations than by as much as a factor of five. For this reason, we choose the SLOR method for the final implementation in this research.

The SLOR algorithm implemented to generate the isothermal coordinate transformation is presented in Figure 13. The first step in the procedure is to calculate finite difference expressions for the derivatives of the metric tensor expression $\sqrt{\tilde{g}}\tilde{g}^{\mu\nu}$ with respect to the computational coordinates $\tilde{x}^{\alpha}$. These derivatives are needed only at interior grid points, so we employ a second order central difference stencil to arrive at the following expressions

$$\left.\frac{\partial\left(\sqrt{\tilde{g}}\tilde{g}^{\mu\nu}\right)}{\partial\tilde{x}}\right|_{i,j} = \frac{\left(\sqrt{\tilde{g}}\tilde{g}^{\mu\nu}\right)_{i+1,\,j} - \left(\sqrt{\tilde{g}}\tilde{g}^{\mu\nu}\right)_{i-1,\,j}}{2} \tag{254}$$

$$\left.\frac{\partial\left(\sqrt{\tilde{g}}\tilde{g}^{\mu\nu}\right)}{\partial\tilde{y}}\right|_{i,j} = \frac{\left(\sqrt{\tilde{g}}\tilde{g}^{\mu\nu}\right)_{i,\,j+1} - \left(\sqrt{\tilde{g}}\tilde{g}^{\mu\nu}\right)_{i,\,j-1}}{2} \tag{255}$$

that are valid for all μ and ν. These derivatives are computed first in the algorithm because their values do not change during the convergence iterations, so the values can be stored and reused as needed.

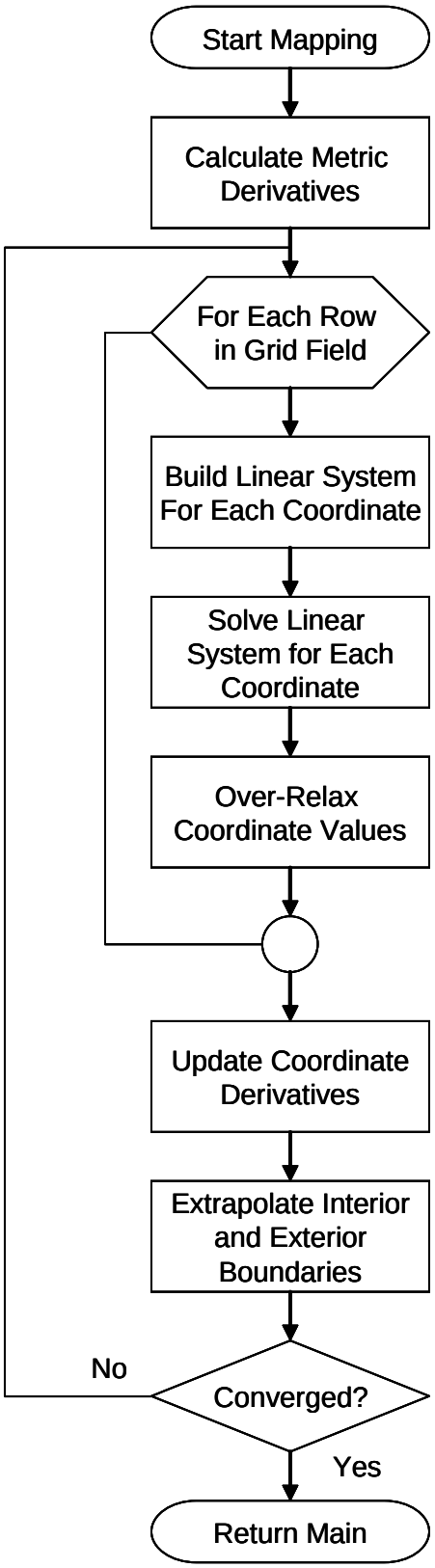

Figure 13: Successive Over–Relaxation by Lines (SLOR) Mapping Solution

Once these derivatives have been computed, a loop is then entered to converge the coordinate mapping. Within this convergence loop, the algorithm successively sweeps through the interior j lines in the grid ranging from $j = 2$ to $j = j_{max} - 1$. At each line in the sweep, the first step is to calculate a matrix that represents the factors in the discretized differential equations that multiply the coordinate values on the particular j line. Next, we calculate two vectors, one corresponding to each isothermal coordinate, that form the right hand sides of the linear systems to determine each coordinate. As with the matrix, these vectors also emerge from the discretized differential equations for the coordinate mapping, but their elements involve coordinates only on lines $j-1$ that have already been determined in the row-wise sweep or on values determined during the previous sweep in the convergence loop. With these vectors established, the linear systems are then solved to determine estimates for the isothermal coordinates on the particular j line.

To form the linear systems, we need to discretize the partial differential equations of the coordinate mapping. As we saw in Section 4.3.2, these equations, given originally as Equations 155, are

$$\begin{aligned} \frac{\partial}{\partial \tilde{x}^\beta}\left(\sqrt{\tilde{g}}\,\tilde{g}^{\beta\lambda}\,\frac{\partial \bar{x}^1}{\partial \tilde{x}^\lambda}\right) &= 0 \\ \frac{\partial}{\partial \tilde{x}^\beta}\left(\sqrt{\tilde{g}}\,\tilde{g}^{\beta\lambda}\,\frac{\partial \bar{x}^2}{\partial \tilde{x}^\lambda}\right) &= 0. \end{aligned} \tag{256}$$

Expanding the first equation and employing the notation adopted for this chapter of $\bar{x}^1 = \bar{x}$, $\bar{x}^2 = \bar{y}$, etc., we obtain

$$\begin{aligned} \sqrt{\tilde{g}}\tilde{g}^{11}\,\frac{\partial^2 \bar{x}}{\partial \tilde{x}^2} + 2\,\sqrt{\tilde{g}}\tilde{g}^{12}\,\frac{\partial^2 \bar{x}}{\partial \tilde{x}\partial \tilde{y}} + \sqrt{\tilde{g}}\tilde{g}^{22}\,\frac{\partial^2 \bar{x}}{\partial \tilde{y}^2} + \left[\frac{\partial\left(\sqrt{\tilde{g}}\tilde{g}^{11}\right)}{\partial \tilde{x}}\right. \\ \left. + \frac{\partial\left(\sqrt{\tilde{g}}\tilde{g}^{12}\right)}{\partial \tilde{y}}\right]\,\frac{\partial \bar{x}}{\partial \tilde{x}} + \left[\frac{\partial\left(\sqrt{\tilde{g}}\tilde{g}^{12}\right)}{\partial \tilde{x}} + \frac{\partial\left(\sqrt{\tilde{g}}\tilde{g}^{22}\right)}{\partial \tilde{y}}\right]\,\frac{\partial \bar{x}}{\partial \tilde{y}} &= 0 \end{aligned} \tag{257}$$

In addition to the finite difference expressions for the derivatives of the metric tensor given by Equations 255, we also need expressions for the other derivatives. The relations for the first order derivatives of the isothermal coordinates $\frac{\partial \bar{x}^\mu}{\partial \tilde{x}^\nu}$ are identical in form to those presented in Section 5.4 as Equation 236 and Equation 237. Expressions for the second order derivatives are also needed. Using second order central difference stencils for these

derivatives, we have

$$\left.\frac{\partial^2 \bar{x}}{\partial \tilde{x}^2}\right|_{i,j} = \bar{x}_{i+1,j} - 2\,\bar{x}_{i,j} + \bar{x}_{i-1,j} \tag{258}$$

$$\left.\frac{\partial^2 \bar{x}}{\partial \tilde{x}\partial \tilde{y}}\right|_{i,j} = \frac{\bar{x}_{i+1,j+1} - \bar{x}_{i+1,j-1} - \bar{x}_{i-1,j+1} + \bar{x}_{i-1,j-1}}{4} \tag{259}$$

$$\left.\frac{\partial^2 \bar{x}}{\partial \tilde{y}^2}\right|_{i,j} = \bar{x}_{i,j+1} - 2\,\bar{x}_{i,j} + \bar{x}_{i,j-1} \tag{260}$$

as shown in [107].

Next, we substitute the first and second derivative finite difference expressions for $\bar{x}$ into Equation 257. For now, we do not substitute the difference expressions for the metric derivatives. Additionally, we assign a superscript iteration index $n-1$ to $\bar{x}$ terms on the $j+1$ line and an index n to terms on the j and $j-1$ lines. The metric tensor derivatives are given an index of $n-1$. These substitutions result in the equation

$$\begin{aligned}
&\left(\sqrt{\tilde{g}}\tilde{g}^{11}\right)_{i,j}^{n-1}\left[\bar{x}_{i+1,j}^{n} - 2\,\bar{x}_{i,j}^{n} + \bar{x}_{i-1,j}^{n}\right] + \frac{1}{2}\left(\sqrt{\tilde{g}}\tilde{g}^{12}\right)_{i,j}^{n-1}\left[\bar{x}_{i+1,j+1}^{n-1} - \bar{x}_{i+1,j-1}^{n}\right. \\
&\qquad \left. - \bar{x}_{i-1,j+1}^{n-1} + \bar{x}_{i-1,j-1}^{n}\right] + \left(\sqrt{\tilde{g}}\tilde{g}^{22}\right)_{i,j}^{n-1}\left[\bar{x}_{i,j+1}^{n-1} - 2\,\bar{x}_{i,j}^{n} + \bar{x}_{i,j-1}^{n}\right] \\
&\qquad + \frac{1}{2}\left[\left.\frac{\partial\left(\sqrt{\tilde{g}}\tilde{g}^{11}\right)}{\partial \tilde{x}}\right|_{i,j}^{n-1} + \left.\frac{\partial\left(\sqrt{\tilde{g}}\tilde{g}^{12}\right)}{\partial \tilde{y}}\right|_{i,j}^{n-1}\right]\left[\bar{x}_{i+1,j}^{n} - \bar{x}_{i-1,j}^{n}\right] \\
&\qquad + \frac{1}{2}\left[\left.\frac{\partial\left(\sqrt{\tilde{g}}\tilde{g}^{12}\right)}{\partial \tilde{x}}\right|_{i,j}^{n-1} + \left.\frac{\partial\left(\sqrt{\tilde{g}}\tilde{g}^{22}\right)}{\partial \tilde{y}}\right|_{i,j}^{n-1}\right]\left[\bar{x}_{i,j+1}^{n-1} - \bar{x}_{i,j-1}^{n}\right] \\
&\qquad = 0
\end{aligned} \tag{261}$$

We now group terms such that Equation 261 takes on the form

$$A_{i,j}\,\bar{x}_{i-1,j}^{n} + B_{i,j}\,\bar{x}_{i,j}^{n} + C_{i,j}\,\bar{x}_{i+1,j}^{n} = D_{i,j} \tag{262}$$

where $A_{i,j}$, $B_{i,j}$, and $C_{i,j}$ are given by

$$\begin{aligned}
A_{i,j} &= \left(\sqrt{\tilde{g}}\tilde{g}^{11}\right)_{i,j}^{n-1} - \frac{1}{2}\left[\frac{\partial\left(\sqrt{\tilde{g}}\tilde{g}^{11}\right)}{\partial\tilde{x}}\bigg|_{i,j}^{n-1} + \frac{\partial\left(\sqrt{\tilde{g}}\tilde{g}^{12}\right)}{\partial\tilde{y}}\bigg|_{i,j}^{n-1}\right] \\
B_{i,j} &= -2\left[\left(\sqrt{\tilde{g}}\tilde{g}^{11}\right)_{i,j}^{n-1} + \left(\sqrt{\tilde{g}}\tilde{g}^{22}\right)_{i,j}^{n-1}\right] \\
C_{i,j} &= \left(\sqrt{\tilde{g}}\tilde{g}^{11}\right)_{i,j}^{n-1} + \frac{1}{2}\left[\frac{\partial\left(\sqrt{\tilde{g}}\tilde{g}^{11}\right)}{\partial\tilde{x}}\bigg|_{i,j}^{n-1} + \frac{\partial\left(\sqrt{\tilde{g}}\tilde{g}^{12}\right)}{\partial\tilde{y}}\bigg|_{i,j}^{n-1}\right].
\end{aligned} \tag{263}$$

and $D_{i,j}$ is

$$\begin{aligned}
D_{i,j} &= -2\left(\sqrt{\tilde{g}}\tilde{g}^{12}\right)_{i,j}^{n-1}\left[\frac{\bar{x}_{i+1,j+1}^{n-1} - \bar{x}_{i+1,j-1}^{n-1} - \bar{x}_{i-1,j+1}^{n-1} + \bar{x}_{i-1,j-1}^{n-1}}{4}\right] \\
&\quad - \left[\left(\sqrt{\tilde{g}}\tilde{g}^{22}\right)_{i,j}^{n-1} + \frac{1}{2}\left(\frac{\partial\left(\sqrt{\tilde{g}}\tilde{g}^{12}\right)}{\partial\tilde{x}}\bigg|_{i,j}^{n-1} + \frac{\partial\left(\sqrt{\tilde{g}}\tilde{g}^{22}\right)}{\partial\tilde{y}}\bigg|_{i,j}^{n-1}\right)\right]\bar{x}_{i,j+1}^{n-1} \\
&\quad - \left[\left(\sqrt{\tilde{g}}\tilde{g}^{22}\right)_{i,j}^{n-1} - \frac{1}{2}\left(\frac{\partial\left(\sqrt{\tilde{g}}\tilde{g}^{12}\right)}{\partial\tilde{x}}\bigg|_{i,j}^{n-1} + \frac{\partial\left(\sqrt{\tilde{g}}\tilde{g}^{22}\right)}{\partial\tilde{y}}\bigg|_{i,j}^{n-1}\right)\right]\bar{x}_{i,j-1}^{n-1}.
\end{aligned} \tag{264}$$

Equation 262 can be recognized as the formulation of our desired linear system by rewriting it as

$$\begin{bmatrix}
B_{1,j} & C_{1,j} & 0 & \dots & 0 \\
A_{2,j} & B_{2,j} & C_{2,j} & \ddots & \vdots \\
0 & A_{3,j} & \ddots & \ddots & 0 \\
\vdots & \ddots & \ddots & \ddots & C_{i_{max}-1,j} \\
0 & \dots & 0 & A_{i_{max},j} & B_{i_{max},j}
\end{bmatrix}
\begin{bmatrix}
\bar{x}_{1,j}^{n} \\ \bar{x}_{2,j}^{n} \\ \vdots \\ \vdots \\ \bar{x}_{i_{max},j}^{n}
\end{bmatrix} =
\begin{bmatrix}
D_{1,j} \\ D_{2,j} \\ \vdots \\ \vdots \\ D_{i_{max},j}
\end{bmatrix}. \tag{265}$$

Proceeding in an exactly analogous way for $\bar{y}$ we obtain the equation

$$A_{i,j}\,\bar{y}_{i-1,j}^{n} + B_{i,j}\,\bar{y}_{i,j}^{n} + C_{i,j}\,\bar{y}_{i+1,j}^{n} = E_{i,j} \tag{266}$$

where $A_{i,j}$, $B_{i,j}$, and $C_{i,j}$ are defined identically to the case for $\bar{x}$ through Equation 263

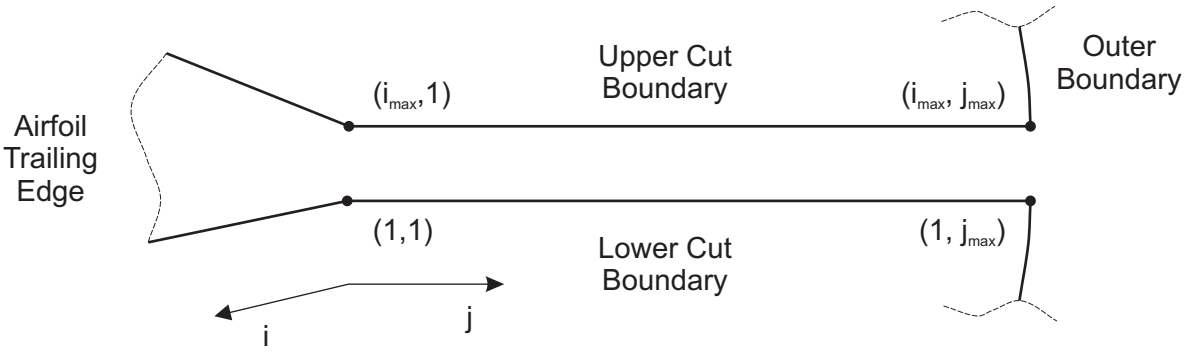

Figure 14: Detail of O–Grid Cut Boundaries

and $E_{i,j}$ is found to be

$$\begin{aligned} E_{i,j} &= -2\left(\sqrt{\tilde{g}}\tilde{g}^{12}\right)_{i,j}^{n-1}\left[\frac{\bar{y}_{i+1,j+1}^{n-1}-\bar{y}_{i+1,j-1}^{n-1}-\bar{y}_{i-1,j+1}^{n-1}+\bar{y}_{i-1,j-1}^{n-1}}{4}\right] \\ &\quad -\left[\left(\sqrt{\tilde{g}}\tilde{g}^{22}\right)_{i,j}^{n-1}+\frac{1}{2}\left(\frac{\partial\left(\sqrt{\tilde{g}}\tilde{g}^{12}\right)}{\partial\tilde{x}}\bigg|_{i,j}^{n-1}+\frac{\partial\left(\sqrt{\tilde{g}}\tilde{g}^{22}\right)}{\partial\tilde{y}}\bigg|_{i,j}^{n-1}\right)\right]\bar{y}_{i,j+1}^{n-1} \\ &\quad -\left[\left(\sqrt{\tilde{g}}\tilde{g}^{22}\right)_{i,j}^{n-1}-\frac{1}{2}\left(\frac{\partial\left(\sqrt{\tilde{g}}\tilde{g}^{12}\right)}{\partial\tilde{x}}\bigg|_{i,j}^{n-1}+\frac{\partial\left(\sqrt{\tilde{g}}\tilde{g}^{22}\right)}{\partial\tilde{y}}\bigg|_{i,j}^{n-1}\right)\right]\bar{y}_{i,j-1}^{n-1}. \quad (267) \end{aligned}$$

Before solving these linear systems to determine the isothermal coordinate values on a particular j line, we must apply the appropriate boundary conditions along the lines $i = 1$ and $i = i_{max}$. These lines corresponds to the cut lines in the O–grid topology that extend downstream from the airfoil trailing edge and connect to the outer boundary circle. In an O–grid surrounding an airfoil, these cut lines will be nearly coincident with a gap corresponding to any finite thickness of the trailing edge. A detail of these lines is shown in Figure 14.

In posing the boundary value problem in Section 4.3.2, we did not discuss boundary conditions along these lines, largely because we had not yet chosen a particular topology and introduced a grid. However, as we saw in Section 4.3.2, we have the freedom to specify a boundary condition on any one coordinate at all boundaries. Therefore, we will choose to specify the condition $\bar{y} = y$ along these boundaries. The values for $\bar{x}$ will then be obtained by linear extrapolation from the grid interior. Using this approach, the $\bar{x}$ coordinates will

relax to the appropriate final values as the solution converges.

These boundary conditions along the grid cuts must be imposed as conditions on the linear systems given by Equations 262 and Equation 266. To impose the $\bar{y} = y$ condition, we redefine the boundary elements of $A_{i,j}$, $B_{i,j}$, $C_{i,j}$, and $E_{i,j}$ as

$$\begin{aligned} A_{1,j} = A_{i_{max},j} &= 0 \\ B_{1,j} = B_{i_{max},j} &= 1 \\ C_{1,j} = C_{i_{max},j} &= 0 \\ E_{1,j} &= x_{1,j} \\ E_{i_{max},j} &= x_{i_{max},j}. \end{aligned} \tag{268}$$

The values of $\bar{x}$ are found from extrapolation using the second order one-sided finite difference expressions

$$\left.\frac{\partial \bar{x}}{\partial \tilde{x}}\right|_{1,j} = \frac{-3\,\bar{x}_{1,j} + 4\,\bar{x}_{2,j} - \bar{x}_{3,j}}{2}$$

and

$$\left.\frac{\partial \bar{x}}{\partial \tilde{x}}\right|_{i_{max},j} = \frac{3\,\bar{x}_{i_{max},j} - 4\,\bar{x}_{i_{max}-1,j} + \bar{x}_{i_{max}-2,j}}{2}$$

Solving these expressions for $\bar{x}_{1,j}$ and $\bar{x}_{i_{max},j}$ respectively, gives

$$\bar{x}_{1,j} = -\frac{1}{3}\left(2\left.\frac{\partial \bar{x}}{\partial \tilde{x}}\right|_{1,j} - 4\,\bar{x}_{2,j} + \bar{x}_{3,j}\right) \tag{269}$$

and

$$\bar{x}_{i_{max},j} = \frac{1}{3}\left(2\left.\frac{\partial \bar{x}}{\partial \tilde{x}}\right|_{i_{max},j} + 4\,\bar{x}_{i_{max}-1,j} - \bar{x}_{i_{max}-2,j}\right). \tag{270}$$

Because we have set $B_{1,j} = B_{i_{max},j} = 1$ and all other elements in the $i = 1$ and $i = i_{max}$ matrix rows to zero, the first row of the linear system corresponds to Equation 269 and the last row corresponds to Equation 270. The boundary conditions for $\bar{x}$ are therefore complete if we set $D_{1,j}$ and $D_{i_{max},j}$ to coincide with these equations as

$$\begin{aligned} D_{1,j} &= -\frac{1}{3}\left(2\left.\frac{\partial \bar{x}}{\partial \tilde{x}}\right|_{1,j} - 4\,\bar{x}_{2,j} + \bar{x}_{3,j}\right) \\ D_{i_{max},j} &= \frac{1}{3}\left(2\left.\frac{\partial \bar{x}}{\partial \tilde{x}}\right|_{i_{max},j} + 4\,\bar{x}_{i_{max}-1,j} - \bar{x}_{i_{max}-2,j}\right) \end{aligned} \tag{271}$$

Once the boundary conditions are set by Equation 268 and Equation 271, the linear systems given by Equation 262 and Equation 266 can be solved to determine the isothermal coordinates on the particular grid line j. We employ an efficient algorithm designed for the solution of tridiagonal systems such as typified by our Equation 265. The algorithm is commonly called the Thomas algorithm in honor of its inventor [110]. This algorithm is widely used in computational fluid dynamics contexts, so we shall not describe it in detail here. An example implementation of the algorithm is provided in [107].

After the coordinates along a line have been determined, the over-relaxation step is then applied to create new estimates for the coordinates based on these solutions and the solutions from the previous sweep through the grid. The relaxation is achieved by calculating

$$\begin{aligned} \bar{x}_{i,j}^{n^*} &= \Omega\ \bar{x}_{i,j}^{n} + (1-\Omega)\ \bar{x}_{i,j}^{n-1} \\ \bar{y}_{i,j}^{n^*} &= \Omega\ \bar{y}_{i,j}^{n} + (1-\Omega)\ \bar{y}_{i,j}^{n-1} \end{aligned} \tag{272}$$

where $*$ indicates the relaxed values. The variable Ω is a constant that indicates the degree of relaxation.

Values of Ω that satisfy $0 < \Omega \leq 1$ are associated with the term *under-relaxation*, indicating a procedure to stabilize an otherwise unstable iterative solution, whereas values $1 < \Omega \leq 2$ correspond to *over-relaxation* [107]. The primary intent of relaxation is to increase stability, and the intent of over-relaxation is to speed convergence. The stability of the iterative scheme is dependent on the value of Ω, with $\Omega = 2$ corresponding to the maximal stability limit for any system. In general, stability can be achieved for higher values of Ω as the grid is refined, and the convergence rate is improved with increasing Ω [107]. For most of the grids examined in this work, we are typically able to choose values of Ω near 1.98 to achieve significant speedup, indicating that the algorithm is quite stable.

After over-relaxation has been applied, the algorithm steps to the next j line in the grid sweep. The linear systems are then rebuilt, the isothermal coordinates along the line are solved, and the results are over-relaxed. This process repeats along successive j lines until the isothermal coordinates throughout the entire grid interior from $j = 2$ to $j = j_{max} - 1$ have been determined.

At the end of each sweep, the next steps within the convergence loop focus on determining the isothermal coordinates along the interior and exterior boundary lines $j = 1$ and $j = j_{max}$. As discussed in Section 4.3.2, we implement boundary conditions $\bar{x} = x$ along both the inner and outer boundaries and determine the values of $\bar{y}$ such that they are consistent with the generalized Cauchy–Riemann equations. The next step is therefore to update the $\bar{y}$ derivatives along these boundaries using the generalized Cauchy–Riemann equations.

Following a procedure directly analogous to that of Section 4.3.2, these equations take the form

$$\begin{aligned} \frac{\partial \bar{y}}{\partial \tilde{x}} &= -\sqrt{\tilde{g}}\tilde{g}^{12}\frac{\partial \bar{x}}{\partial \tilde{x}} - \sqrt{\tilde{g}}\tilde{g}^{22}\frac{\partial \bar{x}}{\partial \tilde{y}} \\ \frac{\partial \bar{y}}{\partial \tilde{y}} &= \sqrt{\tilde{g}}\tilde{g}^{11}\frac{\partial \bar{x}}{\partial \tilde{x}} + \sqrt{\tilde{g}}\tilde{g}^{12}\frac{\partial \bar{x}}{\partial \tilde{y}} \end{aligned} \tag{273}$$

relative to the computational coordinate system $\tilde{x}^{\alpha}$. We use these equations to determine the $\bar{y}$ derivatives along the boundaries $j = 1$ and $j = j_{max}$ after we first update the values of the $\bar{x}$ derivatives based on the coordinates generated during the prior grid sweep. To generate these $\bar{x}$ derivatives, we use finite difference expressions analogous to those given by Equations 239 and 241.

Once these $\bar{y}$ derivatives have been calculated, we use them to extrapolate the values of the $\bar{y}$ coordinate along the inner and outer boundaries. To do this, we associate one sided second order finite difference expressions with these derivatives as

$$\left.\frac{\partial \bar{y}}{\partial \tilde{x}}\right|_{i,\,1} = \frac{-3\,\bar{y}_{i,\,1} + 4\,\bar{y}_{i,\,2} - \bar{y}_{i,\,3}}{2}$$

and

$$\left.\frac{\partial \bar{y}}{\partial \tilde{x}}\right|_{i,\,j_{max}} = \frac{3\,\bar{y}_{i,\,j_{max}} - 4\,\bar{y}_{i,\,j_{max}-1} + \bar{y}_{i,\,j_{max}-2}}{2}.$$

Solving these expressions for the $\bar{y}$ boundary values and labeling the results with the index n^* gives

$$\bar{y}_{i,\,1}^{n^*} = -\frac{1}{3}\left(2\left.\frac{\partial \bar{y}}{\partial \tilde{x}}\right|_{i,\,1} - 4\,\bar{y}_{i,\,2} + \bar{y}_{i,\,3}\right) \tag{274}$$

and

$$\bar{y}^{n^*}_{i,\,j_{max}} = \frac{1}{3}\left(2\,\frac{\partial \bar{y}}{\partial \tilde{x}}\,\bigg|_{i,\,j_{max}} + 4\,\bar{y}_{i,\,j_{max}-1} - \bar{y}_{i,\,j_{max}-2}\right). \tag{275}$$

Equations 274 and 275 give the extrapolated boundary values that we need.

After the boundaries have been extrapolated, we next check for convergence of the mapping solution. As with the overall solution algorithm presented in Section 5.1, the convergence criterion is selected as a relative change in the sum-squared grid residual given by

$$R^n = \sum_{i=1}^{i_{max}} \sum_{j=1}^{j_{max}} \left[\left(\bar{x}^{n^*}_{i,j} - \bar{x}^{n-1}_{i,j}\right)^2 + \left(\bar{y}^{n^*}_{i,j} - \bar{y}^{n-1}_{i,j}\right)^2\right]. \tag{276}$$

Convergence is obtained when the residual R^n satisfies

$$R^n < \tau\, R^1 \tag{277}$$

where τ is a specified tolerance and iteration zero corresponds to the initial grid. As for the main solution algorithm, the tolerance is typically taken within the range $10^{-10} \leq \tau \leq 10^{-4}$. Sensitivity studies with respect to this tolerance are presented in Chapter 6.

If convergence has not been achieved, we step to the next iteration in the mapping solution loop. Before proceeding to the next iteration, we reassign index labels as

$$\begin{aligned} \bar{x}^{n-1}_{i,j} &= \bar{x}^{n^*}_{i,j} \\ \bar{y}^{n-1}_{i,j} &= \bar{y}^{n^*}_{i,j} \end{aligned} \tag{278}$$

and then increment the iteration counter. The process of sweeping through the grid, establishing the linear systems for the coordinates, solving the coordinates, over-relaxing the solutions, extrapolating the boundary values, and checking for convergence is then repeated. Once convergence has been achieved, the mapping solution is exited and the algorithm returns to the main solution convergence loop.

This concludes our exploration of the implementation of a numerical method to solve an arbitrary subsonic flow while simultaneously determining a corresponding incompressible equivalent flow. In the next chapter, we will present and discuss a variety of results obtained by employing this numerical method.

CHAPTER VI

RESULTS AND DISCUSSION

In this chapter, we examine the results from a series of subsonic potential flow problems solved using the numerical method developed in Chapter 5. The selected problems and results are intended to fulfill the following objectives:

- Provide substantiating evidence for the validation of the theory and numerical method
- Depict the sensitivity of the solution to salient numerical solver parameters
- Quantitatively illustrate the nature of the geometric transformations employed by the theory and numerical approach
- Indicate phenomena evident in the equivalent profile shapes that may be useful for aerodynamic design purposes

Toward these ends, the selected problems are subcritical flows over a non-rotating circular cylinder and a NACA 0012 airfoil. These problems were chosen primarily based on the availability of trusted analytical or simulation results in the literature to allow for validation of the method. An additional motivation for the cylinder problem is its simplicity and symmetry that are especially conducive for building an understanding of the performance of the analysis and for developing intuition about the coordinate transformations.

In the first section, we examine the results for the cylinder. First, a series of sensitivity studies are performed in order to establish settings for the numerical solver parameters for use in subsequent analyses. These parameters include grid resolution, tolerances, and location of the far field boundary. The cylinder was chosen for these studies because its geometric simplicity allows many of the grid effects to be readily isolated. Next, we present a set of representative field results for the cylinder solution at a high subcritical Mach number. Finally, we perform a sweep through freestream Mach numbers and compare the

variation of the maximum velocity on the cylinder with results available in the literature. Results in this section are compared to those obtained from a Rayleigh–Janzen expansion developed by Van Dyke [121].

In the second section, we examine flows about the NACA 0012 profile. Field results are presented, and the phenomena apparent in the transformation are discussed. First, we examine a symmetric flow and next, we present the results for a lifting case with circulation. The results are compared to numerical results for the surface pressure distributions determined by Lock [73]. The results in this section are particularly interesting with regards to the way in which the geometric transformations act non-symmetrically in the presence of circulation. We investigate these effects, paying particular attention to the relocation of the stagnation streamline in the coordinate mapping. Finally, we present the results of a study on the dependence of the equivalent incompressible airfoil shape on the freestream velocity and angle of attack.

6.1 Circular Cylinder in Freestream Flow

The qualitative behavior of the subsonic potential flow about a circular cylinder in a uniform flow is well known. Exact incompressible results are available based on the superposition of a uniform stream, a doublet, and for circulatory flows, a vortex. Results obtained throughout the subsonic regime are phenomenologically similar to these incompressible solutions, but modifications in the stream patterns and pressure field occur as the freestream Mach number is increased. Nonetheless, obtaining the exact quantitative flow field for the subsonic potential motion past a circular cylinder is not a trivial analytical task.

The analytical result was first obtained by Cherry for both circulation free flows [25] and for flows with circulation [26, 27]. He obtained the solution through a mapping to the hodograph plane, and the results are valid even in the supercritical regime, up to the point of shock formation. Cherry's solution is presented in the form of a series of hypergeometric functions.

In this section, we will investigate the performance of the mapping technique for solving the problem of subcritical circulation-free flow past a cylinder. At certain points, we will

have occasion to compare our results with those in the literature. In this process, we could compare to the method developed by Cherry; however, the theoretical approach employed by Cherry is extremely challenging. We shall therefore base our comparisons on the simpler but similarly accurate approach presented by Van Dyke, who employs a Rayleigh–Janzen series expansion to determine the maximum velocity on the circle as a function of freestream Mach number [121].

6.1.1 Solution Parameter Sensitivities for $\mathbf{M_\infty = 0.375}$

As with all numerical methods, the approach developed in this dissertation is implemented with a series of control parameters that must be selected prior to carrying out a solution. These parameters, which were indicated at various points throughout Chapter 5, include settings for grid resolution and iteration residual tolerances.

These parameters set the nature and the order of approximation of the solutions obtained by the numerical method. In general, the setting of each of these parameters involves a tradeoff between solution speed and accuracy of results. For instance, larger residual tolerances typically provide less accurate results more quickly, whereas smaller tolerances produce more accurate results more slowly. A similar statement can be made about grid resolution. Setting these parameters represents an implicit choice of the degree of error that one is willing to accept in the results in order to obtain reasonable computational run times.

A way to understand the implications of particular settings is to conduct a sensitivity study in which each of the relevant parameters is systematically varied and representative solution results are tabulated. The problem may be somewhat complicated because, in general, the parametric effects may be coupled and correlated; however, a substantial amount of information can be obtained by determining the main effects of each parameter independently while the others are held fixed at nominal values. The objective in a study of this type is to determine the behavior of the solution as a function of the parameters in order to make an informed decision about accuracy versus analysis speed tradeoffs, with the understanding that increased analysis times are correlated with more stringent grid

resolution and convergence tolerances.

In such a study, the ideal criterion for determining the acceptable level of accuracy would be a measure of error from the exact flow solution. With this information, an analyst could then decide that a numerical solution within, say, 1% of the exact result is acceptable. Unfortunately, however, this information is rarely available, as it is indeed the purpose of a numerical analysis to determine heretofore unknown solutions.

Lacking exact results, the decision can be made based on comparison to numerical results obtained with stringent parameter settings describing a very fine grid with small convergence tolerances. Using these results as a surrogate representation of the correct answer, a selection criterion for a particular parameter setting might be stated as the point of diminishing marginal return. For instance, imagine that the solution error relative to this good solution decays linearly with decreasing tolerances up to some point at which the error no longer improves with further tolerance decreases. One could conclude that it is nonsensical to set a tolerance smaller than the value at this point unless there are other factors at play.

In most cases, a crisp transition point may not be apparent. Typically, error decays smoothly as the solution parameters are made more stringent, at least up to the point at which machine precision is reached. The decay of error with grid refinement and tightened tolerance is often found to logarithmically or exponentially decrease. The point of diminishing returns is therefore subject to interpretation, but one could make a reasonable choice based on a qualitative or quantitative comparison to a critical point such as the -3 dB criterion frequently used as a measure of response cutoff in the study of dynamical systems [88].

There are complicating factors that cloud the use and interpretation of these types of sensitivity studies. For example, the ability to perform these types of studies implies that the analysis is inexpensive enough to allow many runs with different parameter settings. However, in many cases, such studies are too time consuming and therefore impracticable for flows over complex geometries. In these cases, one could attempt to perform less expensive sensitivity studies over simpler geometries and extrapolate or directly carry over

Table 3: Solution Parameter Sensitivities Examined

Name	Symbol	Studied In
Number of circumferential grid points	i_{max}	Section 6.1.1.1
Number of radial grid points	j_{max}	Section 6.1.1.1
Outer loop convergence tolerance	ϵ	Section 6.1.1.2
Inner loop convergence tolerance	τ	Section 6.1.1.2
Outer to inner boundary radius ratio	R/r	Section 6.1.1.3
Relaxation parameter	Ω	Not studied
Off-body grid spacing parameter	ζ	Not studied

these settings to the more complex cases. However, there is no guarantee that the information obtained from a study involving one particular geometry is applicable to the behavior with a different geometry. Because of these complexities, the experience and judgement of the analyst is particularly important in understanding, interpreting, and extrapolating the information gleaned from parameter sensitivity studies.

In this section, we investigate the sensitivities of the numerical method developed in this research to the solution parameters listed in Table 6.1.1. First, we examine the effects of grid resolution. Next, tolerance settings for the inner and outer loops are investigated. Finally, we study the effects owing to the placement of the far field boundary.

In these studies, we do not investigate the effects of the relaxation parameter or the exponential off-body spacing parameter. The relaxation parameter was not systematically examined because it primarily affects only stability and solution speed and not accuracy of the converged solution. The spacing parameter was not investigated because its effects are quite similar to those of radial grid density, which we do investigate in Section 6.1.1.1.

The circular cylinder problem provides a useful platform for these sensitivity studies because of its extreme simplicity. The intent of the explorations conducted is to select parameters that will be used for conducting the validation exercises with the circle and for general guidelines for use in the subsequent airfoil analyses.

For each of these studies, the freestream Mach number is set to $M_\infty = 0.375$ which corresponds to a peak local Mach number near 0.9. No condition on the aft stagnation point is enforced, so these results therefore correspond to cases with zero circulation.

Table 4: Fixed Parameter Settings for Grid Sensitivity Study

Name	Symbol	Setting
Outer loop convergence tolerance	ϵ	10^{-6}
Inner loop convergence tolerance	τ	10^{-6}
Outer to inner boundary radius ratio	R/r	6
Over-relaxation parameter	Ω	1.98
Off-body grid spacing parameter	ζ	0.01

Table 5: Refinement Scheme for Grid Sensitivity Studies

	Uniform		Radial		Circumferential	
Refinement	i_{max}	j_{max}	i_{max}	j_{max}	i_{max}	j_{max}
0	31	31	481	31	31	481
1	41	41	481	41	41	481
2	61	61	481	61	61	481
3	81	81	481	81	81	481
4	121	121	481	121	121	481
5	161	161	481	161	161	481
6	241	241	481	241	241	481
7	341	341	481	341	341	481
8	481	481	481	481	481	481

6.1.1.1 Grid Sensitivity

In order to investigate grid sensitivity, we vary the number of grid points while holding all other solution parameters fixed to the values presented in Table 4. These fixed values are nominal settings found through experience with the numerical method and the subsequent parametric studies presented in this section. To isolate the effects of the radial and circumferential node density, we conduct three grid studies in which the numbers of nodes in each direction are varied in prescribed ways. These studies are as follows:

- Uniform variation of the grid density obtained by changing the numbers of radial and circumferential nodes simultaneously
- Radial variation, holding the number of circumferential nodes constant
- Circumferential variation, holding the number of radial nodes constant

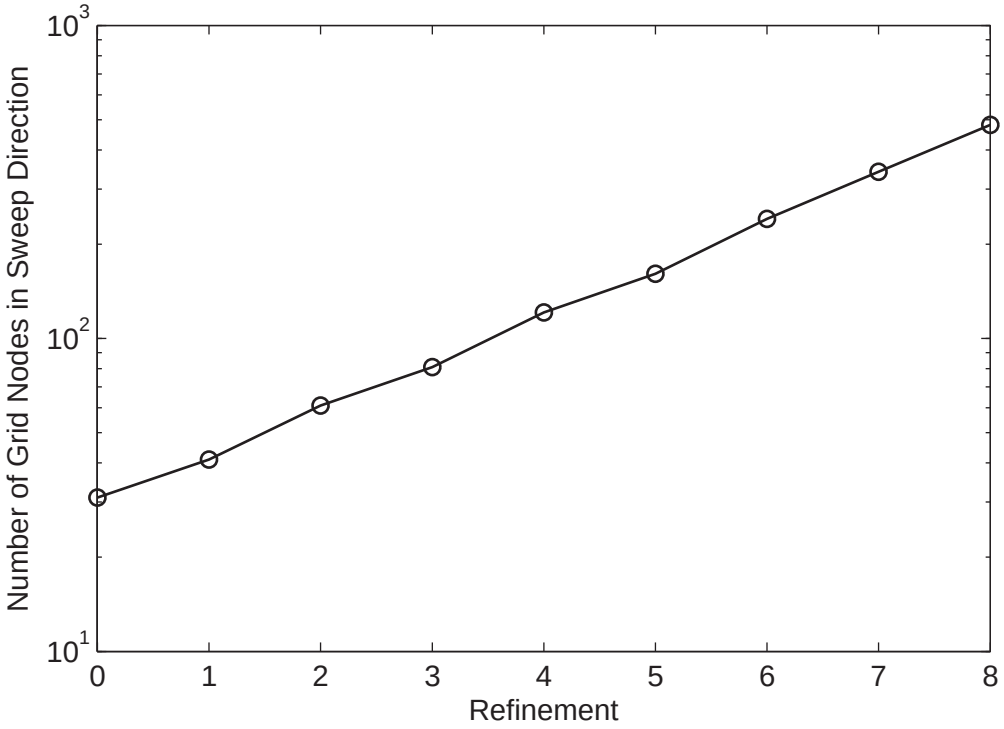

Figure 15: Number of Nodes in Sweep Direction During Uniform, Radial, and Circumferential Grid Sensitivity Studies

The scheme for varying the number of nodes in each study is presented in Table 6.1.1.1. The first setting in each sweep is viewed as the baseline from which improvements can be judged. Subsequent denser grids are generated by refining this baseline grid, and are hence labeled as "refinements." The baseline case is therefore labeled as "refinement 0" for consistency. The number of nodes corresponding to each refinement were prescribed based on a rule of multiplying the number of nodes from the prior refinement by the square root of two and rounding the result to the nearest number ending in one. This approach produces a nice pattern, shown in Figure 15, which each second refinement representing an approximate doubling of grid density in the sweep direction. The practice of rounding to an odd number was chosen based on consideration of the grid distribution in the circumferential direction. In order to produce a layout symmetric about the x-axis, with one node positioned exactly at the leading edge and two coincident nodes at the trailing edge, an odd number of circumferential nodes is required.

For the purposes of comparison, the scheme was organized such that the last refinement in each sweep represents the same grid in each of the three studies. This highly refined grid was chosen to be the case corresponding to an approximation of the correct solution, and the results from the prior refinements were then compared to this case. The number of nodes in the direction not being varied for a particular study was fixed to correspond to the number in this refined grid. Considering this structure, it may be appropriate to think of this last grid as the true baseline for all of the studies and to consider the other grids in the scheme as "coarsenings" instead of refinements. This choice of terminology appears to be mainly one of semantics.

To gauge the quality of the solution, we examine two results for each refinement: the maximum velocity ratio, V_{max}/V_∞, and the drag coefficient, c_d. The maximum velocity is a useful measure because it corresponds to points in the flow where the geometric distortions are the greatest, and therefore, the points where the error in the solution may be large. In obtaining the solutions, we prescribe a freestream flow from the left to the right along the x-axis, so symmetry dictates that the maximum velocity always occurs at the maximum y location on the circle.

The drag coefficient is a useful metric for two reasons. First, it represents an integral measure of the flow solution that encapsulates the distribution of errors along the surface of the body. We calculate it by summing the pressure forces acting normal to the x-direction at each surface panel. Second, we know that the drag coefficient for a two-dimensional subsonic inviscid flow is always zero due to d'Alembert's paradox [6]. Therefore, unlike the situation with other metrics, we can measure the solution quality relative to an exact standard in this case.

The results from these grid refinement studies are presented in Figures 16–19. Figure 16 shows the signed percent difference in the maximum velocity compared to that of the of the final grid refinement. Figure 17 presents the magnitude of the difference on a log scale. In this latter plot, we do not show the results for the last refinement since the percent difference there is by definition zero, and the log of zero is infinite.

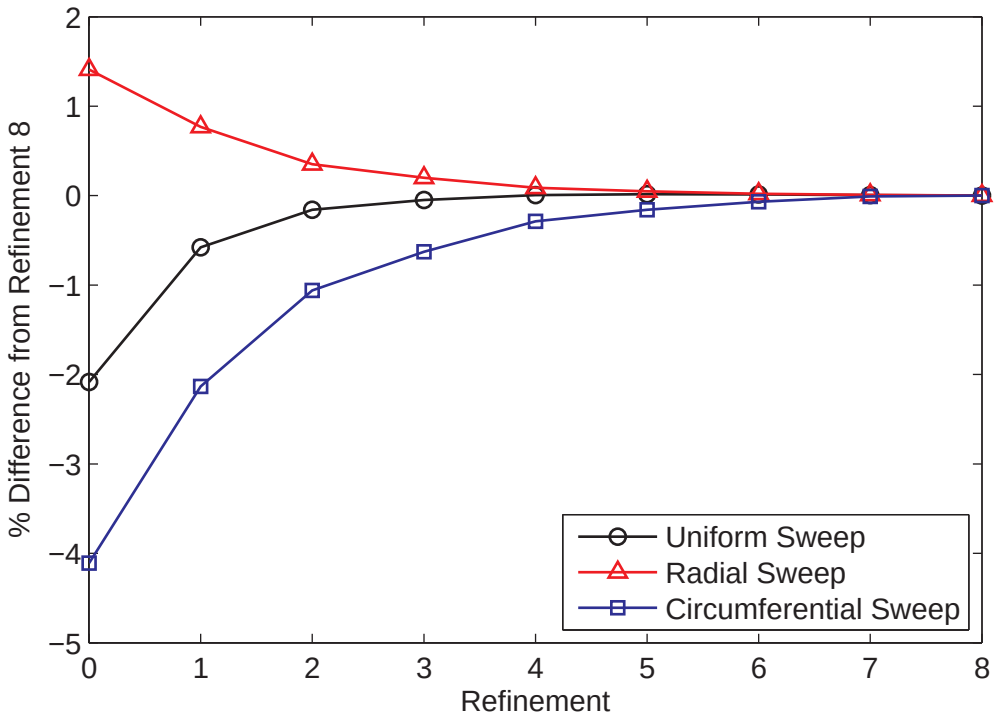

Figure 16: Difference in Maximum Velocity from Finest Refinement

We can note several interesting features in the log plot. The figure clearly indicates a dominant log–linear improvement of the solution with grid refinement. The rate of improvement is substantially the same for both the radial and the circumferential sweeps, excepting the last refinement at which the circumferential sweep achieves a better result. The rate of improvement in the uniform sweep is generally greater than the other sweeps. This result can likely be explained by considering that the uniform refinement is a composition of radial and circumferential refinements such that a near doubling of the effects is present. Unlike the radial and circumferential sweeps, however, the uniform sweep displays an unusual minimum in the error that occurs at Refinement 4. The direct reason for this result is that the signed error crosses zero near this point, but the behavior may indicate that competing factors are involved in the accuracy tradeoff with grid resolution. The behavior suggests that the grid density for Refinement 4 may be especially advantageous; however, this particular result may instead represent a coincidental happenstance. It is also interesting to note that absolute magnitude of the error at Refinement 0 is greater for the circumferential sweep,

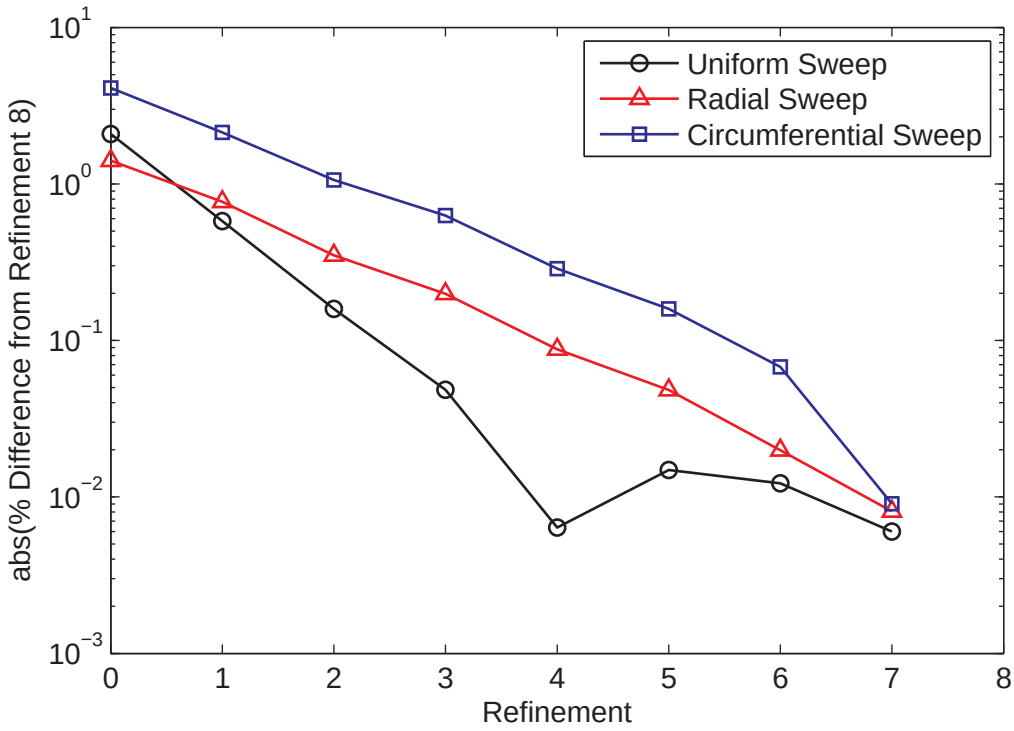

Figure 17: Absolute Value of Difference in Maximum Velocity from Finest Refinement; Log Scale

indicating perhaps that a very sparse grid in the circumferential direction introduces more error than a very sparse grid in the radial direction.

The results for the drag coefficient are presented in Figures 18 and 19. It is apparent in these figures that the drag coefficient, which should be zero, has the greatest error at low grid resolutions for the circumferential and uniform sweeps. As the grids are refined in these studies, the magnitude of c_d generally decreases. In the radial sweep, however, the drag coefficient is nearly invariant, and the prediction is very near zero. This behavior is sensible because the drag coefficient is calculated based on the surface pressure distribution on the circle. The integration errors associated with calculation should decrease with refinement of the grid in the circumferential direction, but they should not be significantly affected by the point distribution normal to the body, i.e. in the radial direction. The small magnitude of the drag coefficient for this sweep occurs because we fix the circumferential resolution at the finest level for the radial sweep.

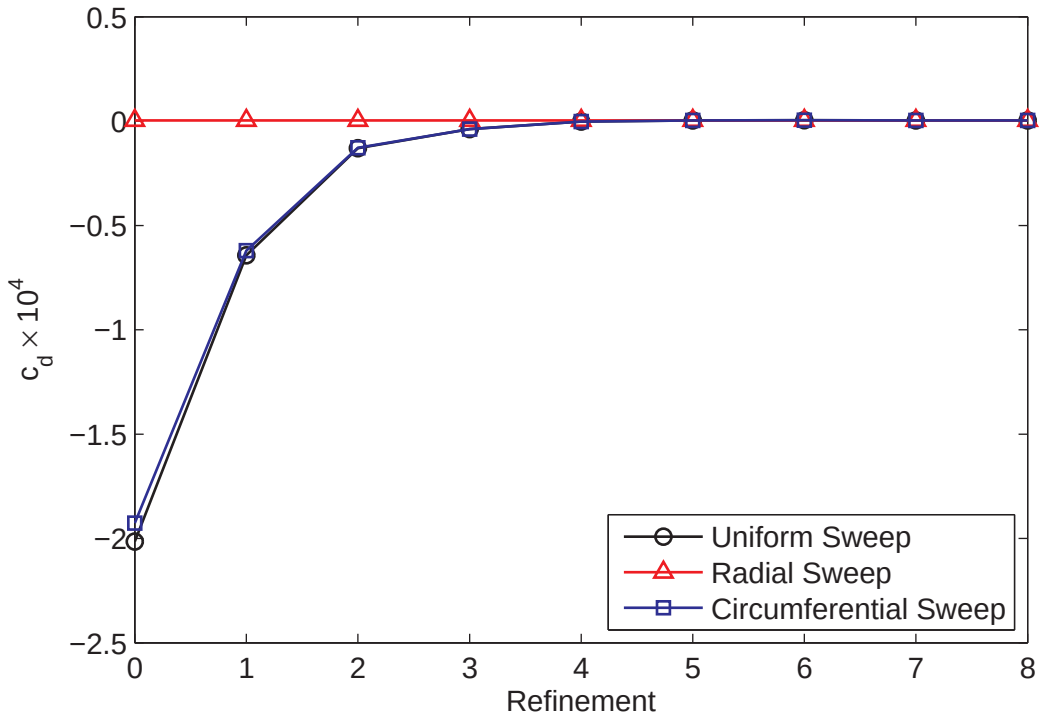

Figure 18: Variation of Panel–Integrated Drag Coefficient with Grid Refinement

Examining Figure 19, we can see that a similar phenomenon occurs for the drag coefficient as for the maximum velocity near Refinement 4 in the uniform and radial studies. Near this point, c_d reaches a minimum and then increases again. This behavior lends additional evidence of the competing error effects that conspire in this region of grid density.

6.1.1.2 Convergence Tolerance Sensitivity

In this study, we investigate the solution sensitivity to the convergence tolerance settings. As described in Chapter 5, there are two convergence loops in the solution algorithm developed in this research. One loop is situated at the level of the global algorithm that repeatedly calls the flow solution, the metric calculation, and the coordinate mapping until the grid residual between subsequent iterations converges. A second loop is used to converge the isothermal coordinate mapping at each iteration within the global loop. For terminological convenience, we shall refer to the first loop as the "outer loop" and the second loop operating on the coordinate mapping as the "inner loop."

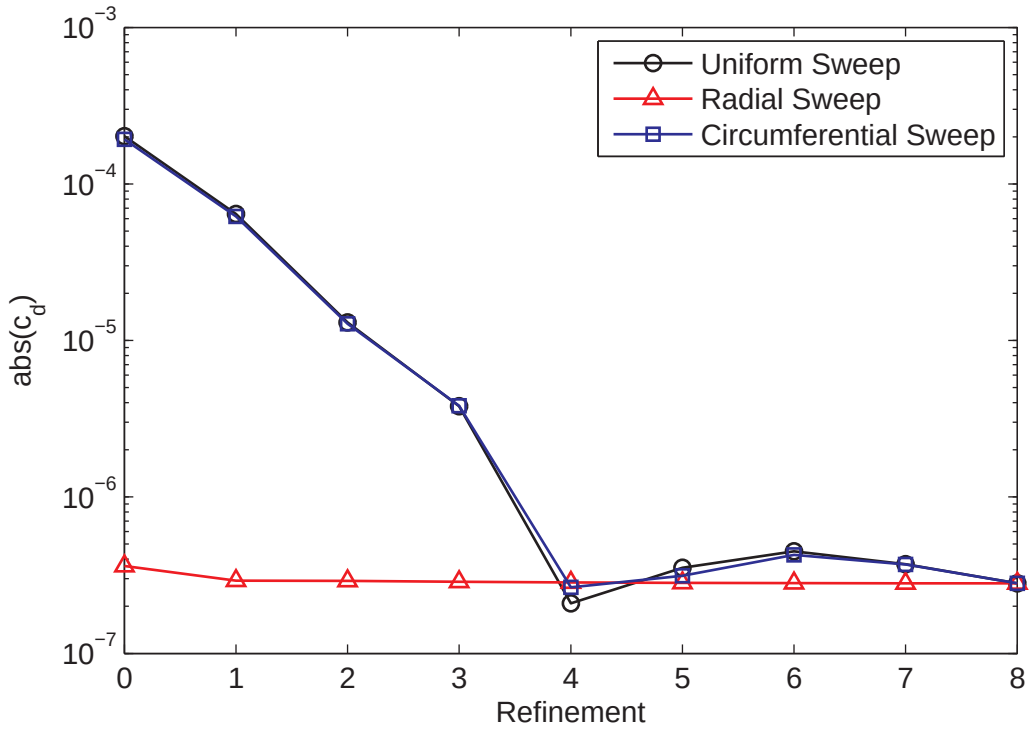

Figure 19: Variation of Absolute Value of Panel–Integrated Drag Coefficient with Grid Refinement; Log Scale

Convergence for the inner loop is measured by comparing the grid sum-squared residual at each iteration to the residual at the first iteration. We repeat the convergence criterion given in Equation 277 here as,

$$R^n < \tau\, R^1 \tag{279}$$

where τ is the specified convergence tolerance that we wish to study and R^n indicates the residual at a particular iteration of the inner loop that is being checked. This form indicates that the convergence criterion is an absolute criterion dictated by the value of the first residual, or we may alternately think of it as a criterion relative to the first residual. It is not a relative criterion in the sense of comparison to the residual of the prior iteration. An example of the typical inner loop converge behavior is shown in Figure 31.

Convergence for the outer loop is judged by comparing the residual to its value at the second iteration. The convergence criterion for this loop was given by Equation 229 which

Table 6: Fixed Parameter Settings for Convergence Tolerance Study

Name	Symbol	Setting
Number of circumferential grid nodes	i_{max}	121
Number of radial grid nodes	j_{max}	121
Outer to inner boundary radius ratio	R/r	6
Over-relaxation parameter	Ω	1.98
Off-body grid spacing parameter	ζ	0.01

we repeat here as

$$R^m < \epsilon\, R^2 \tag{280}$$

where ϵ is the specified convergence tolerance that we wish to study and R^m indicates the residual at a particular iteration of the outer loop that is being checked. The second iteration is chosen for the outer loop as the basis for normalization because of the significant multiple order-of-magnitude change in the residual from the first to the second iteration. This rapid change is likely a result of using the incompressible solution as an initial guess for the barely subcritical solutions typically explored in this research. The numerical algorithm rapidly corrects much of this error in the first iteration, and then a dominant log-linear convergence behavior emerges. An example of the typical outer loop converge behavior is shown in Figure 30.

In order to investigate the sensitivity of the solution to the convergence tolerances τ and ϵ, we first fix the grid settings and other parameters to the values shown in Table 6. Next, we perform two studies, each sweeping through a series of solutions with different tolerance settings. In the first study, we sweep through a range of values of the outer loop tolerance, ϵ, at each of three values of the inner loop tolerance τ. The second study is a transpose of the first in which we sweep through τ at each of three values of ϵ. In both studies, we record the maximum velocity on the circle, the drag coefficient, and the number of outer loop iterations. The maximum velocity measurement is compared to its value at the very stringent tolerance setting of $\epsilon = \tau = 10^{-14}$. This setting is used as a surrogate for the exact answer for comparison. As noted previously, the drag coefficient should vanish because we are considering two-dimensional subsonic inviscid flow.

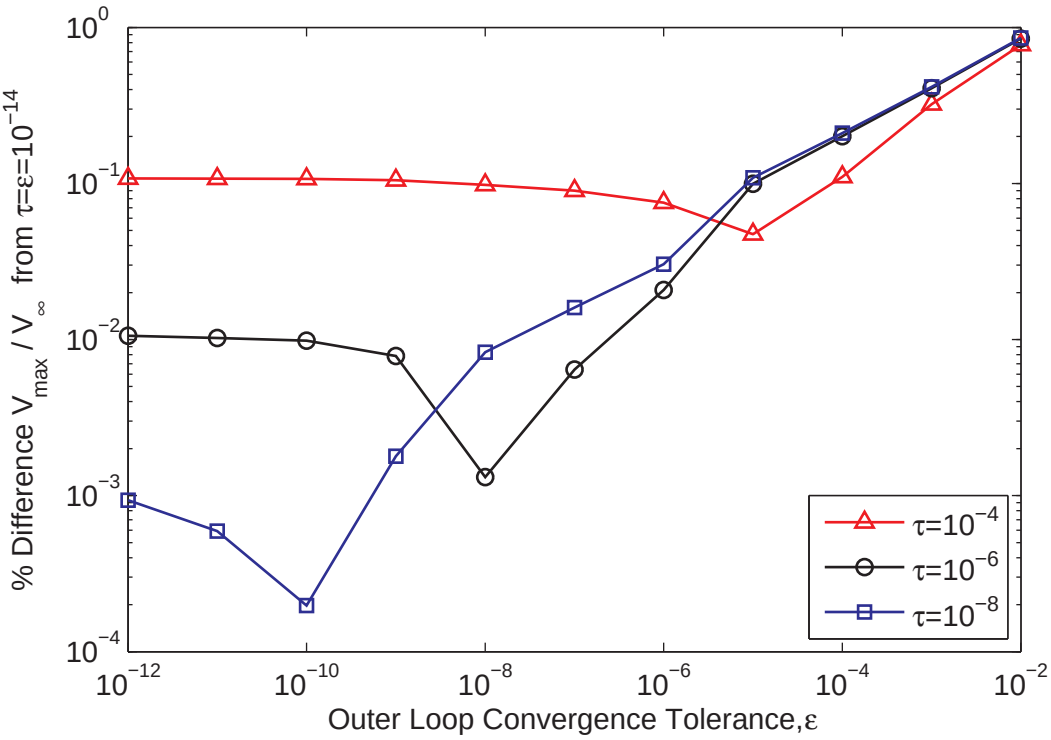

Figure 20: Sensitivity to Outer Loop Tolerance (ϵ) : Maximum Velocity

The results of the first study are shown in Figures 20–22. Figure 20 shows the error in the maximum velocity as a function of the outer loop tolerance ϵ for each of the three specified values of τ. As the tolerance is decreased from the largest value of ϵ, i.e. from right to left in the figure, the error in the maximum velocity begins a log-linear decrease. The rate of this decrease is substantially similar for all three values of τ, and particularly for $\tau = 10^{-6}$ and $\tau = 10^{-8}$. At some point, each of the curves next passes through a point of minimum error and then attains a slightly higher asymptotic error value. The asymptotic behavior is indicative of an interplay in the effects of the inner and outer loop convergence. In other words, no matter how much the outer loop tolerance in decreased, the error cannot be decreased below a certain amount that is dictated by the specified level of the inner loop tolerance. As the inner loop tolerance is decreased and we transition from the $\tau = 10^{-4}$ curve successively to the $\tau = 10^{-8}$ curve, the value of this asymptotic error decreases.

This asymptotic behavior suggests that it is important to select the tolerances in a balanced way. For instance, if we are willing to accept an inner loop tolerance τ of 10^{-6},

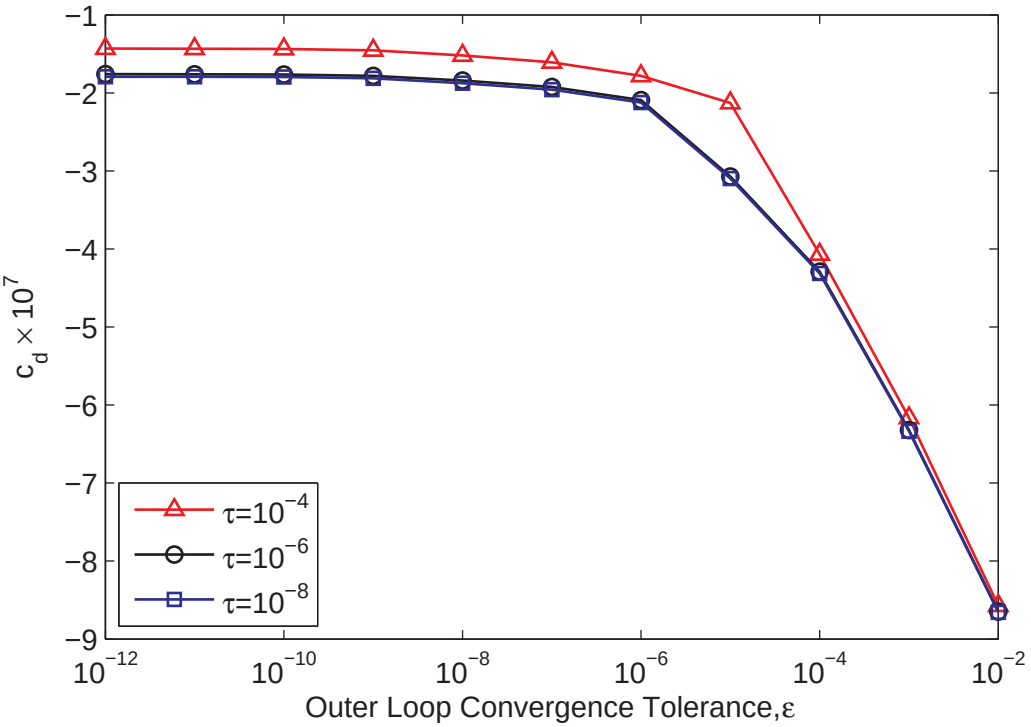

Figure 21: Sensitivity to Outer Loop Tolerance (ϵ) : Drag Coefficient

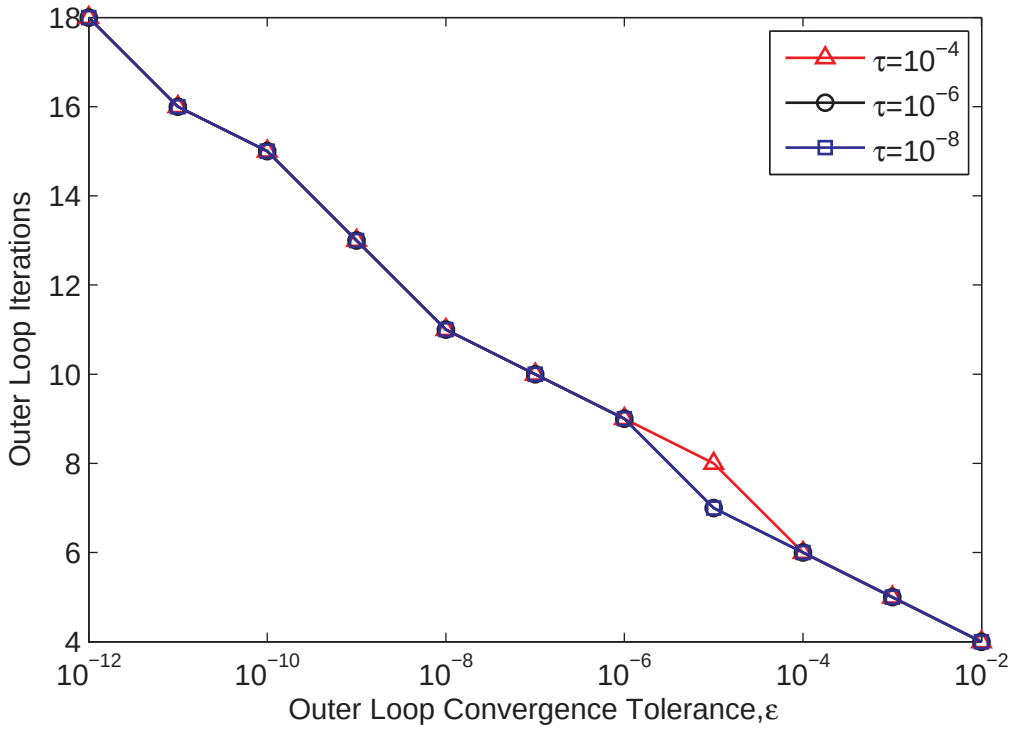

Figure 22: Sensitivity to Outer Loop Tolerance (ϵ): Outer Loop Iterations

Table 7: Approximate Optimal Settings of Convergence Tolerances

Run Time	τ	ϵ
Shorter	10^{-4}	10^{-5}
Intermediate	10^{-6}	10^{-8}
Longer	10^{-8}	10^{-10}

then we should select a value of the outer loop tolerance ϵ subject to $\epsilon > 10^{-8}$. More stringent settings of ϵ are nonsensical, as they do not produce a lesser error. A rather surprising phenomenon that relates to this concept of balanced settings is the minimum that occurs in the error curves. Although a transition from the log-linear behavior to the flat asymptotic behavior might be expected, the substantial magnitude of the minima cannot at present be explained by the author, but it must stem somehow from interacting influences in the outer and inner loop convergence.

The presence and magnitude of these minima suggests that these locations represent optimal settings for the convergence tolerances. That is, we should select the two tolerances based on the locations of these minima and base the setting on the level of computational effort that can be afforded. Table 7 indicates the approximate values of these optimal settings based on the data obtained in the convergence sweeps.

An additional interesting feature of the behavior in Figure 20 is the spacing of the asymptotes compared to the spacing of the levels of τ. The asymptotic error appears to change one order of magnitude in response to a two order of magnitude change in τ. For instance, the transition from $\tau = 10^{-4}$ to $\tau = 10^{-6}$ produces a change in the asymptotic error from 10^{-1} to 10^{-2}. A similar result hold for the transition from $\tau = 10^{-6}$ to $\tau = 10^{-8}$. The author cannot readily explain this behavior, but its presence is evidence of a certain regularity in the nature of the τ and ϵ interplay.

Figure 21 shows the drag coefficient as a function of the outer loop tolerances for each of the three inner loop settings. As ϵ is decreased from the right of the figure to the left, the magnitude of the drag coefficient decreases nearly linearly until it also transitions to an asymptotic value. This overall behavior is consistent with expectations that c_d should move toward zero as tolerances are tightened. The results for $\tau = 10^{-6}$ and $\tau = 10^{-8}$ are

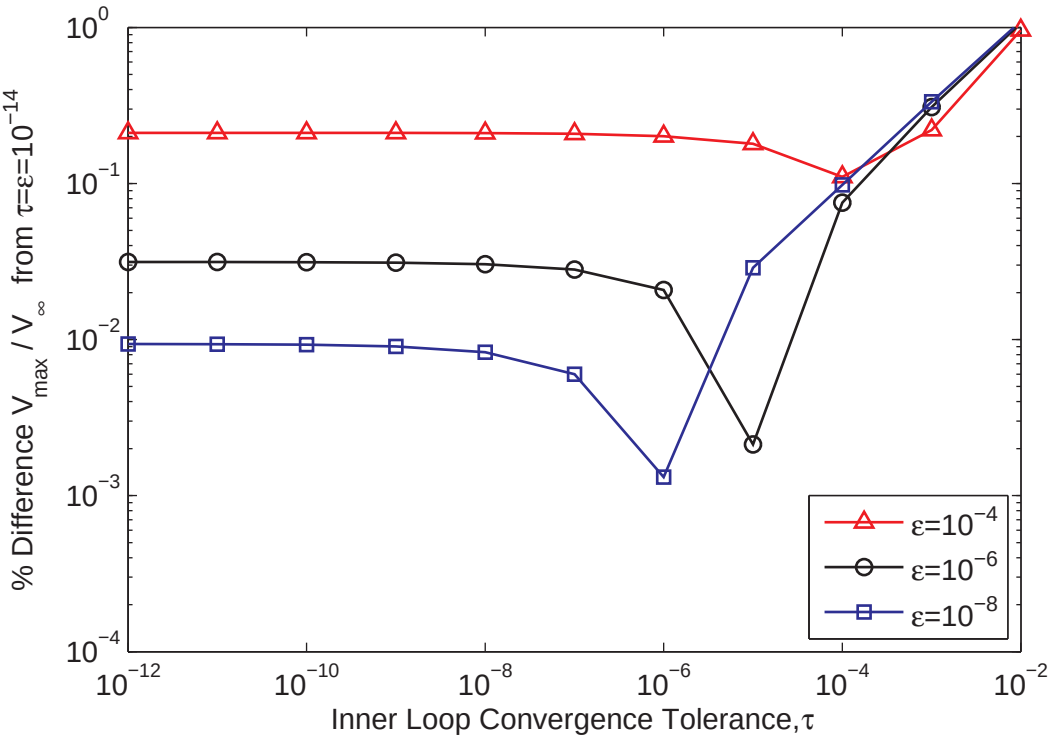

Figure 23: Sensitivity to Inner Loop Tolerance (τ): Maximum Velocity

practically indistinguishable; however, the $\tau = 10^{-4}$ setting produces a slightly lower c_d magnitude for all values of ϵ. This result is somewhat unexpected because the magnitude of c_d would be anticipated to increase with decreasing τ. This phenomenon may be a result of happenstance, stemming from the overall poor solution quality obtained with $\tau = 10^{-4}$. Based on the near coincidence of the $\tau = 10^{-6}$ and $\tau = 10^{-8}$ lines, it is unlikely that c_d is driven by τ as long as the tolerance is set below some threshold, likely around 10^{-6}.

The number of outer loop iterations as a function of ϵ and τ are shown in Figure 22. The plot indicates a nearly log-linear inverse relationship between ϵ and the number of iterations. Interestingly, the value of the inner loop tolerance τ has no discernable effect, except for the outlier result at $\epsilon = 10^{-5}$, $\tau = 10^{-4}$. It should be expected that the number of outer loop iterations would be driven primarily by the outer loop tolerance, but a slight effect owing to the inner loop setting was anticipated.

Figures 23–25 display the results of the sweep through τ conducted for each of three

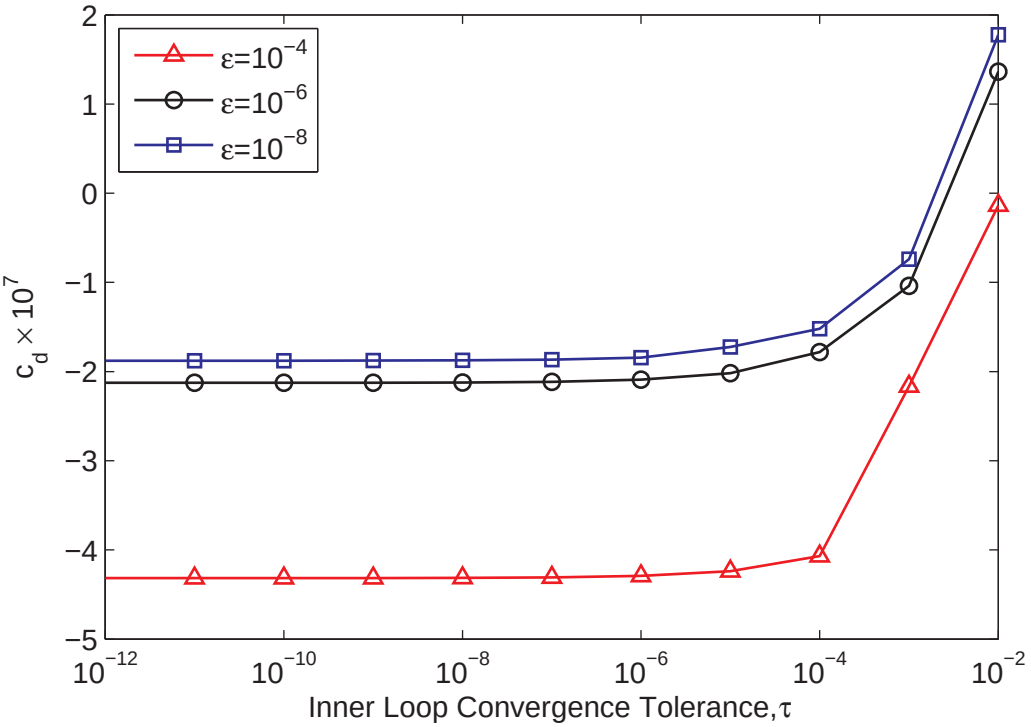

Figure 24: Sensitivity to Inner Loop Tolerance(τ): Drag Coefficient

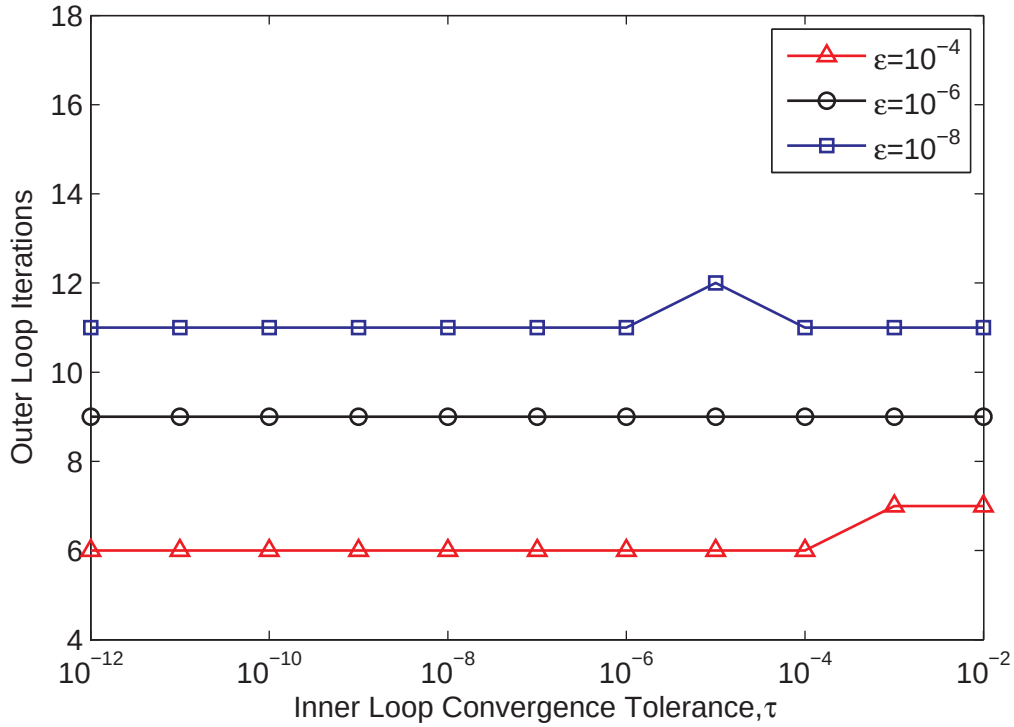

Figure 25: Sensitivity to Inner Loop Tolerance (τ) : Outer Loop Iterations

settings of ϵ. This study corresponds to the transpose of the study presented in Figures 20–22, but it fills additional points in τ. The results provide further evidence for the conclusions drawn above, and no additional conclusions are drawn based on this study. We present the results here simply to provide an alternate means of visualization of these trends and to further substantiate the conclusions drawn above.

6.1.1.3 Sensitivity to Location of the Far Field Boundary

In this section, we examine the sensitivity of the solution to the location at which the outer far field boundary is placed. To gauge this sensitivity, we conduct two studies. In the first, we vary the outer boundary radius while holding the number of radial grid nodes constant. In the second, we maintain an approximately constant density of grid points in the radial direction, increasing the number of grid nodes proportionally to the radius. The scheme for varying the number of radial grid nodes for these studies is shown in Table 8. As we vary the boundary radius in both studies, the other solution parameters are fixed to the values shown in Table 9.

Table 8: Variation of Radial Grid Nodes for Far Field Boundary Sensitivity Studies

R/r	Fixed Radial Nodes j_{max}	Fixed Radial Node Density j_{max}
2	41	41
3	41	61
4	41	81
6	41	121
8	41	161
10	41	201
12	41	241

The results of the studies are presented in Figures 26–29. Figure 26 shows the percent difference in V_{max}/V_∞ as a function of the ratio of the outer to inner boundary radii. To develop these results, the inner boundary radius is fixed and only the outer radius is varied. The percent difference calculation in these results is tabulated relative to the largest radius ratio setting of $R/r = 12$ in the fixed grid density sweep. This normalization was chosen because we presume that the solution improves as the radius ratio is increased (at fixed

Table 9: Fixed Parameter Settings for Far Field Boundary Sensitivity Studies

Name	Symbol	Setting
Number of circumferential grid nodes	i_{max}	121
Outer loop convergence tolerance	ϵ	10^{-8}
Inner loop convergence tolerance	τ	10^{-6}
Over-relaxation parameter	Ω	1.98
Off-body grid spacing parameter	ζ	0.01

grid density) because the outer boundary becomes a better approximation of a boundary at infinity.

In Figures 26 and 27, we see that the error for the study with a fixed number of radial grid nodes deteriorates rapidly as the boundary radius is moved outward. This result stems from the radial grid spacing becoming successively larger with increased radius. The trend of this deterioration is steady until the transition from $R/r = 10$ to $R/r = 12$, at which point a dramatic increase in error occurs. This large increase is likely indicative of a critical minimum in grid density being breached. The apparent improvement of the absolute error at $R/r = 3$ in Figure 27 is a transitory result of the error changing signs in this vicinity, as can be seen in Figure 26. The primary conclusion that can be drawn from these results is that care must be taken to ensure adequate radial node spacing for any particular setting of the far field boundary location.

The situation is different for the study in which the radial node density is fixed. In this case, the error is rapidly reduced as the boundary is moved outward. As shown in Figure 27, the error follows a nearly log-linear reduction pattern. The magnitude is reduced to 0.03% by $R/r = 6$, and the result at this radius is nearly visually indistinguishable from the asymptotic result of zero error in Figure 26. It is also interesting to note the small overall magnitude of the error, even at the setting $R/r = 2$. This result is perhaps indicative of the rapid die-off of the solution magnitude with radius for the Mach number investigated.

The behavior of the drag coefficient is shown in Figures 28 and 29. Interestingly, the magnitude of the drag coefficient increases slightly as the outer boundary is moved outward. This general trend occurs for both the case with a fixed number of radial nodes and for the case with a fixed radial node density. Although this trend is counterintuitive, the magnitude

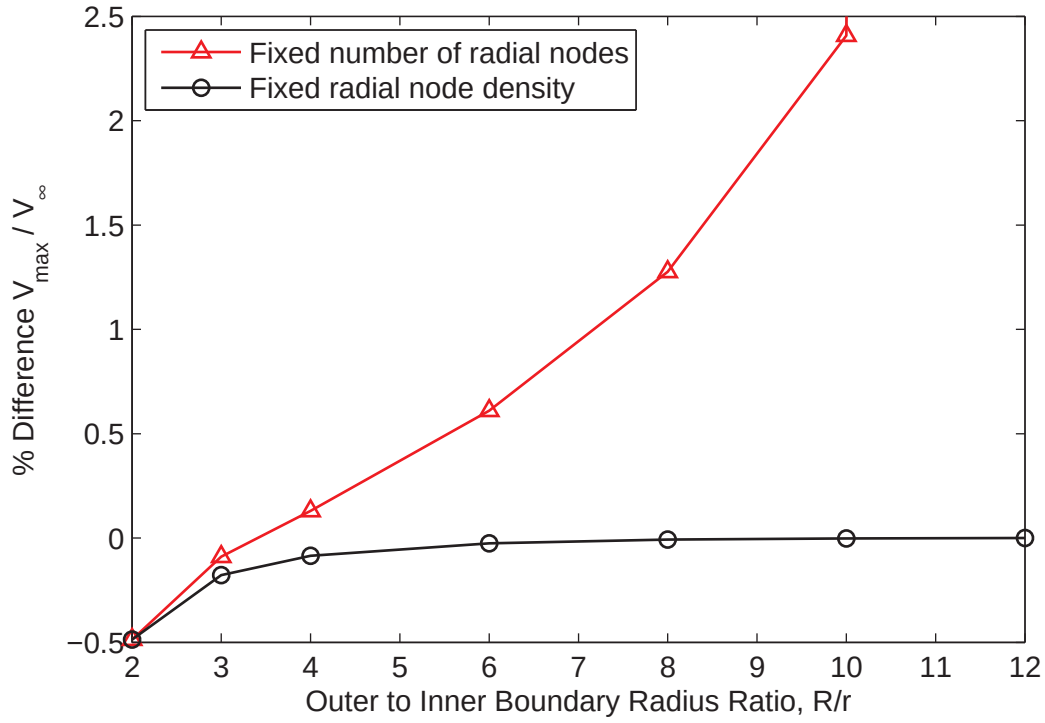

Figure 26: Sensitivity to Outer Boundary Location: Maximum Velocity

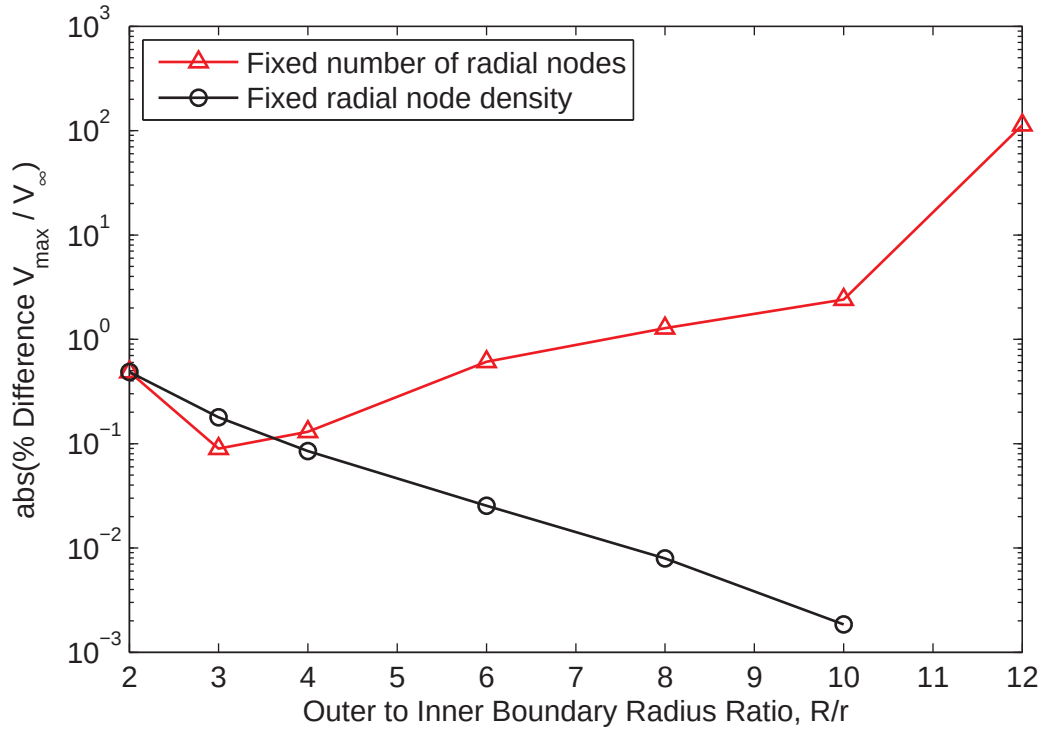

Figure 27: Sensitivity to Outer Boundary Location: Maximum Velocity; Log Scale

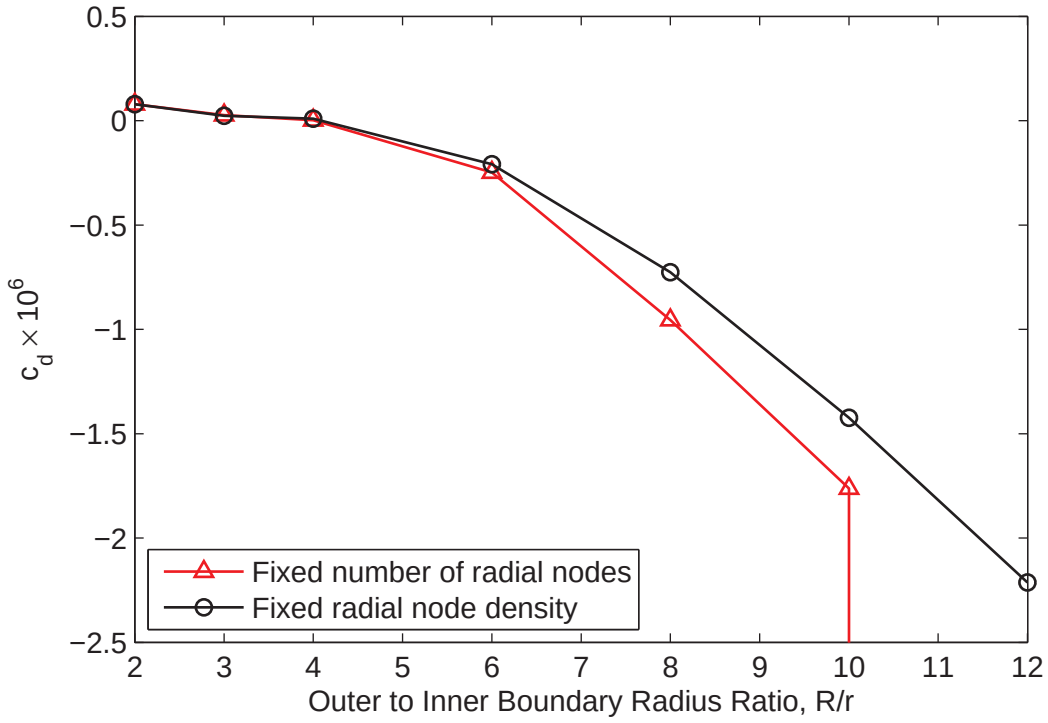

Figure 28: Sensitivity to Outer Boundary Location: Drag Coefficient

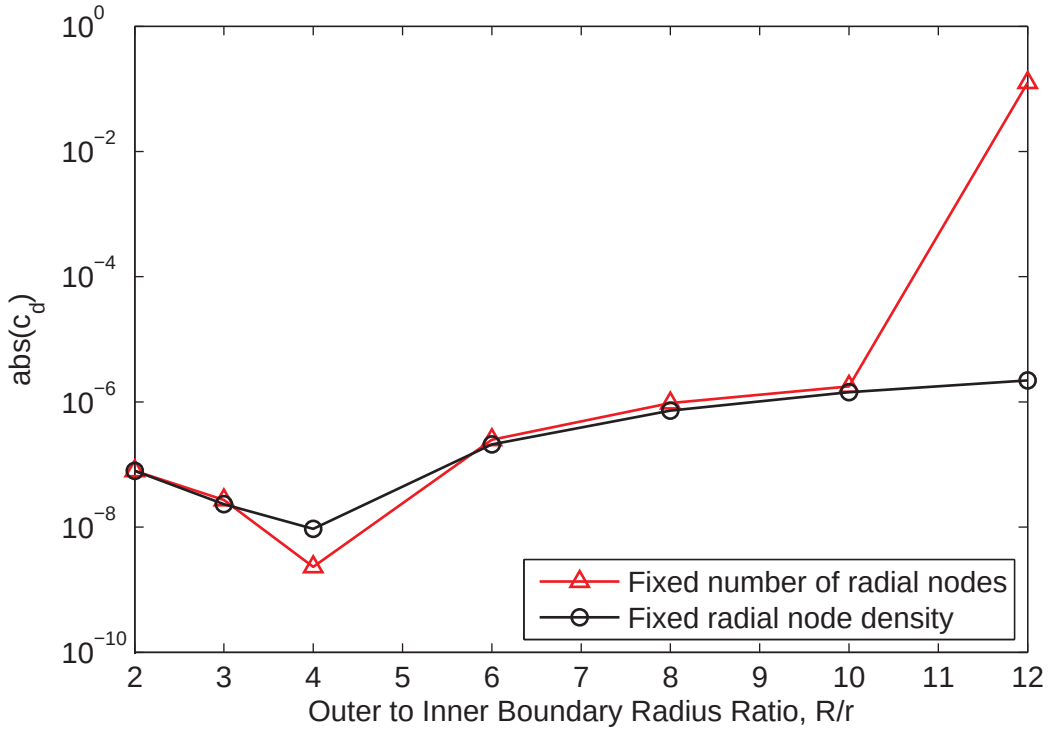

Figure 29: Sensitivity to Outer Boundary Location: Drag Coefficient; Log Scale

Table 10: Parameter Settings for Circle Solutions

Name	Symbol	Setting
Number of circumferential grid nodes	i_{max}	121
Number of radial grid nodes	j_{max}	121
Outer loop convergence tolerance	ϵ	10^{-8}
Inner loop convergence tolerance	τ	10^{-6}
Outer to inner boundary radius ratio	R/r	6
Over-relaxation parameter	Ω	1.98
Off-body grid spacing parameter	ζ	0.01

of the change is weak. The results are substantially similar in magnitude to those obtained during the sweep in radial grid density described in Section 6.1.1.1 and shown in Figures 18 and 19. The only exception to this weak dependence is the result for $R/r = 12$. As discussed above, however, this result likely stems from attempting a solution below a certain critical minimum grid density.

6.1.1.4 Summary of Chosen Parameter Settings

Based on these studies, the solution parameter settings listed in Table 10 were selected for use in obtaining high quality results for the circle solution.

The grid density was set to 121×121 based on the good performance of the Refinement 4 solution from the uniform grid sweep indicated in Figures 17 and 19. This setting represents an advantageous balance of low error for reasonable computational expense.

The convergence tolerance settings were specified as $\tau = 10^{-6}$ for the inner loop and $\epsilon = 10^{-8}$ for the outer loop. This selection was based on the balanced performance of these settings indicated primarily in Figures 20 and 21. This setting represents the intermediate computational expense option among the three approximate optima tabulated in Table 7. This choice was made over the more accurate balanced setting of $\tau = 10^{-8}$, $\epsilon = 10^{-10}$ because the quality of results at the intermediate setting was believed to be adequate for validation purposes without the need of incurring greater analysis time.

The outer boundary location was set to $R/r = 6$, or equivalently $R/c = 3$ where c is the chord, or diameter, of the circle. This setting was based on the small error obtained at this point as shown in Figures 26 and 27. Higher settings would require a greater number of

radial grid points without producing substantial reductions in solution error. An additional benefit of this setting is that it produces domain grids that can readily be visualized in their entirety on a single page in this document.

Theses settings are used to produce the results presented in the subsequent Sections 6.1.2 and 6.1.3. The airfoil results presented in the latter sections of this chapter use generally similar tolerance settings and outer bound location (in the sense of $R/c = 3$), but a higher grid density is employed to match the validation results.

6.1.2 Results for $\mathbf{M}_\infty = 0.375$

This section presents the results for the circle solution at a freestream Mach number of 0.375. The solution parameters are set to the values specified in Table 10. In this section, we first present the solution convergence histories and then show typical surface and field results for the potential flow solution. Finally, we illustrate the effects of the coordinate transformation that generates the equivalent incompressible shape. These effects are shown through field contour plots of the metric tensor components as well as depictions of the distorted coordinate grid.

The solution convergence behavior is shown in terms of the normalized grid sum-squared residual in Figures 30 and 31. Figure 30 displays the overall algorithm (outer loop) convergence, and Figure 31 shows the coordinate mapping (inner loop) convergence at the last outer loop iteration. As described in Sections 5.1 and 5.5, convergence for the outer loop is based on the residual normalized to that of the second iteration, whereas convergence for the inner loop is based on the residual normalized by the result of the first iteration. The inner loop residual shows a nearly perfect log-linear reduction after an initial bobble, whereas the outer loop convergence displays a slight degree of curvature.

The sharp transition in the outer loop residual at the second iteration is, in part, an artifact of the choice of the incompressible solution as the initial guess for generating the metric coefficients. This guess has substantial error for this case because the peak Mach numbers on the circle are in the high subsonic range. The main effects of this poor guess are rapidly corrected during the first outer loop iteration. It was speculated that this

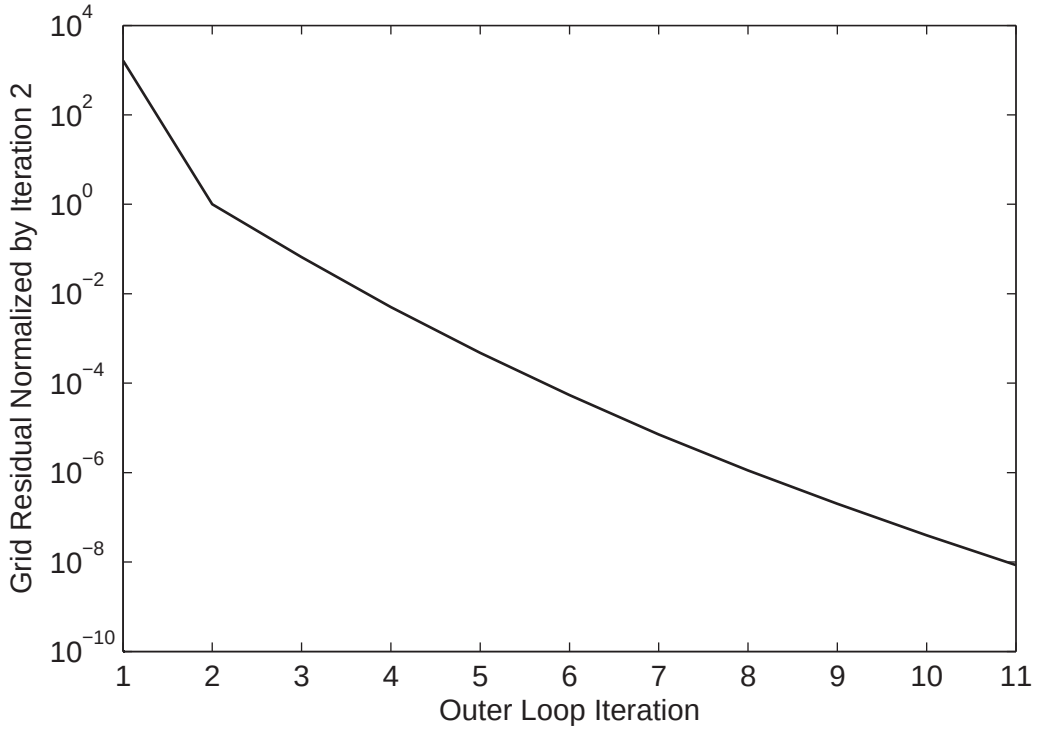

Figure 30: Outer Loop Convergence History for the Circle

situation could be perhaps be improved by an initial guess based on a Prandtl–Glauert correction, but negligible improvement in the overall convergence rate was noted. This lack of improvement may be attributable to the fact that the Prandtl–Glauert correction is valid only for linearized flows, and therefore, errors are large, particularly in the stagnation regions. For all results presented in this work, we therefore simply use the incompressible solution as the initial guess.

The surface pressure distribution is shown in Figure 32. The result is compared to Prandtl–Glauert and Kármán–Tsien corrections of the incompressible result as well as to the Rayleigh–Janzen expansion solution for the maximum velocity obtained by Van Dyke [121]. Van Dyke's solution consists of 29 terms in a series of integer powers of M_∞^2. The velocity is given by the series

$$V_{max} = V_\infty \sum_{n=1}^{29} q_n \left(M_\infty^2\right)^{n-1} . \tag{281}$$

The coefficients q_n obtained by Van Dyke are presented in Table 11. As shown in Figure 32,

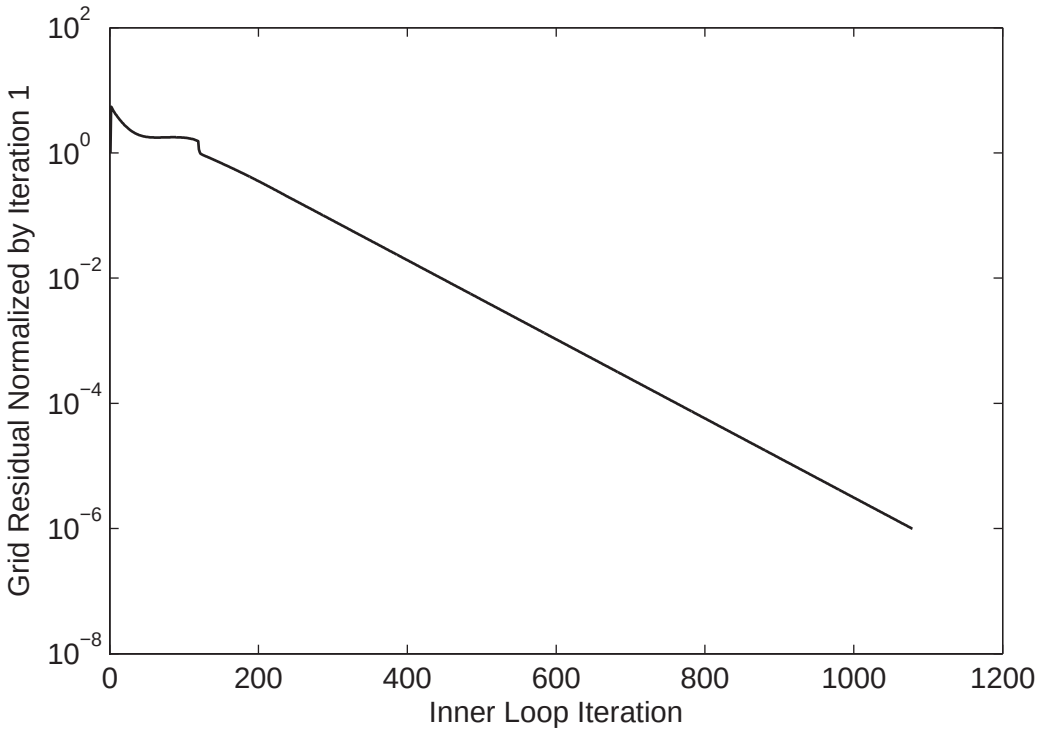

Figure 31: Inner Loop Convergence History at the Last Outer Loop Iteration for the Circle

Table 11: Terms in Van Dyke's Rayleigh–Janzen Expansion for the Circle [121]

n	q_n	n	q_n
1	2.00000000000000	16	$4.26997505742413 \times 10^{8}$
2	1.166666666666667	17	$2.16247145908896 \times 10^{9}$
3	2.57833333333333	18	$1.10463770836747 \times 10^{10}$
4	7.51464814814814	19	$5.68649851009948 \times 10^{10}$
5	$2.55904074326026 \times 10^{1}$	20	$2.94779009123257 \times 10^{11}$
6	$9.62632913824853 \times 10^{1}$	21	$1.53777835504235 \times 10^{12}$
7	$3.87923452464374 \times 10^{2}$	22	$8.06853184029690 \times 10^{12}$
8	$1.64399333300068 \times 10^{3}$	23	$4.25587560801023 \times 10^{13}$
9	$7.23987123576189 \times 10^{3}$	24	$2.25576351728074 \times 10^{14}$
10	$3.28626654734814 \times 10^{4}$	25	1.2010117×10^{15}
11	$1.52864040612112 \times 10^{5}$	26	6.4210705×10^{15}
12	$7.25593930837266 \times 10^{5}$	27	3.446256×10^{16}
13	$3.50326365998740 \times 10^{6}$	28	1.856327×10^{17}
14	$1.71617906236987 \times 10^{7}$	29	1.00329×10^{18}
15	$8.51351821010245 \times 10^{7}$		

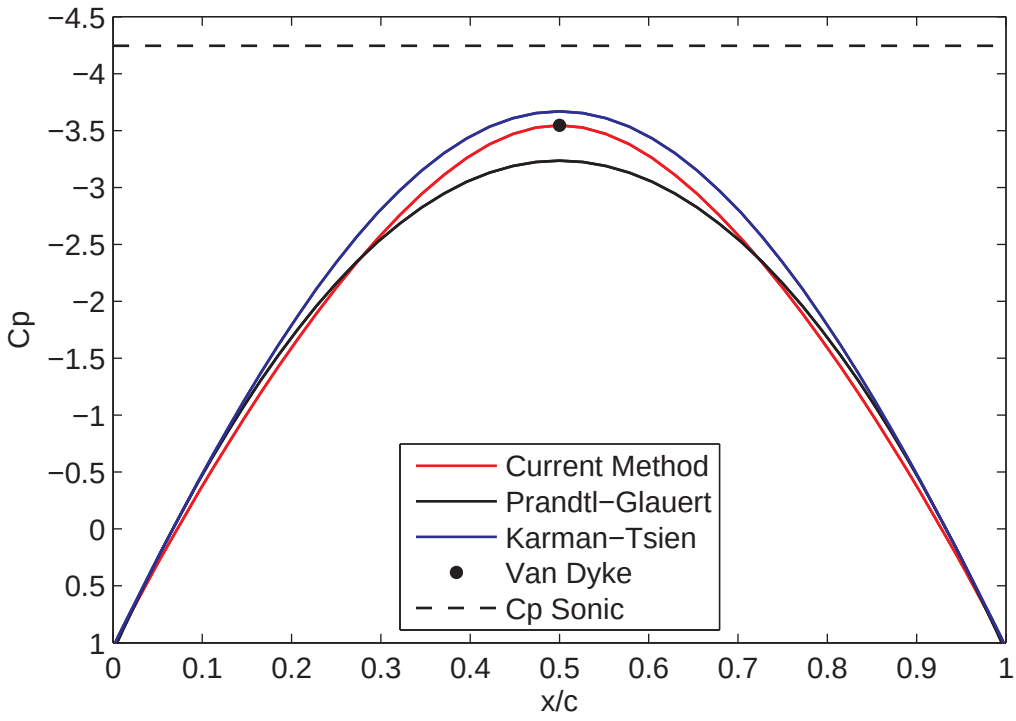

Figure 32: Surface Pressure Coefficients for the Circle

the solution from the present method matches the Van Dyke result and lies generally between the two compressibility corrections.

Figures 33–35 show contours of the pressure coefficient and local Mach number in the domain. Because we are considering potential flow, all thermodynamic variables can be obtained directly as a function of the velocity magnitude, or equivalently, as a function of either M or C_p. We therefore do not present field results for the thermodynamic values because such plots would not supply significant additional information.

Since circulation is not present and the freestream flow follows the x-axis from left to right, the solution presented in these plots is symmetric about the x-axis, with the exception of a sign inversion in the y-velocity. In fact, the circle is the only body with a second axis of symmetry (in this case, about the y-axis), excepting again a sign inversion in the y-velocity. Nonetheless, we choose to plot the entire upper half plane.

The contours of the half-domain in Figure 33 show that the results vary smoothly throughout the field and along the boundaries. No obvious large scale defects associated

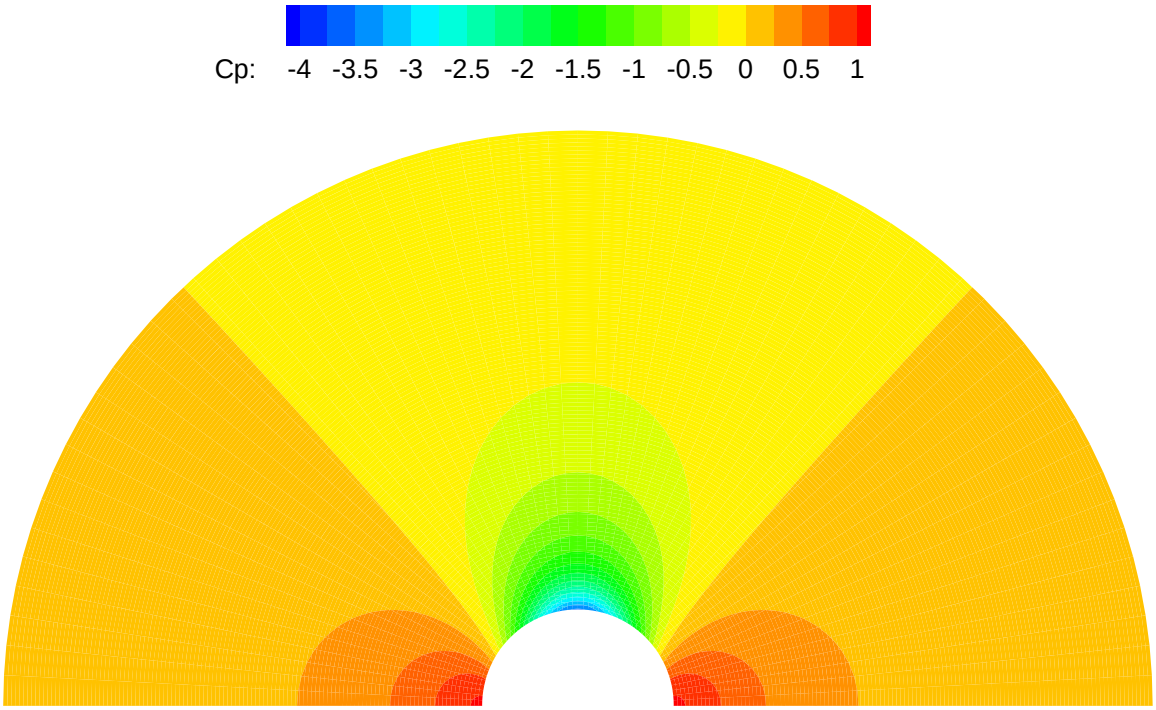

Figure 33: Pressure Coefficient Contours for the Circle

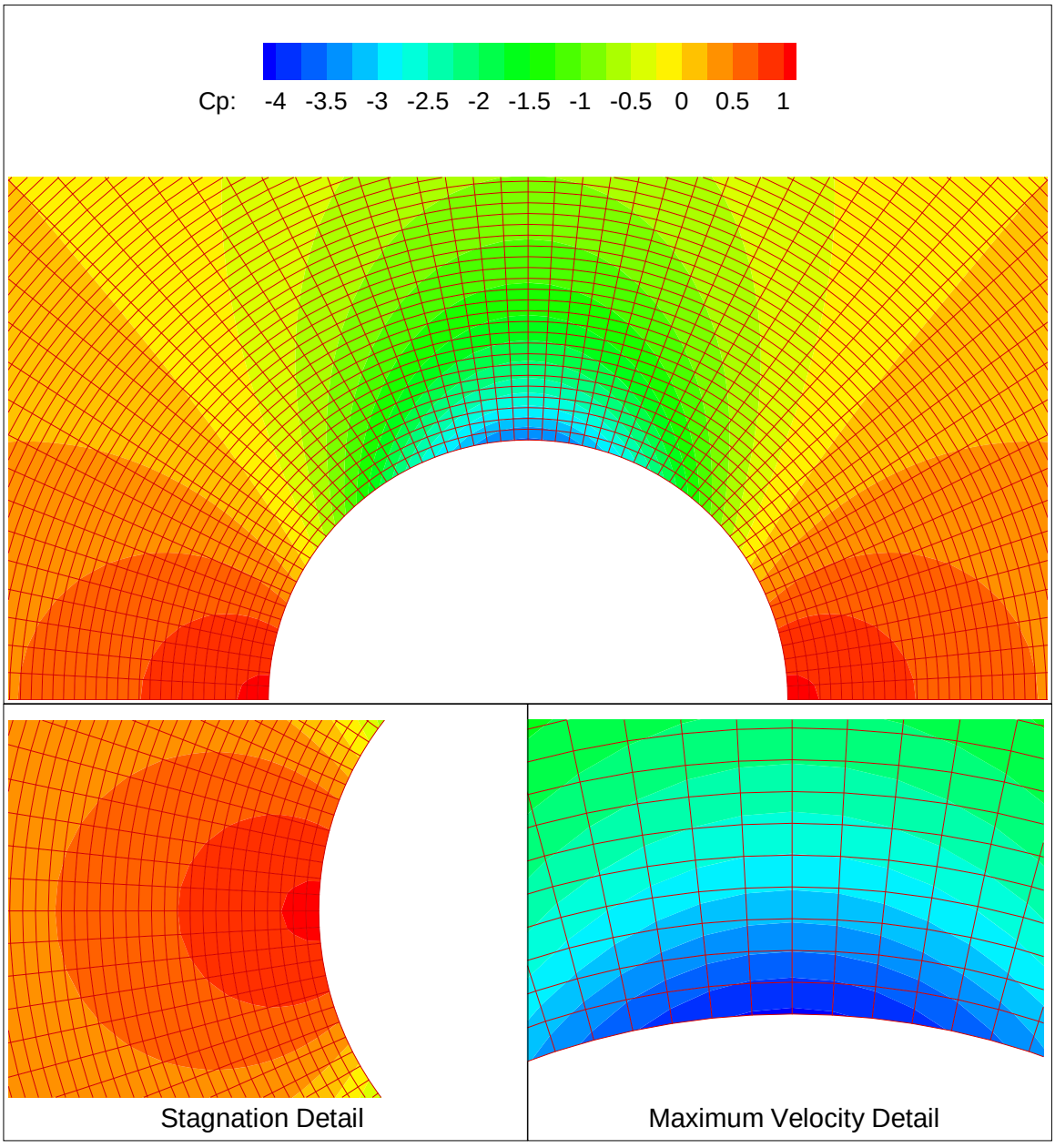

Figure 34: Pressure Coefficient Contours for the Circle; Near-Body Domain

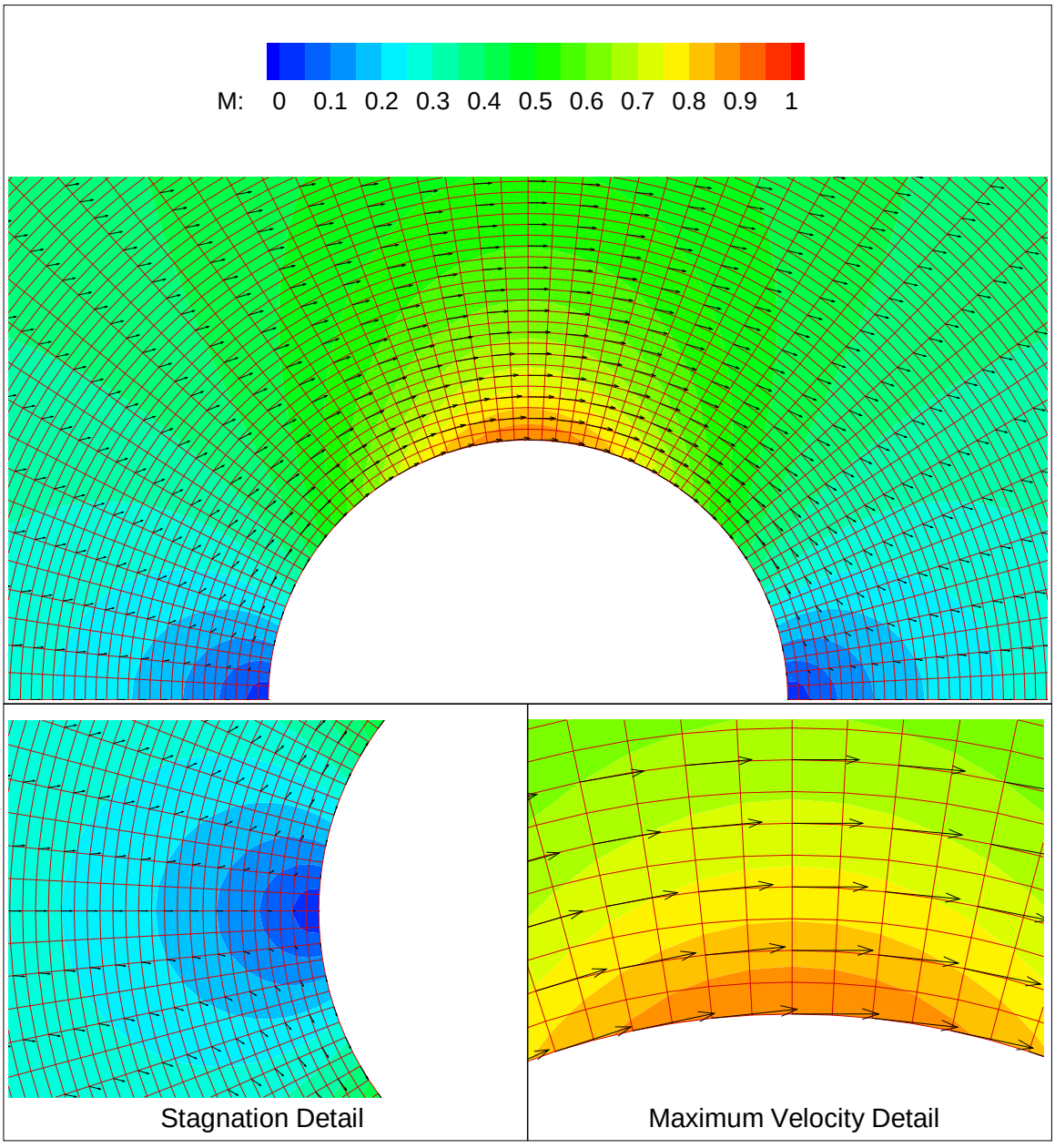

Figure 35: Mach Number Contours for the Circle; Near-Body Domain

with the boundary point extrapolation routine described in Section 5.5 are present. Details of the near-body domain presented in Figures 34 and 35 indicate that the results are smooth and that contour interpolation among grid nodes is adequate. The velocity vector field is also superimposed in Figure 35. The behavior of the results is largely as expected, with stagnation points where the circle intersects the x-axis, a maximum velocity point along the line parallel to the y-axis drawn from the center of the circle, and a smooth die-off behavior of the disturbance with increasing radius.

Having examined the traditional field results to verify that the solution behaves as expected, we now explore some of the features of the mapping solution. Figures 36–38 show countours of the metric tensor components $\sqrt{g}g^{\mu\nu}$. These metric values are particularly important because they collectively serve to link the flow solution to the coordinate mapping. As indicated by the contour levels shown in the figures, the metric components are approximately bounded as $0.7 < \sqrt{g}g^{11} < 1$, $-0.2 < \sqrt{g}g^{12} < 0.2$, and $0.95 < \sqrt{g}g^{22} < 1.45$. The values that would be obtained for a truly incompressible $M_\infty \to 0$ flow that would produce the trivial identity coordinate mapping are $\sqrt{g}g^{11} = 1$, $\sqrt{g}g^{12} = 0$, and $\sqrt{g}g^{22} = 1$. The $\sqrt{g}g^{11}$ and $\sqrt{g}g^{22}$ values are symmetric about the line parallel to the y-axis drawn from the circle center and are also symmetric about the x-axis. The component $\sqrt{g}g^{12}$ is proportional to the y-velocity, however, so it is antisymmetric about both the x- and y-directions. Its symmetry axes are rotated 45° to those of the other two metric components.

The original and distorted domain grids are shown superimposed in Figure 39. The original grid is plotted relative to the (x, y) Cartesian coordinate axes, and the equivalent incompressible grid is plotted relative to the isothermal $(\bar{x}, \bar{y})$ Cartesian coordinate axes. The results show that the body shape seen by the equivalent incompressible flow is oblonged and ellipse-like with major axis oriented in the cross-flow direction. This result is reassuring—the shape in an incompressible flow that produces the same pressure profile of a body with the same chord in a compressible flow must necessarily be thicker. The necessity for this behavior is that the flow must be accelerated more through turning in the incompressible flow in order to produce the same pressure changes as in a compressible flow with lesser turning. This behavior is fundamentally similar to the cross-stream stretching of an

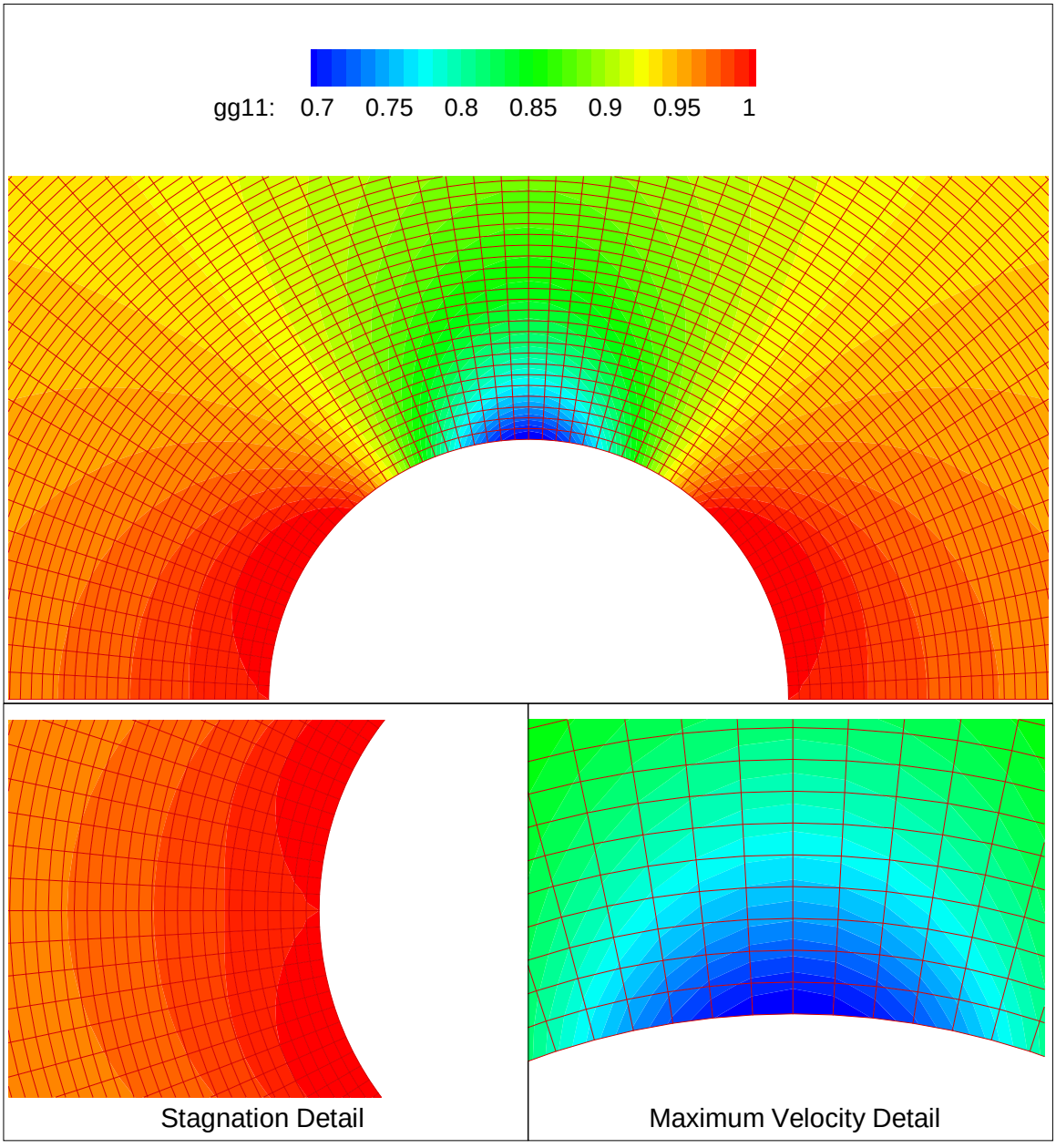

Figure 36: Contours of $\sqrt{g}g^{11}$ for the Circle; Near-Body Domain

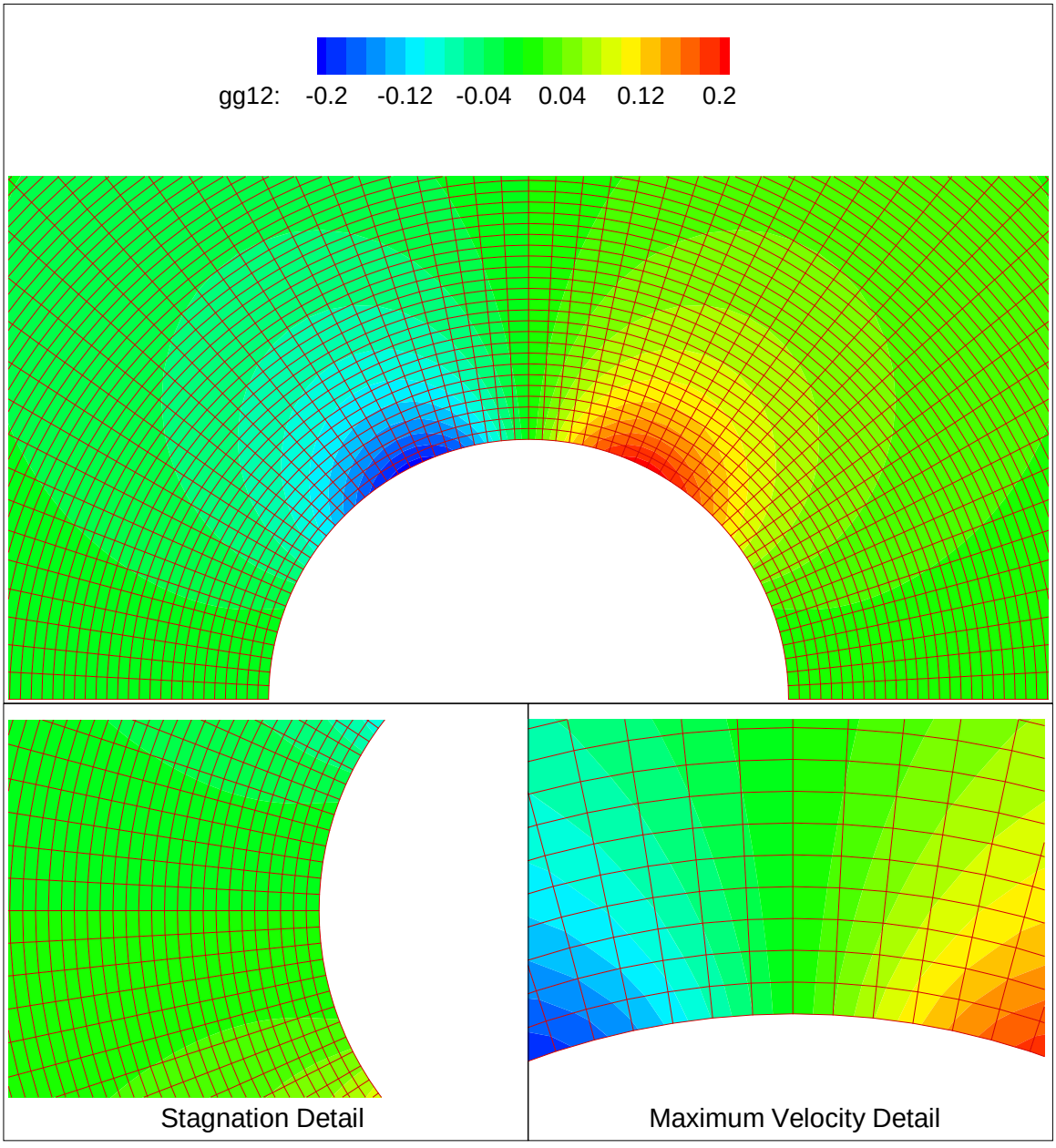

Figure 37: Contours of $\sqrt{g}g^{12}$ for the Circle; Near-Body Domain

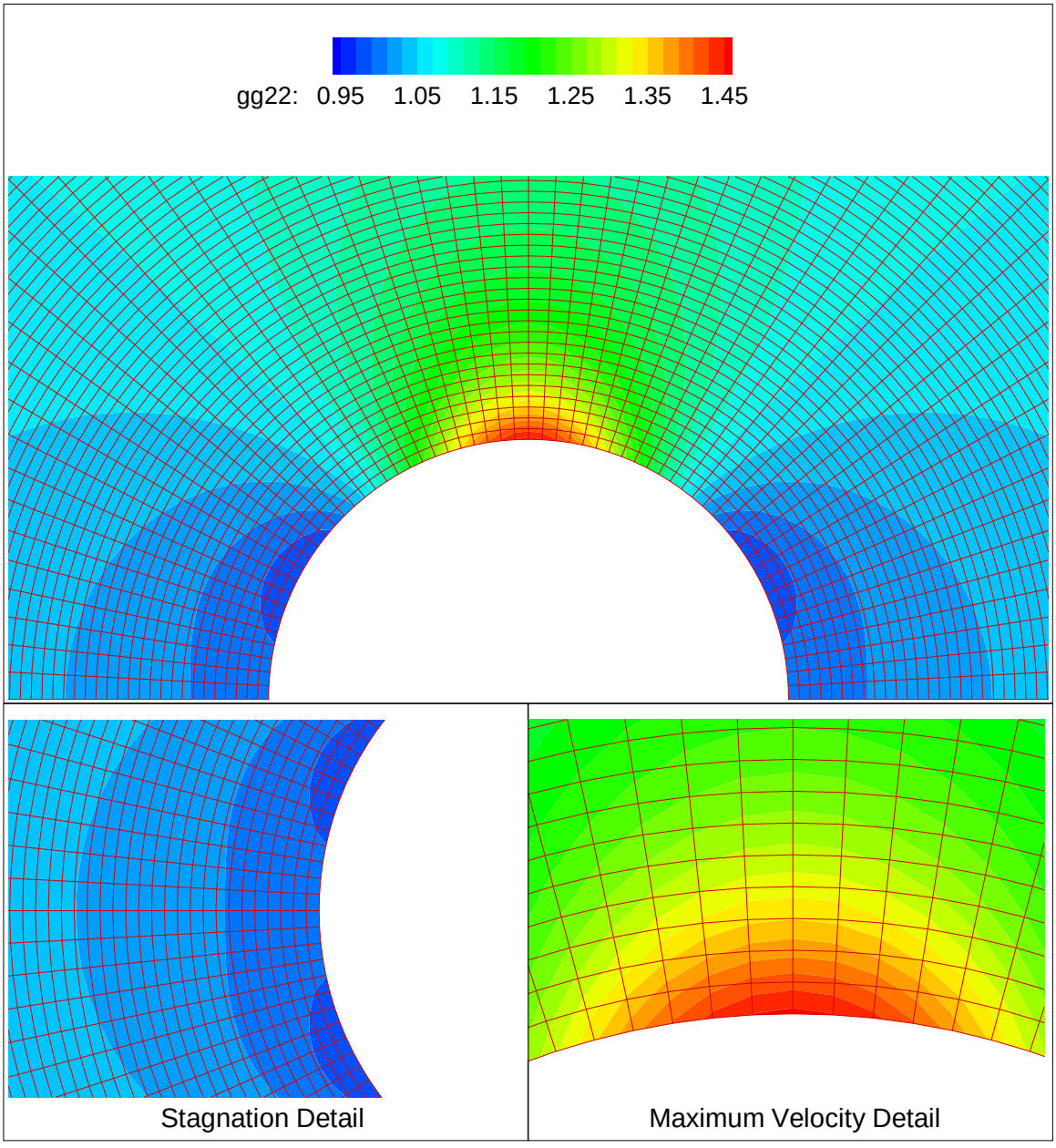

Figure 38: Contours of $\sqrt{g}g^{22}$ for the Circle; Near-Body Domain

airfoil that results from the form of the Prandtl–Glauert rule that describes the relationship between two profiles with the same chord and matched surface pressure coefficients [103]. Although the shape of the distorted body is generally reminiscent of an ellipse, Figure 40 shows that the stretching of the equivalent incompressible shape is more localized than that of an ellipse.

Another interesting feature of this distorted domain is the shape of the far field boundary. Whereas the inner boundary is stretched to a greater thickness, the outer boundary is compacted. Our far field boundary condition was $\bar{x} = x$, so the resulting shrinking is directly apparent in the y-extent of the boundary. The local distortion effects at this boundary are negligible because the flow perturbations are vanishingly small in the far field. The result is therefore a nearly affine scaling of the boundary and its immediate neighborhood. The magnitude of this scaling is

$$\bar{y} = \frac{\rho_\infty}{\rho_0}\, y \tag{282}$$

which can be determined through consideration of the boundary conditions and the generalized Cauchy–Riemann equations in the boundary vicinity, presuming that the vanishing perturbation velocities preclude the necessity to solve the integrability conditions there. Because the inner boundary is stretched and the outer boundary is compacted, this behavior is unlike the effects of the various forms of the Prandtl–Glauert and Göthert rules, which apply a uniform stretching or shrinking throughout the entire domain. That is, if the airfoil boundary is stretched by the application of one of these classical methods, the far field is stretched by the same factor.

Another perspective of the distortion induced by the coordinate mapping is shown in Figure 41. This figure depicts two views of the near-body domain. The first shows a net of coordinate curves of constant $\bar{x}$ and $\bar{y}$ on a plane with Cartesian axes x and y. The second shows the converse relationship with coordinate curves of constant x and y plotted on a plane with axes $\bar{x}$ and $\bar{y}$. Curves of constant x and y on the first plot would form a perfect Cartesian net, whereas the same result would be achieved for curves of contant $\bar{x}$ and $\bar{y}$ on the second plot. These figures are a quantitative representation of the type notionally

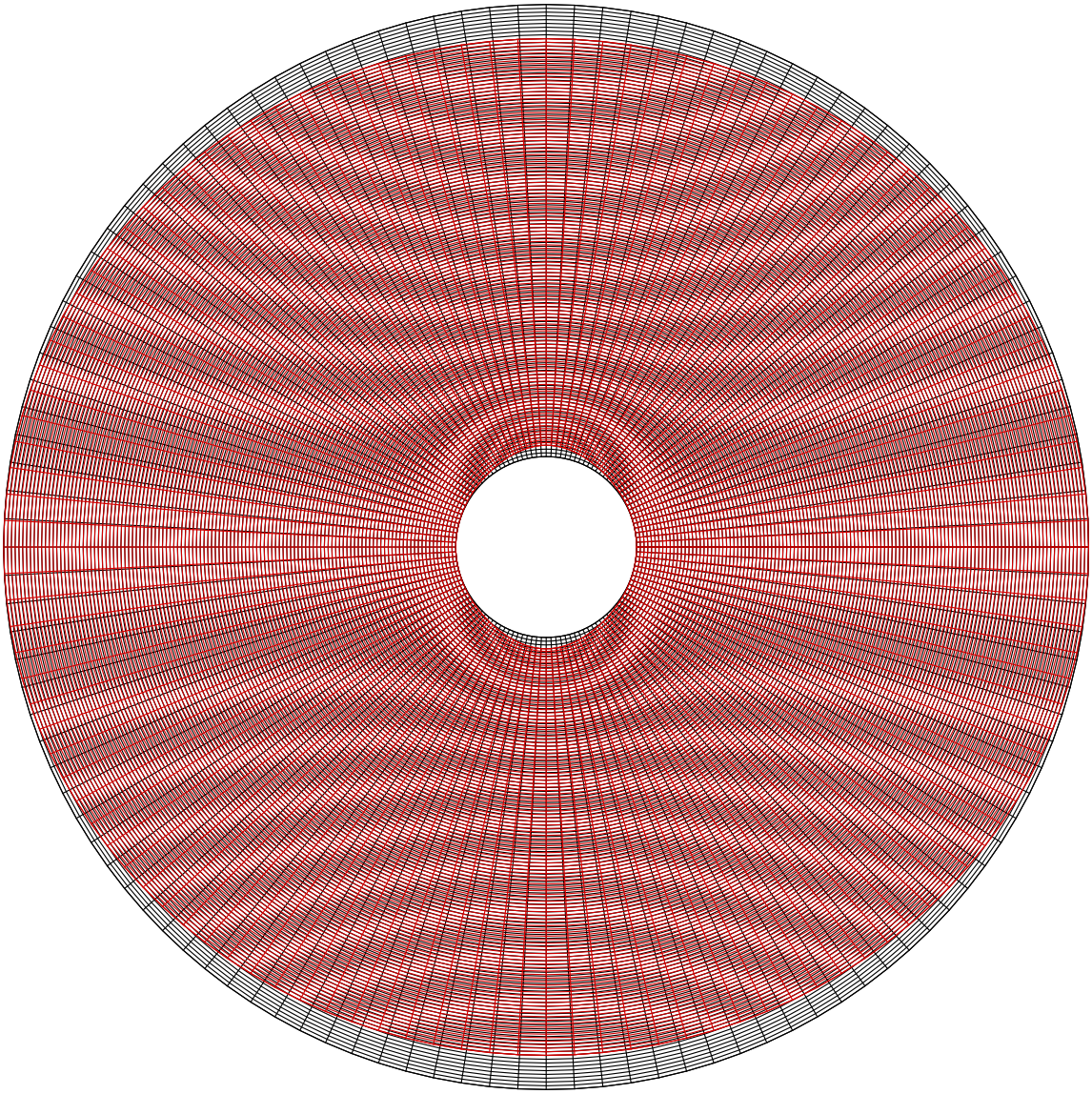

Figure 39: Original (Black) and Equivalent Incompressible (Red) Domain Grids for the Circle

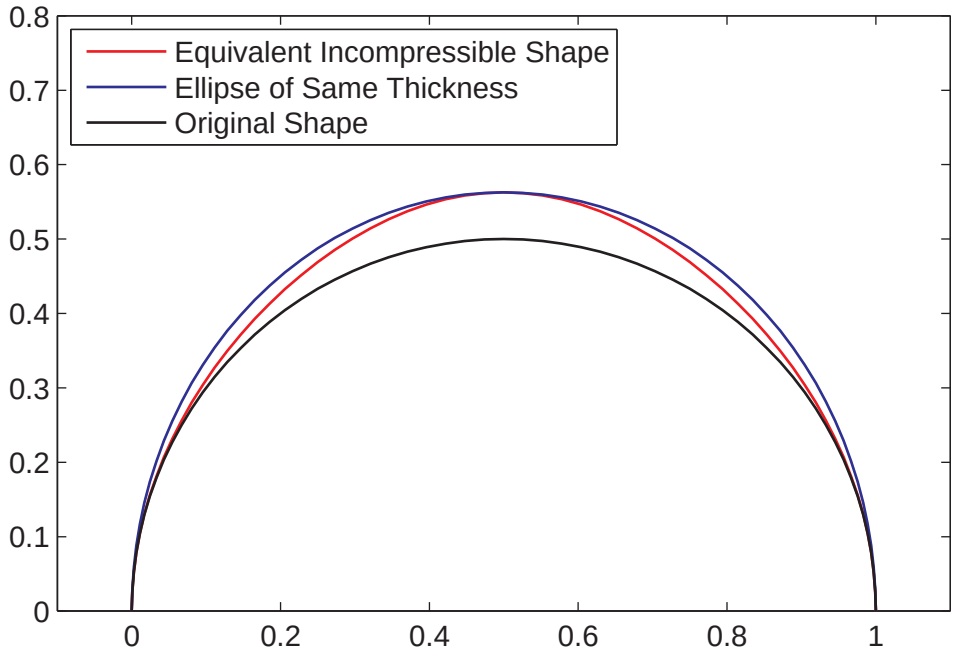

Figure 40: Comarison of the Equivalant Incompressible Shape for the Circle to an Ellipse

depicted in Figure 5.

The main behavior to be observed in these figures is the deviation of the coordinate curves from a perfectly square Cartesian net. The amount of deviation from this square net is indicative of the global and local strengths of the coordinate transformation. Large scale global effects of the transformation tend to stretch the coordinate curves apart, generally mapping the squares uniformly into rectangles. The magnitude of these global effects are driven primarily by the freestream Mach number. Local effects resulting from high flow velocities near the body produce curvature in the coordinate curves.

For the case presented here, global effects are barely visible because the freestream Mach number of 0.375 is too low. We will see more prominent global effects in subsequent results obtained at higher freestream Mach numbers. Although the global effects are weak, the local effects are quite strong, with significant curvature of the coordinate curves in the vicinity of the maximum velocity region.

The ability to capture these types of local effects is perhaps the greatest strength of the method presented in this dissertation compared to the Prandtl–Glauert and Göthert type

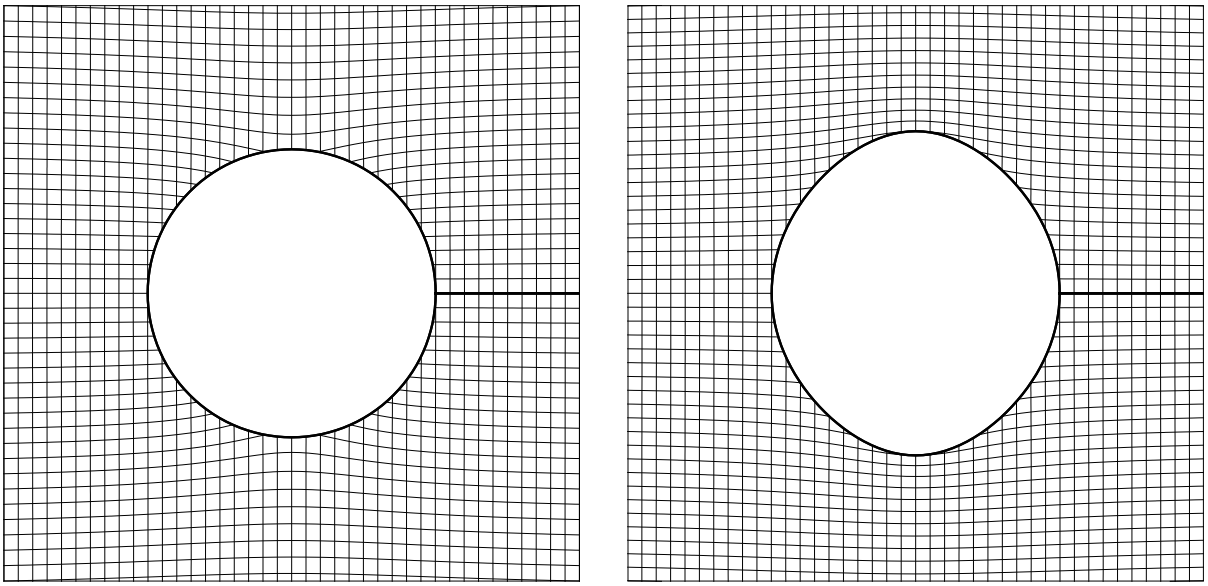

Figure 41: Mapping for the Circle at $M_\infty = 0.375$: **a)** $(\bar{x}, \bar{y})$ Coordinate Curves in the (x, y) Plane; **b)** (x, y) Coordinate Curves in the $(\bar{x}, \bar{y})$ Plane

transformations. Flows over thick bodies such as the circular cylinder cannot credibly be corrected for compressibility with these classical methods because the dominant flow effects are local and not global. Although the Karman–Tsien method captures local effects to some extent, it is limited in accuracy because of its reliance on the tangent gas law. The method developed in this work can be used to develop accurate equivalent incompressible shapes for flows with strong local acceleration for arbitrary γ gases. Such shapes could have uses for investigations in wind tunnels and other testing environments where flow similarity scaling is necessary.

6.1.3 Variation of Solution with $\mathbf{M}_\infty$

In this section, we determine solutions for the flow over a circle for a range of Mach numbers. To obtain these results, the solution parameters remain set to the values indicated in Table 10.

Figures 42 shows the maximum velocity on the circle as a function of the freestream Mach number. In the incompressible limit, the peak velocity ratio is $V_{max}/V_\infty = 2$. The

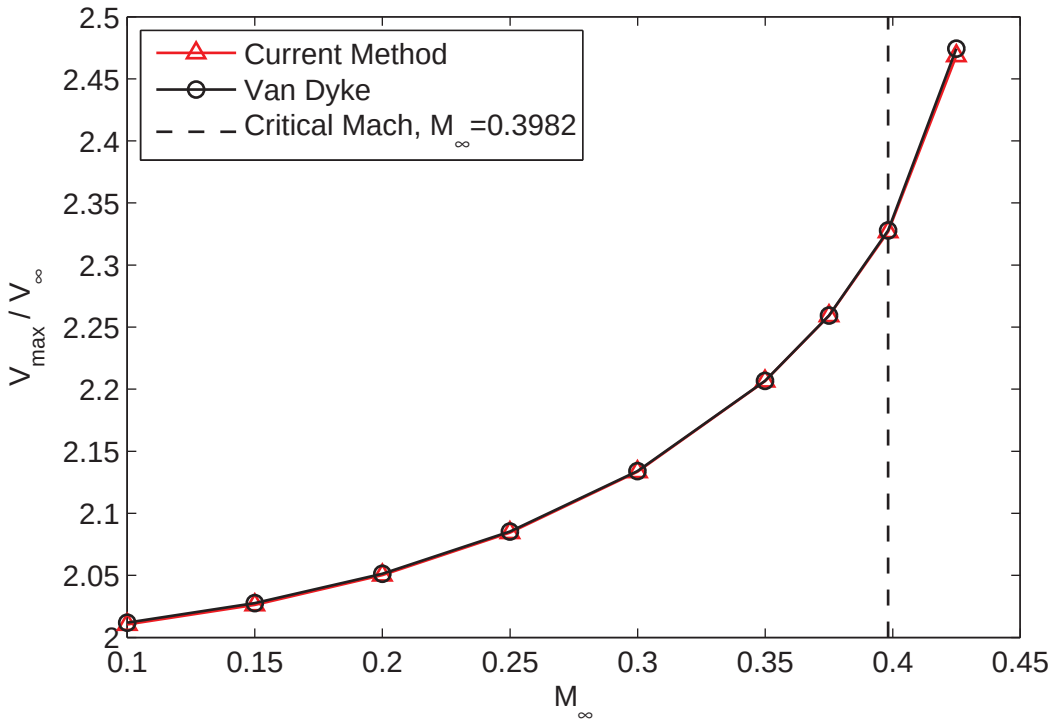

Figure 42: Dependence of Maximum Velocity on Freestream Mach Number

value of this maximum increases with freestream Mach number, passing $V_{max}/V_\infty = 2.327$ at the critical Mach number $M_\infty = 0.3982$. The results produced by the numerical method are compared to those found from Van Dyke's series expansion calculated using Equation 281 and the series terms given in Table 11. Excellent agreement is obtained, as is further indicated by the percent difference shown in Figure 43.

Among the most interesting aspects of Figure 42 is that the results agree well even for the supercritical case at $M_\infty = 0.425$. In Chapter 4, we discussed the likelihood that the transformation method developed in this research is valid only for subcritical flows. The reasoning for this presumption was the well known result that an allowable coordinate transformation cannot change the type of a partial differential equation. In our case, this restriction would seem to imply that our coordinate transformation could not transform a mixed elliptic/hyperbolic type problem in transonic flow above the critical Mach number into a purely elliptic flow governed by the Laplace equation.

Interestingly, however, the result obtained by Van Dyke is not restricted to hold only

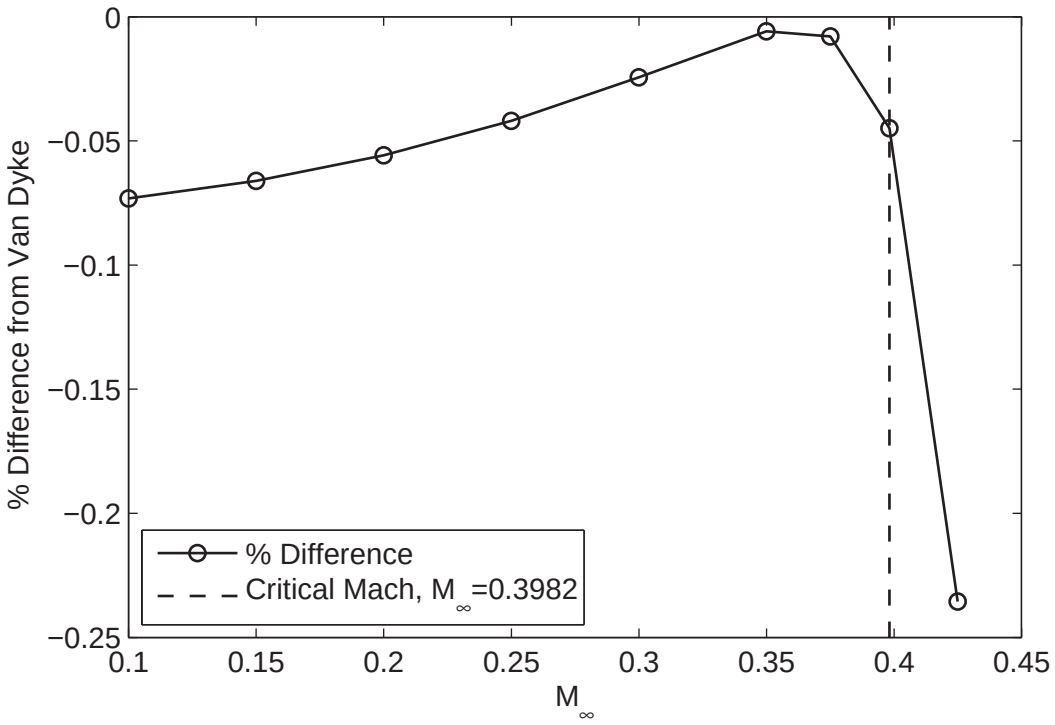

Figure 43: Percent Difference Relative to Van Dyke Results

in the subsonic regime. Indeed, his purpose in developing the high order expansion for the circle was to attempt to answer the so-called *transonic controversy* [123, 124, 121]. This controversy concerns whether or not it is possible to maintain shock free flow about a fixed shape over a range of supercritical Mach numbers. Details of the radius of convergence of the series expansion were expected to yield insights into this question, but concerns regarding the conclusions of these efforts remain [121].

If Van Dyke's result is expected to hold above the critical Mach number and the method developed in this thesis is expected to be invalid in this regime, we are faced either with a contradiction or with a result at $M_\infty = 0.425$ that is obtained by happenstance. One possibility is that the size and magnitude of the supersonic region at $M_\infty = 0.425$ are small enough that the result obtained with the numerical method is nearly correct. If this is the case, we can maintain our conclusion that the method is generally invalid in the supercritical region. This viewpoint is supported by the fact that the error grows substantially from Van Dyke's result at this point (although it is still small), as indicated in Figure 43. Evidence

towards the method's validity only in the subsonic range is also provided by the extreme difficulty with convergence obtained at even slightly higher supercritical Mach numbers.

On the other hand, the fact that the result matches Van Dyke's very closely might suggest that the method can credibly be applied in the lower transonic regime at mildly supercritical freestream Mach numbers. An interesting question is whether the method is actually valid for all shock free isentropic flows with subsonic freestream Mach numbers. If this were the case, the method would have the same validity limits as Van Dyke's series expansion. This possibility is intriguing, but more detailed and careful examinations are needed to substantiate the limits of applicability of the method in this regime. These explorations have not been conducted in this research, but theoretical work in this area is an important future step.

The equivalent incompressible shapes obtained for the sweep of freestream Mach numbers are shown in Figure 44. As we discussed in Section 6.1.2, the general effect of the coordinate transformation is to stretch the circle along the y-axis into a shape somewhat similar to an ellipse. The magnitude of this cross-stream stretching is dependent on the Mach number, with higher Mach numbers lending to greater shape distortion. The quantitative variation of the stretching is shown in Figure 45 along with the $1/\sqrt{1-M_\infty^2}$ Prandtl–Glauert effect. This result emphasizes the prior discussion about the inadequacy of the Prandtl–Glauert method in correcting flows such as this case for the circle which are dominated by local compressibility effects.

6.2 NACA 0012 Airfoil

The NACA 0012 profile is among the airfoils most studied in the field of computational fluid dynamics. The airfoil has gentle curvature around the leading edge, and, like all members in the 4–series family, the shape is defined by globally smooth polynomial and trigonometric functions [1]. These traits make the profile very useful for testing and evaluating numerical methods for subsonic flows.

An example of the use of the NACA 0012 in numerical calculations is provided by Lock, who organized and conducted a series of potential flow solutions for the Advisory Group

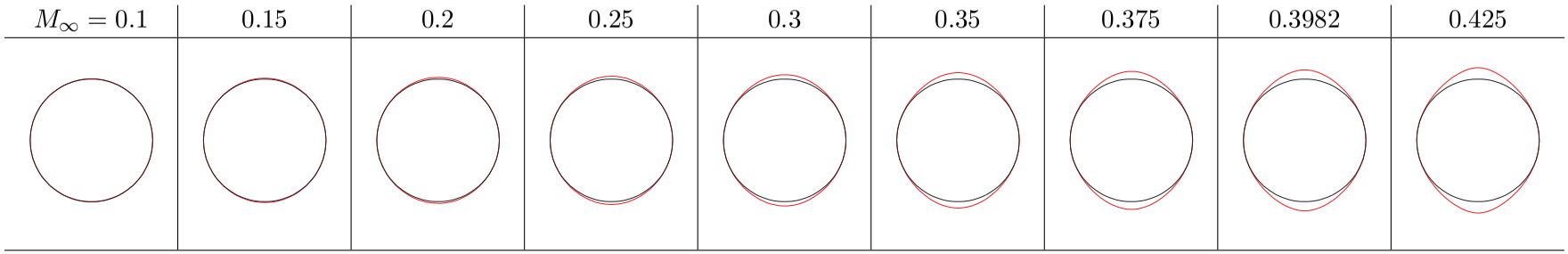

Figure 44: Equivalent Incompressible Shapes to the Circular Cylinder

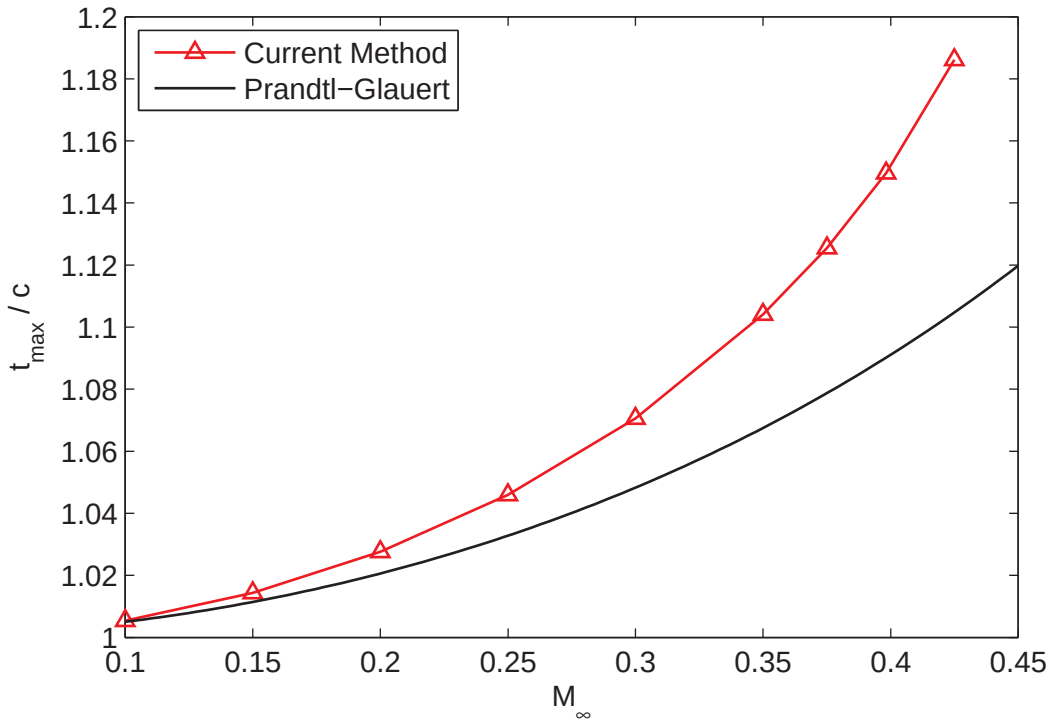

Figure 45: Thickness of Equivalent Incompressible Shapes to the Circle

for Aerospace Research and Development (AGARD) to serve as standard test cases for numerical methods [73]. Solutions were obtained using the hodograph method of Nieuwland [86] and the finite difference approach of Sells [100]. The results computed using these methods were anticipated to be accurate to within 1% of the exact full potential solution. In this report, Lock documents solutions for the NACA 0012 at $M_\infty = 0.72$, $\alpha = 0°$ and $M_\infty = 0.63$, $\alpha = 2°$.

In this section, we explore the results of the mapping method to flows over the NACA 0012. First, we examine the near-critical symmetric flow at $M_\infty = 0.72$. Next, we investigate the lifting flow at $M_\infty = 0.63$, $\alpha = 2°$. The results of these analyses are compared to those obtained by Lock. We conclude the section with a study of the results obtained in a systematic variation of the freestream Mach number and angle of attack. This study reveals many of the salient effects of the coordinate transformation in differing flow conditions, from which we can develop insights that may ultimately be useful for aerodynamic design.

Table 12: Parameter Settings for NACA 0012 at $M_\infty = 0.72, \alpha = 0^\circ$

Name	Symbol	Setting
Number of circumferential grid nodes	i_{max}	121
Number of radial grid nodes	j_{max}	121
Outer loop convergence tolerance	ϵ	10^{-8}
Inner loop convergence tolerance	τ	10^{-6}
Outer boundary radius to chord ratio	R/c	3
Over-relaxation parameter	Ω	1.98
Off-body grid spacing parameter	ζ	3

6.2.1 Symmetric Flow: $\mathbf{M_\infty = 0.72}$*,* $\alpha = \mathbf{0}^\circ$

The focus of this section is to present the solution and the equivalent incompressible flow field for the NACA 0012 at $M_\infty = 0.72$ and zero incidence. The purpose of obtaining these results is twofold. First, this solution corresponds to a case for which full potential results are available for comparison from Lock [73]. Second, the simplicity of the symmetric flowfield represents only a mild step from the circle solution that we can use to build further insights into the behavior of the equivalent flow before introducing the full problem of circulation and asymmetry.

The solution parameter settings used to carry out this flow simulation are presented in Table 12. Insofar as practicable, the majority of these settings have been carried over from those listed in Table 10 for the circle. The number of nodes was kept the same at 121×121, and the convergence tolerance settings τ and ϵ as well as the setting for the over-relaxation parameter Ω were retained. For the case of the airfoil, we reinterpret the nondimensional boundary location as $R/c = 3$ where c is the airfoil chord. This formulation is identical to that of the circle because we had previously defined the location as $R/r = 6$ where $r = c/2$ is the inner circle radius. Although it is likely that these settings applied to the NACA airfoil are no longer optimal, they nonetheless leverage the extensive experience base developed for the circle and have been found to produce good results.

The only substantive alteration to the circle settings is the selection of the exponential off-body spacing parameter as $\zeta = 3$ as compared to $\zeta = 0.01$ for the circle. Whereas $\zeta = 0.01$ corresponds to a nearly linear interpolation of points in the j grid direction, the

larger ζ setting clusters greater grid density very close to the airfoil boundary. The effect of this setting is akin to increasing the overall grid density in the j direction but without the expense of adding additional grid nodes; however, care must be taken not to set ζ too high, or grid density in the far field will prove insufficient for accuracy. The value $\zeta = 3$ was found to be a good compromise setting for the conditions of this particular solution. This setting was changed from that of the circle primarily because the airfoil is thinner relative to the location of the outer boundary. To obtain the necessary grid density near the body, one must either increase the number of j nodes with linear interpolation, or alternately, adopt a nonlinear interpolative procedure by selecting a larger value for ζ. This latter approach was adopted to keep the grid size reasonable for minimized computational expense as well as to keep the grids shown in this thesis to a reasonable and visually appealing density.

The convergence results for the solution are shown in Figures 46 and 47. The behavior of the outer loop convergence is qualitatively very similar to that of the circle shown in Figure 30, with an initially very steep drop in the residual corresponding to the correction of the incompressible guess followed by a smooth convergence history with a slight curvature on the log scale. The number of required iterations is double that of the circle, however. This increase is attributable primarily to the higher freestream Mach number, which implies the initial incompressible guess is more incorrect.

The inner loop residual history is somewhat different from the circle result shown in Figure 31. The initial bobble is more pronounced, with the residual increasing by an order of magnitude before decreasing. After the initial correction, however, the latter two thirds of the convergence history shows log-linear behavior.

The surface pressure distributions are shown in Figures 48 and 49. Figure 48 compares the results to those presented by Lock [73]. The agreement is generally quite good, particularly along the initial rise-up profile from the leading edge toward the suction peak. Results in this region agree to within $1 - 2\%$.

Results in the mid-chord to aft body region show larger absolute differences, particularly near the trailing edge and the location at which C_p changes sign. Much of the error in the aft body and trailing edge region is likely attributable to the low trailing edge point density.

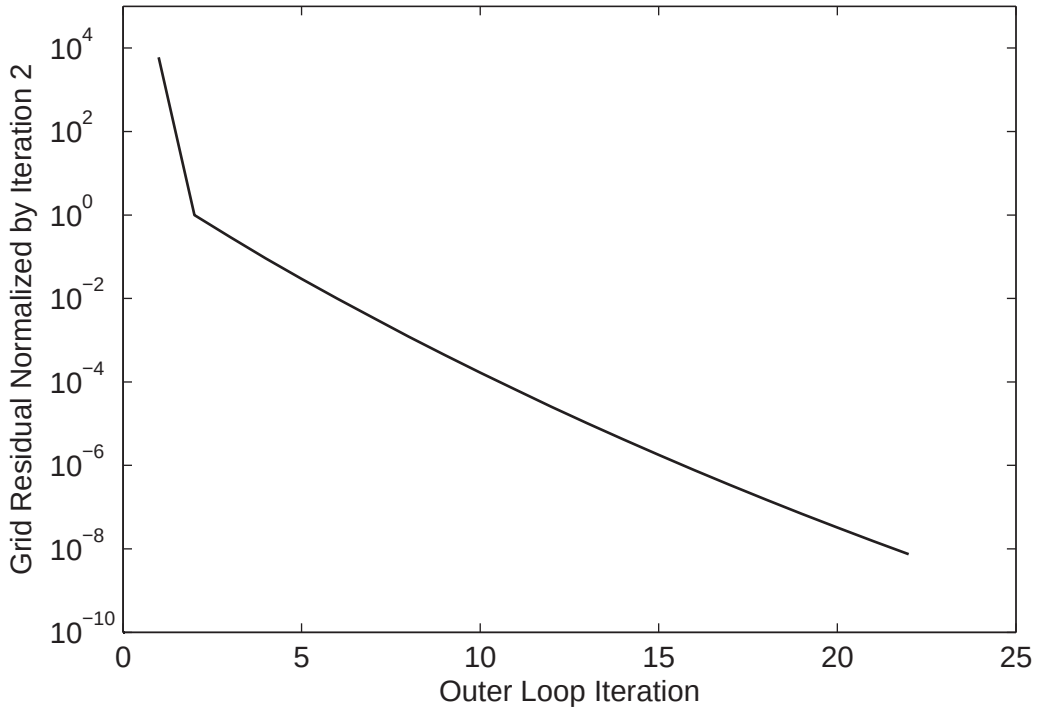

Figure 46: Outer Loop Convergence History for the NACA 0012, $M_\infty = 0.72$, $\alpha = 0^\circ$

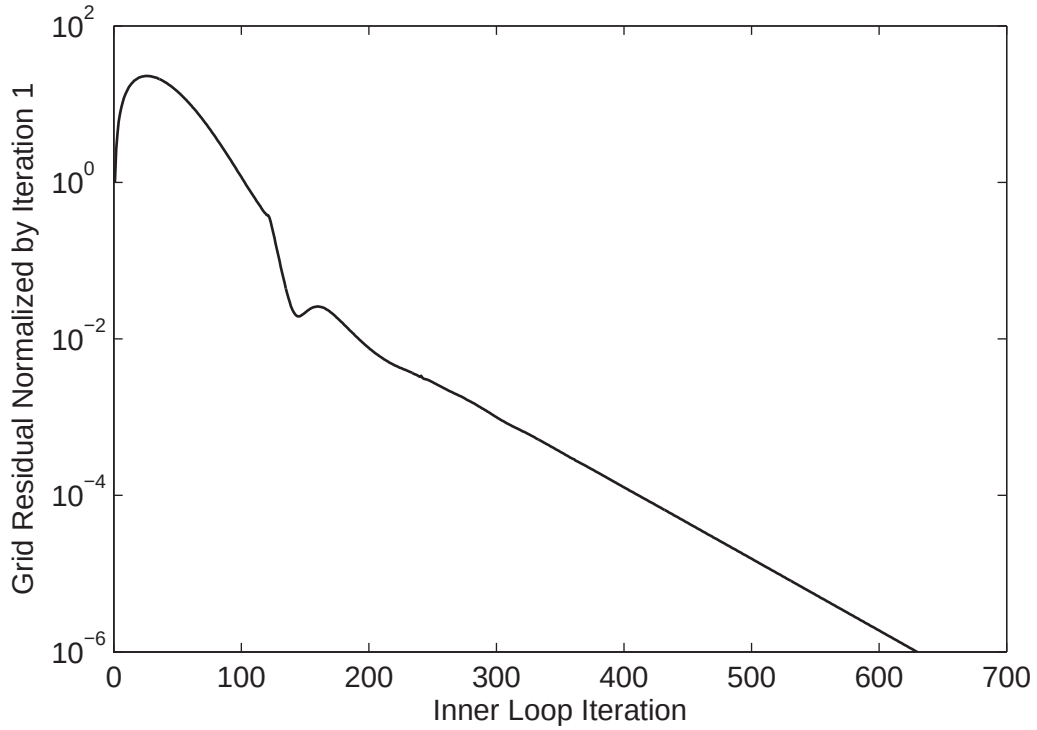

Figure 47: Inner Loop Convergence History at Last Outer Loop Iteration for the NACA 0012, $M_\infty = 0.72$, $\alpha = 0^\circ$

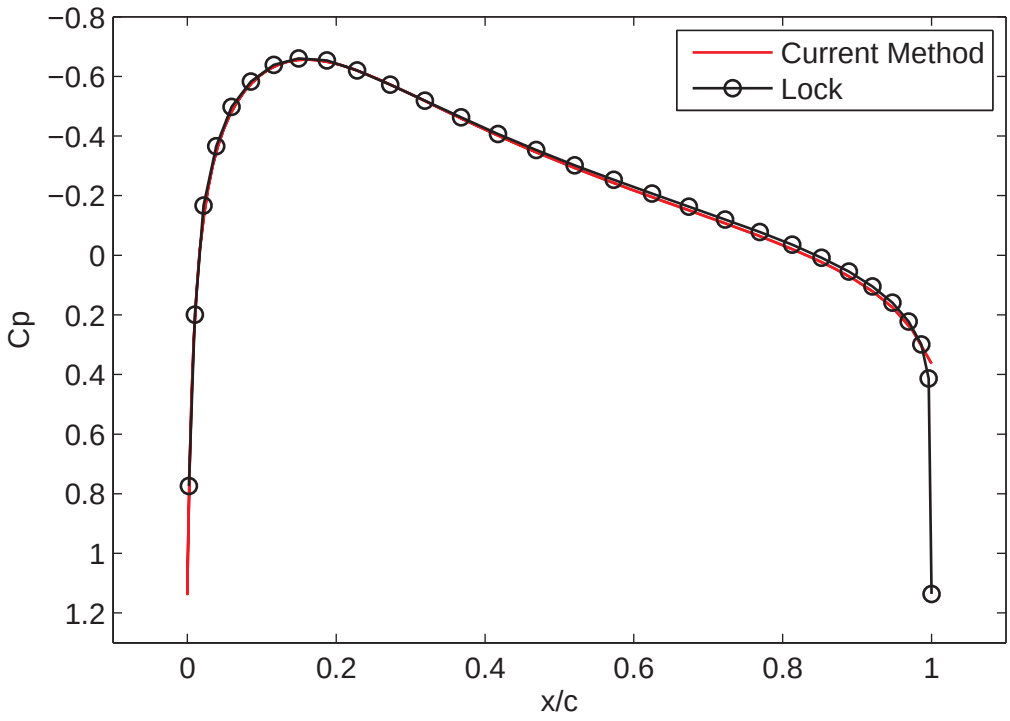

Figure 48: Surface Pressure Coefficients for the NACA 0012, $M_\infty = 0.72$, $\alpha = 0°$

As discussed in Chapter 5, stability considerations with the implementation demanded that airfoils with a sharp trailing edge be parameterized with a node spacing function that smoothly clusters points with greater density at the leading edge and more sparse density at the trailing edge. This lower trailing edge density causes less accurate solutions in this region, although the resulting predictions are nonetheless well behaved and smooth.

Figure 49 shows the pressure distribution at the suction peak compared to those obtained by Prandtl–Glauert and Kármán-Tsien corrections of the incompressible flow. The behavior depicted in this figure is characteristic of one of the weaknesses of the classical compressibility corrections. Because they act by a transformation of the form $C_p|_x = f\left(C_{p,\,\text{incomp.}}|_x\right)$ that depends only on the local incompressible value, they do not capture compressibility effects that might be considered "integral" in nature, i.e. that depend on information not available locally in the incompressible flow solution. The shifting of the suction peak aftward along the airfoil is an example of this type of integral effect that is illustrated in Figure 49.

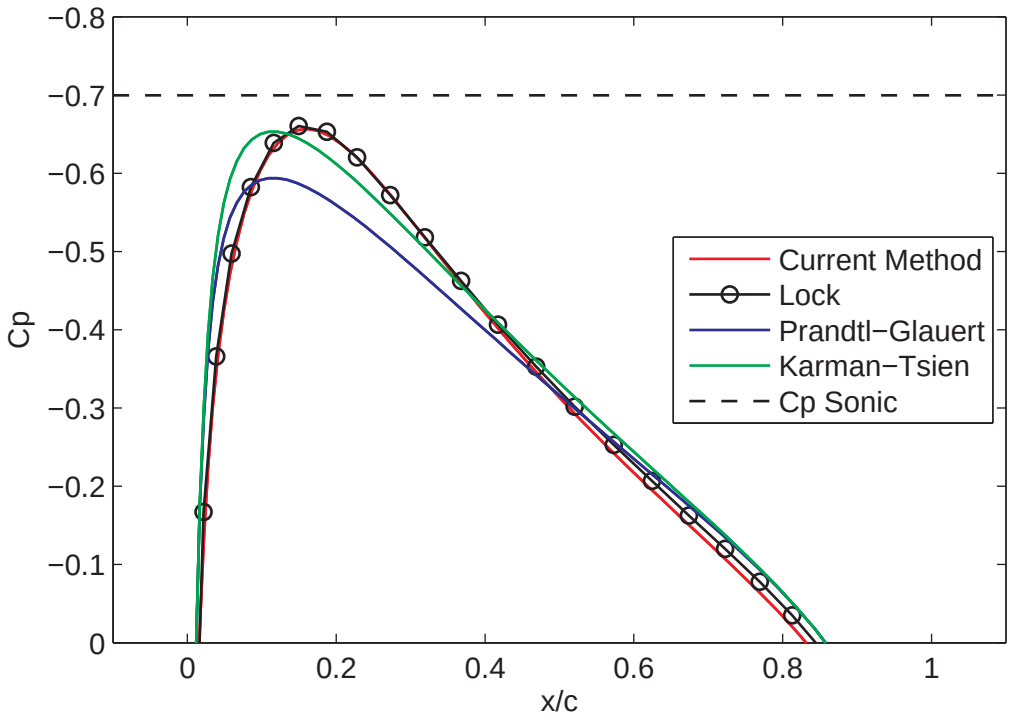

Figure 49: Surface Pressure Coefficients for the NACA 0012, $M_\infty = 0.72$, $\alpha = 0°$; Suction Peak Detail

Whereas the Prandtl–Glauert and Kármán-Tsien methods primarily scale the local incompressible C_p values and therefore miss the shift in x/c of the peak, the numerical method developed in this work captures the shift correctly because the non-local information is propagated appropriately in the iterative mapping procedure.

Contour plots of the field solution are presented in Figures 50–52. The pressure coefficient is depicted in Figures 50 and 51, and the local Mach number is shown in Figure 52. Figure 52 also shows the velocity vector field in the airfoil forebody region. The qualitative behavior of the solution is correct, with a prominent stagnation region at the leading edge and maximum velocity attained slightly fore of 20% chord. The high velocity region extends outward from the airfoil, decreasing in magnitude until it is substantially matched to the freestream at the outer boundary radius. A true aft stagnation point is not numerically attained due to the coarse grid in the trailing edge region. This deficiency is not significant, however, because the trailing edge stagnation region is smaller than that of the leading

edge and lack of good resolution in the region appears to have minor effect on the overall solution.

The converged metric tensor components are shown in Figures 53–55. Results are qualitatively similar to those of the circle, with $\sqrt{g}g^{11}$ and $\sqrt{g}g^{22}$ symmetric about the x-axis and $\sqrt{g}g^{12}$ antisymmetric. It is interesting to note that the maximum of $\sqrt{g}g^{11}$ and the minimum of $\sqrt{g}g^{22}$ coincide and that the location of this extremum is not directly at the leading edge, but rather, slightly offset aftward from the leading edge on the airfoil surface. The location is driven by the fact that the metric components are functions of products of the velocity components and therefore have extrema at non-obvious points along the profile.

Although they can be seen by close inspection of the other contour plots, slight defects in the solution are particularly apparent in Figure 53. These defects can be seen along the minimum contour of $\sqrt{g}g^{11}$ near the suction peak. This contour exhibits two discontinuities between the body surface and the first off-body j line of nodes, one at the forward end of the contour, and a second at the aft end. This defect likely indicates that the off-body grid resolution is not adequate to capture the rapid change in the solution in this region as the j grid lines are traversed. This behavior is typical for cases in which the grid resolution or spacing are not completely adequate, and it is likely linked to the errors seen in the surface C_p aft of the maximum velocity point. Because the results for this case are generally good nonetheless, we present these results here to illustrate this symptom of undesirable solution quality.

We now discuss the coordinate mapping. Figure 56 shows the solved coordinate grid corresponding to the equivalent incompressible domain superimposed over the original domain grid corresponding to the compressible flow. The fine off-body clustering resulting from the setting $\zeta = 3$ for the exponential spacing parameter is also readily apparent. As with the circle, the inner boundary of the equivalent incompressible domain is thickened while the outer boundary is compacted. The overall magnitude of the distortion is greater for this case than for the circle because of the higher freestream Mach number. This greater distortion is particularly evident in the movement of the outer boundary, which is much more significant here than for the circle.

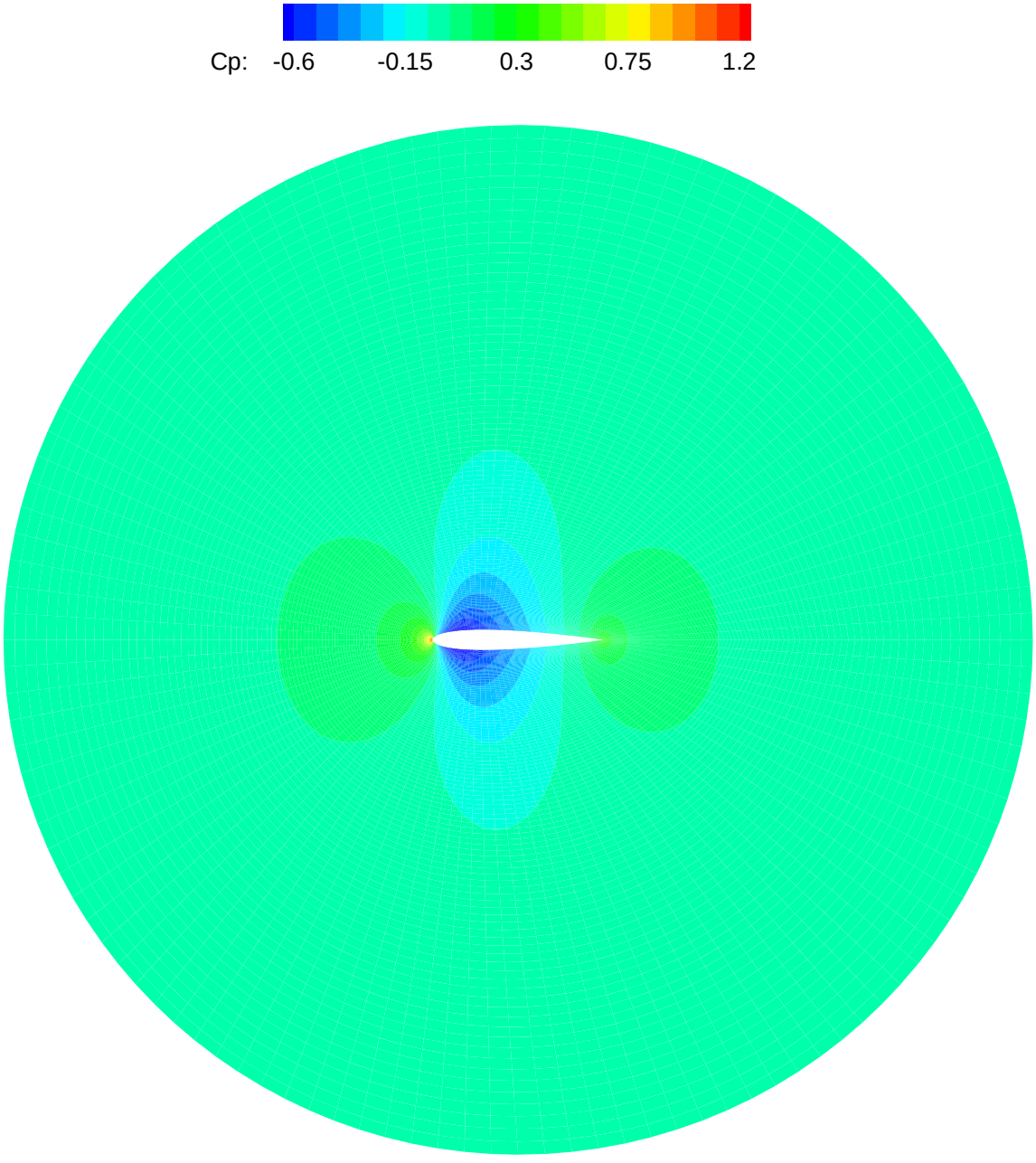

Figure 50: Pressure Coefficient Contours for the NACA 0012, $M_\infty = 0.72$, $\alpha = 0°$

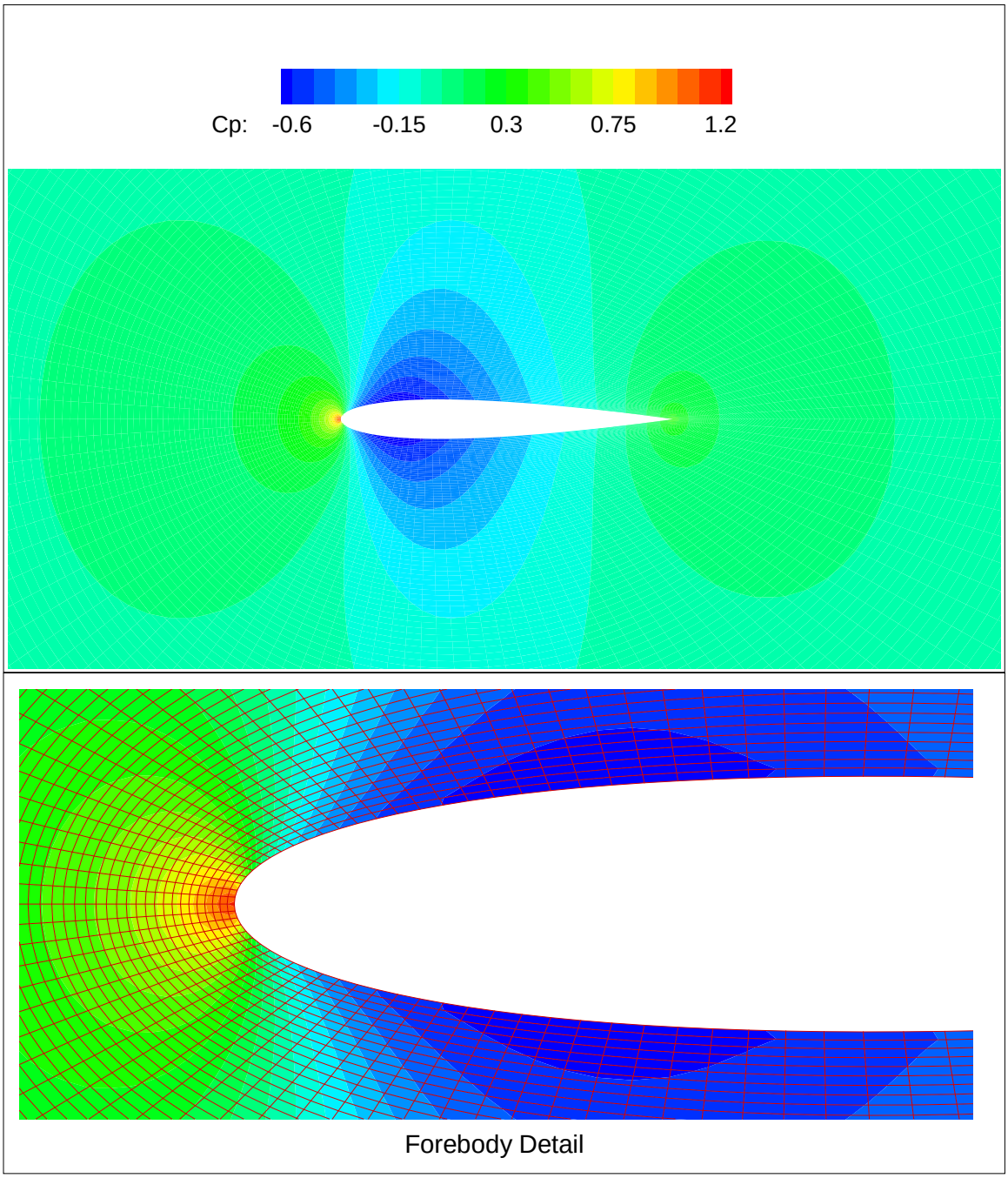

Figure 51: Pressure Coefficient Contours for the NACA 0012, $M_\infty = 0.72$, $\alpha = 0°$; Near-Body Domain

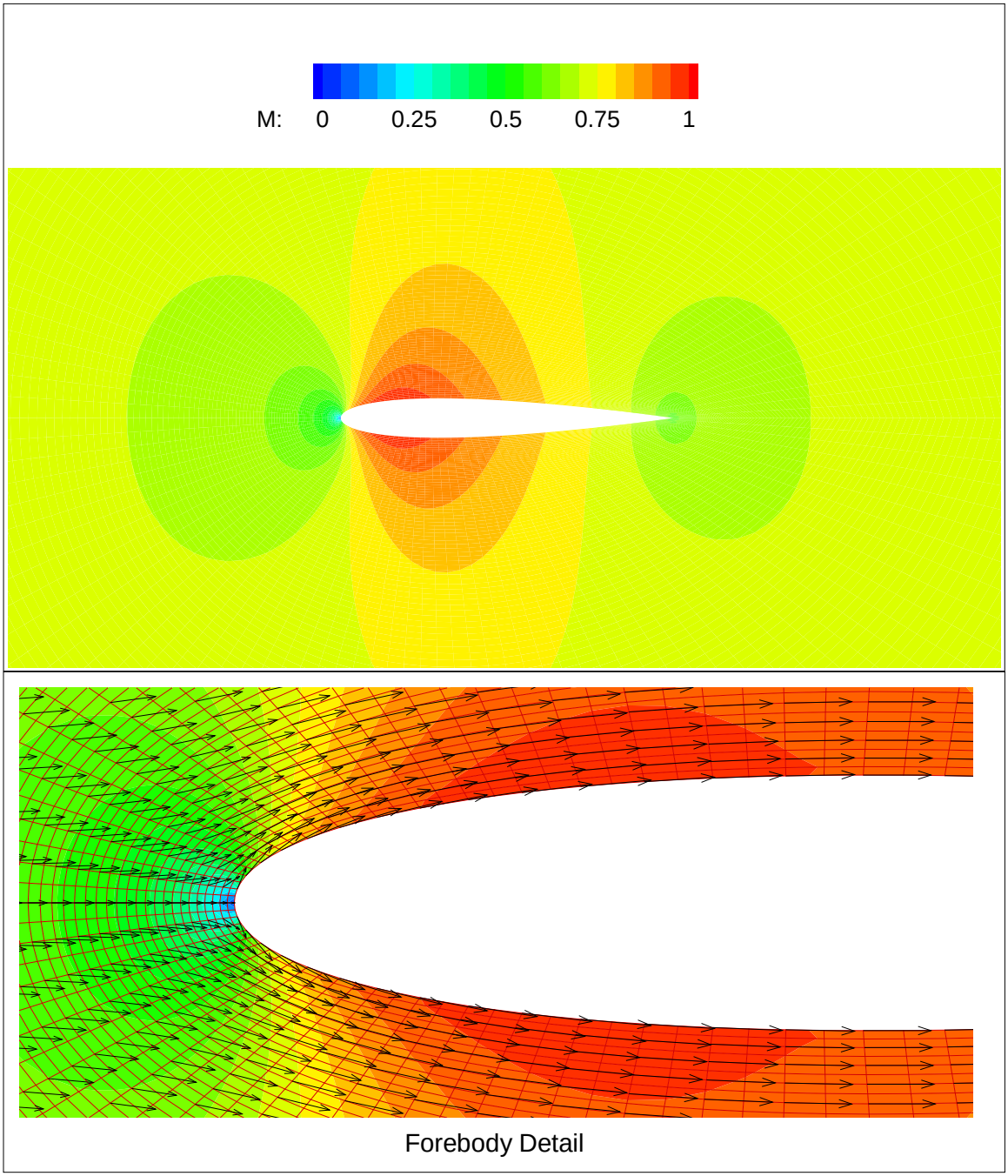

Figure 52: Mach Number Contours for the NACA 0012, $M_\infty = 0.72$, $\alpha = 0°$; Near-Body Domain

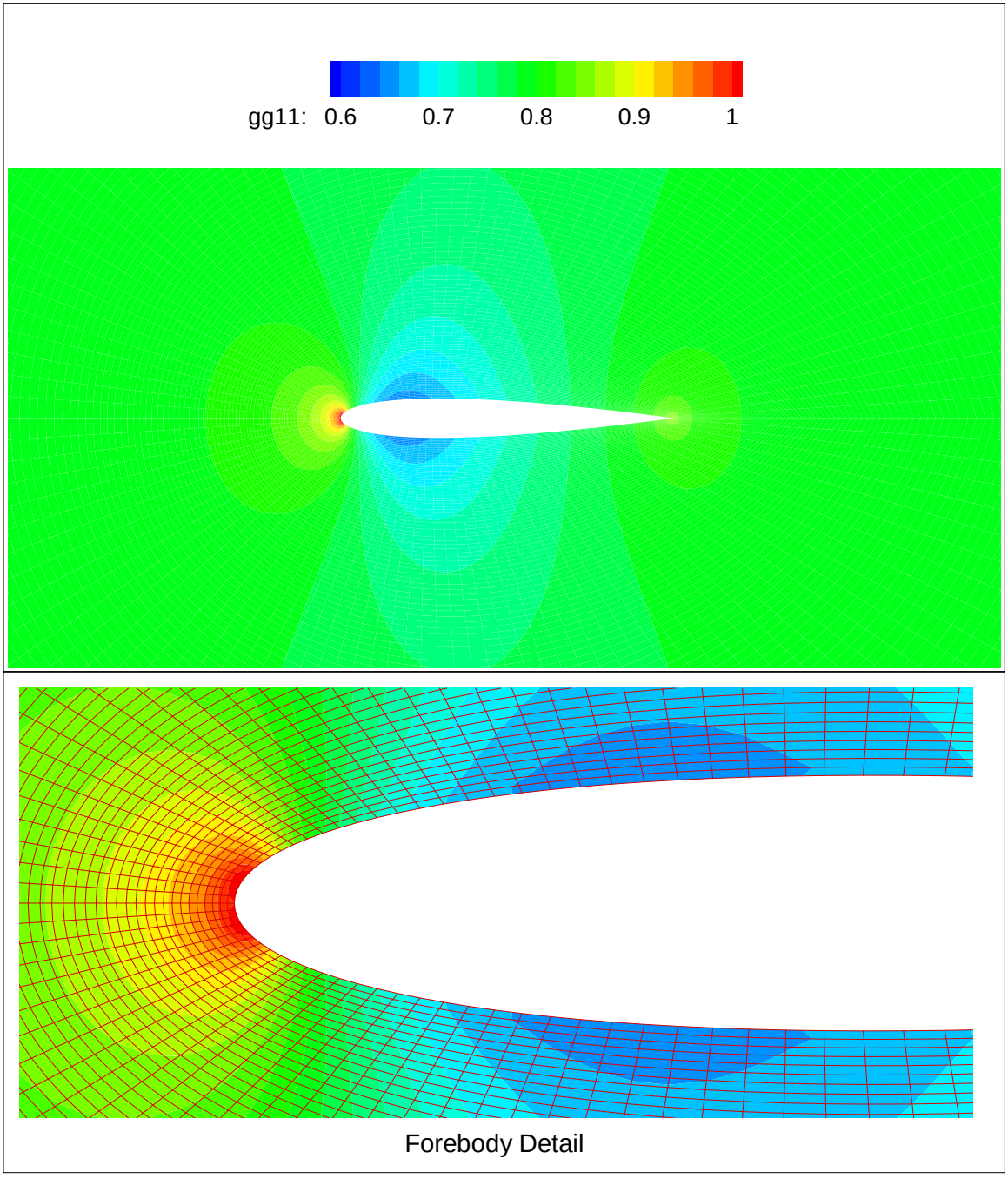

Figure 53: Contours of $\sqrt{g}g^{11}$ for the NACA 0012, $M_\infty = 0.72$, $\alpha = 0°$; Near-Body Domain

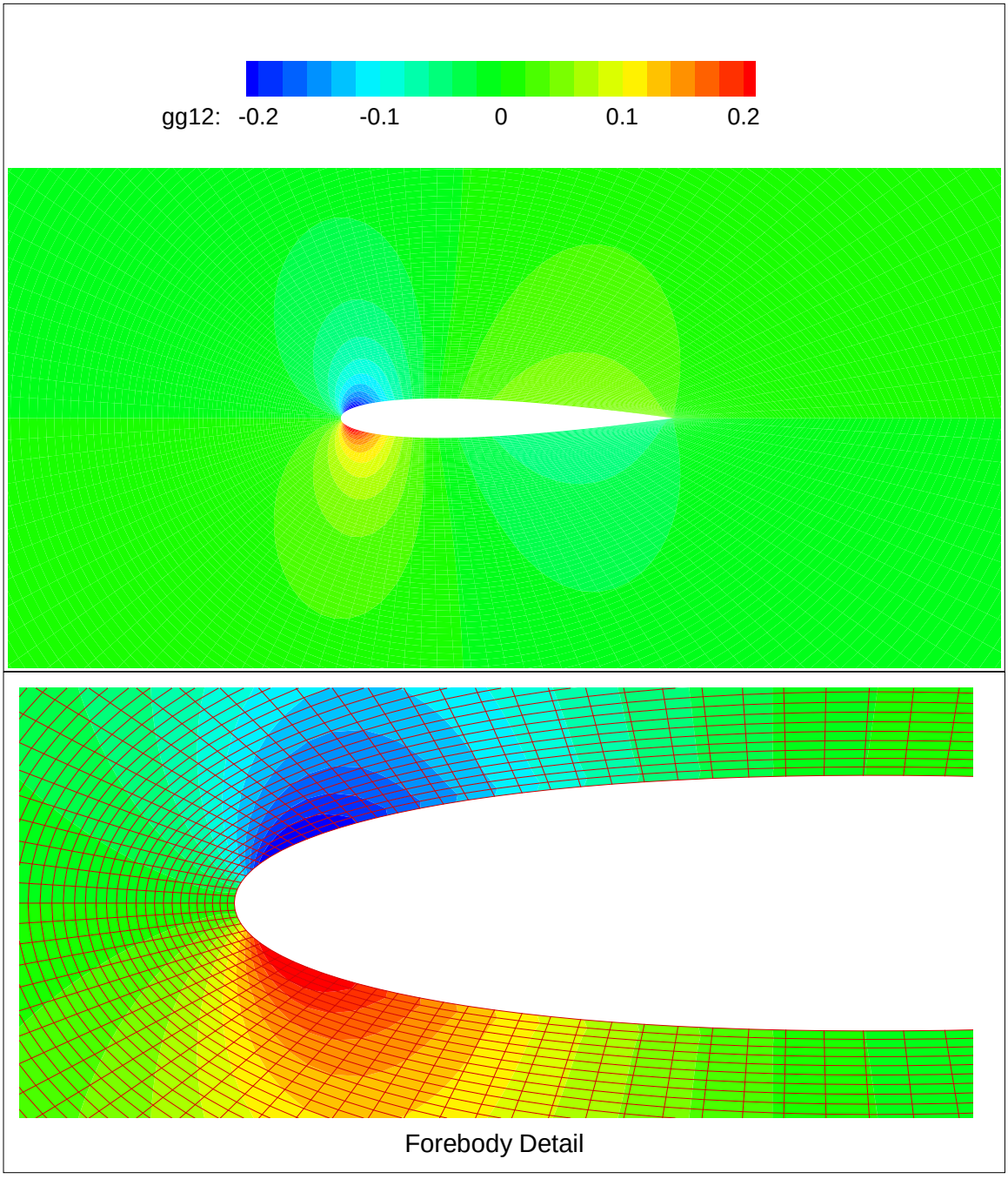

Figure 54: Contours of $\sqrt{g}g^{12}$ for the NACA 0012, $M_\infty = 0.72$, $\alpha = 0°$; Near-Body Domain

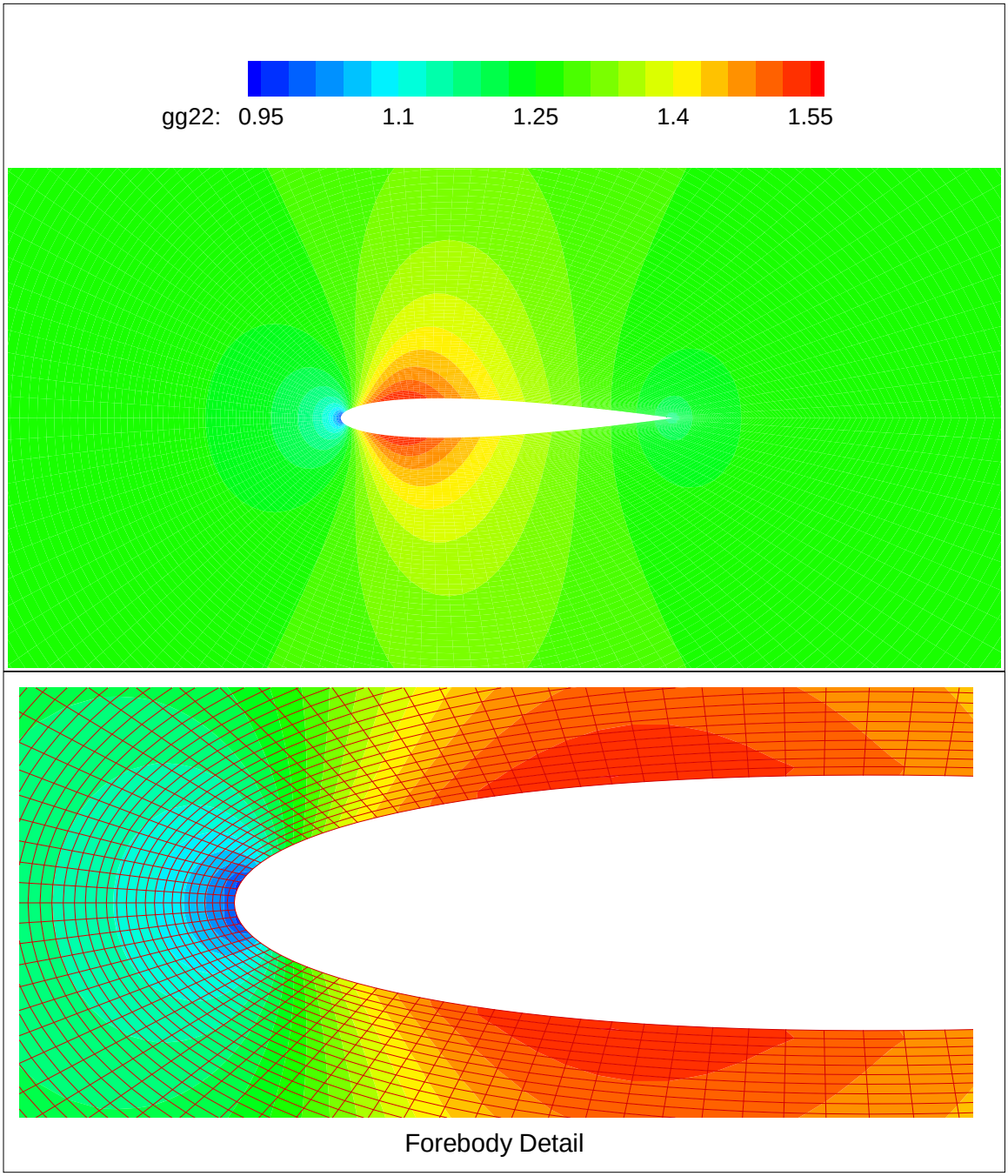

Figure 55: Contours of $\sqrt{g}g^{22}$ for the NACA 0012, $M_\infty = 0.72$, $\alpha = 0°$; Near-Body Domain

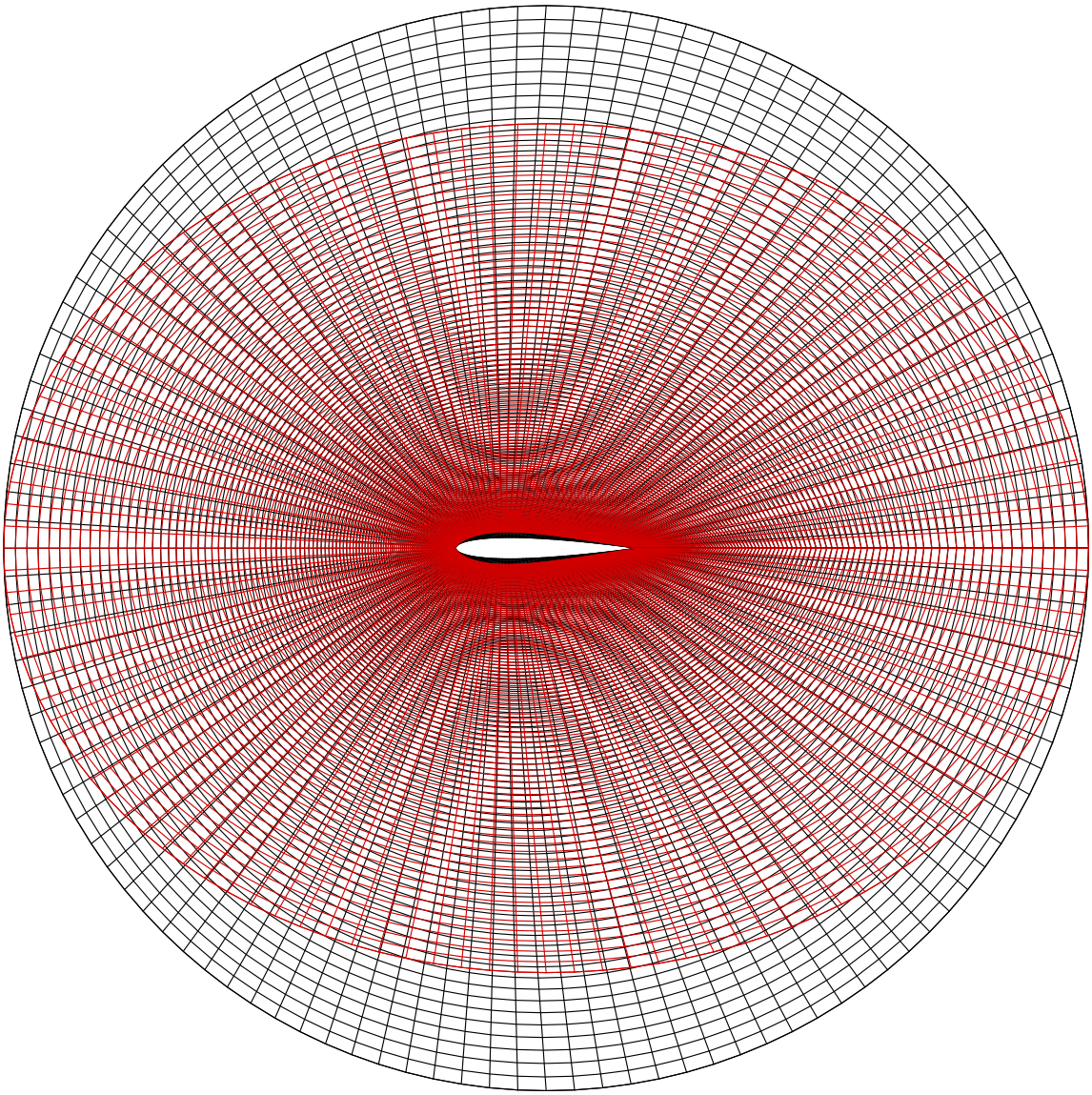

Figure 56: Original (Black) and Equivalent Incompressible (Red) Domain Grids for the NACA 0012, $M_\infty = 0.72$, $\alpha = 0^\circ$

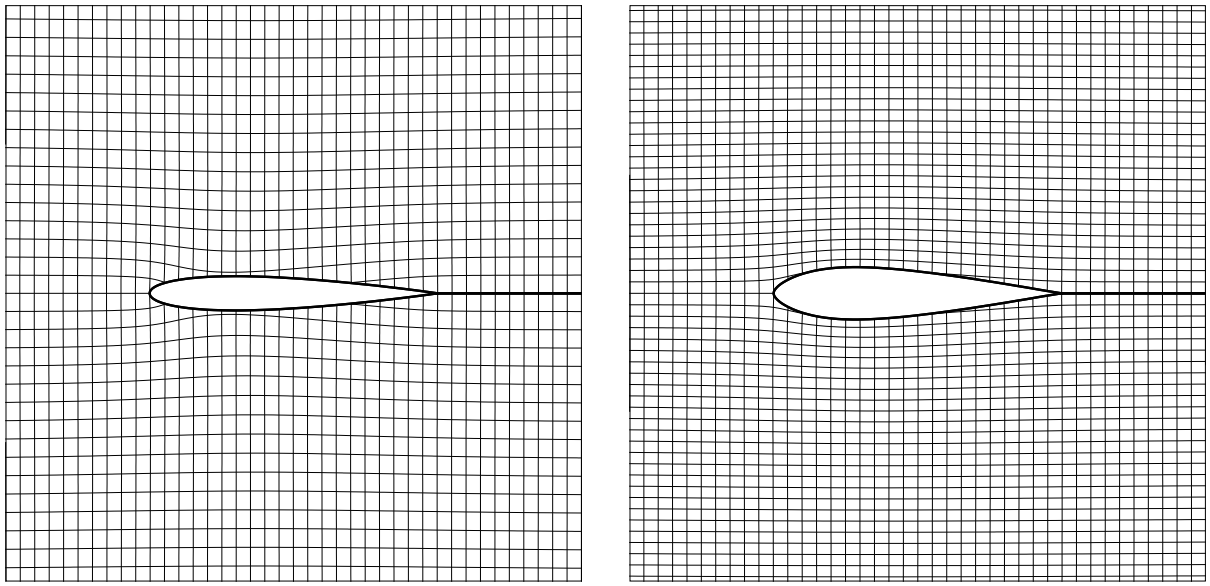

Figure 57: Mapping for the for the NACA 0012, $M_\infty = 0.72$, $\alpha = 0°$: **a)** $(\bar{x}, \bar{y})$ Coordinate Curves in the (x, y) Plane; **b)** (x, y) Coordinate Curves in the $(\bar{x}, \bar{y})$ Plane

The graphic on the left in Figure 57 shows coordinate curves of constant isothermal coordinates $\bar{x}$ and $\bar{y}$ plotted on a plane defined by Cartesian axes x and y. The graphic on the right shows coordinate curves of constant x and y plotted on a plane defined by Cartesian axes $\bar{x}$ and $\bar{y}$. As discussed in relation to the circle, the primary features to examine in these plots are the uniform spacing and the curvature of these coordinate lines. A uniform spacing between the lines that produces rectangular cells from the nominally square net is indicative of the global effect of freestream Mach number. Curvature in the lines is evident of local flow accelerations. Compared to the circle, these results show a greater uniform distortion as evidence by the generally rectangular shaped cells, with long axis along y in the left plot and long axis along $\bar{x}$ in the right plot. This increased distortion is due to the greater Mach number for this case compared to that of the circle. The regions of greatest curvature of the coordinate lines are near the leading edge and near the suction peak where velocity magnitudes are most different from their freestream values.

Table 13: Parameter Settings for NACA 0012 at $M_\infty = 0.63, \alpha = 2^\circ$

Name	Symbol	Setting
Number of circumferential grid nodes	i_{max}	161
Number of radial grid nodes	j_{max}	161
Outer loop convergence tolerance	ϵ	10^{-8}
Inner loop convergence tolerance	τ	10^{-6}
Outer boundary radius to chord ratio	R/c	3
Over-relaxation parameter	Ω	1.995
Off-body grid spacing parameter	ζ	2

6.2.2 Lifting Flow: $\mathbf{M_\infty = 0.63}$, $\alpha = \mathbf{2}^\circ$

In this section, we present results for the flow over the NACA 0012 at $M_\infty = 0.63$, $\alpha = 2^\circ$. In these simulations, the Kutta condition is enforced, so the flows are not only asymmetric but also circulatory.

The parameter settings chosen for the solution are listed in Table 13. The outer and inner loop convergence tolerances as well as the radius to chord ratio of the outer boundary have been set to the same values used for both the circle and the symmetric airfoil flow presented in the last section. Several settings have been altered, however. The number of grid nodes in both the i and j directions has been increased from 121 to 161, and the exponential spacing parameter has been adjusted from $\zeta = 3$ for the NACA 0012 symmetric case to $\zeta = 2$. The reason for these changes is that the lifting flow solution is more difficult to converge and less accurate for a given grid. To produce improved solution quality, higher global grid densities are required. This issue motivated the higher values of i_{max} and j_{max}. The ζ spacing value was reduced from that of the symmetric airfoil case in order to maintain reasonable cell aspect ratios near the body. The aspect ratio issue could alternately have been addressed by further increasing the number of body aligned points i_{max}; however, this result would produce a larger grid and an associated increase in solution expense and degradation of the visual appeal of the grid for display. Because the overall grid density was increased, the over-relaxation parameter Ω was also increased from $\Omega = 1.98$ for the circle and symmetric NACA 0012 to $\Omega = 1.995$. Increased values of Ω are allowable as the grid is refined as in this case, and increases allows a greater convergence rate. Although

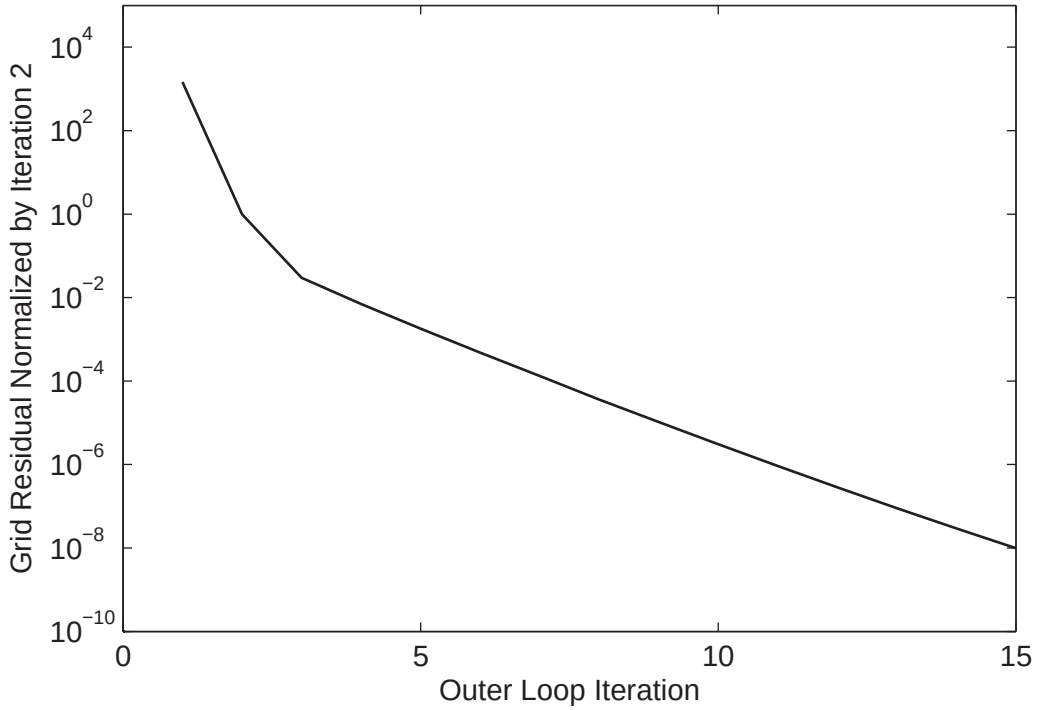

Figure 58: Outer Loop Convergence History for the NACA 0012, $M_\infty = 0.63$, $\alpha = 2^\circ$

not necessarily optimal for this configuration, this choice of parameter settings was found to produce good solution quality, particularly as evidenced in the validation results.

The convergence behavior for the solution is presented in Figures 58 and 59. The qualitative behavior of the outer loop residual history is similar to that of the circle and symmetric airfoil except for the appearance of an intermediate slope that occurs between iterations two and three. The subsequent behavior is nearly log-linear until convergence.

The inner loop convergence displays phenomena not seen in the previous solutions. The large scale behavior is similar, with an initial correction producing a momentary increase in the grid residual followed by a final convergence with a dominant log-linear trend. In the small scale, however, the solution behaves much differently, with jagged peaks in the residual interspersedly superimposed along the final linear trend. It is likely that these peaks emerge from the higher Ω setting chosen for this case. Although it is allowable to increase Ω with grid refinement, the chosen magnitude of the change may have placed the convergence rate closer to the relative stability limit for the particular grid spacing. The

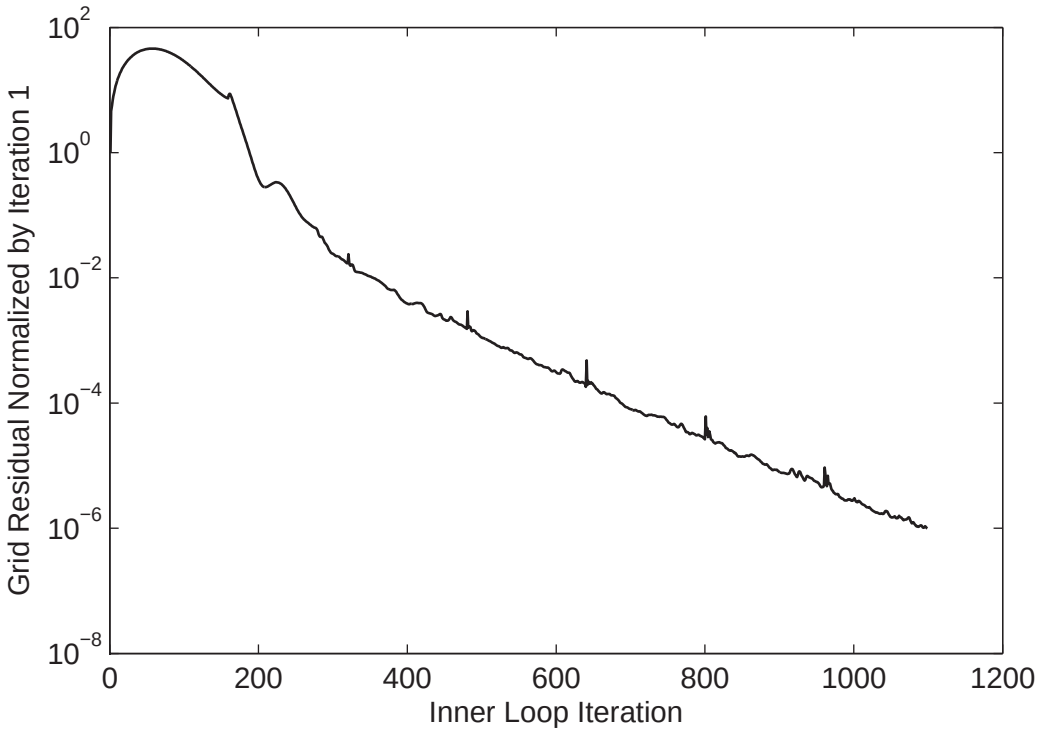

Figure 59: Inner Loop Convergence History at Last Outer Loop Iteration for the NACA 0012, $M_\infty = 0.63$, $\alpha = 2^\circ$

setting of $\Omega = 1.995$ is also very close to the absolute stability limit for all types of systems of $\Omega = 2$. In general, it is desirable to set the relaxation parameter as high as possible for stability in order to minimize the number of required iterations. Because only convergence rate and not solution quality is influenced, the jagged convergence history shown here is acceptable.

The surface pressure distribution is presented in Figures 60 and 61. In Figure 60, the results are compared to the solutions developed by Lock [73]. Overall agreement is excellent. The region of maximal absolute difference occurs in the range $0.2 \lesssim x/c \lesssim 0.4$. As for the symmetric case, the pressure distribution does not extend completely to the aft stagnation point because of the relatively sparse grid near the trailing edge.

A magnified depiction of the solution near the suction peak is given in Figure 61. Prandtl–Glauert and Kármán–Tsien corrections of the incompressible flow over the original airfoil are also shown. Similar to the symmetric solution, the Prandtl–Glauert result

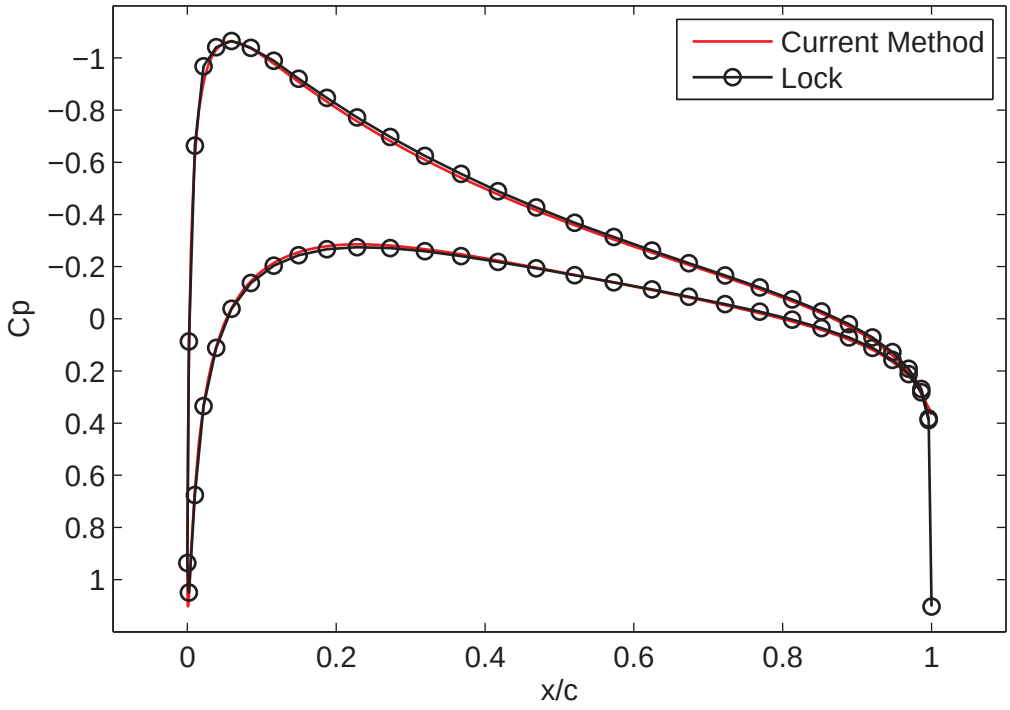

Figure 60: Surface Pressure Coefficients for the NACA 0012, $M_\infty = 0.63$, $\alpha = 2°$

underpredicts the peak, whereas the Kármán–Tsien method overpredicts. The inability of the corrections to capture the integral compressibility effect of the aft shift of the suction peak is also evident in this case.

Field contours of pressure coefficient and Mach number are shown in Figures 62–64. In this asymmetric lifting flow, we see the expected transition of the leading edge stagnation to a point on the lower surface of the profile. The maximum velocity region on the upper surface is prominent with near-sonic peaks, whereas the speed on the lower surface at corresponding x/c is only slightly above the freestream value. In general, the solution is very smooth in the field and along the outer boundary; however, slight defects remain along the airfoil boundary between the first and second line j lines in the maximum velocity region. These defects manifest as discontinuities in the contour shapes at the $j = 2$ line. The problem is in part due to the grid density in this region and in part due to the accuracy of the boundary point extrapolation procedure used to generate the equivalent incompressible airfoil shape from data in the domain interior.

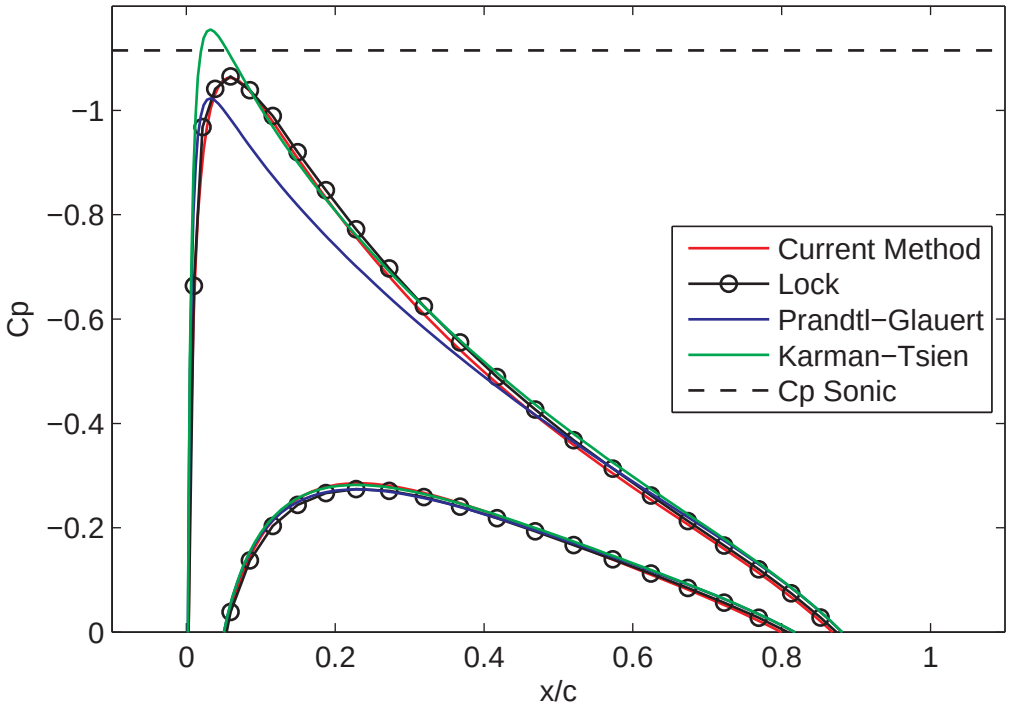

Figure 61: Surface Pressure Coefficients for the NACA 0012, $M_\infty = 0.63$, $\alpha = 2°$; Suction Peak Detail

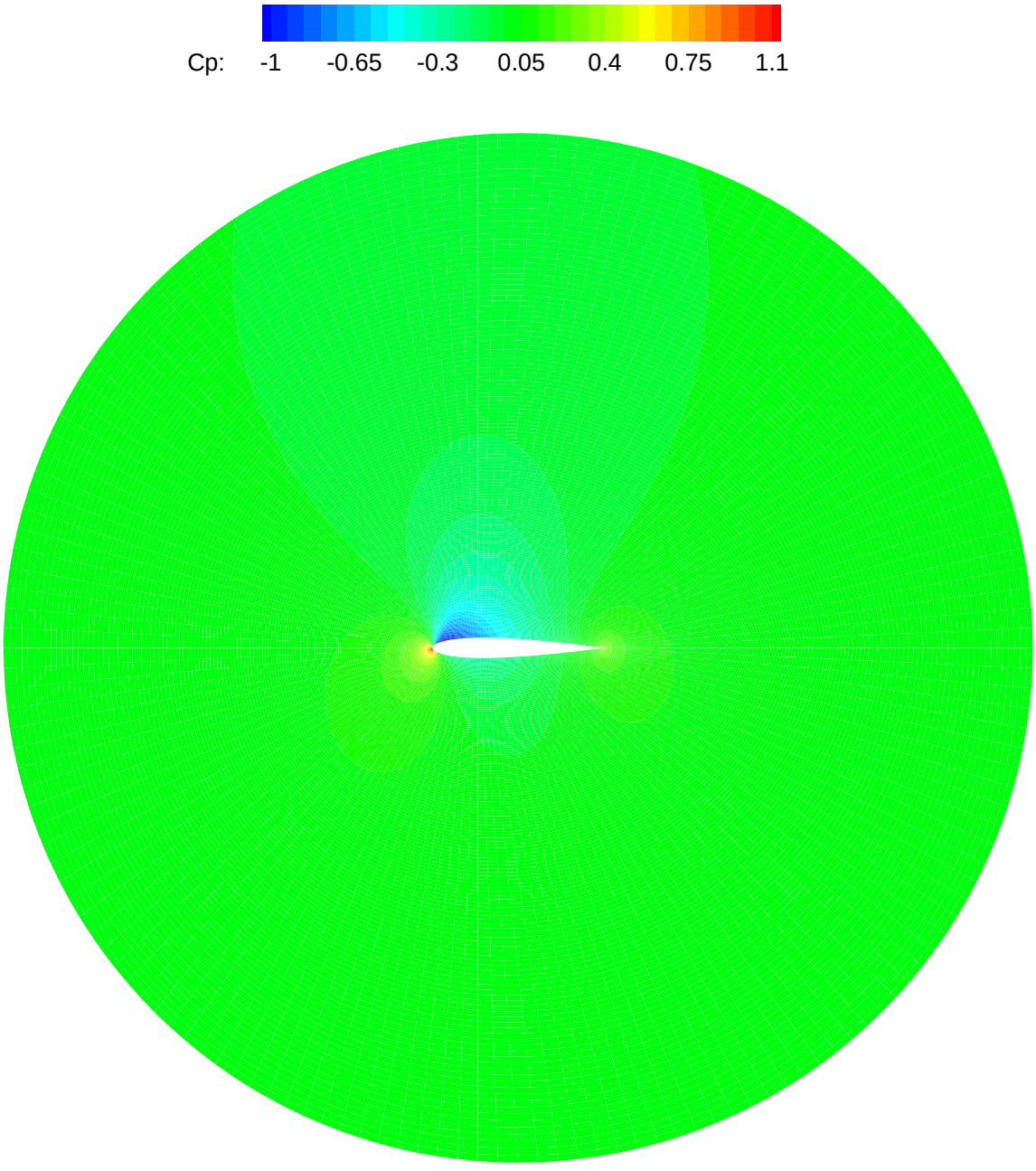

Figure 62: Pressure Coefficient Contours for the NACA 0012, $M_\infty = 0.63$, $\alpha = 2°$

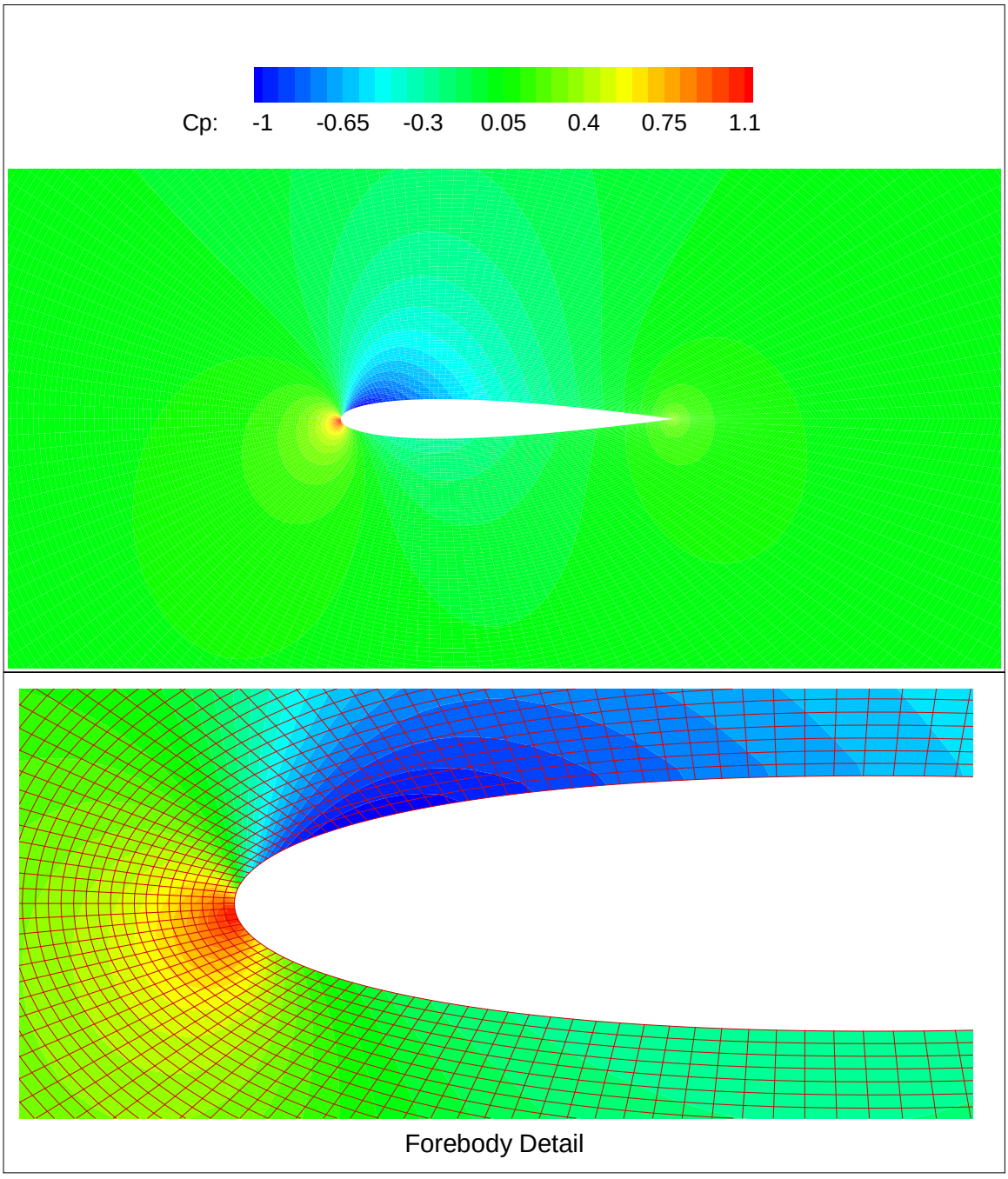

Figure 63: Pressure Coefficient Contours for the NACA 0012, $M_\infty = 0.63$, $\alpha = 2°$; Near-Body Domain

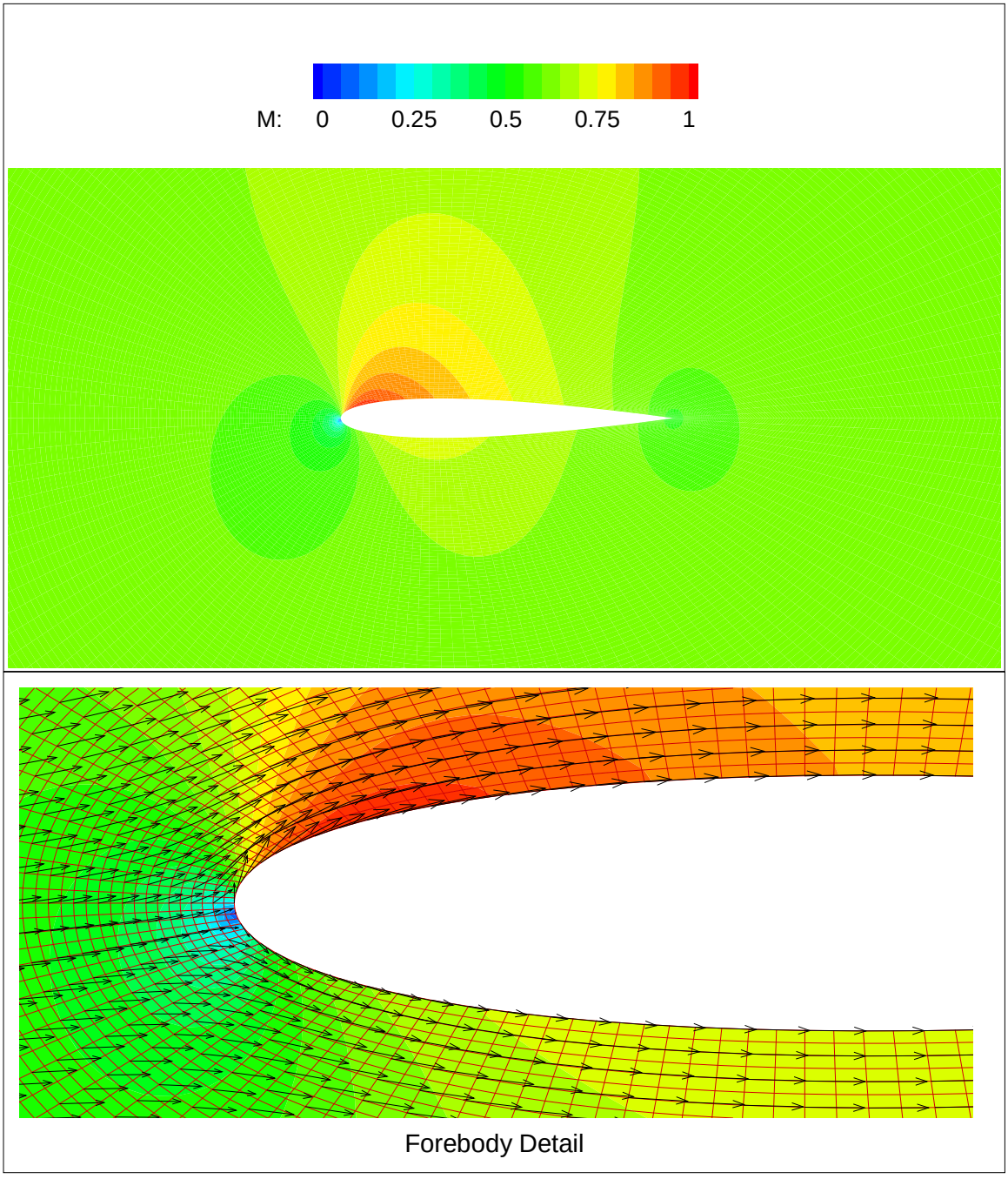

Figure 64: Mach Number Contours for the NACA 0012, $M_\infty = 0.63$, $\alpha = 2°$; Near-Body Domain

Contours of the metric tensor values are presented in Figures 65–67. These figures further highlight some of the interesting extremum locations along the profile for the different metric components. Maximal values of $\sqrt{g}g^{11}$ are obtained on the upper surface between the leading edge and the peak suction region. The $\sqrt{g}g^{12}$ component has a maximum at the lower surface slightly aft of stagnation and a minimum on the upper surface between the leading edge and peak suction. Interestingly, this minimum does not share the same x/c position as the maximum of $\sqrt{g}g^{11}$. These complicated trends emerge from the nonlinear algebraic mappings of the flow parameters into the metric components.

Figure 68 shows the domain grid of the equivalent incompressible flow superimposed the original grid. The near-body clustering caused by setting $\zeta = 2$ is apparent. As for the previous cases, the inner body is thickened and the outer boundary is compacted in the cross-flow direction. The effects of the flowfield asymmetry and circulation cannot be easily noticed in the global grid shape, as this shape is driven primarily by the freestream Mach number at the low angle of attack for this solution.

Coordinate curves for the original and distorted coordinate systems are shown in Figure 69. At this scale, the shapes appear quite similar to those presented for the nonlifting case as Figure 57. The global effect of freestream Mach number manifests itself by distorting the grid from a network of squares into a network of rectangles. Local effects, particularly in the maximum velocity region, are responsible for the curvature of the coordinate lines and the mapping of local regions into rectangles of larger aspect ratio. The greatest difference that can be noticed compared to the symmetric case is that the local curvature of the coordinate lines along the upper surface is slightly more pronounced than that of the lower surface, owing to the higher velocities and accelerations.

A magnified view of the airfoil shape and coordinate lines in the forebody region is shown in Figure 70. The local distortion brought about by the angle of attack is apparent upon inspection of the leading edge region. The dominant effect of angle of attack on the transformation is to cause the leading edge to droop relative to the original airfoil, producing a slight amount of positive camber in the immediate forebody region. The effect also has the appearance of thickening the entire leading edge region slightly. The asymmetric local

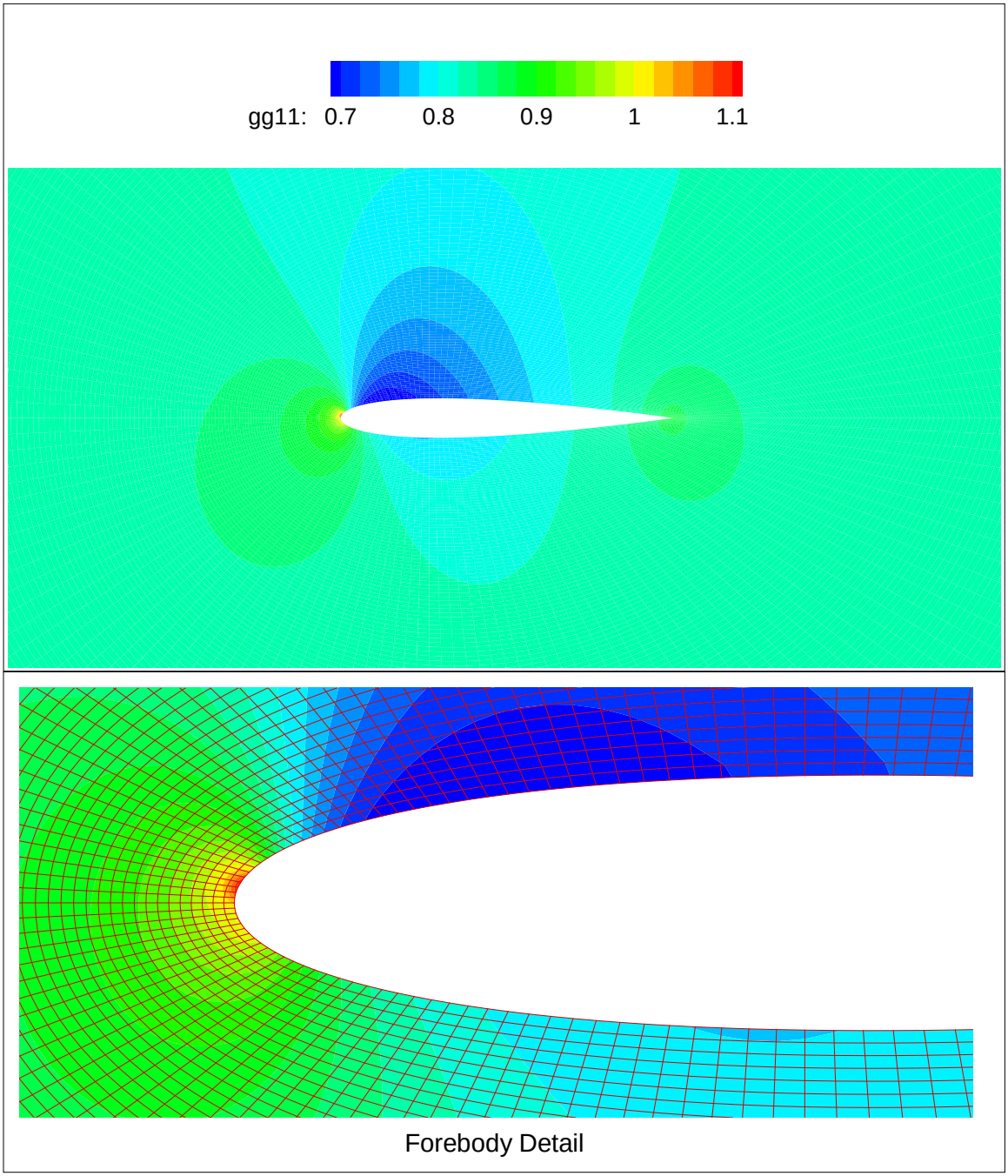

Figure 65: Contours of $\sqrt{g}g^{11}$ for the NACA 0012, $M_\infty = 0.63$, $\alpha = 2°$; Near-Body Domain

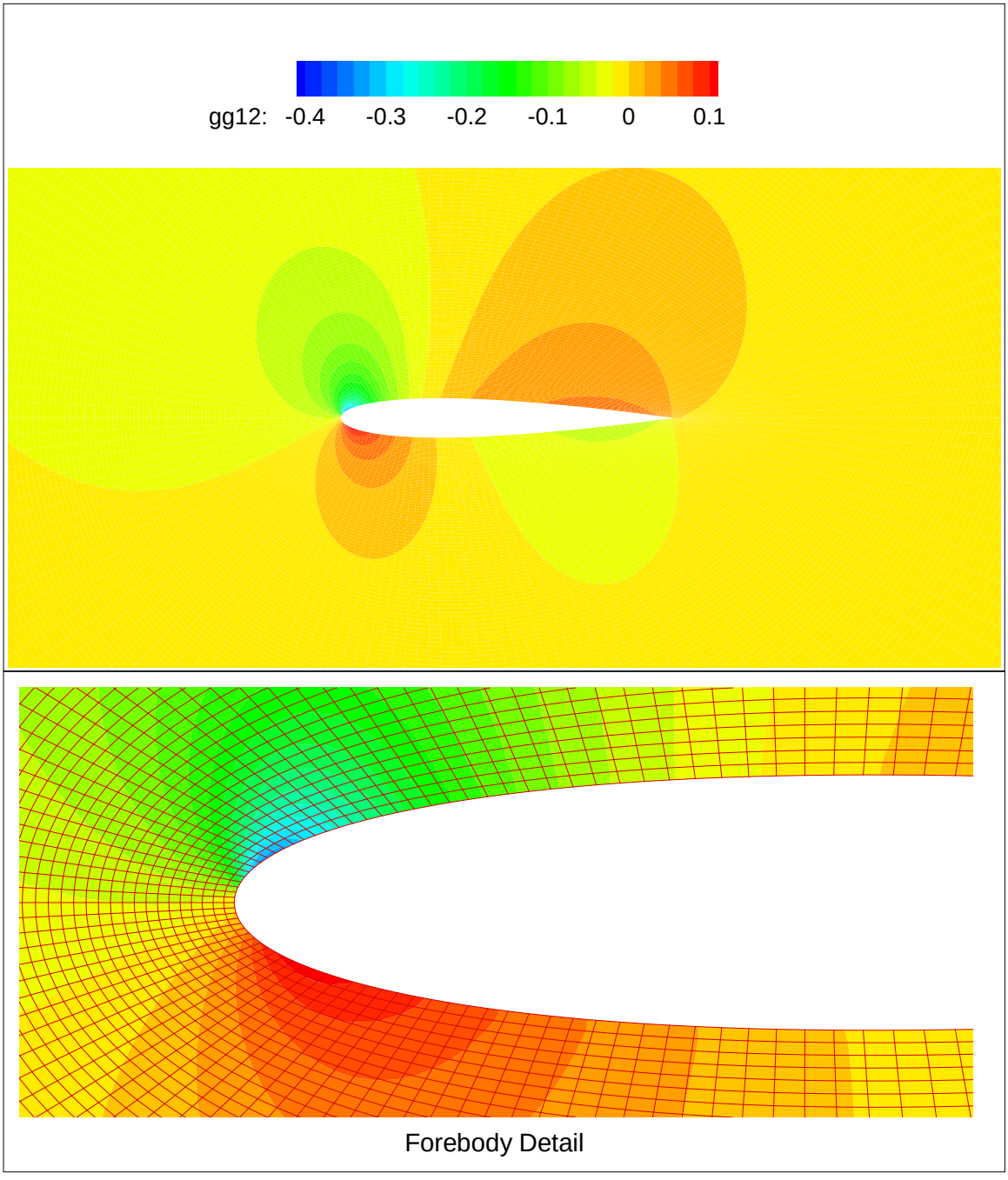

Figure 66: Contours of $\sqrt{g}g^{12}$ for the NACA 0012, $M_\infty = 0.63$, $\alpha = 2°$; Near-Body Domain

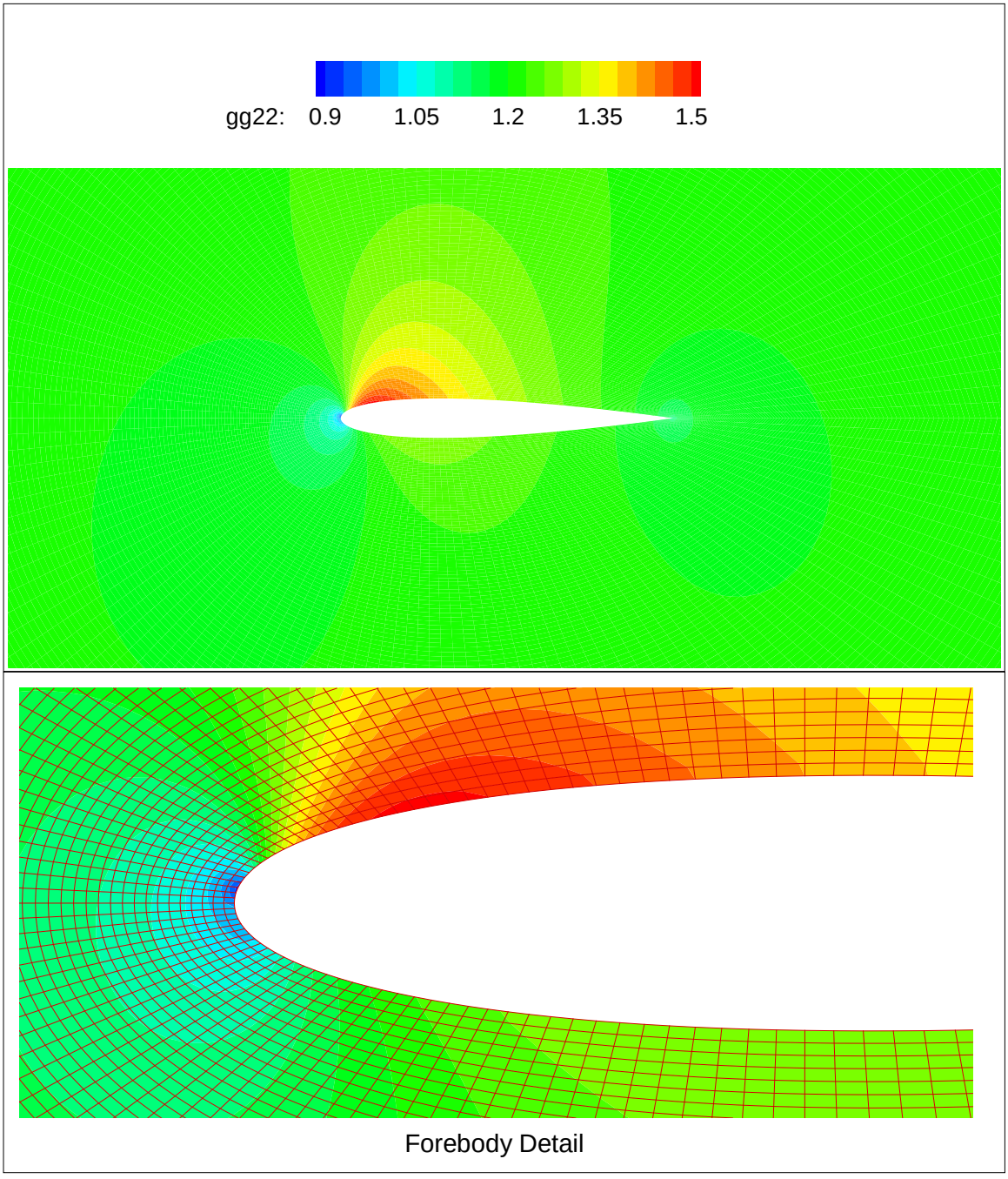

Figure 67: Contours of $\sqrt{g}g^{22}$ for the NACA 0012, $M_\infty = 0.63$, $\alpha = 2°$; Near-Body Domain

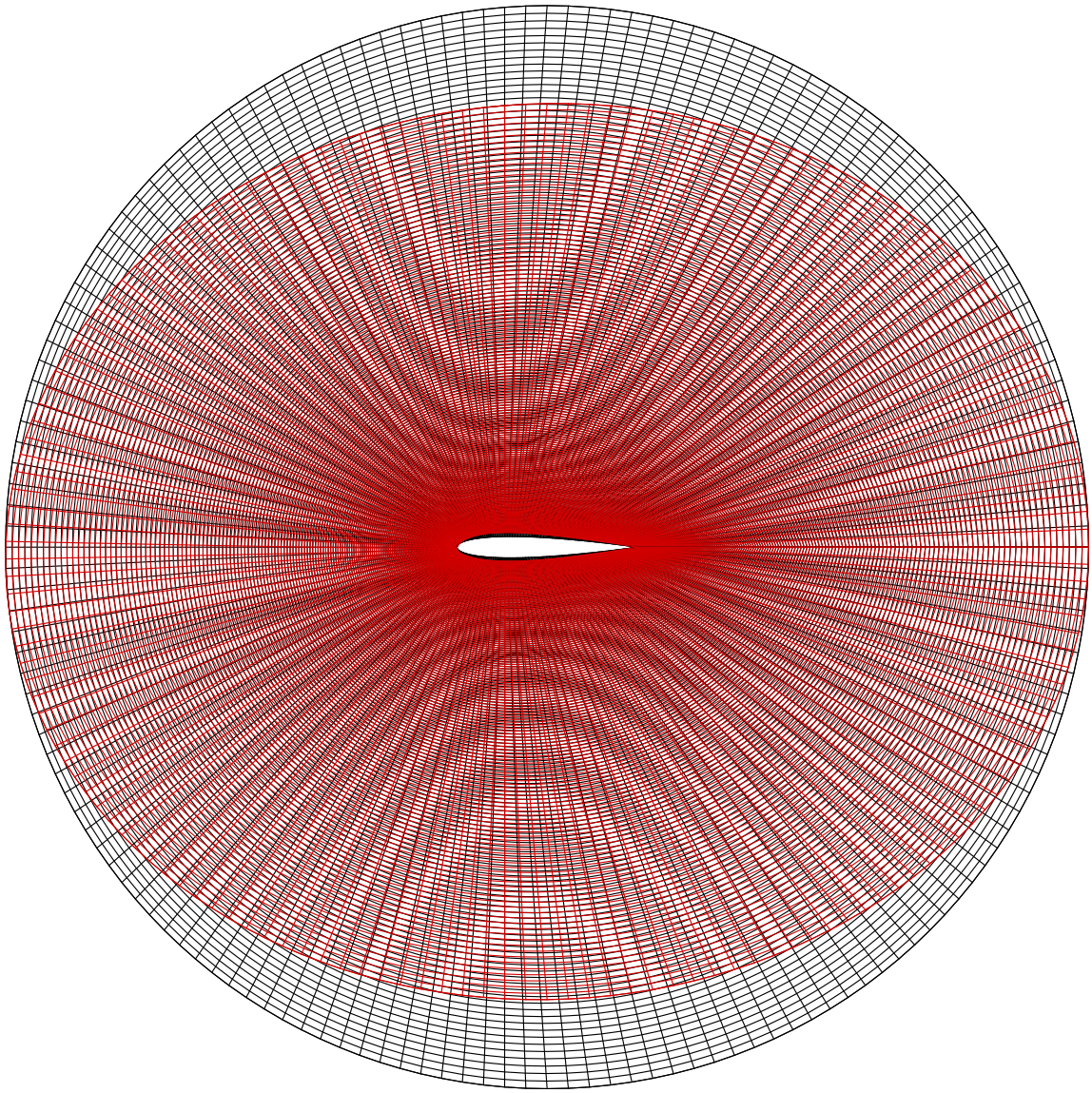

Figure 68: Original (Black) and Equivalent Incompressible (Red) Domain Grids for the NACA 0012, $M_\infty = 0.63$, $\alpha = 2^\circ$

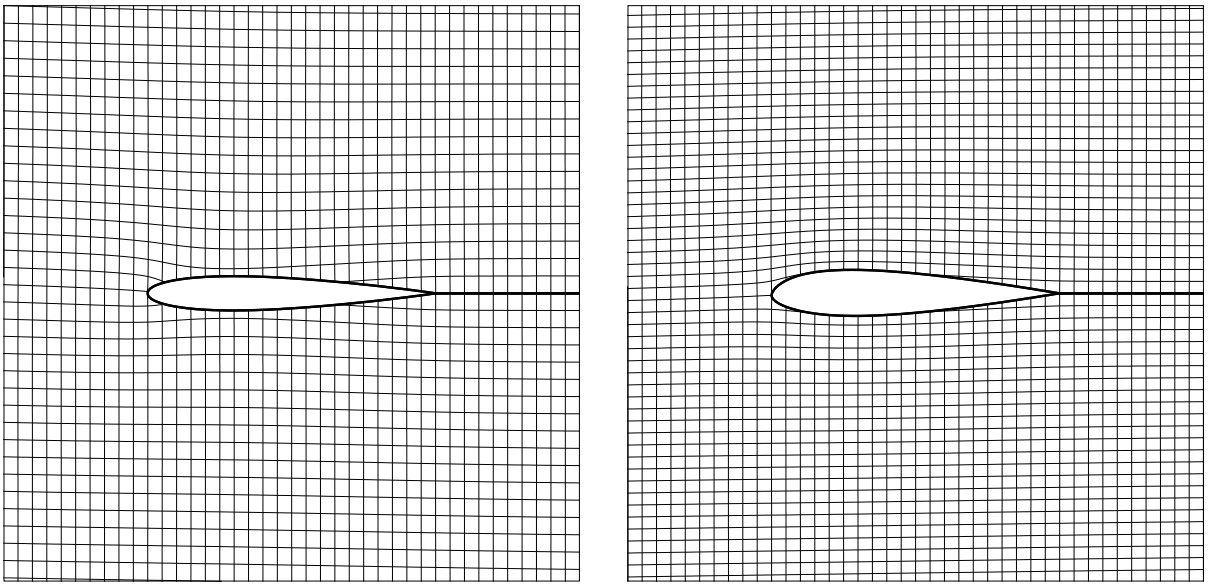

Figure 69: Mapping for the for the NACA 0012, $M_\infty = 0.63$, $\alpha = 2°$: **a)** $(\bar{x}, \bar{y})$ Coordinate Curves in the (x, y) Plane; **b)** (x, y) Coordinate Curves in the $(\bar{x}, \bar{y})$ Plane

curvature of the coordinate lines in the stagnation and maximum velocity regions is also visible in this figure.

An interesting question with regards to this unsymmetrical case with circulation is how the coordinate mapping affects the stagnation streamline of the equivalent incompressible flow. To be precise, we desire to know the location of the leading edge stagnation point and the shape of the stagnation streamline when plotted relative to the isothermal coordinates $\bar{x}$ and $\bar{y}$ forming Cartesian axes. The effect, shown in Figures 71 and 72, is to rotate the leading edge stagnation point downward in correspondence with the leading edge droop. The stagnation streamline therefore deviates downward from the compressible flow streamline as we move forward of the body. The deviation is significant and noticeable at a distance of $2c$ upstream of the airfoil. Although the leading edge stagnation streamline is significantly altered, the trailing edge streamline remains largely indistinguishable from that of the compressible flow. This result occurs because the minor influence of angle of attack in this region produces vanishing asymmetry in the equivalent airfoil in the trailing

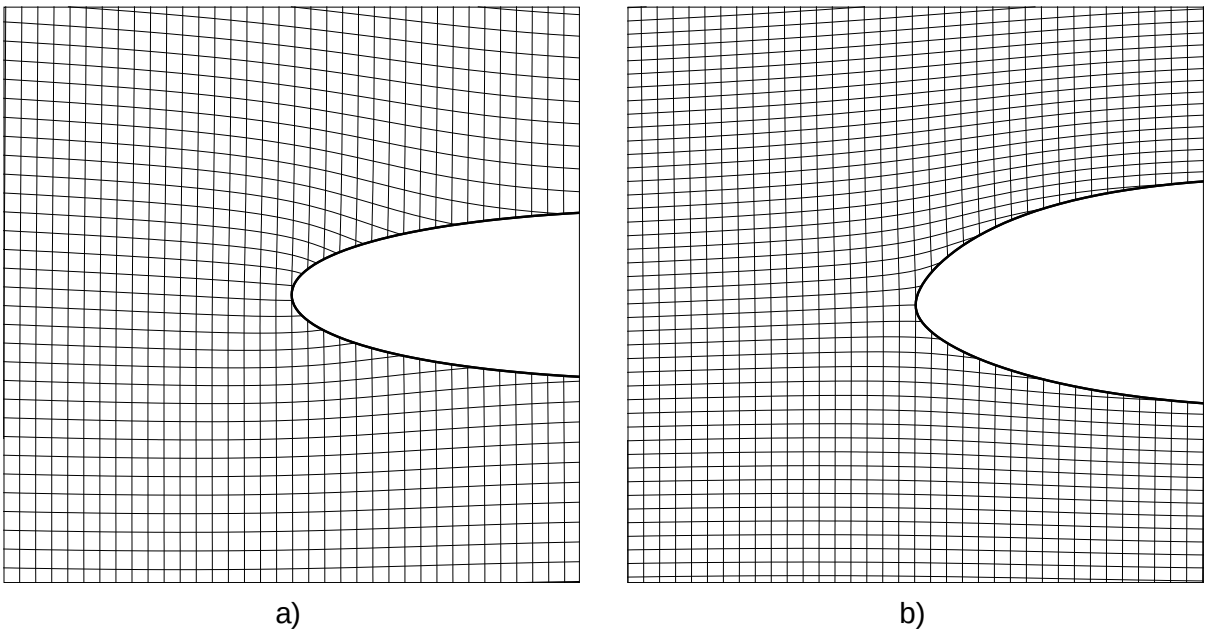

Figure 70: Mapping for the for the NACA 0012, $M_\infty = 0.63$, $\alpha = 2°$: **a)** $(\bar{x}, \bar{y})$ Coordinate Curves in the (x, y) Plane; **b)** (x, y) Coordinate Curves in the $(\bar{x}, \bar{y})$ Plane; Leading Edge Detail

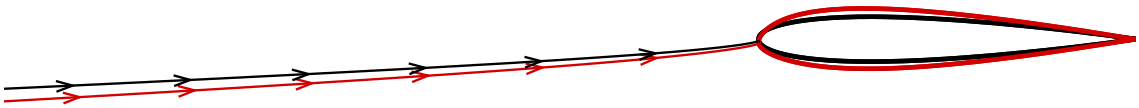

Figure 71: Shift in the Stagnation Streamline from the Original Domain (Black) to the Equivalent Incompressible Domain (Red)

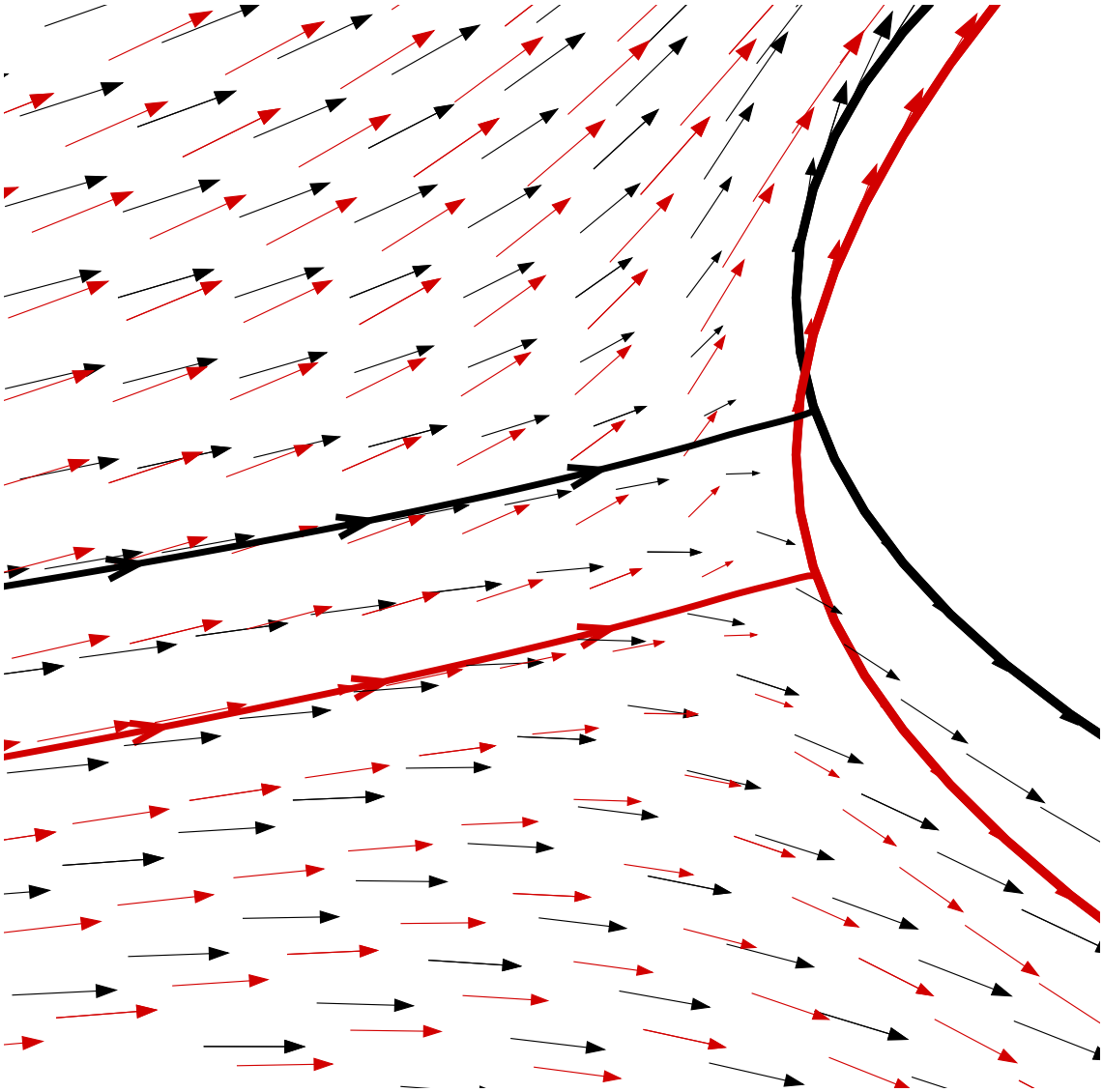

Figure 72: Shift in the Stagnation Streamline from the Original Domain (Black) to the Equivalent Incompressible Domain (Red); Leading Edge Detail

Table 14: Parameter Settings for M_∞ and α Variation Studies with the NACA 0012

Name	Symbol	Setting
Number of circumferential grid nodes	i_{max}	121
Number of radial grid nodes	j_{max}	81
Outer loop convergence tolerance	ϵ	10^{-6}
Inner loop convergence tolerance	τ	10^{-6}
Outer boundary radius to chord ratio	R/c	3
Over-relaxation parameter	Ω	1.98
Off-body grid spacing parameter	ζ	3

edge region. Because the Kutta condition is enforced crisply for both the compressible and equivalent incompressible flows, the trailing edge stagnation streamlines for both flows proceed smoothly along the bisection ray from the finite thickness trailing edge and are for all practical purposes coincident.

6.2.3 Variation of Solution with $\mathbf{M}_\infty$ *and* α

The previous results presented for the NACA 0012 were intended to provide validating comparisons of the method to known results in the literature and to provide general insights into the phenomena associated with the transformed shapes and coordinate systems of typical equivalent incompressible flows. Although insightful, these point solutions do not give an adequate depiction of how equivalent shapes change as a function of the flow parameters. In order to develop such an understanding, we now perform a systematic variation of the angle of attack and freestream Mach number and tabulate the equivalent shapes obtained. To generate these results, the solution parameters were set to the values given in Table 14.

The study conducted consists of solving a two-dimensional matrix of flow solutions corresponding to Mach numbers ranging from 0.3 to 0.7 in increments of 0.1 and to angles of attack ranging from 0° to 8° in 2° increments. The full grid of solutions was not completed because we must limit our results only to subcritical cases. Estimates of the locations of the critical conditions in this matrix were made, and the resulting solutions were then checked to verify that they satisfied the subcritical criterion. In order to examine the most extreme conditions possible, care was taken to consider cases as close to the critical conditions as feasible.

The equivalent incompressible shapes generated in this study are shown in Figure 73. The primary effect that can be distinguished at this scale is the thickening effect of freestream Mach number that is very apparent for the higher Mach cases at zero incidence. The effect of leading edge droop is slightly noticeable upon close inspection.

In order to illustrate the leading edge effects in greater detail, Figure 74 magnifies the airfoil forebody regions. In this view, the leading edge droop with increasing angle of attack is more visible, particularly for the cases at intermediate M_∞ and α. Because lesser droop is visible for the lower Mach but higher angle cases, it appears that the magnitude of the leading edge movement is more dramatically affected by Mach number than angle of attack.

The trends shown in this matrix of shapes are presented in a more quantitative fashion in Figures 75 and 76. Figure 75 depicts the maximum thickness of the equivalent profiles as a function of Mach number and angle of attack. It is clear that the driving influence on thickness is primarily Mach number and not incidence, with incidence having an appreciable additional effect only at higher Mach numbers. The effect of the classical Prandtl–Glauert stretching factor of $1/\sqrt{1-M_\infty^2}$ on the NACA 0012 profile is also plotted in the figure. Interestingly, the transformation developed in this work produces a smaller thickening at lower Mach numbers than the Prandtl–Glauert result and a larger thickening at higher Mach numbers. An additional and very intriguing result is that the x/c location of the maximum thickness corresponds in both the original flow and the equivalent incompressible flow. That is, $\bar{x}/c = x/c$.

The behavior of the leading edge droop with M_∞ and α is shown in Figure 76. The trends are surprisingly regular, with nearly perfectly linear relationships between the displacement and angle of attack for all of the examined Mach numbers. This linear behavior suggests that it may be possible to describe this trend analytically with an analysis based on the coordinate transformation theory. Although this theoretical relationship is not investigated in the current work, one approach toward obtaining it might be first to determine the slopes of the curves with respect to α in nondimensional radian units and then to fit these slopes to a series expansion in M_∞^2. Next, any overall scale could be divided through. This scale would represent a characteristic length for the displacement. The resulting expansion in

$\alpha \diagdown M_\infty$	0.3	0.4	0.5	0.6	0.7
8°					
6°				Supercritical	
4°					
2°					
0°					

Figure 73: Equivalent Incompressible Airfoils to the NACA 0012

$\alpha \diagdown M_\infty$	0.3	0.4	0.5	0.6	0.7
8°	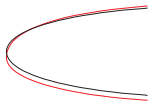				
6°		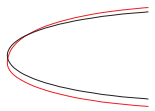		Supercritical	
4°		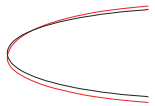	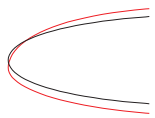		
2°	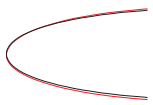	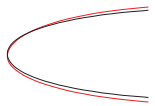	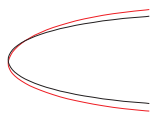	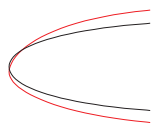	
0°	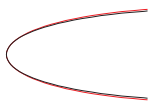	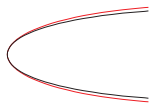	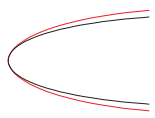	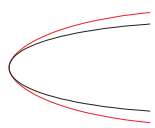	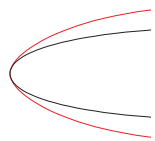

Figure 74: Equivalent Incompressible Airfoils to the NACA 0012; Leading Edge Detail

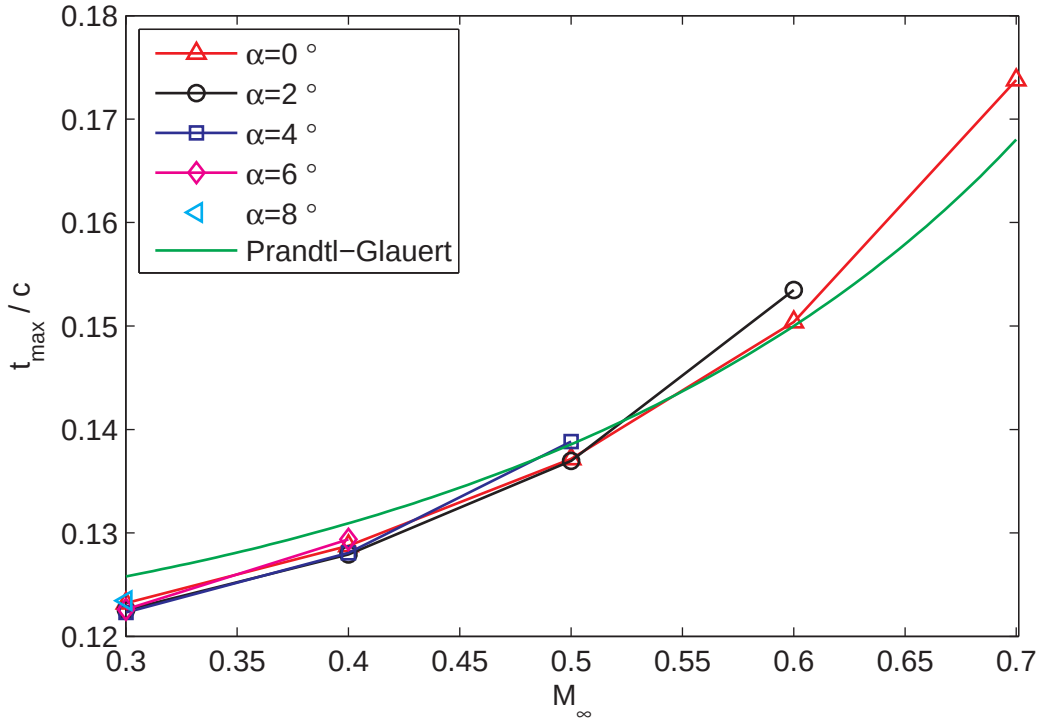

Figure 75: Thickness of Equivalent Incompressible Airfoils to the NACA 0012

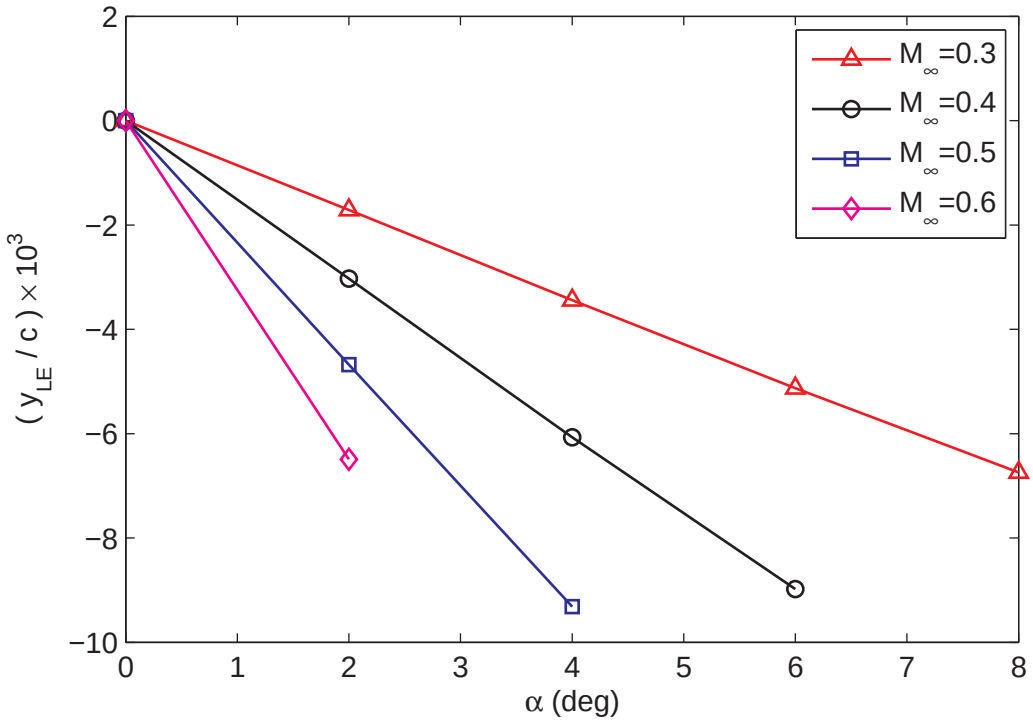

Figure 76: Leading Edge Droop of Equivalent Incompressible Airfoils to the NACA 0012

M_∞^2 would then begin with a first term of unity. By including the three terms in this expansion available based on the number of data points, it may be possible to recognize this series expansion as corresponding to a common function of M_∞^2. This function would represent the desired relationship for the slopes.

This concludes our exploration and discussion of representative results that can be obtained with the numerical mapping method developed in this research. In the next chapter, we conclude the dissertation, summarizing the contributions of the work and suggesting future avenues to continue this line of research.

CHAPTER VII

CONCLUSIONS

In this dissertation, we have journeyed through a vast forest of theoretical and applied mathematical physics. Along the way, we have encountered enchanting creatures and terrible beasts: tantalizing smidgeons of relativity theory, detailed and laborious derivations in the language of Riemannian geometry, the subtleties of coordinate transformations and integrability, the intricacies of numerical discretization and integration, the dark art of setting grid and convergence parameters, and, finally, the magic of equivalent incompressible flows.

This spectrum of topics has likely left the reader in the same exhausted state as the author. Nonetheless, it is important that before we part, we reflect on this journey and on possible future travels. These tasks are the focus of this final chapter.

In the first section, we review and resolve the hypothesis and research questions presented in Chapter 3. The second section summarizes the academic contributions of this research. These contributions include the philosophical underpinning of the general relativistic analogy that inspired this work, the theory necessary to geometrize compressibility, the numerical approach to solve the mapping, and finally, the insights gained about the nature of equivalent incompressible flows.

In the third section, we discuss potential applications of the current theory and numerical method. One area of applicability may be flow similarity scaling. Similarity is used extensively in a variety of experimental scenarios to match test results to real world flows. A second area is inverse design. Through the examination of the equivalent flow, it may be possible to gain design insights to guide in airfoil and shape optimization. These insights could be obtained by leveraging the vast collective knowledge of incompressible flows for application to the subsonic problem.

Next, we discuss possible continuations of this line of research. A variety of directions are

possible. Perhaps the most straightforward is a continued quantification of the phenomena associated with equivalent incompressible flows and their associated mappings. Another avenue is to develop an approximative method to achieve integrability as a consequence of the flow solution. This method would leverage the Taylor series expansion approach outlined in Section 4.3.3 to allow for solutions to the mapping that can be achieved solely with a boundary element technique and without a domain grid. A more significant departure from the present theory would leverage the conceptual approach to develop supersonic flows mapped to a canonical hyperbolic equation. Transonic flows could then be found by domain partitioning and marrying the incompressible and canonical hyperbolic techniques. Next, we discuss the potential for applications to three-dimensional and unsteady flows. Finally, we consider research investigating differential geometric aspects of the gauge transformation and spatial curvature that may shed light on the general relativistic analogy.

The final section describes a substantial lesson learned by the author during this research. Much effort was expended in this dissertation research in trying to solve a problem that is likely unsolvable. The basic thought is that no matter how hard one might try, there are certain significant limitations to the ability to simplify problems by transformation methods. These limitations stem from the current state of mathematics and appear to be largely unavoidable. Although this statement may be obvious to seasoned mathematicians and practitioners of applied physics, this lesson is one of the deepest and most humbling personal takeaways of this work.

7.1 Resolution of Hypothesis and Research Questions

The hypothesis presented in Section 3.1.2 described a procedure for geometrizing the effects of compressibility to produce an equivalent incompressible flow. It states that it is possible to accomplish this goal in the following way: We start with the invariant form of the incompressible continuity equation that involves the metric tensor. This equation is then to be set equal to the invariant form of the compressible continuity equation by selecting the metric tensor in a particular way. The resulting relation casts this new metric tensor in terms related to the original metric corresponding to the coordinate system of the compressible

flow and to the effects of compressibility. In this way, we *geometrize* compressibility through a gauge transformation. Next, we perform a curvilinear coordinate transformation to map the resulting equivalent incompressible flow to a coordinate system in which it becomes identical to the canonical Cartesian form of the Laplace equation where it is easy to solve. Finally, we develop definite mathematical relationships between this simple equivalent flow and the more complicated compressible flow.

The question we ask now is whether this hypothesis has been substantiated by the theory and numerical method presented in this dissertation. The answer is yes; the hypothesis has been proven. In Chapter 4, the theory for the gauge and coordinate transformations was developed. This theory embedded the effects of compressibility into the metric tensor and derived the conditions on a mapping to a canonical Laplacian flow as proposed by the hypothesis. In Chapter 5, a numerical method was devised to implement this theory for performing flow solutions. The numerical method was employed to generate results for several representative cases for which potential flow solutions were available in the literature. These cases included the flow over a non-rotating circular cylinder and a NACA 0012 airfoil in both a symmetric orientation and a lifting configuration, all with high subsonic local Mach numbers. The method was found to reproduce the solutions presented in the literature with good accuracy. Because an incompressible flow solver was used in an unaltered form, solving the equivalent flow iteratively until convergence, we can be assured that the equivalent flow is indeed kinematically incompressible.

In addition to outlining the hypothesis, we also posed a series of specific research questions in Chapter 3. These questions were defined in Figures 2 and 3. Each of these questions was paired with one of the primary tasks required in developing the theory and the numerical implementation. Although not mentioned explicitly in the course of the document, each of these questions was implicitly addressed as the research was presented. Concise answers to the questions and the locations in which greater detail is given in the document are provided in Figure 77 and Figure 78. The questions and their resolutions presented in Figure 77 correspond to those related to the theoretical development, and those indicated in Figure 78 relate to the implementation and exploration of the numerical method to produce

flow solutions. A summary of the tasks completed to answer these questions is provided in the subsequent Section 7.2.

7.2 Summary of Contributions

The four primary academic contributions of this dissertation are as follows:

- The philosophical transformation framework for generating equivalent incompressible flows living in curved spaces, inspired by concepts from the general theory of relativity
- The theory for developing the transformations in the mathematical language of Riemannian geometry
- The numerical method for implementing the transformations for flow fields around arbitrary profile shapes
- The insights gained about equivalent incompressible flows through solutions obtained with the numerical method

In this section, we discuss each of these contributions in turn.

7.2.1 Philosophical Roots

In Chapter 3, we outlined a philosophical approach for embedding the effects of compressibility into the geometry of space. This embedding was accomplished by absorbing the varying density in a steady planar subsonic potential flow into the metric tensor of an equivalent incompressible flow living in the same coordinate system. The result of this process was to produce a gauge transformation of the flat plane on which the compressible flow problem was posed. The effect of this transformation is to introduce curvature into the space, such that the flat plane is warped into a curved surface, as illustrated notionally in Figure 4.

The primary philosophical viewpoint inspiring this approach is that compressibility can be envisioned as a *geometric* effect instead of a purely *physical* effect. This is precisely the viewpoint taken to describe the effects of gravity in the general theory of relativity.

In order to quantify the geometric effects of compressibility in this paradigm, we borrow another element from the general theory: the concept of general covariance. This notion

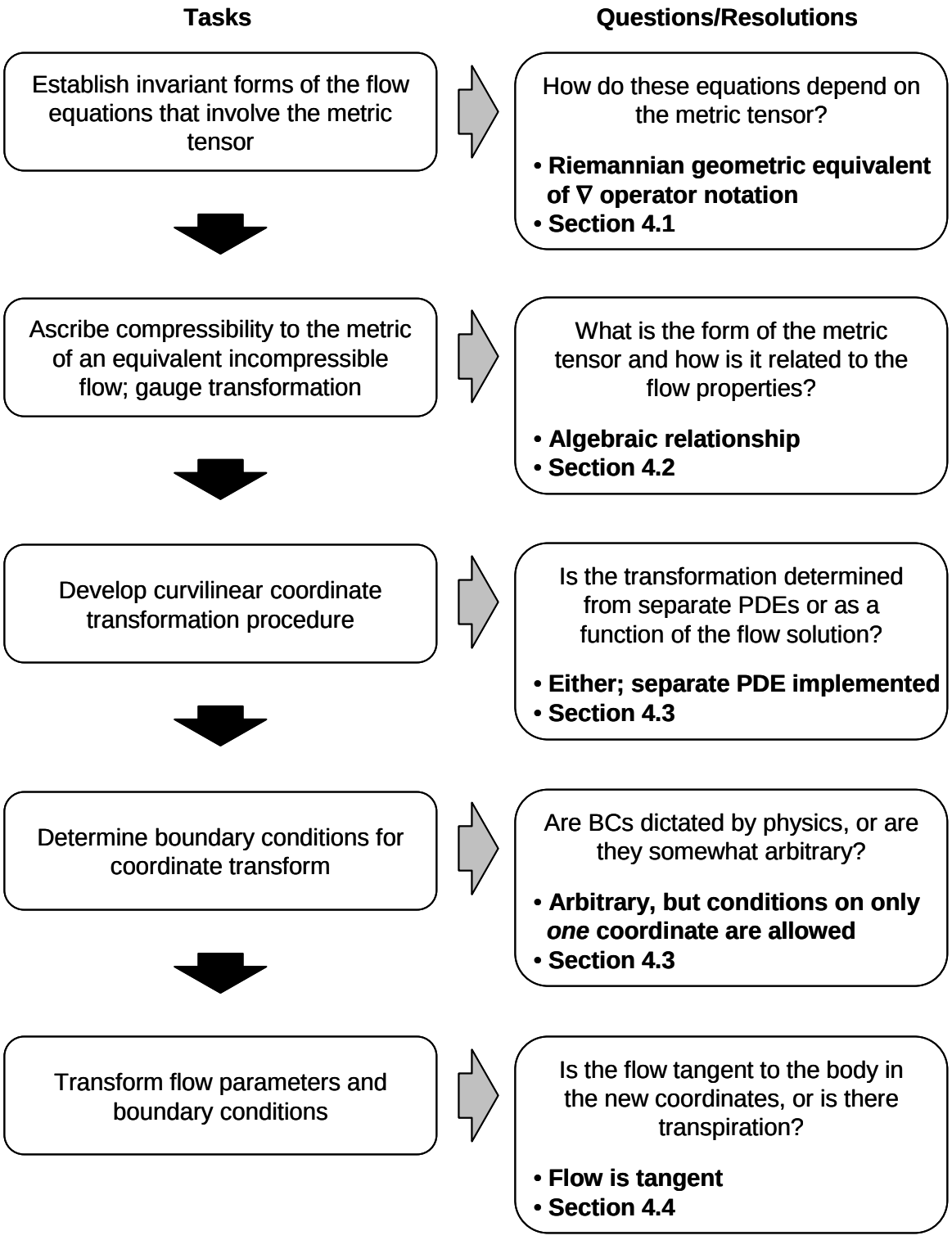

Figure 77: Resolution of Theory Research Questions

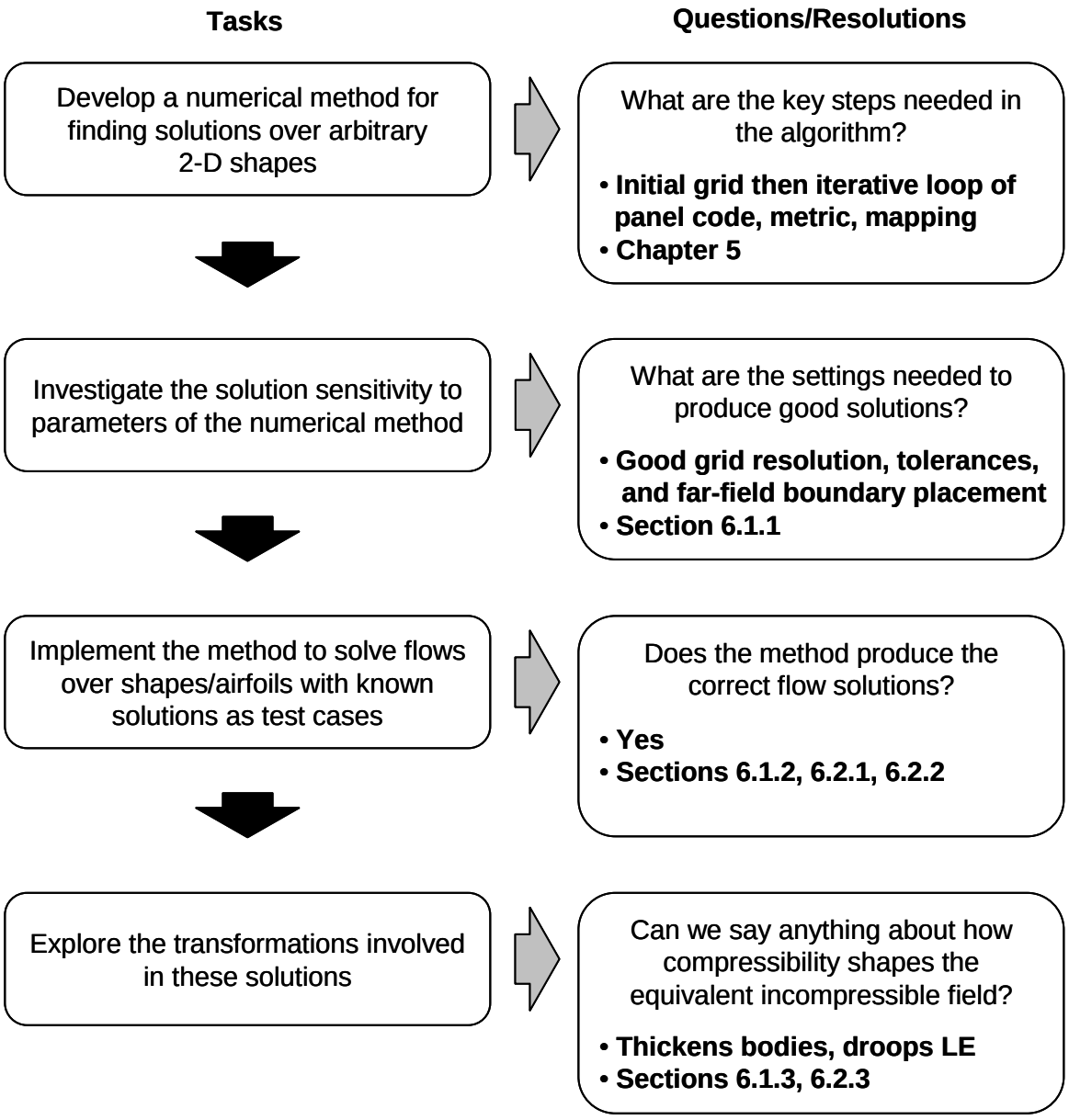

Figure 78: Resolution of Implementation Research Questions

says that if we write physical equations in a coordinate invariant form as a function of the metric tensor, these equations can be transitioned from flat space to curved space simply by replacing a flat space metric with a curved space metric. To apply this principle to our approach, we worked with invariant forms of the compressible and incompressible continuity equations.

The means by which we determined the metric tensor for our approach differs from that of general relativity. Whereas general relativity determines the metric tensor from the effects of gravity through Einstein's equation, a second order hyperbolic differential relation given by Equation 67, we determined the metric tensor from the effects of compressibility by matching the known forms of the invariant continuity equations for a compressible and an incompressible flow. The result produces a metric tensor for the curved space that is an *algebraic* function of the flow parameters corresponding to the original subsonic flow.

In the case of general relativity, the concept of using general covariance and the Einstein equation to geometrize gravity is *physical* and cannot be checked except through experimental verification. In our case, however, the use of the principle of covariance is fundamentally *operational* because we know with certainty the mathematical forms of the compressible and incompressible continuity equations *a priori*. We simply choose the metric tensor of the incompressible flow such that it is guaranteed to be equivalent to the compressible flow because the two invariant equations match exactly when written out in terms of partial derivatives of the coordinates.

Once compressibility has been geometrized, a curvilinear coordinate transformation can be used to transform to a coordinate system in which the flow is governed by the canonical Cartesian form of the Laplace equation. A relevant question is whether the step of a gauge transformation could have been omitted entirely, using instead a curvilinear coordinate mapping to transition from the compressible flow directly to the canonical Laplacian flow.

The answer to this question is likely yes. In some ways, this perspective might even have been simpler—it would have preserved the curvature of space, mapping a plane to a plane, and we would not have needed to discuss gauge transformations. The reason that this approach was not pursued was because of the philosophical interest in a technique involving

spatial curvature. Although the specific nature of this curvature is not investigated in this thesis, it is hoped that the approach will enable further explorations that may shed light on aspects of the compressibility problem that are not evident in a method based only on a coordinate transformation. Specifically, we can ask how the curvature is related to the effects of compressibility and the parameters of the flow. This task is described and proposed as future work in Section 7.4.5.

This philosophical approach is believed to represent a new contribution to the literature. As described in Chapter 1, past work has leveraged transformation techniques related to elements of the special theory of relativity and these approaches produce mappings only within flat spaces. The work linking black holes and acoustics introduced primarily by Unruh [119], Visser [125], Fischer [39], and Bilić [17], provided the first known direct application of ideas involving general relativity and the metric tensor. The approach developed here differs substantially from Visser and Unruh's because we consider the fully nonlinear problem for the two-dimensional steady case. This work is also the first known method to introduce the concept of equivalent incompressible flows that reside within a shaped space obtained by a gauge transformation.

7.2.2 Theory

The mathematical theory developed in Chapter 4 serves as the tangible representation of the philosophical transformation approach summarized above and described in Chapter 3. We now summarize the contributions in this area.

The theory development consisted of several steps. The first step was to derive the differential equations of steady potential fluid motion in their Riemannian geometric tensor forms. These forms were presented alongside the nabla vector operator forms that are more familiar and typical in aerodynamic pedagogy and practice. This parallel approach was chosen as a way to introduce Riemannian tensor analysis to readers who may be unfamiliar with the concept. The results of these derivations included the Riemannian forms of both the incompressible and compressible continuity and momentum equations as well as the tensor form of the full potential equation. These equations are very well known in Cartesian

Table 15: Locations of the Equations of Potential Flow in Riemannian Tensor Form

Equation Name	Location	Number
Incompressible continuity and momentum	Section 4.1.2.1	Equations 96
Compressible continuity and momentum	Section 4.1.2.2	Equations 104
Full potential equation	Section 4.1.2.2	Equation 109

coordinate form as well as in the coordinate independent language of nabla vector operator notation. Transformations of these equations among coordinate systems are thoroughly documented, particularly in literature related to finite difference solutions, where the typical approach involves mapping to a curvilinear computational coordinate system. Nonetheless, the author is unaware of tabulations of the Riemannian tensor forms in the literature. Although they can be written down directly in many cases, their presentation in this work represents a minor secondary contribution of this research that is independent of the broader objectives. The locations at which these equations appear in this document are listed in Table 15.

The next step in the theoretical develop was the geometrization of compressibility through the metric tensor of an equivalent incompressible flow. This step, described in Section 4.2, comprised the mathematical embodiment of the gauge transformation. In this step, the invariant forms of the continuity equations of a given compressible flow and an incompressible flow in the same coordinate system were set equal. The velocities of these two flows were also taken to correspond. The metric tensor of the incompressible flow was then set in such a way that it absorbed the varying density of the compressible flow. With this metric tensor, the continuity equation for the incompressible flow becomes identical to that of the original compressible flow when written out in terms of coordinates. This matching of the continuity equations is precisely the reason that we term this new incompressible flow as "equivalent" to the compressible flow.

In determining this metric tensor, several issues had to be resolved. First and most important was the choice of whether to set the metric such that the equations were matched identically or to set it in some way by satisfying the differential equation formed from the difference in the two continuity equations. We chose to set the metric such that the equations

matched identically, largely because the method was simpler. The second issue regarded the determination of several functions that appeared in the selection of the metric. Through considerations of limiting behavior, it was found that these functions must vanish. Finally, a constant that had remained free in the derivation was set based on consideration of the behavior of the transformation in stagnation regions of the flow.

In the process of the derivation, it was also determined that the generation of the equivalent flow was insensitive to an overall conformal factor multiplying all elements of the metric tensor. This result indicated that any metric from within a conformally equivalent class is allowable. The resulting final form of the conformal equivalence class of metrics for the equivalent flow corresponding to an originally given Cartesian reference system were presented as Equations 129.

After the metric was established, the next task was to determine the curvilinear coordinate mapping to transform the governing equation of the equivalent flow to the canonical Cartesian form of Laplace's equation. This transformation was implemented to allow the flow to be easily solved by a boundary element method and such that the flow would behave in all respects identically to an incompressible flow in Cartesian coordinates. The corresponding coordinates attained in this transformation are termed *isothermal*, for reasons apparently unrelated to the concept of thermodynamic temperature. These coordinates resemble Cartesian coordinates in almost all respects.

The challenge with developing the coordinate mapping is to ensure *integrability* of the coordinates, that is, to require that the mixed second derivatives of the coordinate mapping commute. We investigated two methods for achieving integrability. The first was to solve a separate boundary value problem for the differential equations that pose the integrability condition. The second was to achieve integrability identically as a function of the flow solution. Attaining integrability as a consequence of the flow is highly appealing because the solution of the mapping could be attained directly from the very simple solution to the flow through the Cartesian Laplace equation. Unfortunately, however, it was found that this approach could at best produce approximate solutions. For this reason, the technique involving a separate boundary value problem was the primary method investigated. The

partial differential equations of this boundary value problem are presented as Equations 151 and 153. Associated with these differential equations are the compatibility conditions required by the generalized Cauchy–Riemann relations of Equation 149.

The nature of the boundary value problem for the coordinate transformation was carefully examined. The mapping problem was found to be elliptic in character, and therefore, it requires that boundary conditions be posed on all borders of the domain. These boundary conditions were found to be largely arbitrary in nature, with the only apparent restriction being that boundary conditions on precisely *one* and not both of the isothermal coordinates could be set.

After the mathematical requirements on the coordinate transformation were established, the next step was to describe how the compressible and equivalent incompressible flows are related. The first question investigated in this task was how the boundary conditions for the flows are related. By applying the tensor transformation law to the boundary conditions of the compressible flow, we found that if we require flow tangency for the compressible flow, we also attain flow tangency as the boundary condition for the equivalent canonical Laplacian incompressible flow. This result is very advantageous because it ultimately allows us to select from among the many widely available numerical solution techniques for incompressible flows with these types of boundary conditions.

The next step in relating the two flows is to understand the relationships between the scalar point properties as well as the velocity vectors in the two flows. Because scalars such as the thermodynamic variables are invariant under coordinate transformations, they keep their same values in both the original compressible flow and the canonical Laplacian form of the equivalent incompressible flow. The counterintuitive implication of this result is that the density varies throughout the equivalent incompressible flow field. As pointed out earlier, however, the density must now be given an interpretation that is primarily geometric with respect to this equivalent flow and not physical. Although it varies from point to point, the density does not appear explicitly in the kinematic equation for the fluid motion. The vector properties of the flow such as velocity were shown to transform based on the appropriate covariant transformation law involving the partial derivatives of

the coordinate transformation.

In addition to the scalar and vector properties, we also investigated the transformation behavior of both the angle of attack and the Kutta condition. The angle of attack was found based on consideration of the transformation of the freestream flow. Interestingly, this transformation produced a scaling factor of magnitude $1/\sqrt{1-M_\infty^2}$ which is typical of the Prandtl–Glauert class of linear coordinate transformations. The Kutta condition was found to transform trivially. That is, the flow must leave the body smoothly and along the bisection line of any finite trailing edge angle. The implications of this behavior is that the condition can be applied identically to the both the original flow and its incompressible equivalent.

The final task in the theory development was to compare the method developed in this dissertation to a somewhat similar approach developed by Bers [12, 13, 14]. This comparison showed that the technique employed in this work could be cast in a form representative of the general class of transformations termed by Bers as *quasiconformal*. Although the transformations were of a similar class, our method produced a slightly different transformation behavior from the specific implementation developed by Bers. Whereas Bers' technique was found to introduce cusps at leading edge stagnation points during the transformation, subsequent investigations showed that the method developed in this work produces globally smooth mappings.

The specific nature of the transformation proposed by the theory developed in this work appears to be new. Although similar to that of Bers, it avoids difficulties at the leading edge. The method is also somewhat similar to the Kármán–Tsien method implemented in its full form, including not only the pressure correction but also the shape transformation. The current method is more accurate than Kármán–Tsien, however, because it does not suffer from the limitation to the fictitious tangent gas law that specifies $\gamma = -1$.

7.2.3 Numerical Method

The numerical method developed in this research is described in detail in Chapter 5. The purpose of the method is threefold: 1) solve the compressible flow over arbitrary bodies of

practical engineering interest, 2) determine the shape of the domain corresponding to the canonical Laplacian form of the equivalent incompressible flow, and 3) solve the equivalent flow.

Two possible approaches for solving these flows were proposed. The first approach would be to solve the nonlinear subsonic flow directly with an elliptic finite difference technique and then to solve the domain of the equivalent flow as a second elliptic boundary value problem with a similar method. This approach has the advantage of being direct and non-iterative, but it requires two separate types of solutions each using a domain grid. The second approach is to solve the equivalent incompressible flow with a boundary element method requiring only an airfoil surface grid and then to solve the coordinate mapping with an elliptic boundary value domain solver. Although this approach requires an iterative implementation, it has the great advantage of emphasizing that the equivalent flow is truly "incompressible" in the mathematical sense because we solve it with an incompressible solver. For this reason, we chose this iterative approach for the work in this dissertation.

The solution algorithm consists of four major numerical steps that are illustrated in Figure 7. The first step is the generation of an initial grid for the given subsonic flow. Next, a convergence loop is entered and the subsequent three steps are executed. These steps comprise solving the equivalent incompressible flow using a simple boundary element method, calculating the metric tensor from the resulting flow solution, and finally, solving the coordinate mapping. The loop steps through these three steps repetitively until a convergence criterion based on the sum squared residual of the changing grid coordinates is met.

We now recapitulate each of these four primary steps. We begin with a summary of the initial grid generation procedure described in Section 5.2. The need for a structured grid topology was identified based on the choice of a finite difference method for the mapping solution technique. Both C–grid and O–grid structured topologies were investigated. Experimentation with the method revealed that the O–grid was the preferred choice for the single airfoil cases examined in this research because of requirements on smoothness of the boundary shape and its derivatives as well as smoothness of the point placement spacing.

The generation of the initial O–grid is completed by first placing points along the outer and inner domain boundaries and then interpolating between these boundaries to populate the domain interior. An exponential interpolation function was developed which places points based on the specification of a parameter that determines the density of points near the immersed body.

After the initial grid is produced, the next step is to solve the equivalent incompressible flow. This solution is accomplished by employing a standardly available panel code implementation as described in Section 5.3. While nearly any two dimensional panel code could be used, we selected a constant strength source method with a single discrete vortex to specify the circulation through the Kutta condition. The method was based largely on an implementation of one of the original Hess and Smith formulations by Moran [82]. A particularly appealing advantage of this formulation is its ability to handle profiles with thick trailing edges.

Most pedagogical panel code implementations such as the one chosen for this work typically produce only surface velocity distributions and pressure integrals such as the lift and moment coefficients. For our method, however, we also require solutions to the equivalent incompressible flow at all grid points within the domain interior. Although domain solutions are not typically implemented, they can easily be generated using the singularity strengths produced in the panel code solution. We therefore implement this capability of a domain solution, often termed a field survey, by introducing a simple post-processing step to the panel code solution.

Once an estimate for the incompressible flow solution is developed, the next step in the numerical algorithm is to calculate an estimate of the metric tensor for use in the subsequent coordinate mapping. This calculation procedure is described in detail in Section 5.4. The generation of the metric requires several intermediate steps, including the introduction of an auxiliary computational coordinate system. Finite difference derivatives of the coordinate mapping to and from this auxiliary system are developed from both the original Cartesian coordinate system of the compressible flow and from the current estimate of the isothermal coordinate frame. Additionally, derivatives directly relating the original and isothermal

frames are developed because the metric tensor is known as a function of the velocities of the original compressible flow, and the velocity estimates from the panel code correspond to the frame of the Laplacian flow. The velocities are transformed using these derivatives, and estimates for the metric components are finally calculated.

The final step in the solution loop is to solve the isothermal coordinate mapping itself. We choose to solve the transformation using a finite difference technique for elliptic boundary value problems. A variety of these techniques have been developed, widely used, and documented in the literature. In this work, we investigate two particular methods: Gauss–Seidel iteration by lines and successive over-relaxation by lines (SLOR). Both of these methods function by iteratively sweeping through the grid along lines and solving linear systems corresponding the discretized differential equations of the coordinate mapping. SLOR is a modification to Gauss–Seidel that performs a weighting of the solution estimates based both on the prior and current iterations. This weighting is substantially biased toward the current iteration. The advantage of SLOR over Gauss–Seidel by lines is dramatically increased convergence rate, as long as stability can be achieved. Based on experimentation with the method for our problem, the SLOR technique was found to increase convergence rates by as much as a factor of five without adversely affecting stability. For this reason, SLOR was chosen for the final implementation. Details of this approach are presented in Section 5.5.

The innovation of the numerical method developed in this research does not stem from new approaches for solving incompressible flows or elliptic coordinate mappings. Rather, the innovation is the collective capability provided by integrating these commonly available techniques to provide a stable and practicable method to simultaneously solve a subsonic flow and its incompressible equivalent. The development of this numerical capability is believed to be a significant contribution of this dissertation.

7.2.4 Insights into Equivalent Flow Phenomena

In Chapter 6, we employed the newly developed numerical method to solve subsonic flows and their incompressible equivalents. The four objectives of generating these results were

to validate the theory and numerical method, to determine the sensitivity of the numerical method to solution parameters, to quantify the geometric effects of the transformations, and finally, to indicate phenomena present in the equivalent profile shapes that may be useful for design purposes.

To accomplish these goals, we investigated representative subcritical solutions over both a non-rotating circle in freestream flow and a NACA 0012 profile. For the circle, the first step was to conduct a series of studies to determine the influence of the parameters in the numerical solution method on the solution quality. The results of these studies are presented in Section 6.1.1. The parameters investigated included the number of grid nodes in each coordinate direction, the tolerance settings for both the overall algorithm and the coordinate mapping convergence loops, and the radial location of the far-field boundary. In performing these studies, we tracked the value of the maximum velocity obtained on the circle as well as the drag coefficient.

The studies indicated that good grid resolution is especially important, with circumferential grid density largely driving error in the drag coefficient and both radial and circumferential density affecting the maximum velocity error. The primary result of the study on convergence tolerances was that there exist "balanced" settings of the two parameters that minimize error. It was found, for instance, that setting the overall algorithm tolerance to a very small level while keeping the coordinate mapping tolerance at a substantially higher level produces no improvement in solution error. The study dealing with the placement of the outer boundary indicated that it is imperative to keep good radial point density whenever moving the boundary outward. A second finding was that the outer boundary need not be moved to a location substantially greater than three chord lengths from the inner body to produce high quality results.

After conducting these sensitivity studies, field results for the flow over a circle at the slightly subcritical setting of $M_\infty = 0.375$ were presented in Section 6.1.2. The results for the subsonic flow demonstrated the correct qualitative behavior, and the value for the peak velocity agreed with that found by Van Dyke's series expansion technique [121]. These field

results also represented the first quantitative visual depiction of the coordinate transformation effects involved in generating the equivalent incompressible flow. The overall effect of the transformation was to produce an equivalent body with a shape oblonged in the cross-flow direction. The equivalent shape to the circle generally resembles an ellipse, but the stretching effect is more localized near the maximum velocity region.

In depicting these results, we introduced the visualization technique of cross plotting the isothermal coordinate curves on the Cartesian axes of the original flow field and then plotting the Cartesian coordinates on axes corresponding to the isothermal coordinates of the equivalent flow. The resulting depictions, shown in Figure 41, indicate two primary effects of the coordinate mapping. The first is a global effect evidenced by the mapping of squares into rectangles far from the body. The second is a localized effect that produces curvature of the coordinate curves in regions of high velocities near the body. This curvature corresponds to the local expansion of the aspect ratio of the rectangles comprising the coordinate net. This behavior of transforming squares into rectangles is indicative of quasiconformal mappings such as ours.

The next set of results, presented in Section 6.1.3, were based on a sweep through a range of freestream Mach numbers from 0.1 to the slightly supercritical value of 0.425. The maximum velocities on the circle obtained in this sweep agreed with those from Van Dyke's method to with substantially less than 1% throughout the Mach number range. The general effect of increasing Mach number was found to be an increase in the thickness of the equivalent incompressible shape. The trend indicated that the thickening behavior was substantially more significant than that produced by the Prandtl–Glauert method. This result stems from the fact that the flow over a circle is dominated by locally high flow velocities even at small freestream Mach numbers. The linear approach on which the Prandtl–Glauert method is based cannot correct for these local effects.

In section 6.2.1, we explore the symmetric flow about the NACA 0012 at $M_\infty = 0.72$. The surface pressure distribution obtained in the solution was compared to the results found by Lock [73] and excellent agreement was noted. The field results were found to be smooth and qualitatively correct, excepting slight defects near the body associated with

grid density and the coordinate extrapolation routine. The effects of the transformation on the equivalent flow were noted using plots of the warped domain grid as well as cross plots of coordinate curves. The primary effect was found to be thickening of the profile.

Lifting flow over the NACA 0012 was explored in Section 6.2.2. The flow parameters for this solution were $M_\infty = 0.63, \alpha = 2°$. This case corresponded to another solution presented by Lock [73], and excellent agreement was again obtained. In addition to the previously noted effect of thickening of the equivalent profile, a second effect was noted due to the angle of attack. This effect was a downward droop in the leading edge, producing a very slight but significant amount of camber in the airfoil forebody. The droop and associated asymmetry could be noted in cross plots of the coordinate curves. An interesting effect associated with this leading edge droop is the downward displacement of the leading edge stagnation streamline. This displacement, which grows as we translate upstream of the airfoil, is especially pronounced at a distance of two chord lengths. This effect is illustrated in Figures 71 and 72.

The final set of results comprised a series of solutions for the NACA 0012 at a matrix of freestream Mach numbers and angles of attack. The purpose of this study was to produce data to determine trends in the shapes of the equivalent airfoil as a function of these driving parameters. The results indicated that thickness is driven primarily by freestream Mach, whereas the leading edge droop is affected by both angle of attack and Mach number. The thickness trend with Mach number was found to be less than that predicted by Prandtl–Glauert at low Mach numbers and greater at higher Mach. Interestingly, the x/c location of the point of maximum thickness was found to be invariant with Mach number, i.e. $(\bar{x}/c)_{t_{max}} = (x/c)_{t_{max}}$. The leading edge droop exhibited a nearly perfectly linear relationship to both angle of attack and Mach number. This result suggests that it may ultimately be possible to theoretically quantify the relationship driving this trend.

In addition to their role in validating the theoretical and numerical techniques, a primary contribution of these simulations is the insight that they provide into the shapes of profiles seen by equivalent incompressible flows. As indicated in this review, the primary effects determined for these investigations of the circle and NACA 0012 are a thickening of the

profile with increased Mach number that does not agree with the Prandtl–Glauert result and a droop in the leading edge corresponding to circulatory flows at nonzero angle of attack. The specific nature of these results is a new contribution to the literature. These contributions point toward the value of further investigations of the numerical method for other types of profiles, including nonsymmetric shapes with camber as well as more modern shapes such as supercritical airfoils.

Having summarized the contributions of this research, we now turn to potential applications of the method.

7.3 Potential Applications

Two primary application areas have been envisioned for the theoretical and numerical methods developed in this research. These are flow similarity and inverse design. In this section, we outline some of the potential applications in each area.

7.3.1 Flow Similarity Scaling

The principles of flow similarity are widely known and applied in the field of fluid mechanics. The concept of nondimensional parameters such as the Mach number and Reynolds number has been a crucial factor lending toward our greater understanding of the nature of fluid motion. The great benefit of nondimensionalization is that we can dramatically reduce the number of distinct flows that must be examined. All flows that share the same nondimensional parameters are, for all intents and purposes, the same, regardless of the absolute geometric scale or independent values of dimensional parameters. For instance, a potential flow at a particular freestream Mach number behaves in the same way as a second flow at the same Mach number, even if the freestream temperature in the second flow differs. Similar results hold regarding the uniform scale of objects immersed in flows. This dependence on nondimensional parameters allows experiments to be conducted at smaller scales in test facilities such as wind tunnels, with the knowledge that the results may be directly applied to flows over similar geometries at the real world scale.

In the typical applications of flow scaling with nondimensional parameters, related bodies must be similar in the sense of congruence. That is, it must be possible to obtain one

from the other by multiplying by the same scale factor in all spatial dimensions. This concept is sometimes termed *similarity with similar models* [103]. A more advanced concept describes flow relationships in terms of *similarity with distorted models*. In these types of flow similarity methods, two related geometries are distorted nonuniformly with respect to each other, with differing scaling factors applied to each spatial dimension. This concept is associated with techniques such as the Prandtl–Glauert and Göthert rules as well as the work of this dissertation.

The practical feature of these types of methods is that they allow comparisons to be drawn between flows at *different* nondimensional parametric settings over bodies that are nonuniformly scaled relative to each other. This type of scaling was one of the original motivations of the Prandtl–Glauert and Göthert rules. The fluid mechanics community had accumulated a vast array of information and extensive knowledge about incompressible flows, but as interest in higher speed flight emerged, the necessity for obtaining flow results at increased Mach number became imperative. The question was whether the knowledge base of incompressible flows could somehow be leveraged for the problem of compressibility at higher Mach numbers.

These answers were provided, at least in an approximative and linearized sense, by the Prandtl–Glauert, Göthert, and later, Kármán–Tsien methods. These types of similarity methods, as well as the transonic similarity approach devised originally by von Kármán [127], were used extensively in the 1940s and 1950s for a variety of theoretical and experimental applications including corrections of plane flows and flows over finite wings [72], similarity in ellipsoids and other bodies of revolution [69, 53, 94], transonic similarity for planar profiles and wings [20, 57, 75, 91, 104, 105], and transonic similarity in slender body theory [50, 51]. These citations represent but a few of the many applications of similarity methods in this era, and subsequent use of the Prandtl–Glauert and Kármán–Tsien techniques for correcting solutions obtained by numerical methods for incompressible flows to results approximately valid for the entire subsonic range has become ubiquitous.

The method developed in this research represents a logical extension of methods of the Prandtl–Glauert and Kármán–Tsien types to the fully nonlinear flow problem. As

demonstrated in this dissertation, this method goes farther than these classical techniques, such that it is appropriate to speak of it not as a "compressibility correction" but rather, as a true solution method. Although it can provide solutions to subsonic flows, it is unlikely that the method will see practicable use for this purpose. If the intent is simply to solve the compressible subsonic flow over a profile of specified shape, there is no advantage to the method in its current form because it is more expensive, requiring iterative applications of an elliptic boundary value solver in addition to a panel code solution, while the direct problem of solving a subsonic potential flow requires only a single elliptic boundary value solution.

The advantage of the method, however, is that it produces the equivalent incompressible domain corresponding to the specified original profile shape and freestream flow parameters. The primary potential for use of the method lies in situations in which knowledge of this equivalent flow would be especially useful. One example of this type of situation is in experimental testing.

Experimental testing of aerodynamic devices often involves scaling a model of the geometry to an appropriate size and then performing tests designed such that the nondimensional flow similarity metrics match those of the desired real world flow. Cost and practicability are primary drivers that influence the way in which this testing is conducted. This method may allow tests to be conducted at a lower speed over a geometrically altered geometry. The test results could then be transformed to correspond to the actual case of a higher speed flow over the true geometry. Because the velocities could be lowered, such an approach would reduce the power required to drive the test facility.

Two particular testing arenas in which this general approach may prove useful are wind tunnels and scaled turbomachinery research facilities. Using the method, wind tunnel tests in the subsonic range could potentially be conducted in the incompressible range, decreasing the required test section Mach numbers to perhaps 0.1 or less and correspondingly reducing power requirements for the tunnel. A disadvantage of this approach, however, is that the geometry of the profile to be tested, and perhaps even of the tunnel walls, changes as a function of the desired freestream Mach number and angle of attack. This dependency of

the shape on these parameters reduces the practicability of the method primarily to on-design conditions corresponding to a single equivalent shape, or at most, to a few particular off-design cases for which alternate shapes can be manufactured.

One longer term possibility, however, may be to perform testing with deformable test articles comprised of so-called morphing structures. Recent interest in these types of structures has been significant, primarily because emerging manufacturing techniques and materials may make in-flight shape deformations a possibility for future flight vehicles. If these types of structures ultimately prove successful at producing a wide variety of shape deformation capability at reasonable cost, they may become valuable for the testing problem by leveraging the method developed in this research. Although such an approach might be possible, the author is admittedly highly skeptical about the overall economic feasibility of this approach.

A much more promising area of application for this research is in testing arenas which already use scaling with distorted geometric models to account for compressibility effects. One such area is in turbomachinery research. Typical compressor and turbine test machines are flow scaled to larger absolute sizes and the rigs rotate much slower than the turbomachinery that they intend to replicate. The reduction in rotational speeds reduces stresses in the test article blading and also keeps stresses on rotating instrumentation devices manageable. Additionally, this reduction dramatically reduces the power required to drive the machines, allowing smaller electric motors that cost less to acquire and operate.

Most major aircraft gas turbine engine manufacturers and research establishments operate these types of facilities. Wisler provides a detailed description of the similarity scaling approach and its application in the General Electric low-speed axial research compressor [132]. A depiction of the the low-speed axial research compressor operated by the NASA Glenn Research Center is shown in Figures 79 and 80. The capabilities and features of this facility are described by Wasserbauer, *et. al.* [130]. This facility operates at a nominal design rotational speed of 980 RPM [130], whereas typical high pressure axial compressors in aircraft gas turbine engines operate on the order of $50,000$ RPM.

Because these types of test facilities are intended to mimic actual engine hardware while

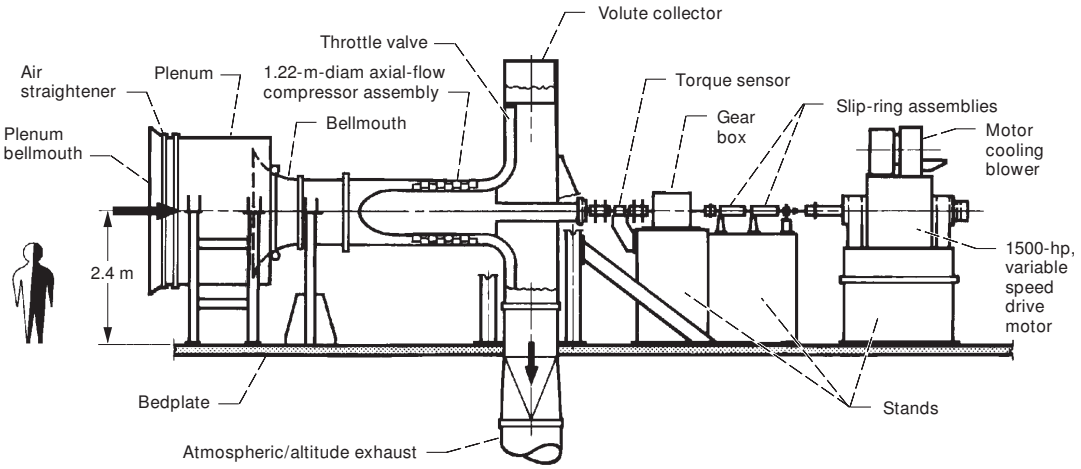

Figure 79: NASA Low-Speed Axial Compressor Facility (From Wasserbauer, *et. al.* [130])

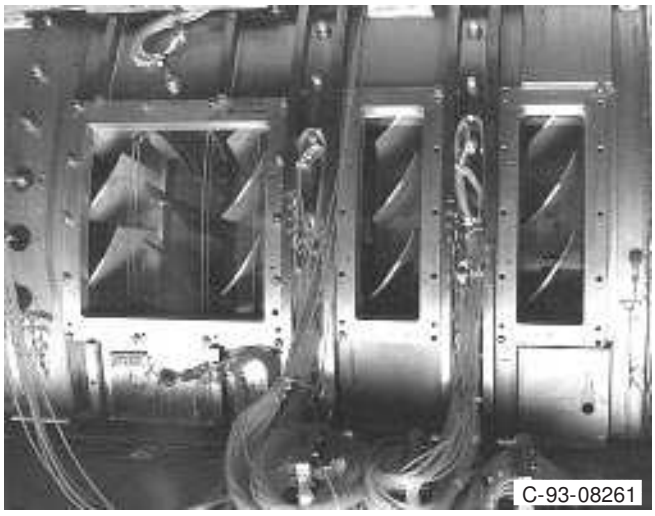

Figure 80: NASA Low-Speed Axial Compressor Test Section Stages (From Wasserbauer, *et. al.*[130])

operating at substantially lower speeds, they typically employ distorted model similarity scaling to adjust the geometry of the test article blading. The compressibility scaling for this geometry is typically based either on the Prandtl–Glauert rule or on an iterative solution approach in which a few shape parameters in the equivalent blading are adjusted to best match the flow to be modeled [132]. The approach developed in this thesis may prove valuable in creating new scaling rules for the equivalent blading and flowpath geometry in these types of machines that allows a better replication of the actual compressor performance to be obtained for more arbitrary blade shapes in the high-speed machine. The advantage of the method in obtaining these similarity rules is that it accurately accounts for the effects of arbitrary local flow gradients on the equivalent geometry at the design condition.

7.3.2 Inverse Design by Leveraging Equivalent Incompressible Flows

A second potential area of applicability of the method developed in this work is the design and inverse design of airfoils. The idea of this application is that because so much is known about incompressible flows, we can possibly leverage the equivalent incompressible flow as means to transfer knowledge to the slightly more challenging regime of subsonic compressible flow. The rich knowledge base of incompressible flows consists of a vast variety of theoretical models, numerical methods, empirical relationships, and heuristics that have been assembled over years of fluid dynamic research.

A particularly important topic to which this knowledge base might apply is viscous effects. For instance, boundary layer theory for incompressible flows is highly developed, with numerous theoretical and numerical models that could possibly be applied to the problem of a subsonic external flow via its incompressible equivalent. An additional and highly interesting possibility is to leverage the heuristic knowledge of pleasant pressure distributions in incompressible flows that avoid separation. Such an approach might ultimately have significant utility for high lift configurations, which have low freestream Mach numbers but high peak Mach numbers and large adverse pressure gradients on their suction surfaces. It might be possible to iteratively alter the design of the original shape such that the resulting equivalent incompressible pressure distribution is known to be shallow enough that

separation will not occur.

This iterative design approach suggests a pursuit of the oppositely posed problem of inverse design. The focus of inverse design is typically to determine the airfoil shape that produces a specified pressure distribution at a given design Mach number and/or angle of attack. Inverse design is often performed using the potential flow model; however, one of the main motivations of inverse design to produce a particularly pleasant pressure distribution that advantageously influences viscous effects such as boundary layer separation. Heuristic and empirical information regarding how these phenomena affect or are affected by the distribution of adverse and proverse surface pressure gradients is used in determining the allowable shapes of this distribution. In most modern contexts, it is desirable to use inverse design techniques to solve for shapes that produce good pressure distributions over a range of flight conditions.

Although this description represents the common embodiment of airfoil inverse design today, our interest here is in a slightly different concept. It may be possible to conduct inverse design based on producing a desired shape of the pressure distribution of the equivalent incompressible flow, rather than the subsonic flow itself. An advantage of this approach is that it would again allow the extensive knowledge base of incompressible aerodynamics to be employed. In particular, the designer could perhaps directly specify the desired shapes of incompressible pressure distributions based on heuristics for separation, etc.

Before this approach could be pursued, however, significant additional work would be required to verify that the boundary layers in the original subsonic flow and the equivalent flow are similar enough that the pressure profile effect on separation behavior carries over between the two flows. If the boundary layer behavior is quite different, owing to compressibility effects within the layer itself, it may be necessary to perform an additional coordinate transformation in the domain of the boundary layer to map the layer corresponding to the compressible flow into that of the incompressible equivalent flow. This mapping would require a coordinate mapping that transforms the compressible boundary layer equations into the incompressible equations.

Inverse design applications would require that several additional interesting research

questions be answered. One question regards the nature of the algorithm. How should this algorithm be structured in an inverse sense? A second question regards uniqueness. In general, it appears that there is *one* equivalent incompressible flow corresponding to a particular choice of M_∞ and α of the original flow for a specified set of coordinate mapping boundary conditions. However, it has been conjectured by the author but not proven that there may be an *infinite number* of compressible flows that correspond to any one incompressible flow. That is, for each incompressible flow there exists an *equivalent subsonic flow* at each possible combination of subcritical Mach number and incidence angle. These questions and their implications would certainly need to be answered as a prerequisite to the pursuit of an inverse design approach.

7.4 Possible Continuations

In the previous section, we discussed potential applications of the method developed in this work. In this section, we suggest possible topics of future research based on the ideas in this thesis.

7.4.1 Additional Quantification of Equivalent Incompressible Shapes

Perhaps the most straightforward avenue of extensions to this research is to further examine and categorize the shapes of equivalent incompressible profiles. This work would comprise a continuation of the explorations conducted in Chapter 6.

In Section 6.2.3, the primary effects of the transformation on profile shapes were found to be a thickening associated with increasing freestream Mach number as well as a droop in the leading edge responding both to angle of attack and Mach number. It is important to note, however, that these results were obtained only for a particular symmetric airfoil profile, namely the NACA 0012. The logical next step is therefore to systematically examine other airfoils with different thickness and camber distributions. The effect of camber has not yet been investigated, but based on the effects of angle of attack for the symmetric profile, it is anticipated that the transformation will generally increase camber of the equivalent shape relative to the original airfoil. The primary focus of such studies would be to isolate individual effects as much as possible and to verify that these effects act consistently and

predicably across a variety of profile types.

Based on the results of these studies, quantitative trends in the shape deformation such as those presented in Figures 75 and 76 could be tabulated. A valuable exercise would be to try to determine the precise theoretical causes of the specific deformation features in terms of the flow parameters of the original subsonic flow as well as the geometric characteristics of the original shape. This process might begin with a fitting approach for the data similar to that described at the end of Section 6.2.3 as a means to determine a series expansion that would point toward the correct theoretical relationship.

7.4.2 Approximate Integrability as a Consequence of the Flow

Another area of future work is to attempt to obtain approximate solutions for the mapping to the equivalent incompressible flow using only a surface grid and not a domain discretization. It is believed that these types of solutions could be obtained by developing the Taylor series approach described in Section 4.3.3 for attaining integrability of the coordinate transformation as a consequence of the flow solution. The solution quality could be selected by specifying the number of terms to carry in the expansion.

A great advantage of this approach, should it prove possible, would be to dramatically reduce the computational expense of generating the mapping. Without the need to solve a domain grid, the elliptic boundary value solver for the coordinate mapping could be omitted from the solution loop. The resulting computational savings would be significant because this solver occupies the greatest fraction of analysis time in the current algorithm.

An additional advantage of the approach is that there would no longer be any need to produce a domain grid at all. With no need to solve the grid interior, the problem could perhaps be posed such that the boundary conditions at infinity are satisfied automatically, also obviating the need for the discrete far-field boundary. This is the typical type of far-field behavior for panel methods, which are based on singularity solutions whose strengths die off naturally to satisfy the infinity conditions.

The issues of computational speed and the reduced complexity of grid generation are

not particularly pressing for the types of two dimensional solutions pursued in this dissertation. Solution times for these flowfields, even with the required domain calculation, are not significantly limiting for most purposes. However, if the method could be extended to three-dimensional flows, these issues become very significant. Whereas creating a structured grid for a two-dimensional problem is nearly trivial, structured grids are very difficult and perhaps impossible for certain arbitrary three dimensional configurations. Similarly, solution expense becomes a much greater driver in three dimensions. For these reasons, an approach that could attain integrability as a function of the flow and allow the solution to be obtained by an iterative surface mesh approach would represent a substantial contribution. Such a method may perhaps prove to be more efficient at solving the compressible flow than other direct solution methods that require volume grids or point distributions.

7.4.3 Supersonic and Transonic Flows

The mapping procedure developed in this work was designed for the production of incompressible flows from purely subsonic flows. Although some interesting evidence of possible applicability at slightly supercritical Mach numbers was indicated in Section 6.1.3, it is highly unlikely that the method holds true applicability in the transonic or supersonic regions. A natural research question is therefore whether the mapping ideas developed in this thesis could perhaps be restructured to apply to the problems of supersonic and transonic flows. We investigate this possibility briefly in this section.

To create the equivalent incompressible mapping, we performed a gauge transformation to set the metric tensor in an equivalent incompressible flow, and we then executed a curvilinear coordinate transformation such that this equivalent flow was posed in the common form of the Cartesian Laplace equation, the $M_\infty \to 0$ limiting form of the full potential equation. A similar approach could perhaps be applicable in supersonic flow by mapping to another flow that holds special importance in this regime. Instead of creating an equivalent incompressible flow, we could perhaps create an equivalent flow corresponding to $M_\infty = \sqrt{2}$. This Mach number is important in the case of linearized supersonic motion because it represents the location at which the linear potential equation takes on the particularly nice

form,

$$\frac{\partial^2 \phi}{\partial \bar{x}^2} - \frac{\partial^2 \phi}{\partial \bar{y}^2} = 0. \tag{283}$$

Whereas the Laplace equation, given in similar notation by,

$$\frac{\partial^2 \phi}{\partial \bar{x}^2} + \frac{\partial^2 \phi}{\partial \bar{y}^2} = 0 \tag{284}$$

is the canonical elliptic form, Equation 283 is the canonical hyperbolic form.

Equation 283 is particularly simple to solve. Indeed, unlike the case for the Laplace equation, we can write down not only particular solutions, but also a general solution. This general solution is

$$\phi = f_1 (x - y) + f_2 (x + y) \tag{285}$$

where f_1 and f_2 are arbitrary functions with the arguments specified in terms of the coordinates as indicated. The function $f_1 (x - y)$ has level curves oriented at a $+45°$ slope to the x-axis, whereas the function $f_2 (x + y)$ has curves with a $-45°$ slope. These functions are typically specified by the boundary conditions for the flow.

There is historical precedent for a mapping to this functional form provided by the Ackeret rule of linearized supersonic aerodynamics [2]. The Ackeret rule is the supersonic equivalent of the Prandtl–Glauert rule. Instead of mapping flows to the incompressible limit where the Laplace equation holds, the Ackeret rule maps flows to the $M_\infty = \sqrt{2}$ condition at which Equation 283 governs the flow [2]. Whereas the scaling factor $1/\sqrt{1 - M_\infty^2}$ appears in applications of the Prandtl–Glauert rule for pressure scaling and/or shape deformation, the factor$1/\sqrt{M_\infty^2 - 1}$ fulfills the same role for the Ackeret rule. This factor is shown as a function of Mach number in Figure 81.

An advantage of developing a mapping solution from arbitrary nonlinear potential supersonic flows to this linear form is that the flow solution for the equivalent flow can be determined nearly instantaneously. Unfortunately, as we saw in this work, this mapping creates a simple flow solution at the cost of an expensive coordinate mapping. We could therefore not necessarily expect the complete solution to be obtained more quickly than a typical nonlinear supersonic potential solution. However, as in the method developed in

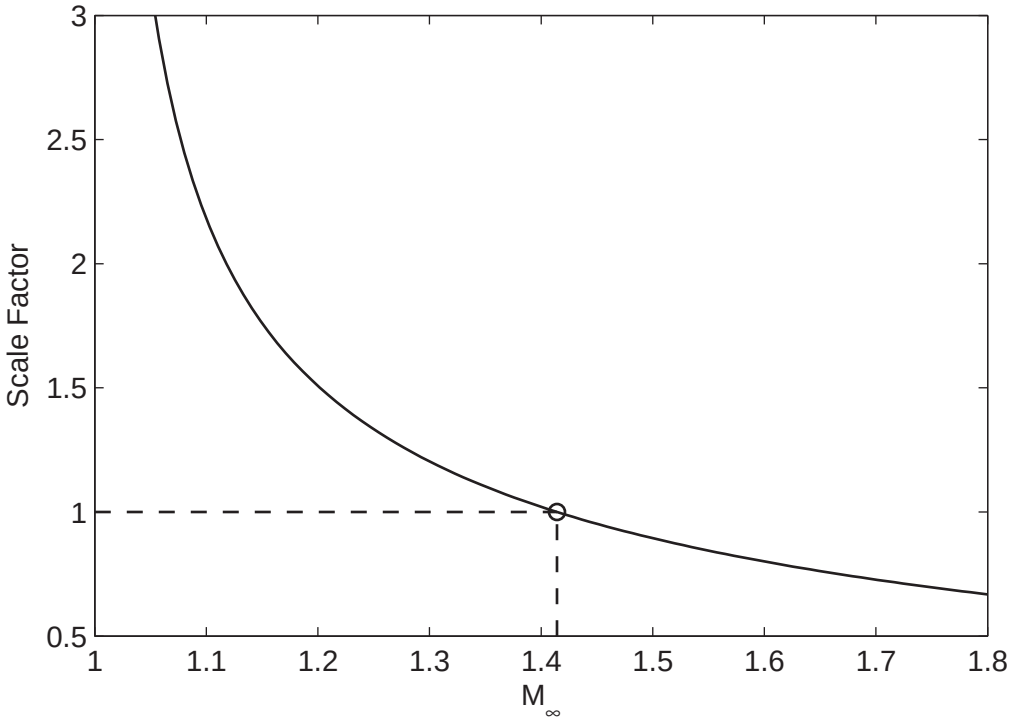

Figure 81: Scaling Factor $1/\sqrt{M_\infty^2 - 1}$ of the Ackeret Rule

this thesis, we could perhaps hope to learn something from the nature of the equivalent shapes generated by the transformation.

We now attempt to gain some insights into these equivalent shapes. If we again choose to specify boundary conditions on the coordinate mapping of $\bar{x} = x$ on both the inner and far-field boundaries, we should then expect the primary shape distortion effect to occur in the $\bar{y}$ direction. A rough order of magnitude estimate of this deformation can be obtained by considering the linearized result represented by the Ackeret scaling factor shown in Figure 81. If the freestream Mach number is less than $\sqrt{2}$, the effect is one of stretching, i.e. the airfoil is thickened, similar to the thickening that we saw for the subsonic case. On the other hand, if M_∞ is greater than $\sqrt{2}$, the scaling factor is less than unity, so we should expect that the effect is to produce an equivalent shape that is thinner than the originally given profile. An example of this stretching and thinning behavior is shown in Figures 82 and 83.

Although this transformation behavior may be approximately correct in certain cases,

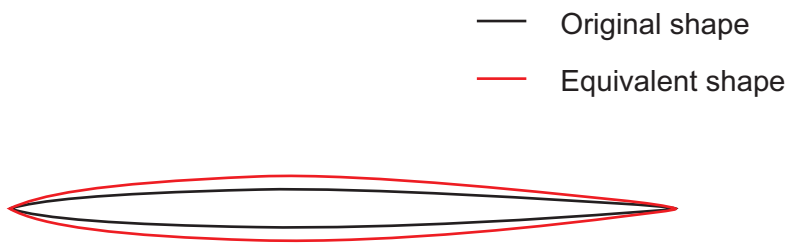

Figure 82: Conjectured Transformation for $1 < M_\infty < \sqrt{2}$ Supersonic Flow; Stagnation Effects Not Shown

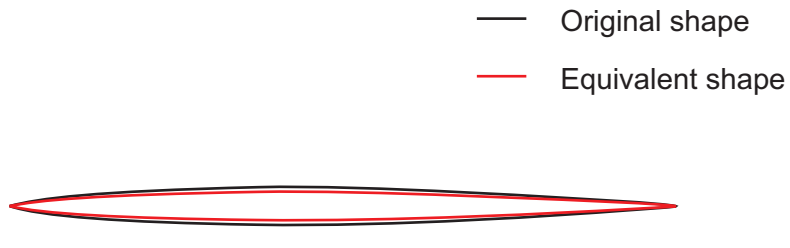

Figure 83: Conjectured Transformation for $M_\infty > \sqrt{2}$ Supersonic Flow; Stagnation Effects Not Shown

there are two complicating effects to the supersonic problem that do not have parallels in the subsonic case. First, all external flows over profiles that have supersonic freestream velocities are necessarily *mixed* flows. That is, they contain regions of flow with supersonic velocities and other regions with subsonic velocities. The subsonic regions correspond to the areas surrounding the stagnation points in the flow. For thin sharp bodies, such as those shown in Figures 82 and 83, these subsonic regions near the stagnation points may be particularly small, and it may be possible to excise tiny portions of the domain in these regions such that the flow transformation can proceed with a globally-applied transformation to the hyperbolic canonical form. For thicker bodies with rounded leading edges, however, the subsonic region would be larger and this approach would not likely be valid.

The second complication for the supersonic case is the presence of shock waves. For sharp thin bodies, these shocks will typically be attached, oblique, and approximately straight. In these cases, we know from Crocco's theorem that the flow will remain isentropic and potential on either side of the shock. It would therefore be possible to continue to solve the flow with the full potential model and to perform a transformation of the appropriate type on either side of the shock. If the shocks are all oblique, the downstream Mach numbers will

all remain supersonic, and the hyperbolic transformation would be applied on both sides.

In these types of problems, shocks would be modeled as jump conditions on the Mach number that drive the transformation in the particular regions of the flow. It would likely be necessary to model shocks as lines of field panels along which the appropriate jump condition could be applied. The locations of these field panels would likely need to be determined iteratively in the solution process. The motion of these panels during iteration could prove to be a substantial complication of the method in terms both of implementation complexity and convergence. It most cases for thin bodies, however, it should be possible to fix the shock angles based on the well known polar relations for straight oblique shocks.

The shock structure surrounding thick bodies with rounded leading edges in a supersonic freestream will present an even more challenging problem. In these types of flows, the shock waves will likely be detached and highly curved, with a nearly normal shock directly upstream of leading edge stagnation transitioning to the appropriately obliqued far-field shock corresponding to the particular magnitude of the freestream Mach number. Flows behind curved shocks are rotational, and hence, nonisentropic. The full potential model fails entirely in these cases. Because the transformation approach assumes irrotational potential motion, the type of methods that we have examined cannot be applied to these flows.

A scenario in which thick rounded bodies with supersonic regions could perhaps be approached with the transformation method is transonic flows. In these types of flows, shock strengths are typically weaker, and it is often permissible at lower transonic Mach numbers to solve the flow with the full potential equation, even through shocks. This approximation is possible because weak shocks produce only very small increases in entropy. If we consider the compression effect of weak shocks to be of first order, the entropy rise is of third order [29].

To apply the mapping method, however, it will likely be necessary to crisply identify not only shocks, but also the location of the sonic line in the flow. These features would need to be treated as field panels with appropriate boundary conditions that transmit flow properties from the subsonic to the supersonic regions of the flow and vice versa. These boundary locations would need to be iterated as a part of the flow solution. In the subsonic

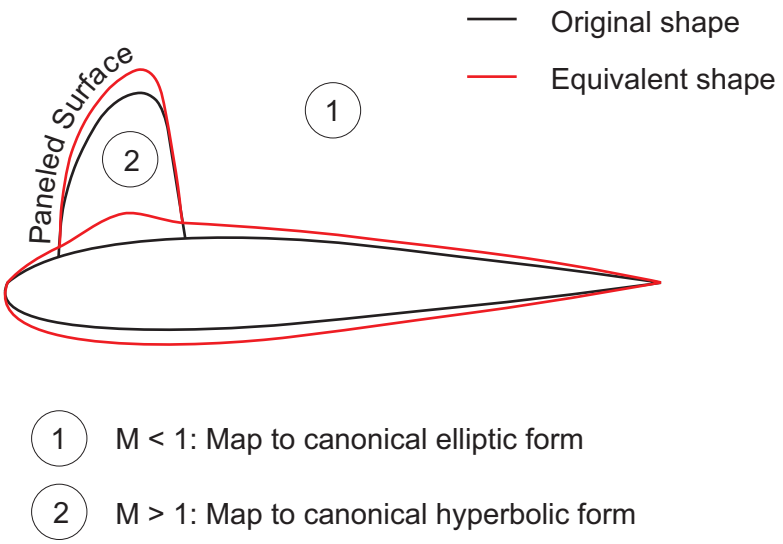

Figure 84: Conjectured Transformation for Low Transonic Flow with Isentropic Recompression

region, the transformation would be performed to arrive at the canonical Laplace equation, as exemplified by the method developed in this dissertation. Within the supersonic region, the mapping would produce the canonical hyperbolic form.

For flows in the lower Mach transonic region and over thinner bodies, the flow-wise transition along the body surface from subsonic to supersonic and again to subsonic regions is generally quite smooth in terms of the flow properties. In particular, the deceleration and recompression from the supersonic zone to the aft subsonic region is either truly isentropic, or at least approximately so with only very weak shocks. In these cases, the equivalent profile shape transition is expected to be smooth, with a thickening throughout the subsonic region followed by thickening of different magnitude in the supersonic region. This thickening behavior in the supersonic region is presumed based on the local Mach numbers being less than approximately 1.2. As we saw in Figure 81, higher Mach numbers may actually produce a local thinning of the profile. A notional depiction of the distorted shape in this type of flow field is presented as Figure 84.

For higher Mach transonic flows over thicker bodies, we expect a shock of appreciable strength to form on the suction surface to terminate the supersonic region. As in the previous case, it is likely that both the shock and the sonic line must be modeled as floating

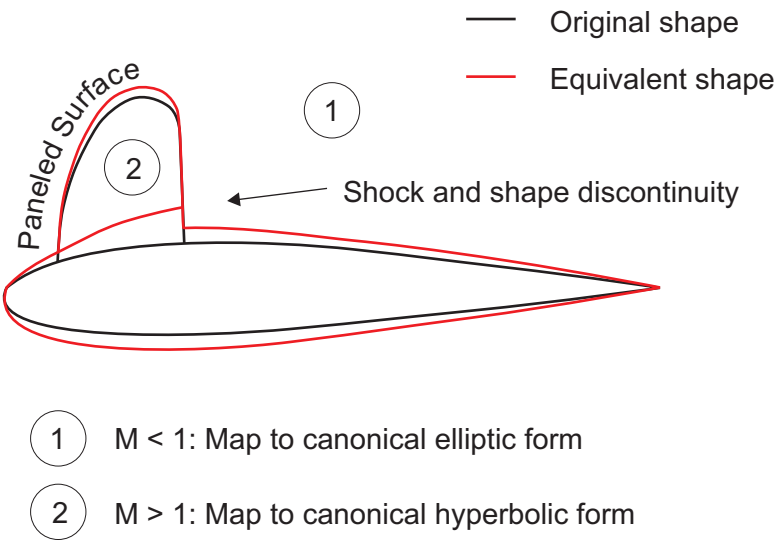

Figure 85: Conjectured Transformation for High Transonic Flow with Shock Recompression

field panels whose geometry is part of the solution. The transformation produced in this case would likely show an appreciable discontinuity in the equivalent shape located at the position of the shock wave. Within the supersonic region, the flow would likely continue to accelerated until abated abruptly by the shock. The corresponding shape change in this region would be increased local thickening followed perhaps by a discontinuous thinning at the shock transition. A notional depiction of this conjectured behavior is shown as Figure 85.

The extensive degree of the complexities and subtleties in these types of supersonic and transonic problems leads the author to be highly skeptical of useful applications of a mapping method to these types of external aerodynamic problems. Even if a consistent series of transformations could be carried out, matching subsonic and supersonic zones as needed, handling shocks, and iterating the locations of field panels to produce both flow solutions and the shapes of equivalent geometries, the question becomes where the value proposition of such a technique lies. Flow solutions in these regimes can currently be handled much more adeptly by other methods, so we should hope to learn something from the equivalent shapes. These shapes, however, would seem to bear no real significance in a useful or practicable way. In the subsonic case, we mapped to incompressible flows, and

we could therefore gain direct insights into the flow behavior based on a well developed knowledge base dating to the dawn of fluid mechanics research. For the supersonic and transonic problems, the shapes would not likely correspond to any actual flow for which we know more than the already complicated mixed flow field over the original airfoils. Indeed, the application of this method to strongly transonic and fully nonlinear supersonic external flows would perhaps cloud our understanding of the flows more than it clarifies.

Although these types of external flows may not be appropriate venues for extension of the method, we mention one much more promising application area for a purely supersonic flow: on-design conditions for supersonic nozzles. Steady isentropic supersonic flow within nozzles represents a well known problem that is typically handled by the method of characteristics. Several features of these flows make them appealing venues for the application of these types of transformation methods. First, they can be considered globally hyperbolic, as on-design conditions typically correspond to shock-free operation. For these types of flows, it may be possible to employ a coordinate transformation to the canonical hyperbolic form and obtain a shape that provides some degree of insight. If further research is conducted in applying these types of transformation methods to supersonic flows, the author recommends this nozzle flow problem as a logical starting point from which much could be learned.

7.4.4 Three Dimensional and Unsteady Flows

Another area for continued research is in applications of the subcritical transformation method to three-dimensional and unsteady flows. Inspired by the tensorial treatment and the relativistic viewpoint, it is natural to think of unsteady flows alongside three dimensional flows, because with careful consideration, they can be treated simply as four-dimensional flows with time forming the last dimension.

As a general rule, mapping problems are dramatically different depending on the number of dimensions considered. For instance, the well known class of conformal mappings, which have seen widespread usage in analytical solutions to incompressible flows, can be used to map any appropriately smooth and well behaved two-dimensional surface to any other similarly nice surface [61]. This type of behavior has been used extensively in geodesy, with

a variety of the techniques used to create flat maps of the Earth being conformal in nature. On the other hand, there are precisely two conformal mappings of three-dimensional spaces onto other three dimensional spaces, namely, inversion and identity [61]. This result stems largely from the fact that the Cauchy–Riemann equations appear to have no mathematically appropriate three-dimensional analog.

Fortunately, however, the method developed in this work leverages quasiconformal mappings. These types of mappings have much greater flexibility, and it is indeed possible to employ them nontrivially in three and higher dimensional cases [31]. This greater flexibility is enabled by the generalization of the Cauchy–Riemann relations to produce the Beltrami equations. These equations, which we typically referred to simply as the generalized Cauchy–Riemann equations, were presented in our formulation as Equations 149.

Although we can think of the three-dimensional and unsteady cases from the same standpoint relative to tensor analysis, we will discuss them separately here. First, we address three-dimensional solutions. The first question that arises is whether the tensorial equations developed in Chapter 4 remain correct. Fortunately, the invariant flow equations all remain valid, and in most cases the three-dimensional versions can be obtained simply by appending one additional element in the range of the free and dummy indices.

A more challenging task, however, is to obtain the correct three dimensional form of the metric tensor derived in Section 4.2. Several of the assumptions and decisions made in the two-dimensional case may no longer hold, largely because the metric has many more components that must be set (6 for $n = 3$ as opposed to 3 for $n = 2$). These issues stem from the way we set the metric tensor by simply equating the continuity equations for the compressible and equivalent incompressible flows and satisfying the resulting differential equation identically. This process produced two equations, enough to specify the metric algebraically up to some overall and apparently irrelevant conformal factor. In the three-dimensional case, however, this process would only provide three equations for the six unknowns in the metric tensor. An important question is therefore whether these remaining three conditions can be specified arbitrarily for convenience or whether there are other factors that drive their settings.

A second area that must be considered is how to develop a suitable grid for three-dimensional applications. Structured grids are very limited in three dimensions, so it may be necessary to complete the coordinate transformation with an unstructured grid. This approach would require substantial changes to the mapping algorithm, as it would no longer be practicable to use a finite difference approach. Rather, a finite volume approach based on treating the coordinate mapping equations as conservation laws would be required. This technique would need to be investigated before solutions over arbitrary three-dimensional bodies could be conducted.

A third area concerns issues related to the panel code in the three dimensional case. Two dimensional panel codes model circulation by applying a very simple trailing edge condition at a single point. Three dimensional panel codes require a more complicated treatment involving a paneled wake surface emanating downstream from the body [58]. Important questions include how this wake transforms in the coordinate mapping.

An intermediate approach between the current two-dimensional implementation and a fully three-dimensional method would be to extend the transformation to finite wing theory. With this approach, the two-dimensional method could be used for developing equivalent wing sections, and approximate three-dimensional effects could be achieved by applying the appropriate corrections for wing planform parameters such as aspect ratio and taper ratio. It may prove possible to develop an approximative transformation method using this approach that could capture the majority of the three dimensional compressibility effects for wings.

Unsteady cases also present challenges that must be addressed. Although all of the equations we developed in Chapter 4 can be immediately generalized to three dimensions simply by adding one index to every summation, special consideration is required for the unsteady case. In specifying the fourth dimension, we must be careful about how the equations are written, and the metric tensor must contain a factor that transforms units of time into units of distance. In the linearized case, this factor is typically the freestream sound speed. In our nonlinear case, we must be more careful because we will have need of using the metric tensor both inside and outside of derivatives, and we therefore need to

consider how we will handle derivatives of this factor.

Another significant theoretical issue for unsteady flows concerns precisely what continuity equation we wish to match in order to obtain equivalence. For instance, in an unsteady incompressible flow, disturbances propagate to all points instantly because we set $\frac{\partial \rho}{\partial t} = 0$. A more appropriate comparison might be made by mapping to the small disturbance acoustic equation, in which signals propagate with finite but constant speed. Also, as with a three-dimensional approach, significant work would be needed to determine how to set the additional degrees of freedom for the metric (which has 20 components for $n = 4$) that cannot be determined simply by setting satisfying continuity identically. These and other theoretical considerations such as the formulation of initial conditions will require further exploration.

These issues are clearly numerous and complicated. It is the opinion of the author that three-dimensional solutions may eventually become practicable, and the equivalent flows produced by these results would prove highly interesting. Unsteady flows, however, appear to involve much complexity while offering little promise of further understanding. One possible exception to this thought is in certain limited cases in nonlinear acoustics where a mapping to a linear acoustic context would be valuable. These situations, however, would likely represent a reduced subset of the full four-dimensional problem, including topics such as directed sound beams propagating in one spatial dimension and spherically symmetric solutions such as blast waves.

7.4.5 Differential Geometry and the General Relativistic Analogy

In Chapters 3 and 4, we described a gauge transformation that absorbs the effects of compressibility into the shape of space. This warping of space was depicted notionally in Figure 4. The notion of curvature inspires several interesting scientific questions. For instance, if space is curved, how can we quantify and describe this curvature? Can we learn something about the flow from it? Investigations of these differential geometric questions were not carried out in this thesis for the flow results obtained using the numerical method. These investigations therefore comprise a very interesting avenue for continued work in this

research area. We now briefly outline some of ways in which this differential geometric research could proceed.

There are two types of curvature of common interest in the differential geometry of two-dimensional surfaces: *intrinsic* and *extrinsic*. Intrinsic curvature is the type that can be deduced by an observer who does not have purview of his entire world but rather, only a local neighborhood. An observer could determine this type of curvature by making geodesic measurements in his neighborhood. That is, intrinsic curvature is curvature in the infinitesimal. For instance, an ant could attach a string to a fixed point and trace the curve on the surface formed from the rotation of the string. He could then measure the ratio of the circumference of the shape to the radius. If this ratio is 2π, the ant knows that he lives on a flat plane. If not, he must conclude that he lives on a shape with nonzero curvature.

A crucial result, due to Gauss, is that all of the information about this type of curvature is contained in the metric tensor [61]. This theoretical quantification of this result is called the *Theorem Egregium* because of its surprising result. For two-dimensional spaces with an orthogonal metric tensor, i.e $g_{12} = 0$, Gauss' result indicates that the intrinsic or *Gaussian* curvature, K, is given by,

$$K = \frac{1}{\sqrt{g}}\left[\frac{\partial}{\partial x}\left(\frac{1}{\sqrt{g_{11}}}\frac{\partial\sqrt{g_{22}}}{\partial x}\right) + \frac{\partial}{\partial y}\left(\frac{1}{\sqrt{g_{22}}}\frac{\partial\sqrt{g_{11}}}{\partial y}\right)\right]. \tag{286}$$

A much more complicated but very similar result is obtained for non-orthogonal metrics.

Because this equation contains factors involving isolated individual metric tensor components in forms such as $\sqrt{g_{11}}$, it *is not* conformal invariant. In our mapping method, we needed only metric tensor components of the form $\sqrt{g}g^{11}$, and we showed that these types of components are independent of any global scale multiplying the individual elements $g_{\mu\nu}$. That is, our results *are* conformally invariant. Because the intrinsic curvature *does* care about an absolute conformal scale and our metric formulation *does not*, we could set any particular conformal factor that we desire to obtain the same mapping results, and the resulting curvature corresponding to this choice would differ from the curvature resulting from any other arbitrary setting. This result seems to imply that conformal portion of the curvature is irrelevant in the two-dimensional case because it is not unique.

Although the conformal portion is nonunique, it may be possible to isolate the non-conformal effects of curvature. This consideration could lead to interesting results, but more work is needed to understand how the decoupling could be accomplished and what understanding it could provide. This avenue is the suggested approach for understanding the intrinsic curvature in the two dimensional case. In three-dimensional cases, the intrinsic curvature becomes much more complicated, with the curvature becoming tensorial in nature. Significant additional work would therefore be necessary to understand intrinsic curvature if the method were extended to three dimensions.

The second type of curvature of interest is extrinsic curvature. This type of curvature cannot be deduced by a local observer and is topological in nature. Primary questions that are related to extrinsic curvature include whether or not the space has boundaries. To answer questions such as these, an observer must be able to sense the large-scale features of his world, for instance, by traveling far from its surface and viewing it from a space of one higher dimension. Alternately the observer could determine whether it is possible to circumnavigate his world and return to the point from which he started. These types of issues are exactly those faced by mankind at the beginning of the era of exploration, when Magellan's voyage ultimately evidenced that the Earth is a sphere and not flat.

Extrinsic curvature, also known as mean curvature and typically notated H, can be quantified mathematically. In the so-called Monge form, it is given by

$$H = \frac{1}{\left(1 + h_u^2 + h_v^2\right)^{3/2}} \left[\left(1 + h_v^2\right) h_{uu} - 2h_u h_v h_{uv} + \left(1 + h_u^2\right) h_{vv}\right] \tag{287}$$

where the surface is parameterized by coordinates u and v as Cartesian coordinates in a plane and h is the height of the surface above the plane [47]. Notation such as h_u and h_{uu} in Equation 287 denotes partial differentiation.

A particular type of two-dimensional space is known as a *minimal surface*. For a minimal surface, $H = 0$; that is, the mean curvature vanishes. This type of surface holds a very strong and significant connection to compressible flow. Chapylgin showed that in the case of the tangent gas approximation $\gamma = -1$, the full potential equation becomes identical to the equation of a minimal surface [16, 22]. That is, Equation 287 with $H = 0$ can be

recognized as the tangent gas potential equation if we replace h by ϕ and nondimensionalize appropriately.

This relationship leads to interesting questions about the connection of our method to mean curvature. Although the mapping techniques we have used are based on the metric tensor and the infinitesimal scale, it would be interesting to know if there are certain interpretations of the method that are extrinsic in nature. This area represents a scientific curiosity, but the author is not certain whether such investigations would be fruitful in providing increased understanding of flow phenomena.

Through these investigations into curvature, it may be possible to develop a more profound viewpoint of the nature of compressibility in fluid flow. Curvature of space is a concept with strong ties to the general theory of relativity. It is therefore expected that a greater understanding of curvature in this context will yield insights into the validity and boundaries of the analogy that we have proposed to draw between compressible flow and general relativistic theory.

7.5 An Insidious Conservation of Mathematical Difficulty

Before closing, I wish to make a short and somewhat personal statement regarding the original intent of this research and the final result. As described in the introduction to this dissertation, my observations about the connection between the ideas of relativity theory and the problem of compressible potential flow were a major motivation in initiating and carrying out this topic. A second but equally important motivation was to use these types of techniques to substantially simplify accurate nonlinear subsonic flow solutions and to dramatically reduce their expense, with the long term goal of achieving these types of results for certain three-dimensional flows including those over high lift configurations.

The idea was to use the transformation to the canonical Laplacian form to allow the flow to be solved with a panel method, such that only a surface grid would be needed. The unfortunate discovery in this research was that although a volume grid could be eliminated for the purposes of the equivalent incompressible flow solution itself, the domain grid was still required in order to solve the resulting boundary value problem for the coordinate

transformation in a numerically exact sense.

Although the mapping technique reduces the complexity of the flow solution, it produces a similarly complex coordinate transformation. It would be appropriate to say that the technique simply transfers the nonlinearity in the problem from the flow and into the geometry.

I went to great lengths to avoid this problem, investigating a wide breadth of geometric methods that could perhaps be employed to "transform away" the underlying difficulty. These methods include but are not limited to:

- Non-Riemannian manifolds and torsion [35]
- Absolute parallelism [21]
- Projective geometry [35]
- Weyl gauge transformations [33, 83]
- Nonholonomic coordinates [59]
- General relativistic methods [129, 111, 97]

Although each of these methods appeared to have something to offer, uncountable reams of white copy paper and two years of exploratory efforts were expended in failed derivations invoking complicated notation. In some cases, no practicable usage could be extracted from the abstract mathematics. In others, mathematical expressions could be cast in the appropriate coordinate forms for use in actual solutions, but the inherent complexity remained.

It seems that there is something at work here, perhaps best described as a conservation of complexity. The fundamental nature of the flow problem can apparently be shifted into the geometry of space in innumerable ways through various transformation techniques. In each of these ways, however, actually solving the flow requires that, at some level, the same mathematical problem be attacked—that of solving a nonlinear partial differential boundary value problem. The transformation simply allows one to choose the step at which this problem appears, be it in a mapping or in the flow solution itself. Escaping this

vicious circle of shuffled complexity would require the invention or discovery of fundamental new mathematical techniques that dramatically simplify nonlinear differential equations. Perhaps this concept is obvious to experts in these fields of mathematics and physics, and my quest was a quixotic one borne out of naïveté.

Although this prospect may seem gloomy, it has in actuality been a pleasure to undertake this winding journey. I have learned much—about mathematics, about physics, about numerical methods—and about the nature of theoretical research. These are experiences that I would not trade. In the end, modest new insights into compressible flow were obtained after all. Hopefully these represent some small contribution to humanity's understanding. Perhaps it is best to summarize these thoughts and conclude with the words of Albert Einstein, whose amazing achievements inspired this much more humble one:

> ... the happy achievement seems almost a matter of course, and any intelligent student can grasp it without too much trouble. But the years of anxious searching in the dark, with their intense longing, their alternations of confidence and exhaustion and the final emergence into light—only those who have experienced it can understand it [32].

Bibliography

[1] Abbott, I. H. and von Doenhoff, A. E., *Theory of Wing Sections*. Dover, 1959.

[2] Ackeret, J., "Luftkräfte auf flügel, die mit grösserer als scahllgeschwindigkeit bewegt werden," *Zeitschrift für Mechanik*, vol. 16, p. 1925, 1925.

[3] Ahlfors, L. V., *Lectures on Quasiconformal Mappings*. D. Van Nostrand Company, 1966.

[4] Amick, J. L., "Comparison of the experimental pressure distribution on an NACA 0012 profile at high speeds with that calcuated by the relaxation method," NACA Technical Note 2174, 1950.

[5] Anderson, Jr., J. D., *Modern Compressible Flow with Historical Perspective*. McGraw Hill, 1990.

[6] Anderson, Jr., J. D., *Fundamentals of Aerodynamics*. McGraw-Hill, 1991.

[7] Arina, R., "Orthogonal and conformal surface grid generation," *Applied Numerical Mathematics*, vol. 46, pp. 249–262, 2003.

[8] Aris, R., *Vectors, Tensors, and the Basic Equations of Fluid Mechanics*. Dover Publications, 1962.

[9] Arynov, A., "The steady relativistic flow of gas with axial symmetry (rotational case)," *Soviet Physics–Doklady*, vol. 4, no. 2, pp. 267–498, 1959.

[10] Bauer, F., Garabedian, P., and Korn, D., *Lecture Notes in Economics and Mathematical Systems: Supercritical Wind Sections III*. Springer-Verlag, 1977.

[11] Bergmann, P. G., *Introduction to the Theory of Relativity*. Dover Publications, 1976.

[12] Bers, L., "On a method of constructing two-dimensional subsonic flows around closed profiles," *NACA Technical Note No. 969*, 1945.

[13] Bers, L., "Velocity distribution on wing sections of arbitrary shape in compressible potential flow. I. Symmetric flows obeying the simplified density-speed relation," *NACA Technical Note No. 1006*, 1946.

[14] Bers, L., "Velocity distribution on wing sections of arbitrary shape in compressible potential flow. II. Subsonic symmetric adiabatic flows," *NACA Technical Note No. 1012*, 1946.

[15] Bers, L., "Partial differential equations and generalized analytic functions," *Proceedings of the National Academy of Sciences*, vol. 36, pp. 130–136, 1950.

[16] Bers, L., *Mathematical Aspects of Subsonic and Transonic Gas Dynamics*. John Wiley & Sons, 1958.

[17] Bilić, N., "Relativistic acoustic geometry," *Classical and Quantum Gravity*, vol. 16, pp. 3953–3964, 1999.

[18] Borisenko, A. and Tarapov, I., *Vector and Tensor Analysis with Applications*. Dover Publications, 1968.

[19] Born, M., *Einstein's Theory of Relativity*. Dover Publications, 1962.

[20] Busemann, A., "Application of transonic similarity," NASA Technical Note 2687, 1952.

[21] Cartan, E., *Elie Cartan–Albert Einstein: Letters on Absolute Parallelism*. Princeton University Press, 1979.

[22] Chaplygin, S. A., "On gas jets," *Sci. Annals Imp. Univ. of Moscow, Phys.–Math. Div.*, vol. 21, 1904.

[23] Chaplygin, S. A., "On gas jets," NACA Technical Memorandum 1063, 1944.

[24] Chapman, C., "Similarity variables for sound radiation in a uniform flow," *Journal of Sound and Vibration*, vol. 233, no. 1, pp. 157–164, 2000.

[25] Cherry, T. M., "Flow of a compressible fluid about a cylinder," *Proceedings of the Royal Society of London. Series A, Mathematical and Physical Sciences*, vol. 192, no. 1028, pp. 45–79, 1947.

[26] Cherry, T. M., "Flow of a compressible fluid about a cylinder. II. Flow with circulation," *Proceedings of the Royal Society of London. Series A, Mathematical and Physical Sciences*, vol. 196, no. 1044, pp. 1–31, 1949.

[27] Cherry, T. M., "Numerical solutions for transonic flow," *Proceedings of the Royal Society of London. Series A, Mathematical and Physical Sciences*, vol. 196, no. 1044, pp. 32–36, 1949.

[28] Chung, T. J., *Computational Fluid Dynamics*. Cambridge University Press, 2002.

[29] Courant, R. and Friedrichs, K. O., *Supersonic Flow and Shock Waves*. Springer, 1948.

[30] Drela, M. and Youngren, H., *XFOIL 6.9 User Guide*. MIT Department of Aeronautics and Astronautics, 2001.

[31] Duren, P., Heinonen, J., Osgood, B., and Palka, B., eds., *Quasiconformal Mappings and Analysis: A Collection of Papers Honoring F. W. Gehring*. Springer, 1997.

[32] Einstein, A., *Notes on the Origins of the General Theory of Relativity*. 1934.

[33] Einstein, A., Lorentz, H., Weyl, H., and Minkowski, H., *The Principle of Relativity*. Dover Publications, 1952.

[34] Eisenhart, L. P., *Riemannian Geometry*. Princeton University Press, 1926.

[35] Eisenhart, L. P., *Non-Riemannian Geometry*. American Mathematical Society, 1927.

[36] Emmons, H. W., "The numerical solution of compressible fluid flow problems," NACA Technical Note 932, 1944.

[37] Emmons, H. W., "Flow of a compressible fluid past a symmetrical airfoil in a wind tunnel and in free air," NACA Technical Note 1748, 1948.

[38] Farlow, S. J., *Parital Differential Equations for Scientists and Engineers*. Dover Publications, 1993.

[39] Fischer, M. R. and Visser, M., "Riemannian geometry of irrotational vortex acoustics," *Physical Review Letters*, vol. 88, no. 11, pp. 110201–1–110201–4, 2002.

[40] Frankl, F., "Potential steady relativistic gas flows," *Soviet Physics–Doklady*, vol. 3, pp. 1110–1111, 1958.

[41] French, A., *Special Relativity*. W.W. Norton & Company, 1968.

[42] Fulton, T., Rohrlich, F., and Witten, L., "Conformal invariance in physics," *Reviews of Modern Physics*, vol. 34, no. 3, pp. 442–457, 1962.

[43] Gardner, C. S., "A relation between time-dependent and steady linearized supersonic flows past conical bodies," *Communications in Pure and Applied Mathematics*, vol. 3, pp. 39–43, 1950.

[44] Glauert, H., "The effect of compressibility on the lift of aerofoils," *Proceedings of the Royal Society, Series A*, vol. 118, p. 113, 1928.

[45] Gorskii, V., "Irrotational relativistic gas flow," *Soviet Physics–Doklady*, vol. 17, no. 11, pp. 1035–1037, 1973.

[46] Göthert, B., "Plane and three-dimensional flow at high subsonic speeds," NACA Technical Memorandum 1105, 1946.

[47] Gray, A., *Modern Differential Geometry of Curves and Surfaces with Mathematica*. CRC Press, 1997.

[48] Grossman, S. I., *Calculus*. Harcourt Brace & Company, fifth ed., 1992.

[49] Hantzsche, W. and Wendt, H., "The compressible potential flow past elliptic symmetrical cylinders at zero angle of attack and with no circulation," NACA Technical Memorandum 1030, 1942.

[50] Harder, K. C. and Klunker, E. B., "On slender–body theory and the area rule at transonic speeds," NACA Technical Note 3815, 1956.

[51] Harder, K. C. and Klunker, E. B., "On slender–body theory at transonic speeds," NACA Report 1315, 1957.

[52] Hess, J. L. and Smith, A. M. O., *Progress in Aeronautical Sciences*, vol. 8, ch. Calculation of Potential Flow about Arbitrary Bodies, pp. 1–138. Pergamon Press, 1967.

[53] Hess, R. V. and Gardner, C. S., "Study by the Prandtl–Glauert method of compressibility effects and critical mach number for ellipsoids of various aspect ratios and thickness ratios," NACA Technical Note 1792, 1949.

[54] Jones, R. T. and Cohen, D., *High Speed Wing Theory*. Princeton University Press, 1960.

[55] Kaplan, C., "Two-dimensional subsonic compressible flow past elliptic cylinders," NACA Report 624, 1938.

[56] Kaplan, C., "The flow of a compressible fluid past a sphere," NACA Technical Note 762, 1940.

[57] Kaplan, C., "On similarity rules for transonic flows," NACA Report 894, 1948.

[58] Katz, J. and Plotkin, A., *Low-Speed Aerodynamics*. McGraw-Hill, 1998.

[59] Kleinert, H., "Nonholonomic mapping principle for classical and quantum mechanics in spaces with curvature and torsion," *General Relativity and Gravitation*, vol. 32, no. 5, pp. 769–839, 2000.

[60] Königl, A., "Relativistic gasdynamics in two dimensions," *Physics of Fluids*, vol. 23, no. 6, pp. 1083–1090, 1980.

[61] Kreysig, E., *Differential Geometry*. Dover Publications, 1959.

[62] Kuo, Y. H. and Sears, W., *General Theory of High Speed Aerodynamics*, ch. Plane Subsonic and Transonic Potential Flows, pp. 490–582. Princeton University Press, 1954.

[63] Küssner, H. G. *Luftfahrtforschung*, vol. 17, no. 11/12, 1940.

[64] Küssner, H. G., "General airfoil theory," NACA Technical Memorandum 979, 1941.

[65] Kythe, P. K., *An Introduction to Boundary Element Methods*. CRC Press, 1995.

[66] Lagerstrom, P. A., "Linearized supersonic theory of conical wings," NACA Technical Note 1685, 1950.

[67] Lawden, D., *Introduction to Tensor Calculus, Relativity and Cosmology*. Dover Publications, 2002.

[68] le Rond d'Alembert, J., *Mémoire sur le réfraction des corps solides*. 1741.

[69] Lees, L., "A discussion of the application of the Prandtl-Glauert method to subsonic compressible flow over a slender body of revolution," Technical Note 1127, National Advisory Committee for Aeronautics, 1946.

[70] Liepmann, H. and Roshko, A., *Elements of Gasdynamics*. Dover Publications, 2001.

[71] Lin, C. C., "On an extension of the von kármán–tsiwn method to two-dimensional subsonic flows with circulation around closed profiles," *Quarterly of Applied Mathematics*, vol. 4, no. 3, p. 291, 1946.

[72] Lin, C. C. and Shen, S. F., "Studies of von Kármán's similarity theory and its extension to compressible flows," NACA Technical Note 2541, 1951.

[73] Lock, R. C., "Test cases for numerical methods in two–dimensional transonic flows," AGARD Report 575, 1970.

[74] Mastin, C. W. and Thompson, J. F., "Quasiconformal mappings and grid generation," *SIAM Journal of Scientific Computing*, vol. 5, pp. 305–310, 1984.

[75] McDevitt, J. B., "A correlation by means of the transonic similarity rules of the experimentally determined characteristics of 22 rectangular wings of symmetrical profile," NACA Research Memorandum A51L17b, 1952.

[76] Miles, J. W., "General solution for rectangular airfoil in supersonic flow," *Quarterly of Applied Mathematics*, vol. 11, no. 1, pp. 1–8, 1953.

[77] Miles, J. W., "On the transformation of the linearized equation of unsteady supersonic flow," *Quarterly of Applied Mathematics*, vol. 12, no. 1, pp. 1–12, 1954.

[78] Miles, J. W., *The Potential Theory of Unsteady Supersonic Flow*. Cambridge University Press, 1959.

[79] Miller, D. C., "The ether-drift experiment and the determination of the absolute motion of the earth," *Reviews of Modern Physics*, vol. 5, pp. 203–242, 1933.

[80] Misner, C. W., Thorne, K. S., and Wheeler, J. A., *Gravitation*. W. H. Freeman and Company, 1973.

[81] Molenbroeck, P., "Ueber einige bewegungen eines gases bei annahme eines geschwindigkeitspotentials," *Archiv. Math. und Phys., Grunert Hoppe*, vol. 9, pp. 157–195, 1890.

[82] Moran, J., *An Introduction to Theoretical and Computational Aerodynamics*. John Wiley & Sons, 1984.

[83] Moriyasu, K., *An Elementary Primer for Gauge Theory*. World Scientific Publishing Company, 1983.

[84] Morse, P. M. and Ingard, K. U., *Theoretical Acoustics*. Princeton University Press, 1968.

[85] Murman, E. M. and Cole, J. D., "Calculation of plane steady transonic flows," *AIAA Journal*, vol. 9, pp. 114–121, 1971.

[86] Nieuwland, G. Y., "Transonic potential flow round a family of quasi-elliptic aerofoil sections," Tech. Rep. NLR-TR T. 172, 1967.

[87] Norton, J. D., "General covariance and the foundations of general relativity: eight decades of dispute," *Rep. Prog. Phys.*, pp. 791–858, 1993.

[88] Ogata, K., *System Dynamics*. Prentice Hall, 4th ed., 2004.

[89] Pathria, R. K., *The Theory of Relativity*. Dover Publications, 2003.

[90] Pauli, W., *Theory of Relativity*. Dover Publications, 1981.

[91] Perl, W. and Klein, M. M., "Theoretical investigation and application of transonic similarity law for two dimensional flow," NACA Technical Note 2191, 1950.

[92] Prandtl, L., "Ueber strömungen deren geschwindigkeiten mit der schallgeschwindigkeit vergliecher sind," *Journal of the Aeronautical Research Institute, Tokyo Imperial University*, no. 65, p. 14, 1930.

[93] Prandtl, L., "General considerations on the flow of compressible fluids," NACA Technical Memorandum 805, 1936.

[94] Reissner, E., "On compressibility corrections for subsonic flows over bodies of revolution," NACA Technical Note 1815, 1949.

[95] Rosen, N., "Special theories of relativity," *American Journal of Physics*, vol. 20, pp. 161–164, 1951.

[96] Sankar, L. N. and Smith, M. J., *Advanced Compressible Flow II*, ch. 5: The Transonic Full Potential Equation. 1995.

[97] Schutz, B. F., *A First Course in General Relativity*. Cambridge University Press, 1985.

[98] Sears, W. R., "Some aspects of non-stationary airfoil theory and its practical application," *Journal of the Aeronautical Sciences*, vol. 8, no. 3, pp. 104–108, 1941.

[99] Sears, W., *General Theory of High Speed Aerodynamics*, ch. Small Perturbation Theory, pp. 61–121. Princeton University Press, 1954.

[100] Sells, C. C. L., "Plane subcritical flow past a lifting aerofoil," Tech. Rep. 67146, R. A. E., 1967.

[101] Shankara, T. and Majhi, S., "Linearized supersonic motion under a Lorentz-like transformation," *Journal of Sound and Vibration*, vol. 82, no. 3, pp. 391–400, 1982.

[102] Shankara, T. and Nandi, K. K., "Transformation of coordinates associated with linearized supersonic motions," *Journal of Applied Physics*, vol. 49, no. 12, pp. 5783–5789, 1978.

[103] Shapiro, A. H., *The Dynamics and Thermodynamics of Compressible Fluid Flow*. The Ronald Press Company, 1953.

[104] Spreiter, J. R., "On the application of transonic similarity rules," NACA Technical Note 2726, 1952.

[105] Spreiter, J. R., "On the application of transonic similarity rules to wings of finite span," NACA Report 1153, 1953.

[106] Synge, J. and Schild, A., *Tensor Calculus*. Dover Publications, 1949.

[107] Tannehill, J. C., Anderson, D. A., and Pletcher, R. H., *Computational Fluid Mechanics and Heat Transfer*. Taylor & Francis, 1997.

[108] Taub, A., "Relativistic Rankine–Hugoniot equations," *Physical Review*, vol. 74, no. 3, pp. 328–334, 1948.

[109] Taub, A., "Isentropic hydrodynamics in plane symmetric space–times," *Physical Review*, vol. 103, no. 2, pp. 454–467, 1956.

[110] Thomas, L. H., "Elliptic problems in linear difference equations over a network," Watson Scientific Computing Laboratory Report, Columbia University, 1949.

[111] Thorne, K. S., Misner, C. W., and Wheeler, J. A., *Gravitation*. W. H. Freeman, 1973.

[112] Todeschini, B., "Hodograph relativistic equations of plane flows," *Meccanica*, vol. 5, no. 2, pp. 69–73, 1970.

[113] Todeschini, B., "Small-perturbation theory of steady plane relativistic flows," *Meccanica*, vol. 5, no. 1, pp. 17–21, 1970.

[114] Tolman, R. C., *Relativity, Thermodynamics, and Cosmology*. Dover Publications, 1987.

[115] Truitt, R. W., *North Carolina State Department of Engineering Research, Bulletin No. 47*. 1950.

[116] Truitt, R. W., "Compressible relativistic flow," *The Physics of Fluids*, vol. 11, no. 10, pp. 2089–2094, 1968.

[117] Tsien, H.-S., "Two-dimensional subsonic flow of compressible fluids," *Journal of the Aeronautical Sciences*, vol. 6, no. 10, pp. 399–407, 1939.

[118] Unger, J., "Anwendung der Lorentz-transformation auf das ueberschall-strömungsfeld eines axial angeströmten kreiskegels," *Zeitschrift für Angewandte Mathematik und Mechanik*, vol. 55, pp. T162–T166, 1975.

[119] Unruh, W. G., "Experimental black–hole evaporation?," *Physical Review Letters*, vol. 46, no. 21, pp. 1351–1353, 1981.

[120] Van Dyke, M., *Perturbation Methods in Fluid Mechanics*. The Parabolic Press, 1975.

[121] Van Dyke, M., "Long series in mechanics: Janzen–Rayleigh expansion for a circle," *Meccanica*, vol. 33, pp. 517–522, 1998.

[122] Van Dyke, M. D., "The similarity rules for second-order subsonic and supersonic flow," NACA Report 1374, 1958.

[123] Van Dyke, M. D. and Guttmann, A. J., "Computer extension of the M^2 expansion for a circle," *Bulletin of the American Physical Society*, vol. 23, p. 996, 1978.

[124] Van Dyke, M. D. and Guttmann, A. J., "Subsonic potential flow past a circle and the transonic controversy," *Journal of the Australian Mathematical Society, Series B*, vol. 2, pp. 243–261, 1983.

[125] Visser, M., "Acoustic black holes: Horizons, ergospheres, and Hawking radiation," *Classical and Quantum Gravity*, vol. 15, pp. 1767–1791, 1998.

[126] von Kármán, T., "Compressibility effects in aerodynamics," *Journal of the Aeronautical Sciences*, vol. 8, no. 9, pp. 337–356, 1941.

[127] von Kármán, T., "Supersonic aerodynamics—principles and applications," *Journal of the Aeronautical Sciences*, vol. 14, no. 7, p. 396, 1947.

[128] von Mises, R., *Mathematical Theory of Compressible Fluid Flow*. Dover Publications, 1958.

[129] Wald, R. M., *General Relativity*. The University of Chicago Press, 1984.

[130] Wasserbauer, C. A., Weaver, H. F., and Senyitko, R. G., "NASA low-speed axial compressor for fundamental research," NASA Technical Memorandum 4635, 1995.

[131] Willmore, T. J., *An Introduction to Differential Geometry*. Oxford University Press, 1959.

[132] Wisler, D. C., "Loss reduction in axial-flow compressors through low-speed model testing," *Journal of Engineering for Gas Turbines and Power, Transactions of the ASME*, vol. 107, no. 2, pp. 354–363, 1985.